

DETERMINATION OF THE ENERGY LEVELS OF Eu^{2+} FOR
NEXT-GENERATION LED PHOSPHORS

A dissertation submitted to the
College of Graduate and Postdoctoral Studies
in partial fulfillment of the requirements
for the degree of Doctor of Philosophy
in the Department of Physics and Engineering Physics
University of Saskatchewan
Saskatoon

By
Muhammad Ruhul Amin

©Muhammad Ruhul Amin, August 2022. All rights reserved.

Unless otherwise noted, copyright of the material in this thesis belongs to
the author.

PERMISSION TO USE

In presenting this dissertation in partial fulfillment of the requirements for a Postgraduate degree from the University of Saskatchewan, I agree that the Libraries of this University may make it freely available for inspection. I further agree that permission for copying of this dissertation in any manner, in whole or in part, for scholarly purposes may be granted by the professor or professors who supervised my dissertation work or, in their absence, by the Head of the Department or the Dean of the College in which my dissertation work was done. It is understood that any copying or publication or use of this dissertation or parts thereof for financial gain shall not be allowed without my written permission. It is also understood that due recognition shall be given to me and to the University of Saskatchewan in any scholarly use which may be made of any material in my dissertation.

Requests for permission to copy or to make other uses of materials in this dissertation in whole or part should be addressed to:

Head of the Department of Physics and Engineering Physics
Physics Building, Room 163
116 Science Place
University of Saskatchewan
Saskatoon, Saskatchewan S7N 5E2 Canada

OR

Dean
College of Graduate and Postdoctoral Studies
University of Saskatchewan
116 Thorvaldson Building, 110 Science Place
Saskatoon, Saskatchewan S7N 5C9 Canada

ABSTRACT

The structural-property relationship of any novel materials, whether nanoscaled or in the bulk form must be understood for their successful applications. Soft X-ray spectroscopy is used to probe the electronic structures of materials. Furthermore, density functional theory calculations are used to interpret the experimental observations, which allows linking the electronic properties to the underlying atomic arrangements and luminescence parameters. In this thesis, InN and phosphor-converted light emitting diodes (pc-LEDs) are studied using these experimental techniques and theoretical methods.

InN is a key material for technological applications in opto-electronic devices because of its relatively small band gap; however there is a persistent and active debate about its varying band gap values and their origin. The electronic structure and the band gap of ammonothermal InN powder samples are studied as a first part of this thesis. Further the origin of the measured band gap is discussed in terms of the presence of oxygen impurities and the impurity phases of InN.

pc-LEDs can significantly reduce global energy consumption and are expected to dominate the lighting market. In pc-LEDs, the energetic position of activator ions with respect to the conduction band (CB) and valence band (VB) of the host lattice determines the electronic and luminescence properties including multicolor emission, adjustable bandwidth, and thermal quenching under application conditions. The second part of my study involves the direct measurements of the energy levels of activator Eu^{2+} ions for three highly efficient color-sensitive Eu^{2+} -doped phosphors such as ultranarrow band blue-emitting oxoberyllates $A\text{ELi}_2[\text{Be}_4\text{O}_6]:\text{Eu}^{2+}$ ($A = \text{Ba}, \text{Sr}$), red-luminescence $\text{SrLi}_2\text{Al}_2\text{O}_2\text{N}_2:\text{Eu}^{2+}$, and blue-luminescence nitridoberyllates $M\text{Be}_{20}\text{N}_{14}:\text{Eu}^{2+}$ ($M = \text{Ba}, \text{Sr}$). New characterization methods with existence techniques such as soft X-ray resonant inelastic X-ray scattering (RIXS) and X-ray excited optical luminescence (XEOL) measurements are used for directly determining the energy level of Eu^{2+} ions. Modern phosphors use the $4f^65d^1$ to $4f^7$ transition of Eu^{2+} , where $4f^65d^1$ is an excited state. We directly determine the energetic separation between the $\text{Eu}^{2+} 4f^65d^1$ state and the CB of host lattice using RIXS measurements. Thus, the location of the $\text{Eu}^{2+} 4f^65d^1$ states is below the CB of the corresponding energy separation. The $4f^7$ energy level is determined from the $4f^65d^1 \rightarrow 4f^7$ transition of Eu^{2+} ions with respect to the $4f^65d^1$ states using XEOL techniques. Therefore, we determine all participating energy levels of Eu^{2+} ions ($4f^65d^1$ and $4f^7$ states) of the studied phosphors. Thus, we identify all radiative processes involved in the design of next generation pc-LEDs. These experimental techniques allow direct access to the intragap states of the Eu^{2+} -dopants, which are the source of the luminescence of Eu^{2+} -doped phosphors.

ACKNOWLEDGEMENTS

I firstly express all of my admiration and devotion to the almighty Allah, the most beneficial who has enabled me to perform this research work and to submit this thesis.

I would like to thank all the people who contributed in some way to the work described in this thesis. Most importantly, I express my profound gratitude to my honourable supervisor, Dr. Alex Moewes, Professor in the department of Physics and Engineering Physics at University of Saskatchewan and Canada Research Chair for Materials Science with Synchrotron Radiation, for believing in me and giving me the opportunity to study in this great country. During my five years in his group, he generously provided me with support, inspiration, guidance, encouragement, and the freedom to pursue this research. I am grateful for the opportunity he has given me by taking on the role of my supervisor. As a foreign student, I am extremely happy to get very collaborative and supportive environment he has cultivated in his entire group.

I am grateful to the other members in the beamteam who were not just my colleagues during the last five years, but also my teammates and friends. Firstly, I am very thankful to Dr. Tristan de Boer and Dr. Amir Qamar, who worked on the same types of projects. They trained me on the calculation methods on a day-to-day basis, and shared their research ideas and thoughts with me. I also would like to thank Patrick Braun and Josha Ho with whom I had less overlap but who were nonetheless wonderful friends and colleagues.

I am thankful to Professor Dr. Gerhard Herzberg's family for considering me for the Gerhard Herzberg Memorial Scholarship for 2019-2020. I am grateful to the Government of Saskatchewan for financial support by Saskatchewan Innovation and the Opportunity Scholarship 2017-2018. I acknowledge support from NSERC and the Canada Research Chair program. I also acknowledge Compute Canada. The calculations presented in this paper were performed on the Cedar high-performance computing cluster, which is part of the WestGrid (www.westgrid.ca) and Compute Canada Calcul Canada (www.computecanada.ca).

Finally, I would like to thank my family, my parents for their endless support, unconditional love and constant encouragement. A very special thank goes to eternal love Nazia Arifa, my wife who came in Canada from eleven thousand kilometres away to accompany me. She is taking care of me and our two kids (Muhammad Rafsan Amin and Muhammad Raizan Amin), who are my main inspiration to work hard. Their smiling face always helped me to erase any hard times and encouraged me to look forward. Thank you all.

Dedicated to my lovely wife, Nazia Arifa and two wonderful kids, Muhammad Rafsan Amin and Muhammad Raizan Amin

CONTENTS

1	Introduction	1
1.1	Motivation for Studying Luminescent Materials	2
1.2	Luminescent Materials	7
1.3	Configurational Coordinate Model	11
1.4	Objective of the Thesis	14
1.5	Outline of the thesis	20
2	Experimental Techniques	22
2.1	X-ray Interactions with Matter	23
2.2	Synchrotron Radiation and Insertion Devices	27
2.3	X-ray Absorption Spectroscopy	30
2.3.1	X-ray Absorption Near-Edge Spectroscopy	34
2.3.2	Extended X-ray Absorption Fine Structure Spectroscopy	37
2.4	X-ray Emission Spectroscopy	38
2.4.1	Nonresonant X-ray Emission Spectroscopy	40
2.4.2	Resonant X-ray Emission Spectroscopy	41
2.4.3	Resonant Inelastic X-ray Scattering	41
2.5	X-ray Excited Optical Luminescence (XEOL) Spectroscopy	43
2.6	Soft X-ray Endstations	44
2.6.1	Resonant Elastic and Inelastic X-ray Scattering Beamline	45
2.6.2	Beamline 8.0.1.1	45
2.6.3	Variable Line Spacing - Plane Grating Monochromator Beamline	46

3	Calculation Methods	47
3.1	Wave Function	48
3.2	Schrödinger’s Equation	49
3.3	Electron Density	50
3.4	Many-Body Hamiltonian	51
3.4.1	Born-Oppenheimer Approximation	52
3.5	Density Functional Theory	53
3.5.1	Hohenberg and Kohn Theorems	54
3.5.2	Kohn-Sham Equations	58
3.6	Exchange Correlation Energy Functionals	62
3.6.1	Local Density Approximation	62
3.6.2	Generalized Gradient Approximation	63
3.6.3	Tran–Blaha modified Becke–Johnson potential	63
3.7	Choice of Basis Set	65
3.8	Calculation Details	69
4	Bandgap and Electronic Structure Determination of Oxygen - Con-	
	taining Ammonothermal InN: Experiment and Theory	70
4.1	INTRODUCTION	72
4.2	EXPERIMENTAL SECTION	74
4.2.1	Synthesis	74
4.2.2	XAS, XES and XEOL Measurements	74
4.3	DFT CALCULATION DETAILS	75
4.4	RESULTS AND DISCUSSION	76
4.4.1	N and O K-edge Absorption and Emission spectra	76
4.4.2	Band Gap	81
4.4.3	X-ray Excited Optical Luminescence (XEOL) Spectra	84
4.5	CONCLUSIONS	86

5	Understanding of Luminescence Properties Using Direct Measurements on Eu²⁺-doped Wide Band Gap Phosphors	89
5.1	Introduction	91
5.2	Experimental Sections	93
5.2.1	Preparation of the Samples	93
5.2.2	XAS, XES and XEOL Measurements	94
5.2.3	Thermal Quenching Measurements	94
5.3	Density Functional Theory (DFT) Calculations	95
5.4	Results and Discussion	97
5.4.1	Oxygen K-edge Spectra	97
5.4.2	Band Gap Determination	99
5.4.3	Density of States (DOS)	102
5.4.4	Band Structure and RIXS Spectra	102
5.4.5	Position of the Eu ²⁺ 5d States in the Band Gap	104
5.4.6	Optical Transition Provided by XEOL	107
5.5	Conclusions	108
6	Unraveling the Energy Levels of Eu²⁺-ions in <i>M</i>Be₂₀N₁₄:Eu²⁺ (<i>M</i> = Sr, Ba) Phosphors	111
6.1	INTRODUCTION	113
6.2	METHODS	115
6.2.1	Synthesis	115
6.2.2	XAS, XES, and XEOL Measurements	116
6.2.3	Density Functional Theory Calculations Details	117
6.3	RESULTS AND DISCUSSION	120
6.3.1	N K-edge Spectra	120
6.3.2	Band Gap Determination	121
6.3.3	Partial Density of States	122

6.3.4	Band Structure and RIXS Spectra	124
6.3.5	Determination of $\text{Eu}^{2+} 4f^6 5d^1$ Energy Levels	125
6.3.6	Determination of $\text{Eu}^{2+} 4f^7$ Energy Levels from Luminescence Spectra	129
6.4	CONCLUSIONS	132
7	Energy Levels of Eu^{2+} States in the Next-Generation LED-Phosphor $\text{SrLi}_2\text{Al}_2\text{O}_2\text{N}_2:\text{Eu}^{2+}$	136
7.1	Introduction	138
7.2	Experimental Techniques and Calculations Method	141
7.2.1	XAS, XES and XEOL Measurements	141
7.2.2	Density Functional Theory Calculations Details	142
7.3	Results and Discussion	143
7.3.1	N K-edge XAS and XES spectra	143
7.3.2	O K-edge XAS and XES spectra	145
7.3.3	Band Gap Determination	146
7.3.4	Partial Density of States	147
7.3.5	Band Structure and RIXS Spectra	149
7.3.6	Energetic Position of the $\text{Eu}^{2+} 5d^1$ States in the Band Gap . .	150
7.3.7	Energetic Position of the $\text{Eu}^{2+} 4f^7$ States from Luminescence Spectrum	154
7.3.8	Energy Levels of Eu^{2+} States in the $\text{SrLi}_2\text{Al}_2\text{O}_2\text{N}_2:\text{Eu}^{2+}$ Phosphor	156
7.4	Conclusions	158
8	Conclusion	161
	Appendix A: Copyright Information	184
A.1	Copyright Agreements for Reproduced Articles	184
A.1.1	Journal of Physical Chemistry C	184

A.1.2	Journal of Material Chemistry C	184
A.1.3	Advanced Optical Materials	184
A.2	Permissions to Reproduce Figures	185

LIST OF TABLES

2.1	Correspondence between X-ray absorption edges and their electronic configurations. Table is taken from Ref. [91].	25
4.1	Measured, calculated and previously reported band gaps for InN. The measured band gap is denoted by $\Delta_{\text{expt.}}$ and the calculated band gap is denoted by Δ_{mBJ} using mBJ functional. The experimental techniques and calculation methods for previously reported band gap determination are also included. All numbers are in eV.	82
5.1	Measured and calculated band gaps. The measured band gap is denoted by $\Delta_{\text{expt.}}$ and the calculated band gap is denoted by Δ_{GGA} and Δ_{mBJ} for PBE-GGA and mBJ functional, respectively. The one available literature band gap value is also included. All units are in eV.	100
5.2	Comparison of the Standard Deviation (σ_1 , for elastic peak; σ_2 , for inelastic peak) and the Eu^{2+} 5d to conduction band energy separations ΔE_{RIXS} from RIXS measurements; ΔE_{TQ} from TQ measurements) from the fits shown in Fig. 5.5. Fitting parameter ($\frac{\Gamma_0}{\Gamma_\nu}$) of Eq. 5.1 is also included in this table.	105

6.1	Measured, calculated, and previously reported band gap values for $M\text{Be}_{20}\text{N}_{14}:\text{Eu}^{2+}$ ($M = \text{Sr}, \text{Ba}$). The measured band gap is denoted by $\Delta_{\text{expt.}}$ and the calculated band gap is denoted by Δ_{GGA} and Δ_{mBJ} for PBE-GGA functional and mBJ functional, respectively. The available literature band gap values are also denoted in the same way. All units are in eV.	122
6.2	Standard deviation for elastic peak (σ_1) and inelastic peak (σ_2) from the fits shown in Figure 6.5(a), and the Eu^{2+} $5d$ to CB energy separations from RIXS measurements (ΔE_{RIXS}) and from TQ measurements (ΔE_{TQ}). Fitting parameter ($\frac{\Gamma_0}{\Gamma_V}$) of Eq. 6.1 is also included in this table.	128
6.3	The available literature values of the bottom of the CB and the lowest $4f^6 5d^1$ states of Eu^{2+} -ions from the RIXS measurements (ΔE_{RIXS}) and from TQ measurements (ΔE_{TQ}).	129
7.1	Measured, calculated, and previously reported band gap values for $\text{SrLi}_2\text{Al}_2\text{O}_2\text{N}_2:\text{Eu}^{2+}$. The measured band gap is denoted by $\Delta_{\text{expt.}}$ and the calculated band gap is denoted by Δ_{GGA} and Δ_{mBJ} for PBE-GGA and mBJ functional, respectively. The available literature band gap value is also denoted in the same way. All units are in eV.	147
7.2	Standard deviation for elastic peak (σ_1) and inelastic peak (σ_2) from the fits shown in Fig. 7.5(b), and the Eu^{2+} $5d^1$ to conduction band energy separations from RIXS measurements (ΔE_{RIXS}) and from TQ measurements (ΔE_{TQ}). Fitting parameter ($\frac{\Gamma_0}{\Gamma_V}$) of Eq. 7.1 is also included in this table.	152
7.3	The available literature values of the energy separation between bottom of the CB and the lowest $4f^6 5d^1$ states of Eu^{2+} -ions from the RIXS measurements (ΔE_{RIXS}) and from TQ measurements (ΔE_{TQ}).	153

8.1	Measured, calculated, and previously reported band gap values of the studied phosphors. The measured band gap is denoted by $\Delta_{\text{expt.}}$ and the calculated band gap is denoted by Δ_{GGA} and Δ_{mBJ} for PBE-GGA functional and mBJ functional, respectively. The available literature band gap values are also denoted in the same way. All units are in eV.	163
8.2	Determined energy separation between the bottom of the conduction band of host material and the lowest $4f^65d^1$ states from the RIXS (ΔE_{RIXS}) and TQ measurements (ΔE_{TQ}).	164

LIST OF FIGURES

1.1	Evolution of luminous efficacy performance of white light sources. Commercially available high-power LED performance is indicated by points along the solid blue curve. The diagram is taken from Ref. [23]. . . .	3
1.2	Schematic setup of a flip-chip pc-LED. Yellow-green, orange-red and/or blue phosphors cover a nUV or blue emitting primary LED and white light is obtained by energy down conversion. The diagram is taken from Ref. [26].	6
1.3	Schematic luminescence process from activator ions in a host crystal. The Figure is taken from Ref. [34].	8
1.4	Schematics of $5d$ energy levels of a free Eu^{2+} ion and Eu^{2+} ions in nitride compounds. Both the nephelauxetic effect and crystal-field splitting affect the Eu^{2+} emission. The Figure is taken from Ref. [34].	9
1.5	A schematic of a configurational coordinate model. The two curves represent the total energies of the ground-state and the excited-state of the Eu^{2+} ions. The vertical blue and red dotted-lines indicate the excitation and emission processes, respectively. Thermal quenching results from the promotion of excited electrons from point C to the conduction band minimum if the temperature is high sufficiently to overcome the activation energy ΔE [59]. The diagram is adapted from Ref. [59].	12

1.6	A schematic comparison of RIXS spectra between Eu^{2+} -doped sample (a) and undoped sample (b) both excited at the conduction band onset. Two Gaussians, blue (elastic feature) and green (loss feature) are used to fit the the experimental spectrum (red). In the case of (a), the black spectrum (fit) is identical with the red spectrum and therefore only the black spectrum is visible. In the case of (b), the black spectrum, the red spectrum, and blue spectrum are identical and thus only the blue spectrum is visible.	17
1.7	A schematic diagram of energy levels of Eu^{2+} -doped phosphor. The band gap is added from XAS and NXES measurements. The energy separation between bottom of the CB and lowest level of $4f^6 5d^1$ -states (vertical pink line, ΔE) is determined from RIXS measurements. The energy level of $4f^7$ with respect to $4f^6 5d^1$ -states is determined from the $4f^6 5d^1 \rightarrow 4f^7$ transition (blue luminescence in this case, λ_{em}) measured by XEOL.	19
2.1	A schematic diagram of an insertion device. Diagram is taken from Ref. [91].	28
2.2	Schematic representation of the X-ray absorption process.	30
2.3	Schematic representation of the the Beer-Lambert law.	31
2.4	Measurement of TEY. The ejected Auger electrons leave behind a positively charged sample. If connected to the ground, the neutralizing current flowing into the sample is proportional to the time-averaged Auger electron creation rate, which is proportional to the core hole creation rate.	32
2.5	Measurement method of TFY.	33
2.6	X-ray absorption spectrum of FeO with XANES and EXAFS regions. The figure is taken from Ref. [91].	36

2.7	Schematic representation of the X-ray emission process.	39
2.8	Initial ($ \psi_i\rangle$), intermediate ($ \psi_j\rangle$), and final ($ \psi_f\rangle$) state wave- functions for a Kramers-Heisenberg X-ray transition in a single-particle band structure.	43
3.1	Schematic flowchart of the iterative procedure used in self-consistent calculations. The diagram is taken from Ref. [107].	61
4.1	(a) SEM image of platelets InN from ammonothermal synthesis at 663 K. (b) SEM image of rods InN from ammonothermal synthesis at 773 K.	75
4.2	Measured and calculated N K-edge XES and XAS spectra. (a): Calcu- lated and measured N K-edge XES spectra. Experimental and calcu- lated (orange) N K-XES spectra of InN are compared with Wurtzite- type $\text{InO}_{0.0625}\text{N}_{0.9375}$ (green) and $\text{InO}_{0.5}\text{N}_{0.5}$ (blue). (b): Measured and calculated N K-edge XAS spectra. Experimental PFY (solid line) and TEY (dotted line) of InN are compared with core hole (solid line) and ground-state calculations (dash - dotted line) of InN, $\text{InO}_{0.0625}\text{N}_{0.9375}$ and $\text{InO}_{0.5}\text{N}_{0.5}$. (c): Second derivatives of the XES spectra of N K-edge of InN, with peaks corresponding to valence band edges indicated by the arrows. (d): Second derivative of PFY (TEY) of XAS spectra of N K-edge of platelets InN in red solid line (dotted line) and rods InN in black solid line (dotted line) with peaks corresponding to conduction band edges indicated by the arrows.	77

4.3	<p>Measured and calculated O K-edge XES and XAS spectra. (a): Calculated and measured O K-edge XES spectra. Experimental (cyan) and calculated (purple) XES spectra of c-In₂O₃ are compared with experimental XES spectra of platelets (red) and rods (black) of InN as well as the calculated hypothetical Wurtzite-type InO_{0.0625}N_{0.9375} (green) and InO_{0.5}N_{0.5} (blue). (b): Calculated and measured O K-edge XAS spectra. Measured PFY, core hole and ground state (dash-dotted) calculations of O K-edge XAS spectra of c-In₂O₃ are compared with measured O K-edge XAS of platelets and rods of InN as well as core hole and ground state calculations of hypothetical Wurtzite-type InO_{0.0625}N_{0.9375} and InO_{0.5}N_{0.5}.</p>	80
4.4	<p>XEOL spectra of InN platelets, c-In₂O₃ and the variation of photon attenuation length with excitation energy. Experimental XEOL spectra of InN at three different excitation energies are presented in (a), (b) and (c). The XEOL spectra exhibit features located at 274 nm, 288 nm, 305 nm, 328 nm, 351 nm, 425 nm, 667 nm, 921 nm and at 973 nm. To fit the two broad peaks located at 425 nm and at 667 nm, three Gaussians and the luminescence spectrum of c-In₂O₃ (green) are used. The variation of photon attenuation length (logarithmic scale) with excitation energy for InN is presented in (d) with data from Ref. [181]. The three stars labeled in this graph represent the three excitation energies in our measurements.</p>	84

- 5.1 Measured and calculated O K-edge XES and XAS spectra of $\text{BaLi}_2\text{Be}_4\text{O}_6:\text{Eu}^{2+}$ (solid lines) and undoped $\text{BaLi}_2\text{Be}_4\text{O}_6$ (dotted lines). (a): NXES spectrum (blue) excited at 561.0 eV and RIXS spectra (black, red and green) collected at various excitation energies for $\text{BaLi}_2\text{Be}_4\text{O}_6:\text{Eu}^{2+}$ and $\text{BaLi}_2\text{Be}_4\text{O}_6$ are compared with ground state (G.S.) calculations (orange). The vertical dotted magenta line indicates that the highest emission energy is observed at the highest excitation energy in the RIXS spectra. (b): Measured PFY, core hole (C.H.) and G.S. calculations of O K-edge XAS spectra of $\text{BaLi}_2\text{Be}_4\text{O}_6:\text{Eu}^{2+}$ and $\text{BaLi}_2\text{Be}_4\text{O}_6$ are compared. The colour-coded arrows indicate where in the conduction band the O 1s electron was excited to obtain the corresponding color-coded emission spectra. Second derivatives of the NXES (c) and XAS (s) spectra, with peaks corresponding to valence band edges and conduction band edges are indicated by the arrow, respectively. . . . 96
- 5.2 XAS and XES spectra of $\text{SrLi}_2\text{Be}_4\text{O}_6:\text{Eu}^{2+}$. The XES (a) and XAS (b) spectra are shown alongside DFT calculations. The calculated ground state (G.S.) and excited state (core hole, C.H.) XAS spectra are shown as solid orange and dash-dotted orange, respectively. The vertical dotted magenta line in (a) is used to guide the eye in finding the highest emission energy among the RIXS spectra. The second derivatives of the experimental NXES spectrum excited at 561.0 eV and the XAS spectrum are shown in panel (c) and (d), respectively. 98
- 5.3 Calculated density of states for $A\text{ELi}_2[\text{Be}_4\text{O}_6]$ ($AE = \text{Ba}, \text{Sr}$) based on ground state GGA-PBE calculations. Calculated partial and total DOS of Ba, Be, Li and two inequivalent O atoms for $\text{BaLi}_2[\text{Be}_4\text{O}_6]$ in (a) and Sr, Be, Li and two inequivalent O atoms for $\text{SrLi}_2\text{Be}_4\text{O}_6$ in (b) are compared. The energy zero is at the Fermi level. 101

5.4	Calculated band structure of $\text{BaLi}_2[\text{Be}_4\text{O}_6]$ in (a) and $\text{SrLi}_2\text{Be}_4\text{O}_6$ in (b) based on ground state GGA-PBE calculations. For both samples, the conduction minimum is at the Z point and the VB maximum between the M and A points. The energy scales are set with respect to the Fermi energy, E_F	103
5.5	(a) Measured luminescence intensity as a function of temperature for $\text{BaLi}_2\text{Be}_4\text{O}_6:\text{Eu}^{2+}$ (black) and $\text{SrLi}_2\text{Be}_4\text{O}_6:\text{Eu}^{2+}$ (blue), along with the fit (solid line) of Equation 5.1 to the measured data. (b) RIXS spectra (red) for $\text{BaLi}_2\text{Be}_4\text{O}_6:\text{Eu}^{2+}$ and $\text{BaLi}_2\text{Be}_4\text{O}_6$ excited at 533.0 eV (at the CB onset) and for $\text{SrLi}_2\text{Be}_4\text{O}_6:\text{Eu}^{2+}$ excited at 533.4 eV (at the CB onset). Two Gaussian black (elastic feature) and blue (loss feature) are used to fit the spectrum (green).	104
5.6	XEOL spectra of $\text{BaLi}_2\text{Be}_4\text{O}_6:\text{Eu}^{2+}$ and $\text{SrLi}_2\text{Be}_4\text{O}_6:\text{Eu}^{2+}$ excited at 140 eV. Both Eu^{2+} -doped samples show a strong ultra-narrow band luminescence feature at 455-457 nm, which is due to the $\text{Eu}^{2+} 5d^1 4f^6 \rightarrow 4f^7$ optical transition. Both spectra were accumulated for the same time.	107
5.7	Energy level diagram of $\text{BaLi}_2\text{Be}_4\text{O}_6:\text{Eu}^{2+}$ and $\text{SrLi}_2\text{Be}_4\text{O}_6:\text{Eu}^{2+}$. Band gaps are determined from our measurements and calculations. DOS calculations show that the upper edge of the VB is dominated by O p-states for both compounds and the lower edge of the CB is dominated by d-states of Ba and Sr for $\text{BaLi}_2\text{Be}_4\text{O}_6:\text{Eu}^{2+}$ and $\text{SrLi}_2\text{Be}_4\text{O}_6:\text{Eu}^{2+}$, respectively. The $\text{Eu}^{2+} 5d^1$ -states are added to the diagram from RIXS measurements and XEOL measurements show the $5d^1 4f^6 \rightarrow 4f^7$ optical transitions. Both compounds emit blue luminescence at 455 nm. . .	108

6.1	Crystal structure of the isotypic compounds $M\text{Be}_{20}\text{N}_{14}$ ($M = \text{Sr}, \text{Ba}$). BeN_4 tetrahedra are presented in green, $M\text{N}_{12}$ ($M = \text{Sr}, \text{Ba}$) cuboctahedra in cyan, and N atoms in blue. The figure is adapted from ref. [209].	115
6.2	(a) NXES spectrum (blue for $M = \text{Sr}$ and black for $M = \text{Ba}$) was excited at 435.0 eV and RIXS spectra were collected at excitation energies of 398.1 eV (green) and 399.0 eV (red), which are compared to the ground state (GS, dotted-dash orange) calculations. The vertical dotted-dash black line indicates the higher emission energy observed at higher excitation energy in the RIXS spectra. (b) Experimental PFY is compared to the CH (solid orange) and the GS (dotted-dash orange) calculations. Two colored downward arrows on the absorption spectra indicate the corresponding excitation energies at which the RIXS spectra were taken. (c) and (d) Second derivative of experimental NXES and XAS spectra with the corresponding valence band and conduction band onsets indicated by black arrows.	119
6.3	The partial density of states for $\text{BaBe}_{20}\text{N}_{14}$ in (a) and for $\text{SrBe}_{20}\text{N}_{14}$ in (b) using GGA-PBE functional. The energy of zero is the Fermi level.	123
6.4	Calculated band structure of $\text{BaBe}_{20}\text{N}_{14}$ in (a) and $\text{SrBe}_{20}\text{N}_{14}$ in (b) based on ground state mBJ functional calculations. For both samples, the conduction minimum and valence band maximum are at the Z point and Γ point, respectively. The energy scales are set with respect to the Fermi energy, E_F	125

6.5	<p>(a) RIXS spectra for $M\text{Be}_{20}\text{N}_{14}:\text{Eu}^{2+}$ ($M = \text{Sr}, \text{Ba}$) excited at the CB onset (398.1 eV). Two Gaussians (blue: elastic scattering at 0 eV and black: inelastic scattering at -0.30 eV for $M = \text{Ba}$ and at -0.31 eV for $M = \text{Sr}$) are used to fit the experimental spectrum (red). (b) Measured luminescence of $4f^65d^1 \rightarrow 4f^7$ transition of Eu^{2+} as a function of temperature for $M\text{Be}_{20}\text{N}_{14}:\text{Eu}^{2+}$ ($M = \text{Sr}$ (blue), Ba (black)) along with the fit (solid line) using Equation 6.1 to the measured data. Temperature-dependent data are published in ref. [209].</p>	127
6.6	<p>X-ray excited optical luminescence spectra of $M\text{Be}_{20}\text{N}_{14}:\text{Eu}^{2+}$ ($M = \text{Ba}$ (black), Sr (blue)) excited at 100 eV. Both compounds exhibit a remarkably narrow emission in the blue spectral region and a broader red-shifted emission band in the green spectral region.</p>	131
6.7	<p>Energy levels of $M\text{Be}_{20}\text{N}_{14}:\text{Eu}^{2+}$ ($M = \text{Sr}, \text{Ba}$). The band gap is added from our XAS and NXES measurements. Our DFT calculations show that the CB minimum is dominated by d-states of Ba/Sr and the VB maximum originates from N p-states, which are added accordingly. The energy separation (0.30 eV for $M = \text{Ba}$ and 0.31 eV for $M = \text{Sr}$) between bottom of the CB and lowest level of $4f^65d^1$-states (vertical pink line) is determined from RIXS measurements. The energy level of $4f^7$ is obtained from the $4f^65d^1 \rightarrow 4f^7$ transition (origin of blue luminescence) measured by XEOL.</p>	133
7.1	<p>Crystal structure of $\text{SrLi}_2\text{Al}_2\text{O}_2\text{N}_2:\text{Eu}^{2+}$. The $[\text{LiO}_3\text{N}]^{8-}$ tetrahedra are presented in green, $[\text{AlON}_3]^{8-}$ tetrahedra in yellow and brown the highly symmetrical cuboid-like polyhedron coordination represents the environment of Sr^{2+}.</p>	140

7.2	<p>(a) Experimental and calculated N K-edge XES spectra of $\text{SrLi}_2\text{Al}_2\text{O}_2\text{N}_2:\text{Eu}^{2+}$ for different excitation energies. NXES spectrum excited at 440.0 eV (blue) and RIXS spectra collected at excitation energies of 399.1 eV (black) and 400.5 eV (green), which are compared to the ground state (GS) calculations. The vertical dotted black line indicates the highest emission energy observed at the highest excitation energy in the RIXS spectra. (b) Experimental PFY is compared to the core hole (CH) and the ground state (GS) calculations. Two colored downward arrows on the absorption spectrum indicate the corresponding excitation energies for the RIXS spectra. (c and d) Second derivative of experimental XES and XAS spectra with the corresponding peaks of valence band and conduction band onsets, respectively indicated by black arrows. . . .</p>	144
7.3	<p>O K-edge XAS and XES spectra of $\text{SrLi}_2\text{Al}_2\text{O}_2\text{N}_2:\text{Eu}^{2+}$. The XES (a) and XAS (b) spectra are shown alongside DFT calculations. The calculated ground state (GS) and excited state (CH) XAS spectra are shown as solid gold and solid magenta, respectively. The vertical dotted magenta line in (a) is used to guide the eye in finding the highest emission energy among the RIXS spectra. The second derivatives of the experimental NXES spectrum excited at 550.0 eV and the XAS spectrum are shown in panel (c) and (d), respectively.</p>	145
7.4	<p>(a) The partial density of states for $\text{SrLi}_2\text{Al}_2\text{O}_2\text{N}_2:\text{Eu}^{2+}$ using the GGA-PBE functional. The energy zero is at the Fermi level. (b) Calculated band structure of $\text{SrLi}_2\text{Al}_2\text{O}_2\text{N}_2:\text{Eu}^{2+}$ based on ground state mBJ functional calculations. The energy scale is set with respect to the Fermi energy, E_F.</p>	148

7.5	<p>(a) Measured intensity of $5d^1 \rightarrow 4f^7$ transition of Eu^{2+} ions as a function of temperature for $\text{SrLi}_2\text{Al}_2\text{O}_2\text{N}_2:\text{Eu}^{2+}$ along with the fit (solid line) of Equation 7.1 to the measured data. (b) Comparison of N K-edge and O K-edge RIXS spectra for $\text{SrLi}_2\text{Al}_2\text{O}_2\text{N}_2:\text{Eu}^{2+}$ excited at the CB onset. Two Gaussian green (elastic feature) and blue (loss feature) are used to fit the spectrum (black).</p>	151
7.6	<p>X-ray excited optical luminescence spectrum of $\text{SrLi}_2\text{Al}_2\text{O}_2\text{N}_2:\text{Eu}^{2+}$ excited at 160 eV, which exhibits red luminescence at 610 nm with 51 nm full width at half-maximum.</p>	155
7.7	<p>Influences of coordination environments of $\text{SrLi}_2\text{Al}_2\text{O}_2\text{N}_2:\text{Eu}^{2+}$ on the $5d^1$ energy levels of Eu^{2+}. Band gap is taken from N K-edge measurements. Energy separation between the conduction band and lowest level of $5d^1$-states is included from RIXS N K-edge measurements and red emission band energy of 2.03 eV is observed from the XEOL measurements.</p>	157

LIST OF ABBREVIATIONS

XES	X-ray emission spectroscopy
XAS	X-ray absorption spectroscopy
NXES	Non-resonant x-ray emission spectroscopy
RXES	Resonant x-ray absorption spectroscopy
RIXS	Resonant inelastic x-ray scattering
XEOL	X-ray excited optical luminescence
TFY	Total fluorescence yield
TEY	Total electron yield
PFY	Partial fluorescence yield
IPFY	Inverse partial fluorescence yield
DFT	Density functional theory
pc-LED	Phosphor-converted light emitting diode
UV	Ultraviolet
CRI	Color rendering index
LAPW	Linearized augmented plane wave
LO	Local orbital
VB	Valence band
CB	Conduction band
LCAO	Linear combination of atomic orbitals
RE	Rare earth
REIXS	Resonant elastic and inelastic x-ray scattering
SGM	Spherical grating monochromator
FWHM	Full width at half maximum
SDD	Silicon drift detector
ALS	Advanced light source
BGO	Bismuth germanium oxide
h-BN	Hexagonal boron nitride
CLS	Canadian light source
DOS	Density of states
EXAFS	Extended X-ray absorption fine structure
GGA	Generalized gradient approximation
LDA	Local density approximation
mBJ	Modified Becke-Johnson exchange correlation functional

PBE	Perdew-Berke-Ernzerhof GGA exchange correlation functional
PL	Photoluminescence
PDOS	Partial density of states
UHV	Ultra-high vacuum
VBM	Valance band maximum
CBM	Conduction band minimum
VLS-PGM	Variable line spacing plane grating monochromator
XANES	X-ray absorption near-edge structure

Chapter 1

Introduction

This dissertation involves studying the electronic and optical properties of nitride materials (InN and highly efficient color-sensitive Eu^{2+} -doped phosphor materials) using several synchrotron-based soft X-ray experimental techniques and density functional theory (DFT) calculations. This introductory chapter presents a brief overview of the motivation behind these particular materials that were investigated.

White phosphor-converted light emitting diodes (pc-LEDs) consist of a blue or a near ultra-violet (nUV) LED chip with a combination of red, green, and blue phosphors to generate white light. A prerequisite for the development of white pc-LEDs was the development of highly efficient blue semiconductor LEDs or nUV LEDs. The emission color of a semiconductor LED depends on the band gap of the materials. Approximately 3.4 eV direct band gap is needed to produce blue emission [1]. GaN is a suitable candidate to produce blue emission. Isamu Akasaki and Hiroshi Amano synthesized GaN crystals by Metal-organic Vapor Phase Epitaxy (MOVPE) technique in 1986 [1]. The technical advance was made by Nakamura, who synthesized an InGaN/AlGaN double heterojunction that emits blue light and has a 2.7% quantum efficiency [2]. This made it possible to generate white pc-LEDs by coating blue semiconductor primary LEDs with energy-convertible phosphors [2]. So the first goal in this study was to investigate the electronic structure and band gap of InN. InN is a

key material for technological applications because of its tunable band gap; however, there is a persistent and active debate about its varying band gap values and their origin. As we know, the synthesis process and impurities play a major role affecting the experimental band gap. For the first time, InN samples were grown by ammonothermal method by P. Becker, J. Hertrampf and R. Niewa. Since the band gap of InN is tunable and the band gap depends on the synthesis process, thus I would expect the large band gap of this InN powder even in the blue emission. For this reason, I have chosen ammonothermal InN powder samples as a first project of my PhD study. After finishing my first project, I turned to the main topic of my PhD. Here, I studied highly efficient color-sensitive phosphors such as ultranarrow band blue-emitting oxoberyllates $AELi_2[Be_4O_6]:Eu^{2+}$ ($AE = Ba, Sr$), blue-luminescence $MBe_{20}N_{14}:Eu^{2+}$ ($M = Ba, Sr$), and red-luminescence $SrLi_2Al_2O_2N_2:Eu^{2+}$.

1.1 Motivation for Studying Luminescent Materials

A phosphor is a solid that can absorb energy from incident radiation and emit light after a series of energy transfer processes. A phosphor is composed of a host lattice and a luminescent center, usually called the activator. In most cases, the activator absorbs the excitation energy, rises to an excited state, and then returns to the ground state by emitting radiation. The nature of both the activator ion and host lattice determines the absorption and emission characteristics. Phosphor emissions are in the visible and in the invisible ranges, such as in the ultraviolet [3, 4] or infrared [5, 6]. However, the most commercially important phosphors are those with visible emissions. Phosphors have generally the form of powders. The particle size, distribution, and morphology of these powder samples determine the applications of phosphors in various demanding areas [7]. Large crystals (4 to 5 μm in size) of high-quality phosphors are required [8] for most commercial applications because quantum efficiencies

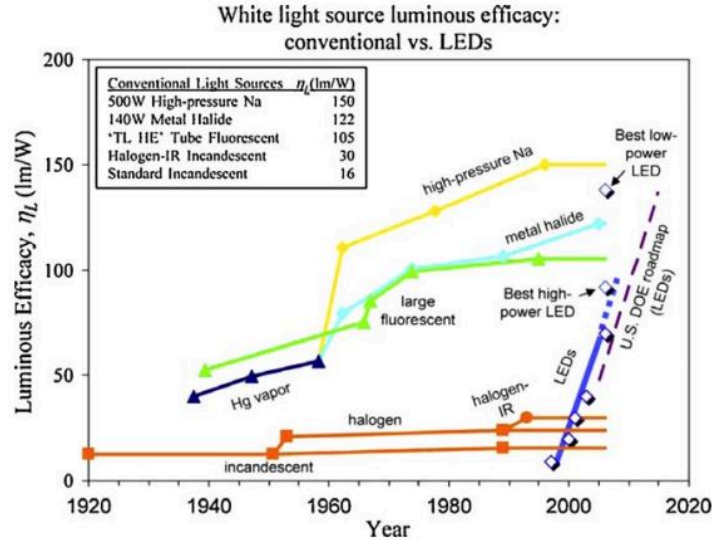


Figure 1.1: Evolution of luminous efficacy performance of white light sources. Commercially available high-power LED performance is indicated by points along the solid blue curve. The diagram is taken from Ref. [23].

(Quantum efficiency is the number of emitted photons per hole in the orbital the luminescence decays to [9]) are higher in crystals than in amorphous hosts [10]. Currently, luminescent materials are used in several applications across different fields. The traditional applications include lighting and emissive display devices [7, 11, 12], amplifiers in optical communication [13], and lasers [3, 14]. In addition, phosphors are also utilized in X-ray detector systems [15, 16] and scintillators [15, 17]. Developments on phosphors for these novel applications are well documented in many reviews and books [11, 17, 18]. Most recently, phosphors have found applications in new areas such as solar cells [19, 20] and white-light-emitting diodes (WLEDs) [12, 21] because of the increasing benefits related to energy efficiency [22].

Currently, conventional white light sources dominate illumination in everyday use; however they have almost reached their physical limit of efficiency. Figure 1.1 shows the progress of white LED efficiency over time compared to conventional light source development. For conventional incandescent lamps and fluorescent lamps, a large

amount of energy is consumed as heat radiation for high-temperature tungsten filament lamps and mercury vapor discharge lamps. Most traditional lighting users are considering alternative lighting options because of its high cost, low efficiency, and environmental concerns [9]. The luminescence efficiency of semiconductor-based WLEDs can be greatly improved by reducing the nonradiative recombination of electron-hole pairs in the p-n junctions and by designing a new structure to enhance external quantum efficiency. To ensure high external quantum efficiency, the phosphor should also have a high absorbance of the incident light.

In 2014, the Nobel Prize in Physics was awarded jointly to Isamu Akasaki, Hiroshi Amano, and Shuji Nakamura “for the invention of efficient blue LEDs”, who developed these bright and energy-saving blue light sources [24]. Therefore, InGaN-based WLEDs were debuted and appeared as a new generation and alternative of solid state lighting (SSL) after highly efficient InGaN-based blue LEDs were invented in 1993 [25]. Further, these lights consume significantly less power and provide higher light quality, better preservation of color point stability (Color point stability describes the ability of a light source to maintain its color properties over time [9]), and longer lifetime than incandescent and fluorescence lamps [26, 27]. LED-based lighting is expected to replace incandescent and fluorescent lamps in general lighting applications with better color rendering index (CRI) (CRI is a quantitative property that measures the ability of a light source to reveal the colors of objects in comparison to that observed under an ideal or natural light source [9]), less energy consumption, and longer bulb lifetime. LEDs are utilised in a variety of ways to produce white light [28]. The first method involves using three different blue, yellow-green, and red LEDs; however the disadvantage of this strategy is that each color of the LED has varied operating lifetimes and driving currents and it requires complex electronics. Other disadvantages include the lack of high external quantum efficiency in green-yellow LEDs, and the temperature sensitivity of emission wavelengths in other LEDs.

Special circumstances still allow for the use of such devices. Phosphor-converted LEDs (pc-LEDs) employ a single LED in conjunction with one or more phosphor materials to convert the LED output [29, 30]. In 1996, the first commercially available white light was created using 1 pc-LED that combined a blue LED with a broad-band yellow phosphor such as $\text{Y}_3\text{Al}_5\text{O}_{12}:\text{Ce}^{3+}$ (YAG:Ce) [31, 32], however the red spectral parts are not contained in the emission of YAG:Ce, which causes poor CRI (usually smaller than 75) and highly correlated color temperature (Correlated color temperature describes the color appearance of a light source by correlating it with the temperature of an ideal blackbody radiator [33]) (mostly higher than 4500 K) [34]. However, for household use, a CRI of around 80 is required. Furthermore, higher CRIs are needed for some special circumstances. Using blue, red, and green multiphosphors with a blue LED (RGB pc-LED) can change the emission spectra. The efficiency and light quality of this approach are limited because of the lost energy of the powerful primary blue LED and insufficient color point stability. To solve these problems, nUV-LED can be used in combination with blue, red, and green multiphosphors, where the multiphosphors absorb nUV-light from the primary nUV-LED and emit the combined corresponding colors generated by phosphors to obtain white light. Here, the generated white light depends only on the phosphors as human eyes are not sensitive to nUV. This approach allows to produce higher CRI (greater than 90), high chromatic stability, and luminous efficacy (Luminous efficacy estimates the number of lumens generated at the cost of an electric power drawn. It is the ratio of luminous flux to input power [33]) because of the larger emission band of blue phosphor than primary blue LED and fills the spectral gap between the blue (from LED) and green (from phosphors) regions when selecting appropriate phosphors [34, 35].

Figure 1.2 demonstrates the schematic setup of the different combination of phosphors with a n-UV or a blue LED to generate white light [26]. Therefore, when trying to

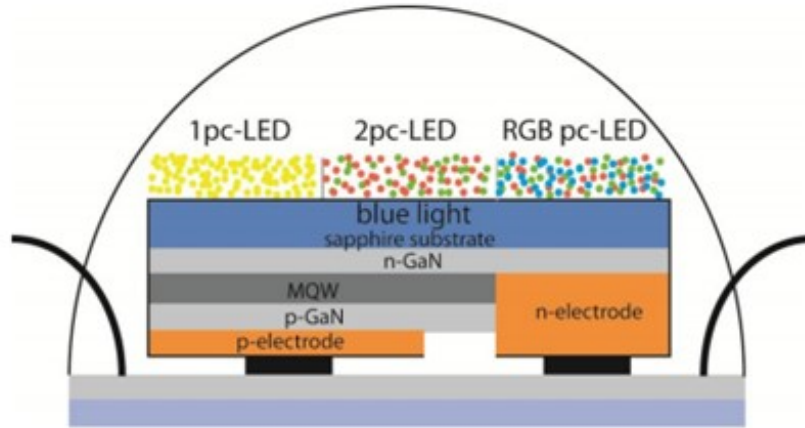


Figure 1.2: Schematic setup of a flip-chip pc-LED. Yellow-green, orange-red and/or blue phosphors cover a nUV or blue emitting primary LED and white light is obtained by energy down conversion. The diagram is taken from Ref. [26].

design a new phosphor for use in a pc-LED, some caution is required. There is a requirement for overlap between pump emissions and the phosphor's excitation spectrum as well as the necessity to optimize particle sizes for the reduction of scattering losses [9]. Furthermore, it is important to obtain emissions in the desired region of the visible spectrum, and the emission being thermally stable [9]. Luminescent materials with similar crystal structures have been investigated; however they do not exhibit the same properties in terms of emission band width and thermal quenching [26, 27, 36–41]. Therefore a deeper understanding of the structure-property relationships is required to design new luminescent materials with improved properties and enhance the luminescence properties of existing phosphors. This ultimately allows control of the luminescence properties of modern phosphors by varying chemical and structural composition of their host lattices. At present, synchrotron-based soft X-ray experimental techniques and DFT calculations are excellent tools to understand the structure-property relationships of luminescent materials [36, 37, 42, 43]. In this thesis, luminescent materials are studied using the synchrotron-based soft X-ray facilities and DFT calculations. This study will broaden and deepen the understanding of the electronic and optical properties of luminescent materials and contribute in the ongo-

ing investigation into efficient narrow-band emitting phosphors. Furthermore, it will play an important role in the advancement of light emitting diodes by introducing new phosphors to the lighting market.

1.2 Luminescent Materials

As stated above, luminescent materials consist of a host material and activators [44]. Most common host materials are aluminates, silicates, nitride, and (oxo)nitrido(silicates). The host lattice affects the luminescence properties and performance of the activator and activator ions determine the luminescence properties. Activator ions doped into a solid host lattice experience a local crystalline environment that has immense influence on the luminescence properties of that activator ion. A transition metal ion or a rare earth ion typically serves as an activator. Activators are coordinated by ligands in a host lattice. The attraction between positively charged activator ion and negatively charged non-bonding electrons of ligands give rise to a crystal field interaction between the activator ion and ligand. This interaction leads to the splitting of d -orbitals of the luminescent centre. Figure 1.3 shows that the activator in phosphors converts nUV or blue emission to visible light. The elemental composition of the host lattice affects the energy of the $5d$ states of the activator ions, which lie energetically in the band gap. The visible luminescence of interest is caused by the $5d \rightarrow 4f$ transition in the activator ions (typically Eu^{2+} or Ce^{3+}). The energetic spacing of the $4f$ and $5d$ states of the activator ions depends on several factors.

Transition metal ions experience considerably stronger crystal field effects than the rare-earth ion because the perturbation in the crystal environment is bound to affect the spectroscopically active d orbitals of the transition metals more than that of the rare-earths. Lanthanides form the most significant class of luminescent dopants introduced in inorganic solids for LEDs. The rare-earth elements include lanthanide elements from La ($Z=57$) to Lu ($Z=71$). The extreme end elements of the series such as La and Lu do not possess electronic levels to initiate any $f-f$ or $f-d$ transitions that

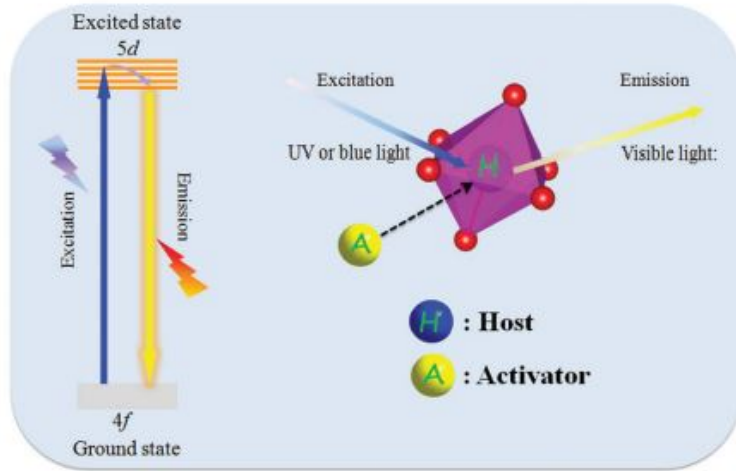


Figure 1.3: Schematic luminescence process from activator ions in a host crystal. The Figure is taken from Ref. [34].

can produce luminescence because $4f$ orbitals are empty for La and the $4f$ orbitals are completely filled for Lu. All other elements of the lanthanide series are characterized by incompletely filled $4f$ orbitals. The $4f$ orbitals have a high probability of being relatively close to the nucleus and they are shielded by the completely filled $5s$ and $5p$ orbitals. Therefore, the host lattice shows a very small influence on the optical transitions occurring within the $4f$ orbitals. The $4f$ orbitals are very localized and atomic-like, which gives rise to narrow atomic-like transitions that are relatively independent of any surrounding host matrix. Most trivalent states of lanthanides show sharp line spectra because of these transitions; however these transitions are spectroscopically forbidden, and hence, they appear with weak intensity most of the time. However, the admixture of forbidden $4f-4f$ transitions with the allowed transitions, for example $4f-5d$ transitions, make it possible for the former to occur. The symmetry of the crystal environment can affect the selection rules controlling the transitions. A transition may be either of magnetic dipole nature, electric dipole nature, or a combination of both. A magnetic dipole transition does not depend on the symmetry, and its strength does not change with the site-symmetry. The electric dipole transition can be forbidden by symmetry. For this reason, the electric dipole

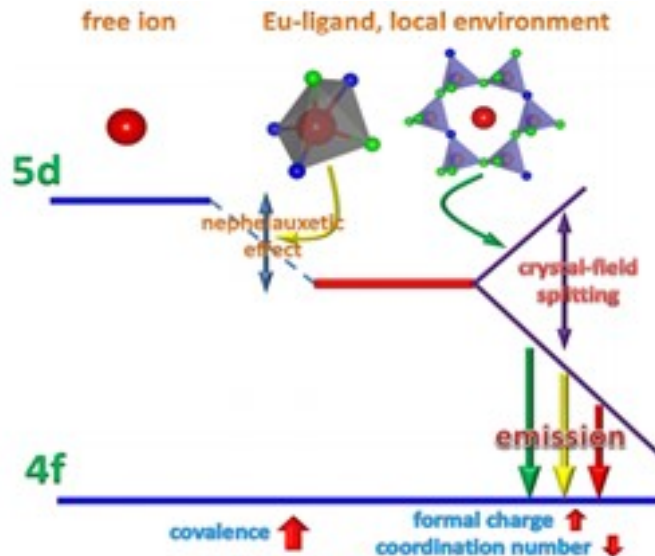


Figure 1.4: Schematics of $5d$ energy levels of a free Eu^{2+} ion and Eu^{2+} ions in nitride compounds. Both the nephelauxetic effect and crystal-field splitting affect the Eu^{2+} emission. The Figure is taken from Ref. [34].

transition is influenced by the crystal site-symmetry, and its strength increases when the lanthanide ion occupies a site with non-inversion symmetry [33]. Electrons in the $4f$ orbitals are arranged in discrete energy levels relatively unaffected by the crystal field because of the strong shielding of the outer orbitals. This remains the reason for the trivalent lanthanides exhibiting similar energy level diagrams in its free-ion state and when doped into a certain host matrix.

Figure 1.4 depicts the nephelauxetic effect (centroid shift) and crystal field splitting for the nitride compound, and the impact of the host crystal on the luminescence of Eu^{2+} ions. These effects lead to an increase or decrease in the energy difference between the $5d$ and $4f$ level known as the blue shift or red shift respectively. With the exception of Ce^{3+} , all other trivalent lanthanides show their narrowband excitation and emission peak positions with a variation of $\pm 500 \text{ cm}^{-1}$ from that of a free ion. Although all lanthanides from Ce^{3+} to Yb^{3+} can show luminescence, not all are favorable for LED phosphors. Trivalent ions like Yb^{3+} , Tm^{3+} , Er^{3+} , Ho^{3+} ,

and Nd^{3+} are more inclined to exhibit upconversion luminescence and are totally out of the frame of LED phosphors [45, 46]. The most prominently used lanthanides for LED applications are Ce^{3+} , Sm^{3+} , Eu^{3+} , Eu^{2+} , Tb^{3+} , and Dy^{3+} . In this study, Eu^{2+} -doped phosphors are studied. Eu^{2+} -doped phosphors involve the substitution of the Sr^{2+} , Ca^{2+} , or Ba^{2+} cations with Eu^{2+} because of the similarity of their ionic radii [Eu^{2+} :1.25, Ca^{2+} :1.06, Sr^{2+} :1.26, Ba^{2+} :1.35 Å] [47]. Eu^{2+} ion has a $4f^7$ electron configuration, and it is the most commonly used activator in luminescent materials for pc-LEDs because of its unique $5d-4f$ transition. Eu^{2+} -doped phosphors exhibit outstanding luminescence properties, which include multicolor emission, adjustable bandwidth, excellent thermal stability, and high luminescence efficiency. In addition, Eu^{2+} -doped phosphors have a strong, broad excitation band covering the emissions from n-UV LED chips, and an intense emission ranging from the UV to the red region [48–50]. Eu^{2+} exhibits broad excitation and emission bands corresponding to the parity-allowed $4f^{n-1}5d \rightarrow 4f^n$ electronic transitions. The spectroscopic features of the $5d-4f$ transitions are strongly influenced by the crystal environment. This implies that the intensity and energy of the transition is strongly affected by the crystal field strength, crystal lattice symmetry, nature of bonds (covalence/ionic), atomic coordination, bond strength, etc.

The energy difference between the $4f$ ground state and $5d$ excited state of the free Eu^{2+} ion is $34,000 \text{ cm}^{-1}$ (4.22 eV) [51]. The energy difference between the two levels is significantly decreased because of the centroid shift and the crystal field splitting when Eu^{2+} ion is doped into a certain host matrix [52]. The $5d$ orbitals experience a centroid downshift depending on the host in which the ion is doped. Furthermore, it can be associated with the covalency of the host. As covalency increases, the interaction between electrons is reduced because they are spread over wider ranging orbitals; this is the well-known nephelauxetic effect, which involves anion polarizability, ion electronegativity, and cation-anions bonding characteristics [53, 54]. Transition ener-

gies are dependent on the electron-electron interactions, which leads to a reduction of the energy required to transition between states. This is attributed to the centroid experiencing downshift because of the reduction of the interelectron repulsion, which is ascribed to the sharing of electrons between the activator ions and surrounding ligand anions. Thus, the degree of the centroid downshift determines the covalency of the host. Since the anion polarizability, symmetry, covalency, and crystal field of the host lattice significantly influences the $5d$ orbitals of Eu^{2+} , its excitation and emission spectra can be tuned by introducing a structural change or variation in the chemical composition of the host. The structural change in the host compound can be achieved by performing crystal-site engineering, anionic-substitution, cationic substitution, cationic-anionic substitution, control of doping concentration, or by mixing of multiple phases [55]. In the crystal-site engineering approach, the Eu^{2+} activator ion is introduced into different cationic sites available in the host [56]. This cationic site bears a different coordination environment, and hence, the emission properties of the activator ions also experience spectral tuning. Thus, the emission of the luminescent materials depends on the energetic position of Eu^{2+} $5d$ state.

1.3 Configurational Coordinate Model

The configurational coordinate model was proposed to explain the luminescence process of an activator and the thermal quenching of the luminescence material [57]. Seitz and Mott have introduced this model known as Mott-Seitz Model [58]. Thermal quenching is one of the most difficult problems of phosphors where the efficiency of the phosphor varies with temperature. Thermal quenching is attributed to the excitation of excited state ($5d$) electrons to the conduction band (CB) for Eu^{2+} -doped phosphors. Thus, these electrons are not available anymore for the luminescence process, and therefore, reduce the light output. This process occurs at high temperatures when the thermal vibrations of atoms surrounding the luminescent center transfer en-

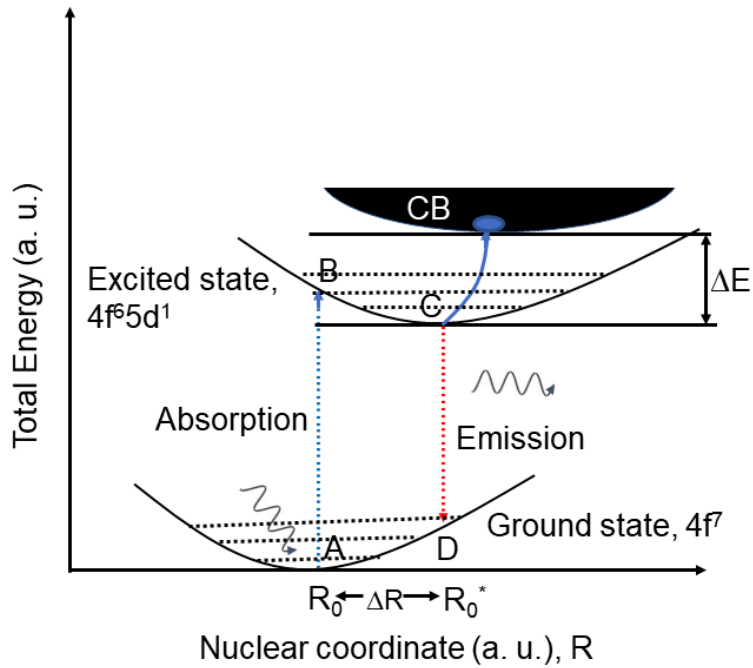


Figure 1.5: A schematic of a configurational coordinate model. The two curves represent the total energies of the ground-state and the excited-state of the Eu^{2+} ions. The vertical blue and red dotted-lines indicate the excitation and emission processes, respectively. Thermal quenching results from the promotion of excited electrons from point C to the conduction band minimum if the temperature is high sufficiently to overcome the activation energy ΔE [59]. The diagram is adapted from Ref. [59].

ergy away from the center leading to a nonradiative recombination and a subsequent dissipation of excess energy as phonons in the host lattice. The thermal quenching of phosphors has a significant impact on their practical applications. Some phosphors have promising photoluminescence properties; however the photoluminescence begins at low temperature, and sometimes, there is no luminescence at room temperature, when luminescence is quenching rapidly, it prevents these materials from meeting the requirements for practical use. The thermal quenching and luminescence process can be explained based on potential energy curves, which represents the total energy of the atom in its ground state $4f^7$ and excited states as a function of nuclear coordinate. Here, total energy implies the sum of the electron and ion energies. The curves in Figure 1.5 represents the total energy of the ground and excited states of the luminescent center.

The ground and excited states are shown in the form of parabolic potential wells.

This parabolic shape is due to the vibration motion and it can be expressed with Hooke's law, which can be explained using the harmonic oscillator [60]. The electrons is promoted from ground-state of activator to its excited-state after absorbing energy. The x-axis represents the interatomic distance between the activator ion and its nearest neighbour anions. R_0 and R_0^* represent the equilibrium distances of the ground-state and excited-state of activators, respectively. The equilibrium positions of the two states are different from each other because of the spatial distribution of the electron orbitals. An expansion of the lattice occurs near the activator ion and activator is raised to the excited-state when the activator absorbs some radiation light [61]. Frank-Condon principle states that in any optical transition, the atomic nuclei remain at rest.

The excitation (EX) and emission (EM) processes are illustrated by vertical blue and red arrows, respectively in Fig. 1.5. Figure 1.5 describes the luminescence process, which starts through energy absorption from $A \rightarrow B$. Undesirable nonradiative relaxation (phonons) takes place from $B \rightarrow C$ with emission occurring from $C \rightarrow D$ followed by the nonradiative relaxation from $D \rightarrow A$. Thermal activation can take place when the localized $5d$ electron of the Eu^{2+} (from C) has an increasing probability to be promoted to the CB of the host upon increasing temperature. This reduces the probability of radiative transition. The probability of the photoexcitation process depends on the energy gap (ΔE) between the $5d$ level and CB minimum. ΔE is related to ΔR , which is the difference between the equilibrium distances of the excited and ground states [62]. If ΔR is large, ΔE is lower. For lower ΔR , the ΔE is large resulting to improve the thermal stability of phosphors [63]. Stronger activator-ligand bonds in a structurally rigid host lattice are expected to reduce ΔR , improving the thermal stability of phosphors. When the temperature is raised, $5d$ electrons will be thermally activated to CB, delocalized, and its energy is dissipated through nonradiative energy transfer to traps or killer centers. Therefore, the smaller ΔE gap results

in larger thermal quenching. Dorenbos proposed a simplified relationship between ΔE and quenching temperature $T_{0.5}$ as [64]

$$\Delta E = \frac{T_{0.5}}{680}, \quad (1.1)$$

where $T_{0.5}$ represents the temperature at which the intensity of the luminescence falls to exactly one-half of its maximum value. Thus, thermal quenching and nature of emission band of luminescence materials depend on the energetic position of the activator ions (here, Eu^{2+}).

1.4 Objective of the Thesis

As mentioned above, the most important properties of luminescence materials such as thermal quenching and nature of emission band under application conditions depend on the energetic position of $\text{Eu}^{2+} 5d$ levels. However, direct measurements of Eu^{2+} state energies are completely lacking, as only few are accessible through standard optical spectroscopy experiments. This is complicated by the fact that the $\text{Eu}^{2+} 5d^1$ state is an excited state, and therefore, it is not accessible by standard methods. We will show that X-ray spectroscopy techniques allow the measurement of these states energies, and therefore, provide a powerful complement to optical studies. Previously, the energetic position of the $\text{Eu}^{2+} 5d^1$ state was determined indirectly by fitting thermal quenching data [37, 64–67]. Thermal quenching measurements of phosphors measure the intensity reduction of emission occurring high temperatures. In this approach, the position of the $\text{Eu}^{2+} 5d^1$ state can be determined from the fitting of intensity as a function of temperature data. The simplest description of thermal quenching in a material can be derived from a description of the decay rate of the $\text{Eu}^{2+} 5d^1$ state [64]

$$\Gamma(T) = \Gamma_\nu + \Gamma_0 e^{-\frac{\Delta E_{\text{TQ}}}{k_B T}}, \quad (1.2)$$

where Γ_ν represents the radiative decay rate, Γ_0 represents the attempt rate for TQ process, k_B represents the Boltzmann's constant, and ΔE_{TQ} represents the energy

barrier for thermal quenching between the lowest $5d$ level and the bottom of the CB. This gives the following form to the luminescence intensity as a function of temperature [64]

$$I(T) = \frac{I_0}{1 + \frac{\Gamma_0}{\Gamma_\nu} e^{-\frac{\Delta E_{TQ}}{k_B T}}}, \quad (1.3)$$

where I_0 denotes the initial luminescence intensity at room temperature (25 °C). The pre-exponential factor Γ_0/Γ_ν and the energy barrier for photoionization ΔE_{TQ} are called Arrhenius parameters, which are the variables in Equation 1.3 when fitting the experimental data. The Arrhenius equation (Equation 1.3) is commonly used to describe the temperature dependence of processes like chemical reactions or electron transitions. Parameter Γ_0/Γ_ν determines how rapidly the decay occurs with temperature and the parameter ΔE_{TQ} determines at what temperature TQ starts to become significant [64]. Thermal quenching data are often unreliable to determine the energetic position of Eu^{2+} $5d$ states because thermal quenching is strongly influenced by the concentration of dopants and the presence of defects [68, 69]; however the Arrhenius equation (Equation 1.3) does not consider these defects and impurities, which tend to reduce the luminescence output.

On the other hand, calculating absolute energies of Eu^{2+} ions is difficult and always requires careful calibration with experimental data. In general, DFT codes have trouble to calculate absolute energies. However, if the calculation of the energies are possible, it would still be necessary to calibrate with the experimental data. Therefore calculating absolute $5d$ energies is currently not possible with sufficient accuracy. In addition, transitions between the localized $4f$ states are easy to calculate with multiplet codes like Quanta [70, 71]. As for the calculations of the $5d$ to $4f$ transitions, the first problem is that the luminescence wavelength depends strongly on the host material because the Eu^{2+} $5d$ energy levels are very sensitive to the

surrounding host lattice. The problem is therefore entirely with the calculation of the Eu^{2+} $5d$ energy levels. The specific problem is that the Eu^{2+} has two open Eu^{2+} shells ($4f^7$ and $4f^6 5d^1$), which require very large matrices (with well over 30000 elements) that are computationally very costly [72].

This study determines the energetic position of Eu^{2+} states with respect to the CB and VB of the host lattice directly using soft X-ray spectroscopy. We utilize the resonant inelastic X-ray scattering (RIXS) [37, 65, 66, 73] and X-ray excited optical luminescence (XEOL) [74, 75] to directly measure the energetic position of Eu^{2+} states; in particular the Eu^{2+} $5d^1$ state with respect to the CB and $4f^7$ ground state of Eu^{2+} with respect to the Eu^{2+} $5d^1$ state for phosphors. In the RIXS measurements, we determine the energetic position of the $5d^1$ state with respect to the CB of the host material by monitoring the energy losses in the RIXS experiments for these phosphors [37, 65, 66, 73]. For the energy loss feature of our RIXS measurements, the CB onset energy is selected for excitation energy. This is because the authors in Ref. [76] reported that the defect associated with energy loss was the strongest for WO_3 from the O K-edge RIXS, when the excitation energy is at the band onset. The energy loss feature is determined by plotting the graph in the energy loss scale, which is obtained by subtracting the excitation energy from the emission energy. A schematic presentation of the RIXS spectra of a Eu^{2+} -doped sample and an undoped sample on the energy loss scale is presented in Fig. 1.6. Thus, the elastically scattered radiation (blue in Fig. 1.6) occurs at 0 eV and any other energy loss features located at lower energies. Then, two spectral features are observed for the Eu^{2+} -doped samples. The additional feature (green feature in Fig. 1.6(a)) observed below the elastic scattering peak represents an energy loss in the incident X-rays attributed to the low-energy excitations [77]. The cross section for the $5d^1$ to CB inelastic scattering is extremely low and the Eu^{2+} concentration is diluted ($\approx 1 - 2\%$), which makes these measurements extremely photon hungry and difficult causing a large error bar in the X-ray measurements. Therefore, due to the low cross section for the $4f^6 5d^1$

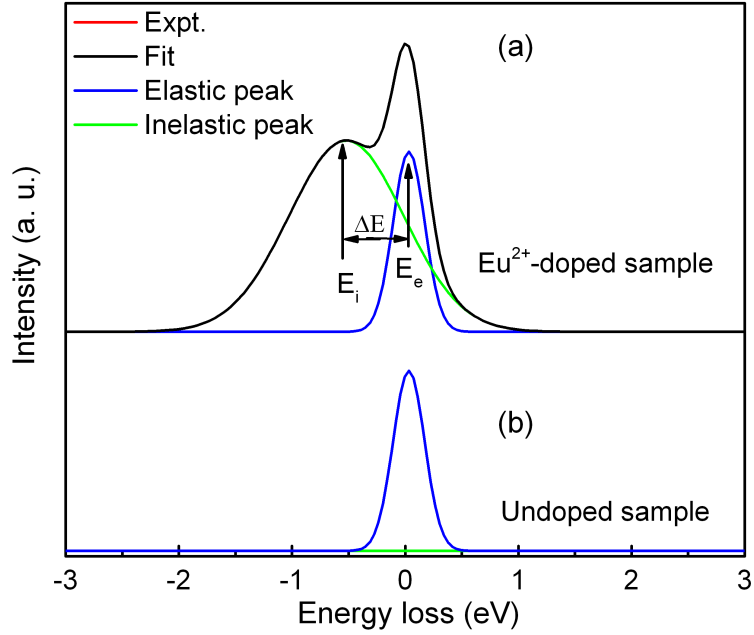


Figure 1.6: A schematic comparison of RIXS spectra between Eu^{2+} -doped sample (a) and undoped sample (b) both excited at the conduction band onset. Two Gaussians, blue (elastic feature) and green (loss feature) are used to fit the the experimental spectrum (red). In the case of (a), the black spectrum (fit) is identical with the red spectrum and therefore only the black spectrum is visible. In the case of (b), the black spectrum, the red spectrum, and blue spectrum are identical and thus only the blue spectrum is visible.

to CB inelastic scattering and low Eu^{2+} concentration, the loss feature is weak and only revealed when the elastic peak is fitted with two Gaussians. The $\text{Eu}^{2+} 4f^6 5d^1$ to the CB separation is determined from the fitting Gaussians using the expression $\Delta E_{\text{RIXS}} = E_e - E_i$, where E_e denotes the elastic scattering peak position (here 0 eV in the energy loss scale) and E_i denotes the inelastic scattering peak position shown in Fig. 1.6(a).

We attribute this energy loss to the promotion of $\text{Eu}^{2+} 5d^1$ electrons to the CB [37, 65, 66, 73], and hence, we can determine the energetic position of the $\text{Eu}^{2+} 5d^1$ state relative to the lower CB edge shown in Fig. 1.7. The undoped samples are measured (Fig. 1.6(b)) to confirm the existence of the energy loss feature and it is found that undoped samples show no energy loss feature (the peak at 0 eV in the energy loss scale is perfectly gaussian) and an elastic peak of undoped sample with a width that corresponds to that determined from the fits for the doped samples. The only dif-

ference between the Eu^{2+} -doped and undoped samples is correlating the energy loss feature for low energy excitations to the doping with Eu^{2+} . Further, we determine the energy loss feature at higher excitation energy with respect to the CB onset for three samples and find that the spectra are identical for all samples at this higher excitation energy. Thus these phenomena lead to energy loss features when exciting further above the CB onset have the same source in the samples and should be seen as being because of phonons. However, different energy loss is observed for all samples when excitation occurs at the CB onset. The energy loss exciting at the CB onset varies sample to sample, as expected for the $5d$ -CB separation. This is because the $5d$ -CB separation is different for different samples. The phonon density rises rapidly over the first few tenths of an electronvolt above the CB minimum, and it quickly dominates the RIXS spectrum at ligand edges [78]. This explains the quenching of the $5d$ -CB energy loss peak with higher excitation energy and differences between the doped and undoped samples, as well as the differences between Eu^{2+} -doped samples with different host lattice.

XEOL spectroscopy is an X-ray photon-in optical photon-out process. XEOL is used to monitor the optical luminescence using a selected X-ray photon energy, which can excite a core-level electron of a given element of interest to bound, quasi-bound, and continuum states, providing elemental, and in some cases site-specific information [79–81]. In this thesis, XEOL measurements are used to determine the $\text{Eu}^{2+} 4f^7$ energy level with respect to the $4f^6 5d^1$ states from the $4f^6 5d^1 \rightarrow 4f^7$ transition of Eu^{2+} ions, which is shown in Fig. 1.7. XEOL measurements provide the wavelength of the Eu^{2+} transition $4f^6 5d^1 \rightarrow 4f^7$ of the luminescence materials and yield a luminescence wavelength (energy). Thus, the $\text{Eu}^{2+} 4f^7$ states reside below the $4f^6 5d^1$ levels of the corresponding energy of the luminescence wavelength shown in Fig. 1.7. Therefore, RIXS measurements and XEOL techniques allow direct access to the intragap states that are the source of the luminescence of Eu^{2+} -doped phosphors. The band gaps

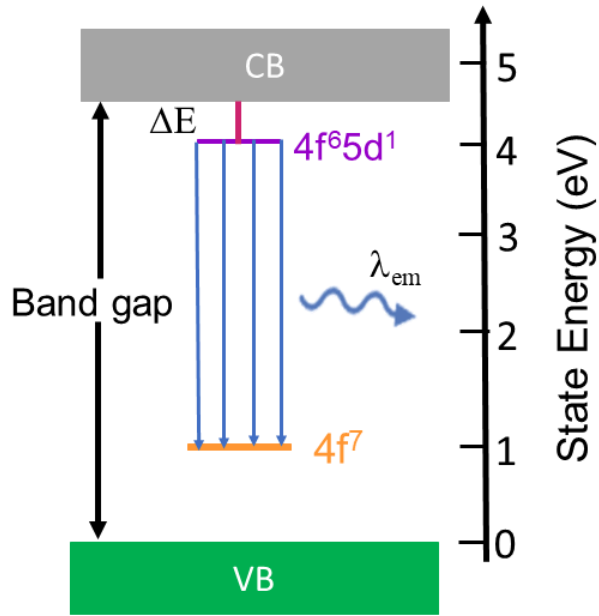


Figure 1.7: A schematic diagram of energy levels of Eu^{2+} -doped phosphor. The band gap is added from XAS and NXES measurements. The energy separation between bottom of the CB and lowest level of $4f^65d^1$ -states (vertical pink line, ΔE) is determined from RIXS measurements. The energy level of $4f^7$ with respect to $4f^65d^1$ -states is determined from the $4f^65d^1 \rightarrow 4f^7$ transition (blue luminescence in this case, λ_{em}) measured by XEOL.

of the material are determined by combining the measured occupied and unoccupied density of states on a common energy scale. The band gap is determined from the energy difference between the top of the VB, probed by non-resonant X-ray emission spectroscopy (NXES), and the bottom of the CB, probed by X-ray absorption spectroscopy (XAS). The top of the VB and the bottom of the CB are determined from the first peaks above the noise in the second derivative at the upper edge of the NXES and lower edge of the XAS spectra, respectively [37, 82]. Thus, we determine all participating energy levels of Eu^{2+} ions ($4f^65d^1$ and $4f^7$ states), the VB, the CB, and band gaps of phosphors. Figure 1.7 shows a schematic diagram of all participating energy levels of a Eu^{2+} -doped sample. Therefore, we identify all radiative processes involved, and therefore, we inform the design of the next generation pc-LEDs. In addition, we perform DFT calculations to interpret the experimental band gap, density of states (DOS), band structure, and XAS and X-ray emission spectroscopy (XES)

spectra. With these measurements and calculations, we gain complete insight into all key properties such as emission, band gap, thermal quenching behaviour, and all pertinent energy levels of the Eu^{2+} -doped phosphors studied here.

1.5 Outline of the thesis

In this thesis, the electronic and optical properties of InN thin films and highly efficient color-sensitive Eu^{2+} -doped phosphors material systems have been studied using several synchrotron-based experimental techniques. Techniques employed include XAS, XES, XEOL spectroscopy, and RIXS spectroscopy. Each of these techniques provide distinct information about the electronic and optical properties of the material being studied. These experimental techniques are described in Chapter 2.

Complementary theoretical calculations were performed to gain insight into the material properties from the measured spectra. These calculations are used to generate calculated spectra used to interpret measured spectra. Furthermore, various theoretical approaches are used to interpret the measured results. The calculation methods are described in Chapter 3.

My starting project focused on the electronic structure of InN [82], which is presented in Chapter 4. The goal of this work is to study the electronic structure and band gap of ammonothermal InN experimentally and theoretically using soft X-ray synchrotron spectroscopy measurements and DFT calculations, respectively. The measured and calculated band gaps of InN are found to be 1.7 ± 0.2 eV and 0.89 eV, respectively. The origin of the measured band gap is discussed in terms of the presence of oxygen impurities and impurity phases of InN.

After finishing my first project, I turned to the main topic of my PhD. Here, I stud-

ied highly efficient color-sensitive phosphors such as ultranarrow band blue-emitting oxoberyllates $AELi_2[Be_4O_6]:Eu^{2+}$ ($AE = Ba, Sr$), blue-luminescence $MBe_{20}N_{14}:Eu^{2+}$ ($M = Ba, Sr$), and red-luminescence $SrLi_2Al_2O_2N_2:Eu^{2+}$. The ultranarrow band blue-emitting oxoberyllates $AELi_2[Be_4O_6]:Eu^{2+}$ ($AE = Ba, Sr$) is presented in Chapter 5 [65], blue-luminescence $MBe_{20}N_{14}:Eu^{2+}$ ($M = Ba, Sr$) in Chapter 6 [66], and finally, the red-luminescence $SrLi_2Al_2O_2N_2:Eu^{2+}$ is presented in Chapter 7 [83]. Our collaborator in the Department of Chemistry at University of Munich, Germany, synthesized the oxoberyllates $AELi_2[Be_4O_6]:Eu^{2+}$ ($AE = Ba, Sr$) and nitridoberyllates $MBe_{20}N_{14}:Eu^{2+}$ ($M = Ba, Sr$) samples using a solid state reaction method [84]. The red luminescence $SrLi_2Al_2O_2N_2:Eu^{2+}$ was synthesized by our collaborator, Lumileds Phosphor Center Aachen, Germany, according to the powder sample synthesis published by Hoerder *et al.* upon optimization to obtain a phase pure powder sample [85]. These phosphor materials are of interest for use in lighting applications as part of pc-LEDs. In this case, the $4f^65d^1 \rightarrow 4f^7$ transition of Eu^{2+} is responsible for the visible emission band. A key issue when building a pc-LED is the choice of the phosphor host as the choice of host will affect the color of the light output as well as the overall device efficiency.

The concluding remarks for the exciting area of research presented in this thesis are provided in Chapter 8.

Chapter 2

Experimental Techniques

The interaction of soft X-rays with matter is the primary mechanism for studying the properties of materials. X-rays have a wavelength comparable to the size of an atom, and they have energies in the range of most binding energies of core electrons. Thus, X-rays spectroscopy techniques are a powerful tool for probing the properties of matter. A specific set of core electrons can be excited by tuning a monochromatic X-ray beam to the corresponding energy. Coupled with the fact that X-ray penetration depths range from nanometers to micrometers, X-ray spectroscopy provides a bulk-sensitive, element-specific probe of the properties of matter and can be used to obtain *in situ* nondestructive measurements. This study is entirely based on soft X-ray spectroscopy and density functional theory calculations. The soft X-ray energy range lies between 50 eV and 2000 eV [86], and it is important for materials research because the core energy levels of many elements are within this range. For example, all 1s electrons (K-shell) for the lighter elements ($3 \leq Z \leq 14$) and higher lying electron shells for all heavier elements are found within the soft X-ray energy range.

Soft X-rays are generated inside the synchrotron ring by bending magnets or insertion devices, then guided by mirrors, monochromatized by diffraction gratings, and finally delivered to the sample in the experimental station; this configuration is known as a “beamline”. All spectra reported in this thesis were obtained at the Resonant

Elastic and Inelastic X-ray Scattering (REIXS) beamline [87] and at the Variable Line Spacing-Plane Grating Monochromator (VLS-PGM) beamline [88] at Canadian Light Source (CLS) as well as at the B1.8.0.1 beamline at the Advanced Light Source (ALS) at Lawrence Berkeley National laboratory [89]. In this thesis, X-ray absorption spectroscopy (XAS), X-ray emission spectroscopy (XES), resonant inelastic X-ray scattering (RIXS), and X-ray excited optical luminescence (XEOL) spectroscopy are utilized to analyze the InN powder samples and the highly efficient color-sensitive Eu^{2+} -doped phosphors. This chapter involves describing how X-rays interact with matter, and how each of the techniques provides structural, electronic, and optical properties of these materials.

2.1 X-ray Interactions with Matter

When an X-ray interacts with matter, the phenomena of reflection, refraction, diffraction, and absorption are all taking place with different degrees of strength. The main phenomena of the interaction of X-ray and matter relevant to our energy range are as follows. First, the X-ray may be transmitted with no change in energy or momentum and no influence on the substance. Second, the X-ray may reradiate at exactly the same energy (elastic scattering) or undergo a reduction in energy (inelastic scattering). Finally, the X-ray may be absorbed by the substance. The latter effect provides information about the electronic and optical properties of material and it is relevant for the research carried out in this thesis. Thus, the X-ray absorption mechanism is considered here first.

The X-ray absorption mechanism follows Fermi's Golden rule, where the interaction Hamiltonian is the appropriate operator for an electromagnetic wave. The X-ray absorption coefficient μ is given by [90]

$$\mu(E) \propto \sum_{i,f} |\langle \psi_f | (\hat{e} \cdot \hat{p}) e^{(i\vec{k} \cdot \vec{r})} | \psi_i \rangle|^2 \rho_f, \quad (2.1)$$

where \hat{e} , \hat{p} , \vec{k} , \vec{r} , ψ_i , and ψ_f represent the electromagnetic field of the incident X-ray, electron momentum vector, X-ray wavevector, position vector in the appropriate coordinate system for the material, the initial state wave function, and the final state wave function, respectively. The summation is conducted over all possible initial and final states.

The argument of the exponent is less than 1 because the X-ray energies are less than 2000 eV, and the distance r is less than 1 Å. Therefore, we can expand the exponent in a McLaurin series as

$$e^{(i\vec{k} \cdot \vec{r})} = 1 + i\vec{k} \cdot \vec{r} - (\vec{k} \cdot \vec{r})^2 + \dots \quad (2.2)$$

The first order approximation of the exponential is sufficient to describe most experimental spectra. In this case, Equation 2.1 reduces to the dipole approximation

$$\mu(E) \propto \sum_{i,f} |\langle \psi_f | (\hat{e} \cdot \hat{p}) | \psi_i \rangle|^2 \rho_f. \quad (2.3)$$

This approximation implies that the oscillating electric field of the X-ray induces all X-ray induced electron transitions $|\psi_i\rangle \rightarrow |\psi_f\rangle$. The electric field of the X-ray is constant across the orbital because of the small effective radius of the core electrons. The electronic state of an electron in an atom is defined by the principal, orbital angular momentum and spin quantum numbers n , l , and s , respectively. The principal quantum number can have positive integer values 1, 2, 3 and so on. The angular quantum number determines the shape of the orbitals and the values of l depend on the principal quantum number. For a given value of n , l has possible integer values from 0 to $(n-1)$. The total angular momentum is the vector sum of the orbital and spin momenta, that is $j = l + s$, where $s = 1/2$. For both the core

Table 2.1: Correspondence between X-ray absorption edges and their electronic configurations. Table is taken from Ref. [91].

n	l	j	Configuration	Edges
1	0	$\frac{1}{2}$	1s _{1/2}	K
2	0	$\frac{1}{2}$	2s _{1/2}	L ₁
2	1	$\frac{1}{2}$	2p _{1/2}	L ₂
2	1	$\frac{3}{2}$	2p _{3/2}	L ₃
3	0	$\frac{1}{2}$	3s _{1/2}	M ₁
3	1	$\frac{1}{2}$	3p _{1/2}	M ₂
3	1	$\frac{3}{2}$	3p _{3/2}	M ₃
3	2	$\frac{3}{2}$	3d _{3/2}	M ₄
3	2	$\frac{5}{2}$	3d _{5/2}	M ₅
4	0	$\frac{1}{2}$	4s _{1/2}	N ₁
4	1	$\frac{1}{2}$	4p _{1/2}	N ₂
4	1	$\frac{3}{2}$	4p _{3/2}	N ₃
4	2	$\frac{3}{2}$	4d _{3/2}	N ₄
4	2	$\frac{5}{2}$	4d _{5/2}	N ₅
4	3	$\frac{5}{2}$	4f _{5/2}	N ₆
4	3	$\frac{7}{2}$	4f _{7/2}	N ₇

and bound final states, the total angular momentum must be conserved. Photons have an angular momentum of 1. Thus, dipole transition can only have a final state angular momentum of $l \pm 1$, where l represents the angular momentum of the initial state. In a radiative process, the change in the primary quantum number Δn is not confined in terms of the bound state quantum number. The change in angular momentum Δl is ± 1 . The change in the total angular momentum is $\Delta j = 0, \pm 1$ [91]. However, a transition between two states both with $j = 0$ is not permitted [92]. For example, dipole transitions from the $2s$ to the $1s$, or from the $3p$ to the $2p$ level are forbidden [91]. For historical reasons, labels denoting X-ray transitions to or from a core state are in a different set of symbols than typically used to describe atomic orbitals. Table 2.1 describes the electronic configurations and their corresponding edges. Traditionally, the symbol for the lowest energy level in an X-ray transition is used to denote the process.

For example, a $2p \rightarrow 1s$ transition is denoted by the symbol K_α , and a $3p \rightarrow 1s$ transition is denoted by the symbol K_β , and so on [92].

The effect of the second-order term in the power series expansion of Equation 2.2 can be found as low energy and low intensity characteristics in the X-ray absorption measurement. These properties are related to the quadrupole transition, and they must be included as an additional component in Equation 2.3

$$\mu(E) \propto \sum_{i,f} |\langle \psi_f | (\hat{e} \cdot \hat{p})(1 + i\vec{k} \cdot \vec{r}) | \psi_i \rangle|^2 \rho_f. \quad (2.4)$$

The final-state of a quadrupole transition has an angular momentum $l \pm 2$. Quadrupole transitions occur when the $1s$ electrons in transition metals are excited. Quadrupole features are sometimes visible because many transition metals have a large number of partially occupied d states near the Fermi level.

2.2 Synchrotron Radiation and Insertion Devices

When a moving charged particle is accelerated in a direction perpendicular to its trajectory, usually by a magnetic field, synchrotron radiation and cyclotron radiation are produced. The difference between the two methods is that cyclotron radiation is emitted by nonrelativistic particles, whereas synchrotron radiation is emitted by highly relativistic particles. The relativistic particles' frame is spatially compressed relative to the laboratory frame in synchrotron radiation; this results in the emitting of most radiation power into a narrow lobe in the direction of the particle's travel, with a small fraction of the radiation emitted into a wider trailing lobe (when viewed in the lab frame). The forward radiation cone has an opening angle of about $2\gamma^{-1}$ radians [93], and the average power radiated by a relativistic charged particle varies with γ^2 [93]; γ represents the particle's Lorentz factor. Therefore, the resultant radiation is highly collimated and bright from highly relativistic electrons.

Synchrotron radiation experiments of the first generation were parasitic. The storage ring parameters were far from optimal for yielding the best beam characteristics because the primary focus of these facilities were the particle collisions. Second-generation synchrotron radiation facilities, which comprise storage rings dedicated to the production of synchrotron radiation. The bending magnet and a region of strong uniform magnetic field normal to the plane of the ring were key to these facilities. The spectrum of synchrotron radiation produced by this uniform magnetic field is broad, and it culminates around a critical energy defined by [91]

$$E_c = \frac{3\hbar c\gamma^3}{2\rho} = \frac{3\hbar e B \gamma^2}{2m_0}, \quad (2.5)$$

where ρ , B , and m_0 represent the radius of the curvature of the particle as it travels through the region of uniform magnetic field, the magnetic field, and rest mass of the charged particle, which is typically an electron, respectively. The critical energy is tuned by varying B in an attempt to maximize the flux in the desired energy range because the particle energy (and therefore γ) is a fixed parameter of the storage

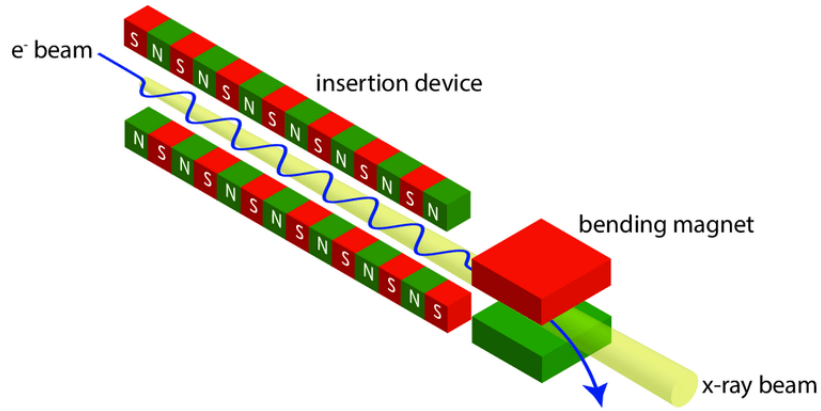


Figure 2.1: A schematic diagram of an insertion device. Diagram is taken from Ref. [91].

ring. In most core-level X-ray spectroscopy experiments, only a small portion of the bandwidth corresponding to a particular core-level transition is desired. Thus, the majority of the bend magnet's emission profile would be discarded, and this is inefficient and might cause thermal loading concerns.

Insertion devices are placed in the straight sections of storage rings. They produce significantly higher fluxes compared to the bending magnets. A schematic diagram of an insertion device is presented in Fig. 2.1. Figure 2.1 shows that insertion device operates by forcing the electrons to produce an oscillatory path in the plane of the storage ring, employing a set of magnets that produce magnetic fields [91]. There are two types of insertion devices, which are the wiggler and undulator. These insertion devices are used to increase the usable flux of the beam. The average magnetic field experienced by the particle is therefore $B_0 = B/\sqrt{2}$; however, the field strengths achievable in wigglers and undulators are higher than those of the standard bend magnets because of the use of powerful permanent magnets [94].

The distinction between wigglers and undulators lies in their dimensionless deflection

parameter K , which is defined as [91]

$$K = \frac{eB_0}{2\pi m_0 c} \lambda_{ID} . \quad (2.6)$$

where λ_{ID} denotes the period of the insertion device. The value of K acts as a ratio of the maximum angular deflection δ of the electrons to the opening half-angle of the synchrotron radiation γ^{-1} [91]

$$\delta = K\gamma^{-1} . \quad (2.7)$$

For a wiggler, the period of the magnetic array is sufficiently large that $K \gg 1$. Figure 2.1 shows that electrons only emit radiation in the forward direction during a small portion of their sinusoidal trajectory, which is twice per λ_{ID} . Therefore, they behave like 2N bend magnets linked up end-to-end, with a similar emission profile and critical energy [95].

In undulators, the period is substantially shorter (so that $K \leq 1$), which implies that the maximum angular deflection of the insertion device is less than the opening angle of the synchrotron radiation. This allows for coherent interference between the electrons and radiation field, and it has a variety of implications on the properties of the beams. First, the angular spread of an undulator beam is reduced by a factor of \sqrt{N} [93], which when combined with the enhancement factor of N from having multiple bend sections, implies that the undulator will have a factor of about N^2 the emitted power of a single bend magnet [93]. Further the coherent interference narrows the (in-plane) spectrum into sharp peaks located at the odd harmonics of a single wavelength because the even harmonics are subject to destructive interference [96].

Stronger magnetic fields in undulators must be tempered by shorter magnet periods, which limits their range to below 10 keV even in their higher harmonics because K

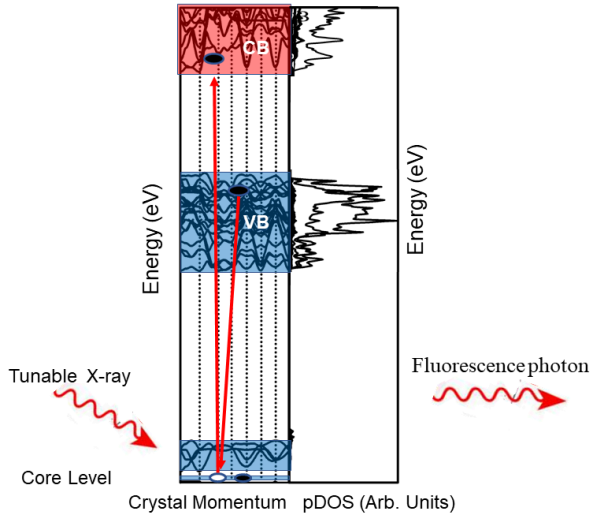


Figure 2.2: Schematic representation of the X-ray absorption process.

is proportional to B . W wigglers and superconducting superbend magnets can produce photons exceeding 100 keV. An undulator-based soft X-ray beamline is ideal for their experiments considering its characteristic high flux and the atomically thin nature of the samples because all $1s$ electrons (K-shell) for the lighter elements ($3 \leq Z \leq 14$) and Sc, Ti, V, Cr, Mn, Fe, Co, Ni, Cu, and Zn $2p$ core level reside below 2 keV binding energy.

2.3 X-ray Absorption Spectroscopy

Figure 2.2 is a schematic representation of the process of X-ray absorption. Figure 2.2 depicts that the transition occurs from a core electron to the unoccupied density of states (conduction band) by the incoming synchrotron radiation. The left panel in Fig. 2.2 shows the calculated band structure and the right panel describes the corresponding projected density of states. There is a possibility that a core electron will absorb an X-ray and be promoted to an excited state when an incident X-ray has an energy around the binding energy of a core electron of a material. Most transitions are not interesting because the X-ray absorption cross-section of a given edge varies slowly and smoothly over a broad energy range [97] when the incident X-ray is outside

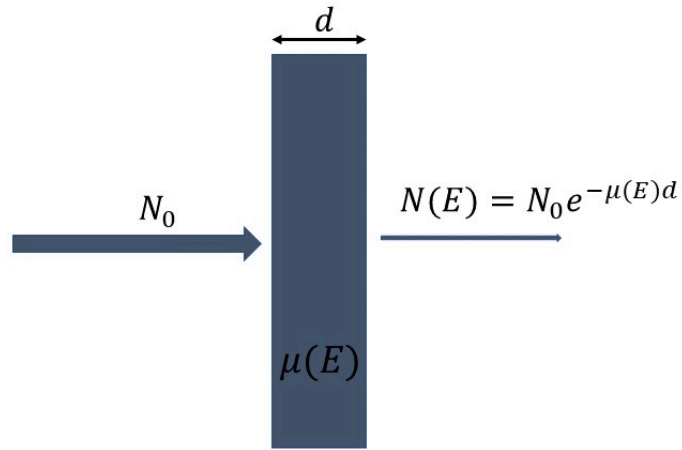


Figure 2.3: Schematic representation of the Beer-Lambert law.

of the absorption edge. The exception to this is when the incident X-ray energy is resonant, or close to resonant, to the binding energy of a core electron. In this case, the electron can be promoted to a bound state within the conduction band of the material, in this regime, the X-ray absorption cross-section varies considerably over a small energy range.

The X-ray absorption spectroscopy is concerned with the change in the absorption coefficient $\mu(E)$ of the system described by the Beer-Lambert law

$$N(E) = N_o \exp^{-\mu(E)d} , \quad (2.8)$$

where, d represents the thickness of the sample; and $N(E)$ and N_o represent the number of incoming and transmitted photons, respectively, under investigation as a function of incident photon energy. Furthermore $\mu(E)$ is called the linear attenuation coefficient because physically, it describes the logarithmic fraction of the photons absorbed per unit length where

$$\mu(E) = \frac{1}{d} \log \frac{N_o}{N(E)} , \quad (2.9)$$

when the X-rays travel through the sample. $\mu(E)$ depends on several factors including the density of the material and the type of atoms in the sample. Figure 2.3

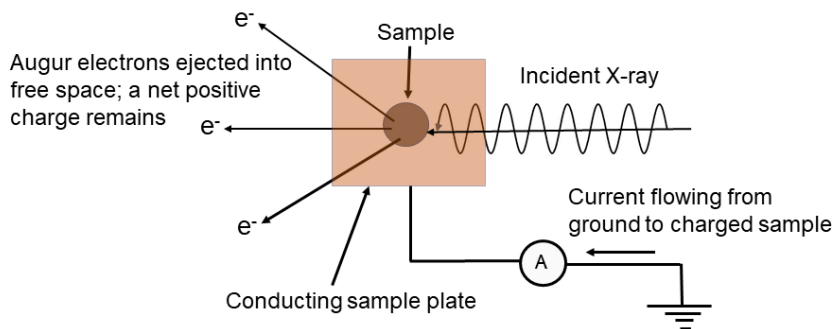


Figure 2.4: Measurement of TEY. The ejected Auger electrons leave behind a positively charged sample. If connected to the ground, the neutralizing current flowing into the sample is proportional to the time-averaged Auger electron creation rate, which is proportional to the core hole creation rate.

represents the X-ray absorption process of the material by Beer-Lambert law. X-ray absorption techniques measure this coefficient either directly or indirectly. During the X-ray absorption transition, a core electron is excited to a conduction band state, and a vacant core level (a core hole) is left behind. This core hole is filled almost immediately with an electron from a state higher in energy (either another core level or valence state), and the resulting released energy can be absorbed by Auger electrons or be emitted as photon. An absorption spectrum displays either the number of absorbed photons or the linear absorption coefficient $\mu(E)$ as a function of incoming photon energy. Experimentally, there are several methods used to measure the XAS spectrum. However, for this study, mostly the surface sensitive total electron yield (TEY) mode and the bulk sensitive either total fluorescence yield (TFY) mode or partial fluorescence yield (PFY) mode are used to record the XAS spectra.

The TEY method relies on the detection of Auger electrons. This method is used because the number of total electrons leaving the sample is proportional to the number of core holes created, which is proportional to the number of photons absorbed. The

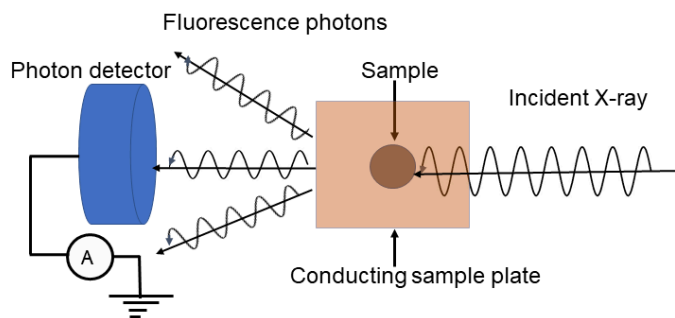


Figure 2.5: Measurement method of TFY.

Auger effect occurs when a core electron is removed, which leaves an unstable core hole behind, and a higher shell electron decays to fill the core hole by transferring its energy to another outer shell electron; this is removed from the sample and called the Auger electron. This process is more likely for shallow core holes in low Z elements ($Z < 15$). Furthermore, the mean free path of the escaping electrons is very small, and electrons are detected at only less than 10 nm of the sample surface [98]. Thus, this method only probes the surface of the material of interest. The main problem for TEY is sample charging, which occurs when the electrical conductivity of the sample is sufficiently low and the incoming photon flux is sufficiently high so that photoelectrons cannot be replenished at the rate necessary to maintain an electrically neutral sample; the electron emission in this case will be reduced. The surface sensitive TEY XAS spectrum may not be representative of the true XAS spectrum of the bulk sample if the surface of the sample is oxidized or contaminated.

The TFY method relies on the detection of emitted photons. The reason behind using this method is very similar to that for the TEY method. It is assumed that the total number of emitted photons detected is proportional to the number of core holes created. This method is more bulk sensitive because it is governed by the attenuation

length of the emitted photons, which is considerably larger (100 nm to μm) than that of emitted electrons [98]. When the observed TEY or TFY is not proportional to the total linear absorption coefficient, the recorded spectra might become distorted [98]. The energy-dependent penetration depth of the incoming photons and the escape depth of the electrons in the TEY or the photons in the TFY are the only factors that need typically be taken into account. Sometimes charging of the sample can be a problem when the large number of electrons removed by the bright synchrotron beam cannot be sufficiently replenished. Saturation can arise when the escape depth of the electrons becomes comparable to the penetration depth of the incoming X-rays. When saturation arises, the measured spectra will not increase further upon increasing the number of incoming photons. Self-absorption is a problem of TFY measurements. After emission, the emitted photons travel through the bulk of the sample and may be reabsorbed by the sample before reaching the detector. This is referred to as self-absorption. The probability with which a photon will be reabsorbed depends strongly upon its energy. The self-absorption of X-ray fluorescence photons can suppress the peak height in the measured fluorescence yield spectra of the dense systems and the fluorescence yield is not proportional to the linear absorption coefficient anymore [98]. PFY is based on a similar method of TFY; however only emitted photon within a certain energy window are detected. In principle, this method is superior to the TFY method because elastically scattered photons and photons from other unwanted atomic sites and edges can be filtered out. Only photons emitted from the sample within the desired energy range are detected.

2.3.1 X-ray Absorption Near-Edge Spectroscopy

In an absorption spectrum, different excitation energy ranges provide different information about the structure of the material. The XAS spectrum is divided into two energy regions: the X-ray absorption near-edge structure (XANES) region, and the

extended X-ray absorption fine structure (EXAFS) region, which are shown schematically in Fig. 2.6. The features in the immediate vicinity of an absorption edge are referred to as XANES. A photoelectron is generated after an X-ray photon absorbed by a core level. This photoelectron may not be ejected into the vacuum continuum above the ionization threshold, but instead may only have sufficient energy to be promoted to an unoccupied states but bound level. The core hole resulting from the absorption process can be filled either via an Auger process or capture of an electron from another shell followed by emission of a fluorescent photon. The XANES differs from traditional photoemission experiments. In the traditional photoemission experiments, the initial photoelectron itself is measured, however in the XANES the fluorescent photon, Auger electron or inelastically scattered photoelectron is recorded. The XANES provides information about the electronic structure of the sample. An example, a transition between K state ($1s$, $l = 0$, symmetric) and a bound excited state of mostly (symmetric) d -character is observed for a material with high intensity. According to the dipole approximation, only p -states (antisymmetric) are accessible from the s -states. Therefore the upper upper bound state must have both p -type (antisymmetric) and d -type character. The environment around the absorbing atom cannot be inversion symmetric because of the partial p -character. Thus, the presence of bound-state resonant absorption peaks provides information on the local symmetry of the system. The features of the XANES spectrum depend on the transition probability rate $T_{i \rightarrow f}$ between an initial state $|\psi_i\rangle$ to a set of final state $|\psi_f\rangle$ [99], which is described by Fermi's Golden Rule [90]

$$T_{i \rightarrow f} = \frac{2\pi}{\hbar} |\langle \psi_f | \hat{H} | \psi_i \rangle|^2 \rho_f . \quad (2.10)$$

where $|\langle \psi_f | \hat{H} | \psi_i \rangle|$ represents the transition matrix element. \hat{H} denotes the perturbation Hamiltonian, which is responsible for the transition and ρ_f denotes the density of states in which the final state is embedded. \hat{H} for X-ray absorption is the electric dipole operator. The use of a dipole transition operator is a simplification,

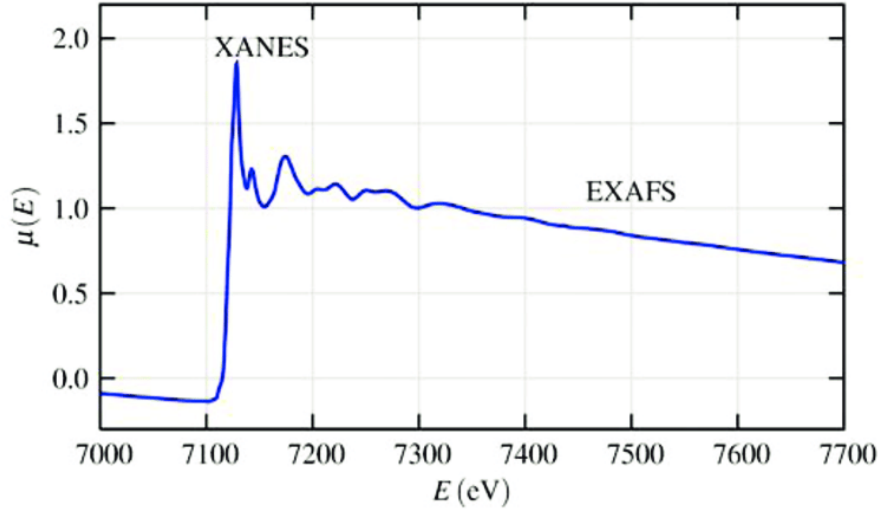


Figure 2.6: X-ray absorption spectrum of FeO with XANES and EXAFS regions. The figure is taken from Ref. [91].

because the expansion of the field description of a photon has higher components such as the electric quadrupole and magnetic dipole. However, the contribution of these higher order terms to the overall electronic transition probability are smaller than the dipole contribution, and in any event, all terms higher than dipole symmetry are completely irrelevant in light atoms.

The intensity of transitions to bound-state unoccupied orbitals depends on their density and selection rules. Suppose, five $5d$ -metals Re , Os , Ir , Pt and Au have XANES spectra. The ground state electronic configuration of Re is $[Xe]6s^24f^{14}5d^5$. There are only 5 electrons left until the $5d$ shell is completely filled. As one moves to the right in the periodic table from Re , the five available $5d$ -states are filled. In Au , these states are all occupied. In the elements Re to Pt , the intensive XANES feature is seen because of available bound but unoccupied $5d$ -states [91]. As Au has no such unoccupied states, the XANES feature is not seen and only excitation directly into the unbound continuum is observed [91].

The unoccupied descriptor is obtained because of Fermi's Golden Rule [90]. Equation 2.10 indicates that the transition rate for an electron to be promoted into an unoccupied state (which is proportional to the absorption spectrum) should be the DOS in the final state ρ_f accessible by the transition and modified by the transition probability from the initial state $|\psi_i\rangle$ to a set of final state $|\psi_f\rangle$. The final DOS in resonant absorption differs from the ground state only in that there is an electron in the conduction band; therefore unoccupied states are probed.

2.3.2 Extended X-ray Absorption Fine Structure Spectroscopy

The EXAFS measurement is monitored by increasing the incident X-ray energies at approximately 50 eV above an absorption edge and extending up to several hundred [91]. The energies above the XANES region create photo-excited electrons, which are essentially free electrons moving in a wave-like manner through the crystal. The free electrons created by photon absorption can scatter off of neighbouring atoms, and the amount of scatter depends on the electron momentum and distance to the neighbouring atom. This scatter introduces fluctuations in the EXAFS spectra, which can be used to deduce local structure information. The mean-free paths of the photoelectrons associated with EXAFS is the order of a few Angstroms. Thus EXAFS probes only the immediate neighbouring of the absorbing atom. For this reason, EXAFS is an important technique in nanocrystalline solids and liquids, as it yields information of the short-range structure of materials [91].

For EXAFS, we approximate the final state as $|\psi_f\rangle = |\psi_0\rangle + |\psi_s\rangle$, where $|\psi_0\rangle$ represents the free electron state and $|\psi_s\rangle$ represents the scattered state. For the first-order approximation, Equation 2.3 can be modified as

$$\begin{aligned}
\mu &\propto |\langle \psi_f | (\vec{e} \cdot \vec{p}) | \psi_i \rangle|^2 \\
&\propto |\langle \psi_0 | (\vec{e} \cdot \vec{p}) | \psi_i \rangle|^2 + \langle \psi_0 | (\vec{e} \cdot \vec{p}) | \psi_i \rangle \langle \psi_s | (\vec{e} \cdot \vec{p}) | \psi_i \rangle \\
&\propto \mu_0 + \mu_0 \chi
\end{aligned} \tag{2.11}$$

where μ_0 represents the background absorption for an isolated atom and the EXAFS oscillations, χ represents the effect of scattering.

The standard expression for χ can be written as [91]

$$\chi(k) = \sum_j \frac{N_j f_j(k) e^{-2k^2 \sigma_j^2}}{k R_j^2} \sin[2k R_j + \delta_j(k)] \tag{2.12}$$

The summation is over all the j considered shells, each shell containing N_j atoms. R_j denotes the distance between the absorbing atom and backscattering atom of species j . N_i represents the number of scattering species j atoms. f_j denotes the scattering factor for the scatters in the j -th shell and it depends on the backscattering atom and is so small for the first four or five elements. Thus these atoms cannot be detected by EXAFS. f_j increases significantly and exhibits progressively complex oscillatory behaviour as a function of k with increasing atomic number Z [100, 101]. $\sin[2k R_j + \delta_j(k)]$ represents the oscillatory term. The denominator of R_j^2 takes into account the inverse-square decrease in the electron density of the spherically expanding electron wave from the absorbing atom. The exponential term in Equation 2.12 accounts for the fact that the neighbouring atoms are not stationary but vibrating with amplitude σ_j parallel to k [91].

2.4 X-ray Emission Spectroscopy

The XAS process creates a core hole that is filled quickly by an electron from a higher energy state. Sometimes the energy gained from this transition is released as a photon, and when the X-ray fluorescence intensity is integrated as a function of incident

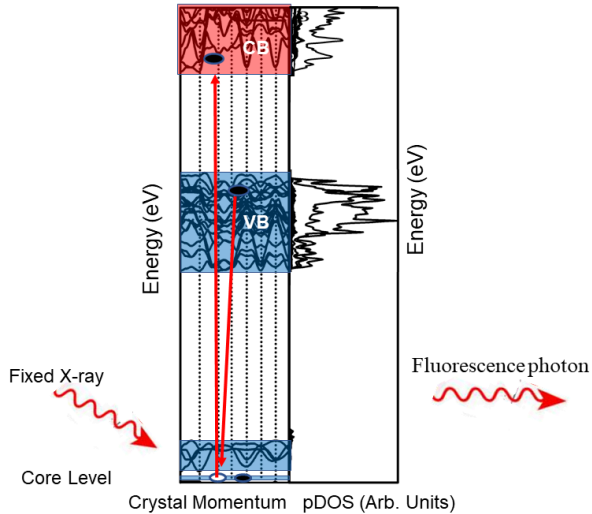


Figure 2.7: Schematic representation of the X-ray emission process.

X-ray energy, a TFY mode XAS spectrum is acquired. An XES spectrum can be acquired when a high-resolution spectrometer is available: the incident X-ray energy is fixed and the intensity of the X-ray fluorescence is measured as a function of emission energy. An XES spectrum can be acquired from the decay of another core state to fill the deeper core hole; however the most interesting spectra (and the spectra most relevant to material properties) are when a weakly bound valence electron decays to fill the core hole. Figure 2.7 is a schematic representation of the XES process.

XES relies on emitted X-rays, and therefore, it is bulk sensitive in the same manner as the TFY or PFY mode of XAS. An XES spectrum is acquired nonresonantly when the incident X-ray energy is well above resonance (NXES), which effectively decouples the absorption transition from the emission transition. However, the XES spectra can be acquired when the incident X-ray energy is resonant with a particular absorption feature (RIXS), and this can reveal many interesting properties, such as charge transfer $d-d$, or magnetic transitions [77], or momentum preserving transitions within the band structure [78].

2.4.1 Nonresonant X-ray Emission Spectroscopy

Nonresonant X-ray emission spectroscopy (NRXES) is performed by exciting the sample significantly above the resonant threshold, on the order of at least 15 to 20 eV. The core electron is ionized into vacuum continuum states and there is no longer bound when excitation is performed in this energy range. If the atom originally had N electrons before emission, the final state is an $N - 1$ electrons with a hole in the valence band after a valence electron has refilled the core. Like placing an electron in the unoccupied states in the final state of an X-ray absorption event allows probing the unoccupied states, so does placing a hole in the occupied states allows one to probe them. The intensity of emitted photon can be described by the Fermi's Golden rule [90]

$$I(\hbar\omega) \propto \sum |\langle \psi_f | (\hat{e} \cdot \hat{p}) | \psi_i \rangle|^2 \rho_f, \quad (2.13)$$

where the initial state $|\psi_i\rangle$ corresponds to a system with a hole in the core level and a delocalized electron and the final state $|\psi_f\rangle$ corresponds to a system with the core level filled, a hole in the valence band and a delocalized electron. ρ_f is the density of state of the final state. Since the final quantum state during XES measurements has a hole present in the valence band, the final state rule states that the emission spectra should be calculated with a hole in the valence band. When doing simulations this hole in the valence band is generally ignored, because the hole is delocalized and is assumed not to have a significant effect on band energies. This is unlike absorption spectroscopy where the core hole is highly localized, and the core hole effect must be accounted for in the calculations. There is no preferential absorption by any particular nonequivalent site of the atom being excited, because the excitation energy is above threshold; however photons will still be preferentially absorbed by the core level of the atom with binding energy closest to the excitation energy.

2.4.2 Resonant X-ray Emission Spectroscopy

Resonant X-ray emission spectroscopy (RXES) measurements are performed by measuring emission spectra while resonantly exciting electrons into bound conduction band states. For RXES, the incident X-ray is tuned to the features in XAS. By tuning the incident energy during the RXES measurements, one can selectively excite the nonequivalent sites of the same element and orbital.

The difference between NRXES and RXES is site selectivity. One measurement approach resonantly excites the sample, and therefore, it is possible to selectively excite, within the same crystal, sites of the same atomic species that have different local symmetry (called nonequivalent sites). Core holes will be preferentially created on only one nonequivalent site, and therefore, RXES probes only the local occupied pDOS of the resonantly excited site, instead of the sum of the pDOS from all nonequivalent sites as in NRXES. RXES spectra can provide detailed information to the occupied electronic environment surrounding each site. Indeed, taking the time to measure the occupied pDOS of each different site is only useful if there are different nonequivalent sites to probe. There is no difference between RXES spectrum and NRXES spectrum for highly homogeneous material.

2.4.3 Resonant Inelastic X-ray Scattering

Resonant inelastic X-ray scattering (RIXS) occurs when incident X-rays resonantly excite a core level electron to a higher energy unoccupied intermediate state in the vicinity of the absorption threshold. The intermediate state corresponds to a system with a hole in the core level and a locally bound electron in the conduction band. The final state of the system is achieved when the core hole is filled quickly by an electron from the valence band and energy is released as a photon. Thus, the final state corresponds to a system with the core level filled, a hole in the valence band, and a locally bound electron in the conduction band. A schematic representation of

RIXS is presented in Fig. 2.8. The excitation and decay steps in RIXS process can be described by using the Kramers-Heisenberg formula. According to the Kramers-Heisenberg formula, the intensity $I(\hbar\omega_{in}, \hbar\omega_{out})$ of the emitted photons as a function of the emission energy is given by [90, 102, 103]

$$I(\hbar\omega_{in}, \hbar\omega_{out}) \propto \sum_f \sum_j \left| \frac{\langle \psi_f | \hat{T}_f | \psi_j \rangle \langle \psi_j | \hat{T}_i | \psi_i \rangle}{E_i + \hbar\omega_{in} - E_j + i\frac{\Gamma_m}{2}} \right|^2 \delta(E_i + \hbar\omega_{in} - \hbar\omega_{out} - E_f), \quad (2.14)$$

where ψ_i , ψ_j , and ψ_f denote the initial, intermediate, and final states, respectively, E_i , E_j , and E_f represent the energies of the initial, intermediate, and final states, respectively. The energy of the incident and emitted photons is given by $\hbar\omega_{in}$ and $\hbar\omega_{out}$, respectively, while \hat{T}_i and \hat{T}_f represent dipole radiative transition operators that govern transitions from the initial to the intermediate states and the intermediate to the final states, respectively. The intermediate state lifetime broadening Γ_m reflects the lifetime of the core hole. As the energy difference between the initial and intermediate states approaches the excitation energy, the denominator becomes very small, which allows for resonant excitation to occur. The intermediate lifetime broadening Γ_m functions to maintain the denominator from going to zero on resonance. Its physical interpretation is that there is some uncertainty as to exactly what energy the system is at in the intermediate state.

The incident X-rays ($\hbar\omega_{in}$) and outgoing photons ($\hbar\omega_{out}$) have different energy. The reduction in energy of the incident photon compared to the outgoing photon ($\hbar\omega_{in} - \hbar\omega_{out}$) is the energy loss in the inelastic scattering process. This amount of energy provides RIXS peaks as shown in Fig. 2.8. In the special case of $\hbar\omega_{in} = \hbar\omega_{out}$, there is no net energy loss and it is called resonant elastic X-ray scattering. One mechanism for generating a RIXS feature is to promote an electron to an unoccupied conduction band-state followed by relaxation of a lower-lying state to the core, resulting in the

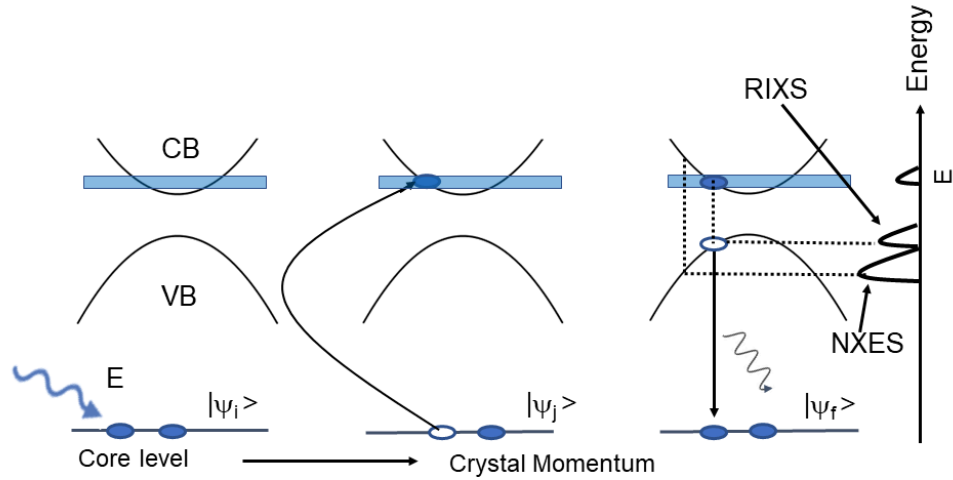


Figure 2.8: Initial ($|\psi_i\rangle$), intermediate ($|\psi_j\rangle$), and final ($|\psi_f\rangle$) state wavefunctions for a Kramers-Heisenberg X-ray transition in a single-particle band structure.

formation of an electron-hole pair. RIXS is a one-step process and it involves two dipole allowed transitions. Due to the double dipole transition, the selection rules modify. In RIXS $\Delta l = 0, \pm 2$ becomes a selection rule [91]. The powerful implication of this is that it allows to study the forbidden d to d , or f to f transitions [91]. The RIXS mechanism is a second-order process. For the phosphors materials, we get weak RIXS feature because we tune the exciting radiation to energies where the absorption is small.

2.5 X-ray Excited Optical Luminescence (XEOL) Spectroscopy

XEOL spectroscopy is an X-ray photon-in optical photon-out process. XEOL is used to monitor the optical luminescence using a selected X-ray photon energy for excitation, which can excite a particular core-level electron of a given element of interest to bound, quasi-bound, and continuum states, this provides elemental and in some cases site specific information [79–81]. Owing to the high energy of the incident

X-rays and the core-level photoelectrons, XEOL process is a complex phenomenon; this phenomenon can be described as follows [104]:

- A core hole is created within femtoseconds by the annihilation of an X-ray.
- The core hole is immediately filled by electrons from shallower levels creating Auger and X-ray fluorescence processes.
- The new shallower core holes left behind are filled by even shallower core or valence electrons, which creates a cascade process.
- The energetic photoelectrons and Auger electrons create more electrons and holes on their paths as they travel through the absorbing medium and lose energy through inelastic scattering.
- Electrons and holes thermalize at the bottom of the conduction band (CB) and the top of the valence band (VB), respectively.
- Electrons and holes in the CB and VB, respectively, radiatively recombine to produce luminescence with small photon energy.

Furthermore, defects can produce intense or suppress optical emissions with photon energy significantly lower than the bandgap of material. Thus, XEOL is different from conventional UV-visible photoluminescence. It can be site specific because the core level is specific to a given element and it involves energy transfer via secondary processes to the optical channel.

2.6 Soft X-ray Endstations

A soft X-ray endstation contains the following elements: a diffraction grating to disperse the radiation from the insertion device or bend magnet by energy, a moveable aperture to select a small energy range from the grating's output, and highly reflective mirrors to focus the beam and direct it to the target, all these elements work within a

ultra high vacuum (UHV) environment so that the soft X-ray beam is not attenuated by air. At the end of the beamline is the experimental endstation and a chamber that contains a number of instruments to monitor the experimental endstation, a chamber that contains a number of instruments to monitor the sample's electronic, optical, and X-ray output as it is exposed to the soft X-ray beam. These chambers commonly contain equipment for controlling the orientation and temperature of the sample. Three "beamlines" are used for the experiments of this study.

2.6.1 Resonant Elastic and Inelastic X-ray Scattering Beamline

The resonant elastic and inelastic X-ray scattering (REIXS) beamline uses an elliptically polarizing undulator (EPU, insertion device 10ID-2 of the CLS) to produce soft X-rays ranging from 95 - 2000 eV [87]. Two separate gold-coated sagittal cylindrical mirrors are used to collect and collimate the X-rays from the EPU. These mirrors have three different interchangeable gratings corresponding to low, medium, and high energy [87]. The beamline delivers 10^{12} photons/s of flux on the low energy grating at 100 eV with 25 μm exit slits. Depending on the desired energy range, four selectable mirror coatings on the plane mirrors (Ni, Si, C, and Au) are used to suppress high-order harmonics. REIXS has a large spherical grating spectrometer, which uses Rowland circle geometry to measure high-resolution XES spectra. The monochromator's energy resolving power ($E/\Delta E$) varies across this range, from about 10^5 near 100 eV to 10^4 near 1000 eV. The spectra were normalized to the incident flux impinging on the sample monitored by a highly transparent gold mesh.

2.6.2 Beamline 8.0.1.1

The soft X-ray fluorescence endstation of beamline 8.0.1.1 (BL8) at the ALS was used in this research as well. BL8 is an undulator-based beamline with a 50 mm undulator

period [89]; its energy range is from 80 to 1250 eV. The appropriate energy is selected by a spherical grating monochromator. There are three different interchangeable gratings that correspond to low, medium, and high energy ranges with rulings of 150, 380, and 925 lines/mm, respectively [89]. At the maximum flux, BL8 delivers on the order of 10^{15} photons per second per mm^2 with $E/\Delta E$ of roughly 10^4 [89]. BL8 allows for the measurements of both the TFY and TEY modes and the spectra were normalized to the incident flux impinging on the sample monitored by a highly transparent gold mesh. The spectrometer is a grating incidence detector in Rowland circle geometry [89]. There are four spherical gratings that correspond to different energy ranges; the low and mid-low energy gratings have a 5 m radius and have 600 and 1500 lines/mm, respectively; the mid-high and high energy gratings have a 10 m radius and have 600 and 1500 lines/mm, respectively. The incident X-ray intensity is measured with a highly transparent gold mesh.

2.6.3 Variable Line Spacing - Plane Grating Monochromator Beamline

In this study, the variable line spacing - plane grating monochromator (VLS-PGM) beamline at the CLS was used to monitor optical luminescence using a selected X-ray photon energy for excitation. The VLS-PGM uses X-rays in the energy range of 5 - 250 eV. The source for the X-rays is a permanent magnet undulator with a 185 mm undulator period [88]. The appropriate energy is selected by a planar grating monochromator with variable spacing. There are three different interchangeable gratings that correspond to low, medium, and high energy ranges with central lines of 500, 1000, and 600 lines/mm, respectively [105]. VLS-PGM delivers on the order of 9×10^{11} photon/s of flux per 100 mA ring current on all three gratings with 50 μm slits. The $E/\Delta E$ of VLS-PGM is better than 10^4 [88]. The measurements on all three beamlines are conducted in UHV.

Chapter 3

Calculation Methods

All materials are made of atoms, which consist electrons and nuclei that interact with each other according to Coulomb's law. When a solid is formed, the valence electrons become delocalized and arrange in bands and subsequently can move in the solid. On the other hand, core electrons do not play much of a role in solid-state properties. Studying the electronic structure of materials is an important part of research in material science. The main principle behind the electronic structure theory is to fix the ions at specified locations within the framework of the Born-Oppenheimer approximation. Next step is to construct the Hamiltonian of the electronic motions and determine all of its eigenfunctions. Thus, the energy of the corresponding eigenstates is obtained as eigenvalues. This chapter focuses on the theories, methods, and applications of electronic structure theory that are relevant to this study. To write this chapter, I have followed the references [90, 106, 107]. Density functional theory (DFT) is widely acknowledged as the most significant technique for studying the electronic structure of a many-body system. DFT provides an approximation for solving the Schrödinger equation for many-body systems.

DFT is an efficient and powerful method for calculating the band structure and electronic properties of materials. A typical material contains approximately 10^{23} particles. However, the Schrödinger equation cannot be used to compute the eigenfunctions as well as eigenvalues for such materials. DFT ensures that the Schrödinger equation

does not need to be used to solve wave functions to compute all the parameters of a many-body interacting system. DFT is an exact theory, however, it still requires various approximations to determine electronic properties.

3.1 Wave Function

The wave function in quantum mechanics contains all the information of a particular system. The time-independent wave function is the most usable form because of its simplicity. The wave function itself is physically meaningless and it is not a physically observable quantity; that implies that the wavefunction is purely a mathematical term. The probability interpretation of the wave function provides the physical meaning of the wave function. The probability of finding the particle within the volume element $d\mathbf{r}_1 d\mathbf{r}_2 \dots d\mathbf{r}_N$ at a time t is obtained by multiplying the square of the wave function by the volume elements [90, 108] as

$$P(d\mathbf{r}_1 d\mathbf{r}_2 \dots d\mathbf{r}_N, t) d\mathbf{r}_1 d\mathbf{r}_2 \dots d\mathbf{r}_N = |\Psi(\mathbf{r}_1, \mathbf{r}_2, \dots, \mathbf{r}_N, t)|^2 d\mathbf{r}_1 d\mathbf{r}_2 \dots d\mathbf{r}_N. \quad (3.1)$$

where

$$P(d\mathbf{r}_1 d\mathbf{r}_2 \dots d\mathbf{r}_N, t) = |\Psi(\mathbf{r}_1, \mathbf{r}_2, \dots, \mathbf{r}_N, t)|^2 = \Psi(\mathbf{r}_1, \mathbf{r}_2, \dots, \mathbf{r}_N, t)^* \Psi(\mathbf{r}_1, \mathbf{r}_2, \dots, \mathbf{r}_N, t) \quad (3.2)$$

Equation (3.1) describes the probability that particles $1, 2, \dots, N$ are located simultaneously in the corresponding volume element $d\mathbf{r}_1 d\mathbf{r}_2 \dots d\mathbf{r}_N$ [109].

Since the probability of finding the particles somewhere in space must be unity and, therefore, it can be written as

$$\int d\mathbf{r}_1 \int d\mathbf{r}_2 \dots \int d\mathbf{r}_N |\Psi(\mathbf{r}_1, \mathbf{r}_2, \dots, \mathbf{r}_N, t)|^2 = 1, \quad (3.3)$$

which is known as the normalization condition for the wave function. Equation (3.3) provides insight regarding the requirement that a wave function must fulfill to be

physically acceptable. The wave function must be continuous over the full spatial range and square integrable [110]. The wave function is used to calculate the expectation values of operators that provides the expectation value of the corresponding observable for that wave function [111]. For an observable $A(\mathbf{r}_1, \mathbf{r}_2, \dots, \mathbf{r}_N)$, the expectation value is then,

$$A = \langle \hat{A} \rangle = \int d\mathbf{r}_1 \int d\mathbf{r}_2 \dots \int d\mathbf{r}_N \Psi^*(\mathbf{r}_1, \mathbf{r}_2, \dots, \mathbf{r}_N, t) \hat{A} \Psi(\mathbf{r}_1, \mathbf{r}_2, \dots, \mathbf{r}_N, t). \quad (3.4)$$

3.2 Schrödinger's Equation

The Schrödinger wave equation is a fundamental equation of quantum mechanics that describes the dynamics of quantum mechanical systems. It cannot be proved to be true like Newton's equation. It is a partial differential equation that describes the evolution of a quantum state of a physical system. In 1926, E. Schrödinger proposed an equation for describing the so-called wave behavior of matter, for example, the electron based on the de Broglie hypothesis. This equation was later named the Schrödinger equation. The time dependent Schrödinger equation for N particles can be written as [112]

$$i\hbar \frac{\partial}{\partial t} \Psi(\mathbf{r}_i, t) = \hat{H} \Psi(\mathbf{r}_i, t), \quad (3.5)$$

where \mathbf{r}_i denotes the position coordinate of the i -th particle, $\hbar = \frac{h}{2\pi}$ denotes the reduced Planck constant, t denotes the time, and \hat{H} denotes the Hamiltonian, which is defined as [112]

$$\hat{H} = -\frac{\hbar^2}{2} \sum_{i=1}^N \frac{1}{m_i} \nabla_i^2 + V(\mathbf{r}_1, \mathbf{r}_2, \dots, \mathbf{r}_N, t). \quad (3.6)$$

The first term in Eq. 3.6 represents the kinetic energy of the system and the second term represents the potential energy of the system. If the Hamiltonian is independent of time, the Schrödinger equation can be written as

$$\hat{H}\Psi(\mathbf{r}_1, \mathbf{r}_2, \dots, \mathbf{r}_N) = E\Psi(\mathbf{r}_1, \mathbf{r}_2, \dots, \mathbf{r}_N) , \quad (3.7)$$

where \hat{H} can be written as

$$\hat{H} = -\frac{\hbar^2}{2} \sum_{i=1}^N \frac{\nabla_i^2}{m_i} + V(\mathbf{r}_1, \mathbf{r}_2, \dots, \mathbf{r}_N) , \quad (3.8)$$

and E stands for the system's total energy.

3.3 Electron Density

The electron density or electronic density describes the probability of finding an electron in a particular position near an atom or molecule and it is defined as the number of electrons per unit volume in an electronic system. Neglecting the spin coordinates, electron density $\rho(\mathbf{r})$ can be stated as a measurable observable

$$\rho(\mathbf{r}) = N \int d\mathbf{r}_2 \dots \int d\mathbf{r}_N \Psi^*(\mathbf{r}_1, \mathbf{r}_2, \dots, \mathbf{r}_N) \Psi(\mathbf{r}_1, \mathbf{r}_2, \dots, \mathbf{r}_N), \quad (3.9)$$

which depends on spatial coordinates [113, 114]. Usually X-ray diffraction can be used to determine density $\rho(\mathbf{r})$ [115]. When quantum-mechanical effects are significant, $\rho(\mathbf{r})$ provides the probability to find any electron within volume element $d\mathbf{r}$ from total number of electrons N . The following are some fundamental properties of $\rho(\mathbf{r})$:

- (i.) $\rho(\mathbf{r}) \rightarrow 0$ as $\mathbf{r} \rightarrow \infty$.
- (ii.) Integration of the density gives the total number of electrons, $\int \rho(\mathbf{r}) d\mathbf{r} = N$.

$\rho(\mathbf{r})$ is a function of three degrees of freedom. To use the electron density as a variable in an approach, it must be ensured that it truly contains all necessary information about the system. This implies that it must include information on the total number of electrons N as well as the external potential characterized by V_{ext} [115]. The total number of electrons can be obtained by the integration of the electron density over the spatial coordinates [115]

$$N = \int \rho(\mathbf{r}) d\mathbf{r}. \quad (3.10)$$

The external potential is characterized uniquely by the ground-state electron density. The term uniquely indicates an additive constant as proved by the first Hohenberg and Kohn (HK) theorem.

3.4 Many-Body Hamiltonian

A solid is composed of positively charged heavy particles (nuclei) and negatively charged lighter particles (electron). Suppose a system has N nuclei, then it is a problem of $N + ZN$ electromagnetically interacting particles. Therefore, it becomes a many body problem. Quantum mechanics is required since the particles are so light. The Hamiltonian of the many-body system is the starting point for the quantum theory of materials. For a system composed of atomic nuclei and electrons, such as a crystalline solid, the many-body Hamiltonian \hat{H}_{ne} contains [106]

$$\hat{H}_{ne} = \hat{T}_e + \hat{T}_n + \hat{V}_{ee} + \hat{V}_{nn} + \hat{V}_{en}, \quad (3.11)$$

where the electronic kinetic energy

$$\hat{T}_e = -\frac{\hbar^2}{2} \sum_{j=1}^N \frac{\nabla_j^2}{m_e}, \quad (3.12)$$

nuclear kinetic energy

$$\hat{T}_n = -\frac{\hbar^2}{2} \sum_{i=1}^M \frac{\nabla_i^2}{M_i}, \quad (3.13)$$

electron-electron Coulomb repulsion

$$\hat{V}_{ee} = \frac{1}{2} \frac{1}{4\pi\epsilon_0} \sum_{i \neq j}^N \frac{e^2}{|r_i - r_j|}, \quad (3.14)$$

nuclei-nuclei Coulomb repulsion

$$\hat{V}_{nn} = \frac{1}{2} \frac{1}{4\pi\epsilon_o} \sum_{I \neq J}^M \frac{e^2 Z_I Z_J}{|R_I - R_J|}, \quad (3.15)$$

and electron-nuclei Coulombic potential

$$\hat{V}_{en} = -\frac{1}{4\pi\epsilon_o} \sum_I^M Z_I e \sum_i^N \frac{e}{|r_i - R_I|}, \quad (3.16)$$

where Z , N , and M represent the atomic number, total number of electrons, and total number of nuclei, respectively. The factor of $1/2$ is for avoiding double counting in the sum.

The time-independent Schrödinger equation for this Hamiltonian can be written as

$$\hat{H}_{ne} \Psi = E \Psi. \quad (3.17)$$

This equation can only be solved analytically for few-body system and all other cases require numerical techniques and approximations.

3.4.1 Born-Oppenheimer Approximation

The Born-Oppenheimer (BO) approximation allows to decouple the electronic and ionic motion. Max Born and J. Robert Oppenheimer proposed this approximation in 1927 [116]. The BO approximation represents the assumption that the motion of atomic nuclei and electrons in a system can be separated. The very essential ingredient of the BO approximation originates from the fact that the mass of an atomic nucleus in a system is much larger than the mass of an electron; this implies that there must be a large difference in speed between them. Thus, the nuclei are nearly fixed with respect to the electron motion. As a result, the kinetic energy of the nuclei becomes zero, and the potential energy remains constant. After applying this approximation, the system becomes NZ interacting negative particles, moving in the potential of the nuclei. Thus, the complete Hamiltonian \hat{H}_{ne} is replaced by the so-called electronic Hamiltonian [116]

$$\hat{H}(\mathbf{r}; \mathbf{R}) = \hat{T}_e + \hat{V}_{ee} + \hat{V}_{ext}, \quad (3.18)$$

where \hat{V}_{ext} denotes the potential energy of the electrons in the potential of the nuclei. The terms \hat{T}_e and \hat{V}_{ee} deals with a many-electron system and they are independent of the particular kind of many-electron system. This part is universal. System-specific information (which nuclei, and on which positions) is given entirely by \hat{V}_{ext} . The solution of the Schrödinger equation for this electronic system can be written as

$$\hat{H}\Psi = E_e\Psi. \quad (3.19)$$

with the electronic Hamiltonian \hat{H} , the electronic wave function $\Psi = \Psi(\mathbf{r}_1, \mathbf{r}_2, \dots, \mathbf{r}_N; \mathbf{R})$, and the electronic energy E_e , where \mathbf{R} represents the ionic coordinates.

The most difficult part to solve Equation (3.19) is the interaction between electrons, where all many-body quantum effects are hidden. Many approximate methods have been developed to solve the Schrödinger equation by mapping the N -electron Schrödinger equation into effective one-electron Schrödinger-like equations, which are easier to tackle computationally. In the present work, DFT is used to approximate the ground-state energy of Equation (3.19), where the electron density is the essential quantity.

3.5 Density Functional Theory

DFT is a successful theory to calculate electronic structure. The name DFT can arise because of the use of functionals (*i.e.* function of another function) of the electron density. Instead of using the many-body wave function $\Psi(\mathbf{r})$, the DFT approach uses electron density functionals (for N electrons) described by Equation (3.9). Thus, the electron density is the fundamental variable in DFT to explain the quantum many-electrons system. DFT is a method for calculating the ground-state electronic density and energy of a many-electron system by solving the Schrödinger equation. Thus,

DFT is referred to as the ground-state theory. DFT is a variational method that is currently the most promising and successful method for calculating the electronic properties of the material. It works with a wide range of systems including atoms, molecules, and solids as well as nuclei and quantum and classical fluids. DFT is computationally simple and can be applied to large systems such as those containing hundreds or even thousands of atoms because the density depends only on \mathbb{R}^3 . This is why DFT has become one of the most effective tools for doing calculations on molecular and condensed matter systems for describing their properties [117]. Kohn and Sham (KS) DFT and Hohenberg and Kohn (HK) DFT are the most used density functional theories. DFT describes the ground-state energy of each system as a functional of its electron density $\rho(\mathbf{r})$ as $E_g = E[\rho(\mathbf{r})]$. From the theoretical point of view, the HK's DFT [113] has achieved significant progress in material science research. They demonstrated that the total energy of a system can be described as a functional of the electron charge density. Kohn and Sham developed an expression for a system's total energy based on the HK theory, which is referred to as KS-DFT [118].

3.5.1 Hohenberg and Kohn Theorems

There are two HK theorems, which are named as the first and second HK theorems. These HK theorems are the starting point for any study of DFT and thus, they are the foundation of the DFT. The first and second HK theorems were stated and proved by P. Hohenberg and W. Kohn [113]. The statement and proof of the HK theorems are described below [106].

- First theorem: The external potential $V_{ext}(r)$ is a unique functional of the electron density $\rho(r)$. As a result, the total ground-state energy E of any many-electron system is also a unique functional of $\rho(r)$, that is $E = E[\rho]$.
- Second theorem: The functional $E[\rho]$ for the total energy has a minimum equal

to the ground-state energy at the ground-state density.

Let us consider that \hat{H} is an electronic Hamiltonian for a system of N electrons. When a system is in the state Ψ , it satisfies $\hat{H}\Psi = E\Psi$. Thus, the average energy can be written as [106]

$$E[\Psi] = \frac{\langle \Psi | \hat{H} | \Psi \rangle}{\langle \Psi | \Psi \rangle}, \quad (3.20)$$

where

$$\langle \Psi | \hat{H} | \Psi \rangle = \int \Psi^* \hat{H} \Psi d\mathbf{r} \quad (3.21)$$

and

$$E[\Psi] \geq E_g. \quad (3.22)$$

According to the variational principle, the energy calculated from a guessed Ψ is an upper bound to the true ground-state energy, E_g [90]. Completely minimizing the functional $E[\Psi]$ with respect to all allowed N -electrons wave functions yields the true ground-state Ψ_g and energy $E[\Psi_g]=E_g$; that is,

$$E_g = \min_{\Psi} E[\Psi] = \langle \Psi_{min} | \hat{T} + \hat{V}_{ext} + \hat{V}_{ee} | \Psi_{min} \rangle. \quad (3.23)$$

Therefore, the variational principle states a process to determine the ground-state wave function Ψ_g , the ground-state energy, and other properties of interest for a system of N electrons with a certain nuclear potential V_{ext} . This implies, the ground-state energy is a functional of the number of electrons N and the nuclear potential V_{ext}

$$E_g = E_g[N, V_{ext}]. \quad (3.24)$$

It is well known that the external potential determines all properties of the system [117]. The first HK theorem states that the ground state density $\rho(r)$ uniquely

determines the external potential up to an arbitrary constant. The energy of the system can be expressed as

$$\begin{aligned}
E &= \langle \Psi | \hat{H} | \Psi \rangle \\
&= \langle \Psi | \hat{T} + \hat{V}_{ext} + \hat{V}_{ee} | \Psi \rangle \\
&= \int V_{ext}(\mathbf{r})\rho(\mathbf{r})d\mathbf{r} + \langle \Psi | \hat{T} + \hat{V}_{ee} | \Psi \rangle,
\end{aligned} \tag{3.25}$$

which is used for the proof of the first HK theorem.

Assume two potentials $V_{ext}(\mathbf{r})$ and $V'_{ext}(\mathbf{r})$ differ by more than a constant, and yield the same charge density $\rho(r)$. Thus, the related Hamiltonians, \hat{H}_1 and \hat{H}'_2 have different ground wavefunctions, Ψ_1 and Ψ'_2 , but each yields the same charge density, $\rho(r)$. Consider E_g and E'_g as the two ground-state energies for \hat{H}_1 and \hat{H}'_2 , respectively. Using Ψ'_2 as a trial function of \hat{H}_1 , the Raleigh-Ritz minimal principle states that [106]

$$\begin{aligned}
E_g < \langle \Psi'_2 | \hat{H}_1 | \Psi'_2 \rangle &= \langle \Psi'_2 | \hat{H}'_2 | \Psi'_2 \rangle + \langle \Psi'_2 | \hat{H}_1 - \hat{H}'_2 | \Psi'_2 \rangle \\
&= E'_g + \int [V_{ext}(\mathbf{r}) - V'_{ext}(\mathbf{r})]\rho(\mathbf{r})d\mathbf{r}.
\end{aligned} \tag{3.26}$$

Likewise, it can be written as

$$\begin{aligned}
E'_g < \langle \Psi_1 | \hat{H}'_2 | \Psi_1 \rangle &= \langle \Psi_1 | \hat{H}_1 | \Psi_1 \rangle + \langle \Psi_1 | \hat{H}'_2 - \hat{H}_1 | \Psi_1 \rangle \\
&= E_g - \int [V_{ext}(\mathbf{r}) - V'_{ext}(\mathbf{r})]\rho(\mathbf{r})d\mathbf{r}.
\end{aligned} \tag{3.27}$$

After adding Equations (3.26) and (3.27), an inequality is obtained, which is

$$E_g + E'_g < E_g + E'_g . \tag{3.28}$$

The inequality in Equation 3.28 represents an obvious contradiction. Therefore, two different $V_{ext}(\mathbf{r})$ cannot have the same $\rho(\mathbf{r})$ for their ground states. As a result, $\rho(\mathbf{r})$

determines the total number of electrons N in the atom and the external potential $V_{ext}(\mathbf{r})$, and thus, all the properties related to the ground state. Thus, the total energy can be expressed as a functional of the electron density

$$\begin{aligned} E[\rho] &= T[\rho] + E_{ne}[\rho] + E_{ee}[\rho] \\ &= \int V_{ext}(\mathbf{r})\rho(\mathbf{r})d\mathbf{r} + F_{HK}[\rho], \end{aligned} \quad (3.29)$$

here

$$F_{HK}[\rho] = T[\rho] + E_{ee}[\rho]. \quad (3.30)$$

The functional $F_{HK}[\rho]$ is independent on potential V_{ext} and it contains the functional for the kinetic energy, $T[\rho]$, and electron-electron interaction, $E_{ee}[\rho]$. The big challenge in DFT is to obtain the explicit form of the functional F_{HK} .

According to the second HK theorem, the energy functional is variational. The second HK theorem describes that for any \mathbf{r} , the trial electron density $\tilde{\rho}(\mathbf{r})$ satisfies the conditions, $\tilde{\rho}(\mathbf{r}) \geq 0$ and $\int \tilde{\rho}(\mathbf{r})d\mathbf{r} = N$, as well as the inequality $E_g \leq E[\tilde{\rho}]$ holds, where $E[\tilde{\rho}] = T[\tilde{\rho}] + E_{ne}[\tilde{\rho}] + E_{ee}[\tilde{\rho}]$.

Based on the first HK theorem, assume that the ground-state wave function is Ψ_g and its corresponding electron density is $\rho(\mathbf{r})$. Thus, the ground-state density $\rho(\mathbf{r})$ uniquely determines the external potential, $V_{ext}(\mathbf{r})$. Consider a trial density $\tilde{\rho}$ that determines its corresponding wave function $\tilde{\Psi}$ with a arbitrary variation from Ψ_g ; then, it can be written as

$$\begin{aligned} \langle \tilde{\Psi} | \hat{H} | \tilde{\Psi} \rangle &= \int \tilde{\rho}V_{ext}d\mathbf{r} + T[\tilde{\rho}] + E_{ee}[\tilde{\rho}] \\ &= E[\tilde{\rho}] \geq E_g[\rho]. \end{aligned} \quad (3.31)$$

Thus, the energy will be at its lowest value when the electron density equals the electron density in the ground-state. The above two theorems lead to the fundamental statement of the DFT, *i.e.*,

$$\delta\left\{E[\rho] - \mu\left(\int \rho(\mathbf{r})d\mathbf{r} - N\right)\right\} = 0. \quad (3.32)$$

The ground-state energy and density are the minimum of some functional $E[\rho]$ subject to constraint $\int \rho(\mathbf{r})d\mathbf{r} = N$, which gives the correct number of electrons. Electronic chemical potential μ is the Lagrange multiplier of this constraint. Suppose, $\mu(\mathbf{r}) = \frac{\delta E[\rho]}{\delta \rho(\mathbf{r})} = V_{ext}(\mathbf{r}) + \frac{\delta F_{HK}[\rho]}{\delta \rho(\mathbf{r})}$. Then, Equation (3.32) provides the Euler-Lagrange equation

$$\mu(\mathbf{r}) - \mu = 0. \quad (3.33)$$

The ground-state properties can be determined using the density as the variational variable and a universal functional $F_{HK}[\rho]$ according to the HK theorems. The functional $F_{HK}[\rho]$ exists; however, its explicit form completely remains unknown.

3.5.2 Kohn-Sham Equations

The KS equations established the relationship between the ground-state density of a system and its ground-state wave function. Walter Kohn has received the Nobel Prize in chemistry in 1998 to calculate electronic properties of solids based on DFT. The key step is to rewrite the functional $F_{HK}[\rho]$ as [107]

$$\begin{aligned}
F_{HK}[\rho] &= T[\rho] + E_{ee}[\rho] \\
&= T[\rho] + E_{ee} + T_s - T_s \\
&= T_s + E_{ee} + \underbrace{T[\rho] - T_s}_{V_c} \\
&= T_s + E_{ee} + V_c \\
&= T_s + E_{ee} + V_c + V_H - V_H \\
&= T_s + V_H + V_c + \underbrace{E_{ee} - V_H}_{V_x} \\
&= T_s + V_H + \underbrace{V_c + V_x}_{V_{xc}} \\
&= T_s + V_H + V_{xc}
\end{aligned}
\tag{3.34}$$

where $T[\rho]$ and $E_{ee}[\rho]$ denote the kinetic energy and self-interaction Coulomb potentials of the many-electron systems. $T_s[\rho(\mathbf{r})]$ represents the kinetic energy functional of a system of noninteracting electrons with density $\rho(\mathbf{r})$. V_H denotes the Hartree potential, defined by $V_H = \frac{1}{2} \int \int \frac{\rho(\mathbf{r}_1)\rho(\mathbf{r}_2)}{|\mathbf{r}_1 - \mathbf{r}_2|} d\mathbf{r}_1 d\mathbf{r}_2$. Now, V_x denotes the exchange potential functional, given by the difference between the exact many-electron Coulomb potential functional and the Hartree potential functional. V_c denotes the correlation potential functional, given by the difference between the exact many-electron kinetic energy functional and the kinetic energy functional of a system of noninteracting electrons gas. $E_{xc}[\rho]$ represents the exchange correlation energy functional defined as $V_{xc} = V_c + V_x$ [106].

Except for the exchange correlation energy, the KS equations can accurately express all the above terms in terms of the electronic density. According to Kohn and Sham, the Hamiltonian-called the Kohn-Sham Hamiltonian is [106]

$$\begin{aligned}
\hat{H}_{KS} &= \hat{T}_s + \hat{V}_H + \hat{V}_{ext} + \hat{V}_{xc} \\
&= -\frac{\hbar^2 \nabla_i^2}{2 m_e} + \int \frac{\rho(\mathbf{r}_1)}{|\mathbf{r} - \mathbf{r}_1|} d\mathbf{r}_1 + V_{ext}(\mathbf{r}) + V_{xc}[\rho(\mathbf{r})] .
\end{aligned} \tag{3.35}$$

The exact ground-state density $\rho(\mathbf{r})$ of an N-electron system is

$$\rho(\mathbf{r}) = \sum_i^N |\psi_i|^2, \tag{3.36}$$

which is the sum of the density of a set of N noninteracting single-particle wave functions (orbitals), ψ_i . The single-particle wave functions ψ_i are the N lowest-energy solutions of the KS equation [106]

$$\left[-\frac{\hbar^2}{2m_e} \nabla_i^2 + V_{KS}(\mathbf{r}) \right] \psi_i = \varepsilon_i \psi_i , \tag{3.37}$$

where ψ_i represents KS orbitals, ε_i represent KS orbital energies, and V_{KS} represents the one-body effective fictitious external potential, which is defined as [106]

$$V_{KS}(\mathbf{r}) = V_{ext}(\mathbf{r}) + \int \frac{\rho(\mathbf{r}_1)}{|\mathbf{r} - \mathbf{r}_1|} d\mathbf{r}_1 + V_{xc}[\rho(\mathbf{r})], \tag{3.38}$$

and it depends on $\rho(\mathbf{r})$. In Equation (3.38), $V_{xc} = \frac{\delta E_{xc}}{\delta \rho}$ represents the exchange correlation potential. The KS equations are Equations (3.36), (3.37), and (3.38), in which E_{xc} is the only unknown term. The KS equations are well-known for determining the exact total energy of a system. Equation (3.37) needs to be solved iteratively until the self-consistent orbitals are determined based on the density dependence of the one-electron KS effective potential, $V_{KS}(\mathbf{r})$. Figure 3.1 depicts the flowchart of the iterative procedure of the solution of Equation (3.37). In this process, a trial electron density is considered, and then, this trial electron density is used to construct the KS Hamiltonian. Then, the KS Schrödinger equation (3.37) is solved, which yields the quasiparticle wavefunctions ψ_i , which in turn yields an updated electron density. This procedure is repeated until the newly obtained electron density has to within

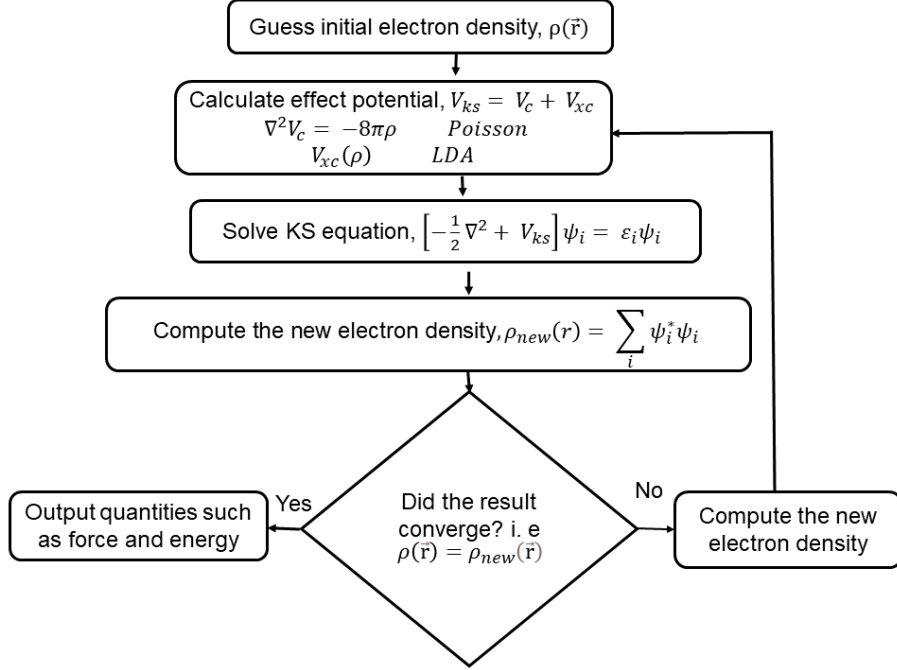


Figure 3.1: Schematic flowchart of the iterative procedure used in self-consistent calculations. The diagram is taken from Ref. [107].

some tolerance, converged with the electron density from the previous cycle. Once this condition is satisfied, $\rho(\mathbf{r})$ is consistent, and a solution has been obtained and the calculation is finished.

Finally, the total energy can be determined from the KS eigenenergies and the ground-state density $\rho(\mathbf{r})$ as

$$E = \sum_{i=1}^N \varepsilon_i - \int d^3r \left[\frac{1}{2} V_H(\mathbf{r}) + V_{xc}(\mathbf{r}) \right] \rho(\mathbf{r}) + E_{xc}[\rho(\mathbf{r})].$$

The ground-state density and total energy can be determined if each term in the KS energy functional is known. However, the exact form of the exchange correlation energy functional, E_{xc} is not known, and it is impossible to find an exact expression for E_{xc} except for a free electron gas. Currently, the biggest challenge faced in the modern DFT is to find the approximate form for the exchange correlation energy functional with a sufficient accuracy. Kohn and Sham [117, 118] developed a form for the exchange-correlation (XC) energy functional that was exact for the uniform

electron gas system; this is known as local density approximation (LDA).

3.6 Exchange Correlation Energy Functionals

The success of a DFT calculation method depends on the quality of the XC. The exchange arises from antisymmetry caused by the Pauli exclusion principle. The most difficult challenge in DFT is to find the exact form of E_{xc} . It will be extremely difficult to express E_{xc} mathematically in a closed form. It would be a great achievement to find such a mathematical form in DFT. It is necessary to apply an approximation for E_{xc} because the general form of the XC energy in terms of the density is unknown. There are two common approximations for E_{xc} widely used by scientists: local density approximation (LDA) and generalized gradient approximation (GGA). In this work, LDA and GGA-based functionals were utilized mostly. In addition, modified Becke-Johnson potential (TB-mBJ) is used to calculate the band gap of the studied materials. Higher-order functionals include the meta-GGA functionals, which include the KS energy densities of occupied molecules, and the hyper-GGA functionals (HGGA), which incorporate the HF exchange energies or some other functionals; they are not further discussed.

3.6.1 Local Density Approximation

LDA is the widely used approximation for XC functional $E_{xc}[\rho]$. According to LDA, the density can be considered locally as an uniform electron gas with the same exchange and correlation energy at each point in the system as uniform electron gas of the same density. Kohn and Sham first proposed this approximation [118]. By construction, LDA is expected to perform well when the density $\rho(\mathbf{r})$ of a system varies extremely slow with \mathbf{r} . However, LDA approximation works well in many other systems. In LDA, $E_{xc}[\rho]$ functional has the following form [106]

$$E_{xc}^{LDA}[\rho(\mathbf{r})] = \int \rho(\mathbf{r}) \varepsilon_{xc}^{LDA}[\rho(\mathbf{r})] d\mathbf{r}, \quad (3.39)$$

where ε_{xc}^{LDA} represents the XC energy per particle in an uniform electron gas, which is a function of only density $\rho(\mathbf{r})$. The uniform electron gas is a hypothetical solid in which all nuclear charge is uniformly distributed across the space. This material is totally isotropic and identical on any length scale.

3.6.2 Generalized Gradient Approximation

The logical step toward improving LDA is that the XC energy not only depends on the local density but also on the density in the neighbour, which allows us to consider the variations of the electron density in very inhomogeneous systems. The LDA is suitable for smooth $\rho(\mathbf{r})$, *i.e.*, for solids that close to the uniform electron gas. However, LDA is not accurate in non-uniform systems such as molecules, clusters, and layers. The GGA improves on this estimation by taking into account the gradient of electron density [106].

The $E_{xc}[\rho]$ for GGA can be written as

$$E_{xc}^{GGA}[\rho] = \int \rho(\mathbf{r}) \varepsilon_{xc}^{GGA}[\rho(\mathbf{r}), |\nabla\rho(\mathbf{r})|] d\mathbf{r} \quad (3.40)$$

and the general procedure for constructing the GGA functional is to express the correlation energy as [106]

$$E_{xc}^{GGA}[\rho(\mathbf{r})] = \int \rho \varepsilon_{xc}^{LDA}[\rho(\mathbf{r})] d\mathbf{r} + \int F_{xc}[\rho(\mathbf{r}), |\nabla\rho(\mathbf{r})|] d\mathbf{r}, \quad (3.41)$$

where $F_{xc}[\rho(\mathbf{r}), |\nabla\rho(\mathbf{r})|]$ represents the XC enhancement factor. The GGA does not have a single form, and can take many different forms [119–121], each of which corresponds to a different enhancement factor. The GGA succeeds in reducing the effects of LDA overbinding [122], and it works better when applied to molecules. The most popular GGA functional is the Perdew-Burke-Ernzerhof (PBE) [119].

3.6.3 Tran–Blaha modified Becke–Johnson potential

DFT can be used to investigate the electronic structure of solids [113]. The most common exchange correlation functional for calculating the electronic structure of

solids in DFT is GGA functional [119]. However, the GGA functional underestimates the band gap of the materials. The GGA functional does not show a derivative discontinuity, which results in the difference between the KS band gap, that is defined as the difference between the eigenvalues of the conduction-band minimum and the valence-band maximum, and the experimental band gap, that is defined as the difference between the ionization potential and the electron affinity. By utilizing semi-local values, the Tran and Blaha proposed modified Becke-Johnson potential (TB-mBJ) to reproduce derivative discontinuities accurately. Thus the semi-local TB-mBJ potential determines the band gaps of solids with better agreement of experiments. For this reason, I have used TB-mBJ potential for calculating band gap of my studied materials.

The TB-mBJ potential [123] consists of a modified version of the BJ potential [124] for exchange and LDA [118] for correlation. The TB-mBJ potential is given by [123]

$$v_x^{TB-mBJ}(\mathbf{r}) = cv_x^{BR}(\mathbf{r}) + (3c - 2)\frac{1}{\pi}\sqrt{\frac{5}{6}}\sqrt{\frac{t(\mathbf{r})}{\rho(\mathbf{r})}} \quad (3.42)$$

where $\rho(\mathbf{r})$ represents the electron density, $t(\mathbf{r})$ represents the kinetic energy density, and $v_x^{BR}(\mathbf{r})$ represents the Beeke-Roussel (BR) exchange potential suggested to model the Coulomb potential created by the exchange hole. The parameter in Eq 3.42 is given by

$$c = \alpha + \beta g^p \quad (3.43)$$

where

$$g = \frac{1}{V_{cell}} \int_{cell} \frac{|\nabla\rho(\mathbf{r})|}{\rho(\mathbf{r})} d\mathbf{r} \quad (3.44)$$

represents the average of $\frac{|\nabla\rho(\mathbf{r})|}{\rho(\mathbf{r})}$ in the unit cell of volume V_{cell} . The parameters in Eq 3.43 are $\alpha = -0.012$, $\beta = 1.023 \text{ Bohrs}^{\frac{1}{2}}$, and $p = \frac{1}{2}$, which were determined according to a fit to the experimental band gap of solids [123]. The c values greater than

1 represent the less negative (i.e. less attractive) potential, particularly in low-density regions. Currently, the most reliable semi-local technique for band gap prediction is the TB-mBJ potential [125].

3.7 Choice of Basis Set

One electron KS equation for an infinite set can be written as [107]

$$\hat{H}_{sp}\phi_m(r) = \varepsilon_m\phi_m(r) \quad (3.45)$$

where $\hat{H}_{sp} = -\frac{\hbar^2}{2m_e}\nabla_m^2 + \int \frac{\rho(\mathbf{r}_1)}{|\mathbf{r}-\mathbf{r}_1|}d\mathbf{r}_1 + V_{ext}(\mathbf{r}) + V_{xc}[\rho(\mathbf{r})]$ denotes the single-particle Hamiltonian. For DFT, $V_{xc}[\rho(\mathbf{r})]$ represents the exchange-correlation operator in the LDA, GGA or another approximation.

To solve 3.45, a basis set has to be chosen in the following form [107]

$$\phi_m(r) = \sum_{p=1}^P c_p^m \phi_p^b \quad (3.46)$$

If the complete basis set is chosen ($P = \infty$), an exact solution of Eq. 3.46 can be obtained, which is not practical. Therefore it needs to select finite basis set that can generate a very good solution of Eq. 3.46.

For a given m, substituting Eq. 3.46 in Eq. 3.45 and multiplying by $\langle \phi_i^b |$ ($i = 1, 2, \dots, P$) from the left-side, it can be written as [107]

$$\sum_{i=1}^P \sum_{p=1}^P [\langle \phi_i^b | H_{sp} | \phi_p^b \rangle - \varepsilon_m \langle \phi_i^b | \phi_p^b \rangle] c_p^m = 0 \quad (3.47)$$

The nontrivial solutions to Eq. 3.47 exist only if the determinant of the matrix of Eq. 3.47 is zero, *i.e.*

$$\det \sum_{i=1}^P \sum_{p=1}^P [\langle \phi_i^b | H_{sp} | \phi_p^b \rangle - \varepsilon_m \langle \phi_i^b | \phi_p^b \rangle] = 0 \quad (3.48)$$

Diagonalization of the Hamiltonian matrix will lead to P eigenvalues and P sets of coefficients that express each of the P eigenfunctions in the given basis.

Variety of basis sets are available for instance, linear combination of atomic orbitals, numerical basis sets, pseudopotential schemes, or space partitioning methods. However each set has its own advantages and drawbacks. For a periodic Hamiltonian, the eigenfunction can be expressed in terms of plane wave basis set as [107]

$$\psi_{\vec{k}}^n = \sum_K c_K^{n,\vec{k}} e^{i(\vec{k}+\vec{K})\cdot\vec{r}} \quad (3.49)$$

where index m and p of Eq. 3.46 correspond to (n,\vec{k}) and $\vec{k} + \vec{K}$, respectively. Finite basis set can be done by limiting the set to all \vec{K} with $K \leq K_{max}$, where K_{max} denotes the radius of reciprocal space. Therefore, all reciprocal lattice vectors that are inside this sphere are taken into the basis set. The corresponding free electron energy of K_{max} is called cut-off energy, which is as follows [107]

$$E_{cut} = \frac{\hbar^2 K_{max}^2}{2m_e} \quad (3.50)$$

The main problem with a plan wave basis is that of describing the rapid changes in the wavefunctions close to the nucleus of an atom. To solve this problem, the potential in the inner regions (close to the nucleus) can be replaced by a pseudopotential, that is described to yield very smooth tails of the wavefunctions inside the atoms. More to the outer regions of the atoms, the pseudopotential continuously evolves into the true potential. However, this approximation does not allow to calculate properties involving the core states of a material.

A more efficient basis set close to the nucleus is required to avoid the use of pseudopotentials. The first attempt of this will be the augmented plane wave (APW) basis set. The electrons are free in the region far away from the nucleus. Plane waves are used to explain free electron. Close to the nuclei, the electrons describe efficiently by atomic like functions. In the APW basis set, space is split into two regions. A sphere of radius R_{MT} is drawn around each atom and this sphere is called a muffin tin sphere. The part of space occupied by spheres is the muffin tin region. The space

outside the spheres is called the interstitial region. A linear combination of radial functions times spherical harmonics is used to describe the basis sets in the muffin tin region and a plane wave expansion is used to describe the basis sets in the interstitial region. Thus, one APW can be expressed as [107]

$$\phi_{\vec{K}}^{\vec{k}}(\vec{r}, E) = \begin{cases} \frac{1}{\sqrt{V}} \exp(i(\vec{k} + \vec{K}) \cdot \vec{r}) & \vec{r} \notin R_{MT}^i \\ \sum_{l,m} A_{l,m}^{i,\vec{k}+\vec{K}} u_l^i(r, E) Y_m^l(\hat{r}) & \vec{r} \in R_{MT}^i \end{cases} \quad (3.51)$$

In Eq. 3.51, V represents the volume of unit cell, u_l^i denotes the radial portion of the spherical wave, Y_m^l represents the spherical harmonic, and R_{MT}^i denotes the used as a short-hand for indicating when \vec{r} is within the ‘‘muffin-tin’’ radius of nuclei i or in the interstitial region. Both $A_{l,m}^{i,\vec{k}+\vec{K}}$ and energy E are undetermined parameters. Boundary condition (Wave functions must be continuous at the interface between the muffin tin and the interstitial region) can be used to determine the coefficients $A_{l,m}^{i,\vec{k}+\vec{K}}$. An infinite sum over provides the perfect match between the plane waves and spherical harmonics. In practice, a truncation must occur at some value l_{max} . If the number of nodes per unit of length is identical within and outside of muffin thin region, the cut-off for the plane waves (K_{max}) and for the angular functions (l_{max}) are comparable quantity. This yields the condition $R_{MT}^i K_{max} = l_{max}$. This allows to determine a good l_{max} for a given K_{max} . The presence of unknown energy E in the radial portion u_l^i makes these equation fairly difficult to solve.

The linearized augmented plane wave (LAPW) method enables to solve the radial potion. Taylor series expansion of u_l^i about a known energy E_0 can be written as [107]

$$u_l^i(r, E) = u_l^i(r, E_0) + (E_0 - E) \frac{\partial}{\partial E} u_l^i(r, E) \Big|_{E=E_0} + O(E_0 - E)^2 \quad (3.52)$$

Considering only the first two terms of Equation 3.52, APW becomes linear equation in energy E as shown in Equation 3.53 [107].

$$\phi_{\vec{K}}^{\vec{k}}(\vec{r}, E) = \begin{cases} \frac{1}{\sqrt{V}} \exp(i(\vec{k} + \vec{K}) \cdot \vec{r}) & \vec{r} \notin R_{MT}^i \\ \sum_{l,m} (A_{l,m}^{i,\vec{k}+\vec{K}} u_l^i(r, E_0) + B_{l,m}^{i,\vec{k}+\vec{K}} \frac{\partial}{\partial E} u_l^i(r, E) |_{E=E_0}) Y_m^l(\hat{r}) & \vec{r} \in R_{MT}^i \end{cases} \quad (3.53)$$

The E_0 is not universal and it would be different for different states (s -, p -, d - and f -states). If valence and/or semi-core states (not fully confined within the muffin-tin sphere) correspond the different values of l (such as the p - and d - states), an improved basis set is used to include terms corresponding to u_l^i for different values and with different energies, denoted by $E_{1,l}^i$. Then, the final LAPW is [107]

$$\phi_{\vec{K}}^{\vec{k}}(\vec{r}, E) = \begin{cases} \frac{1}{\sqrt{V}} \exp(i(\vec{k} + \vec{K}) \cdot \vec{r}) & \vec{r} \notin R_{MT}^i \\ \sum_{l,m} (A_{l,m}^{i,\vec{k}+\vec{K}} u_l^i(r, E_{1,l}^i) + B_{l,m}^{i,\vec{k}+\vec{K}} \frac{\partial}{\partial E} u_l^i(r, E_{1,l}^i) |_{E=E_{1,l}^i}) Y_m^l(\hat{r}) & \vec{r} \in R_{MT}^i \end{cases} \quad (3.54)$$

All electrons can be treated with a (L)APW basis; however it is usually for the valence states. The core electrons are very tightly bound to the nuclei, which are always inside R_{MT} , and they are nearly identical to those in a free atom (although they may have a slightly different binding energy than the free atom case). To save time, the free atom orbitals are often used for these states. To treat “semi-core” states that are not valence level but still extend quite close to R_{MT} (such as, for example, Se 3d states), the LAPW basis set can be further modified by adding local orbitals (LOs) to it. The LAPW + LO basis set is defined as [107]

$$\phi_{\vec{K}}^{\vec{k}}(\vec{r}, E) = \begin{cases} 0 & \vec{r} \notin R_{MT}^i \\ (A_{l,m}^{i,LO} u_l^i(r, E_{1,l}^i) + B_{l,m}^{i,LO} \frac{\partial}{\partial E} u_l^i(r, E_{1,l}^i) |_{E=E_{1,l}^i} + C_{l,m}^{i,LO} u_l^i(r, E_{2,l}^i)) Y_m^l(\hat{r}) & \vec{r} \in R_{MT}^i \end{cases} \quad (3.55)$$

The local orbital implies for a particular atom i , l , and m . The same $u_l^i(r, E_{1,l}^i)$ and $\frac{\partial}{\partial E} u_l^i(r, E_{1,l}^i) |_{E=E_{1,l}^i}$ as in the LAPW basis set are used for the highest of the two valence states. The lower valence state is sharply peaked at an energy $E_{2,l}^i$. A single radial function $u_l^i(r, E_{2,l}^i)$ at that same energy will be sufficient to describe it. Thus,

LOs represent semi-core states very accurately, and they are considerably quicker to compute than the large number of regular LAPW functions it would take to describe such a state [107].

3.8 Calculation Details

The WIEN2k program was developed by Karlheinz Schwarz and Peter Blaha at the Technische Universität Wien. It is based on the LAPW + LO method to solve KS equations of DFT [126, 127]. WIEN2k is developed for crystalline materials, and it utilizes the crystalline symmetry and periodic boundary conditions to reduce the complexity of the problem.

Most of the calculations in this study were conducted utilizing the GGA XC functional. However, band gap of the studied materials was calculated using TB-mBJ potential. Crystal structures of the materials and space groups are the only input of our calculations. Our collaborator determined the experimental crystal structure of our samples by XRD method; which we used in our calculations. All calculations involved discretizing the first Brillouin zone into a k-point mesh of 1000 points per fundamental unit cell, and a cut-off of -6.0 Ryd (measured with respect to the average interstitial potential) was used to discriminate between the core and valence states. All calculations were extended to the outer Brillouin zones such that $R_{MT}^{min} K_{max} = 7$; *i.e.*, the product of the smallest atomic sphere and largest reciprocal lattice vector was 7. All ground-state electron densities were calculated self-consistently from initial guesses until the calculated electron density converged within margins of less than 0.0001 Ryd in energy and 0.001 e^- in charge (both per unit cell).

Chapter 4

Bandgap and Electronic Structure Determination of Oxygen - Containing Ammonothermal InN: Experiment and Theory

Authors: M. Ruhul Amin¹, T. de Boer¹, Peter Becker², Jan Hertrampf², Rainer Niewa², and Alexander Moewes¹

¹Department of Physics and Engineering Physics, University of Saskatchewan, 116 Science Place, Saskatoon, Saskatchewan , S7N 5E2, Canada

²Institute of Inorganic Chemistry, University of Stuttgart, Pfaffenwaldring, 55, 70569 Stuttgart, Germany

Reference: M. Ruhul Amin, T. de Boer, Peter Becker, Jan Hertrampf, Rainer Niewa, and Alexander Moewes, *Journal of Physical Chemistry C* 2019, **123**, 8943-8950 [82].

Summary and Author Contributions

InN is a key material for technological applications in opto-electronic devices due to its relatively small band gap, but there is a persistent and active debate about its varying band gap values and the origin of this. Initially reported band gap values for polycrystalline InN were in the range of 1.8 eV - 2.10 eV, which is about

twice the value of the one recently obtained for single crystalline thin films between 0.7 eV and 1.0 eV. In this manuscript [82], the goal of this work was to characterize the electronic properties of InN samples synthesized using ammonothermal synthesis. Several InN samples were grown and structurally characterized with XRD by P. Becker, J. Hertrampf and R. Niewa. The samples were characterized with XES, XAS, DFT and XEOL by M. R. Amin under the supervision of A. Moewes. The manuscript preparation was performed by M. R. Amin. With recent advancements in ammonothermal synthesis, there has been a renewed interest in utilizing this technique to grow semiconductors. The band gap was determined using two techniques: via XES-XAS separation and also via XEOL. The element-specific nature of XES and XAS allowed us to determine that substitutional oxygen was present in these samples, while XEOL allowed us to determine the presence of trapped gas within the system. This work has been published in The Journal of Physical Chemistry C [82].

Abstract

The electronic structure and band gap of InN synthesized by the ammonothermal method are studied by synchrotron-based soft X-ray absorption spectroscopy (XAS), emission spectroscopy (XES), X-ray excited optical luminescence (XEOL) spectroscopy, and density functional theory (DFT). The measured N K-edge XAS and XES spectra and the XEOL spectra are used to estimate the band gap of InN and it is found to be 1.7 ± 0.2 eV for both independent measurements, which is close to the initially reported values in the range of 1.89 eV - 2.10 eV for polycrystalline InN and about twice of the value recently obtained for single crystalline thin films between 0.70 eV and 1.0 eV. The possible origin of the measured increased band gap is discussed in terms of the presence of oxygen impurities and other impurity phases. Oxygen K-edge XES and XAS measurements are performed and reveal the presence of oxygen impurities. To gain insight in the structure of InN in the presence of oxygen impurities, we per-

form DFT calculations for hypothetical Wurtzite-type $\text{InO}_{0.5}\text{N}_{0.5}$ and $\text{InO}_{0.0625}\text{N}_{0.9375}$ and the known c- In_2O_3 and find that the measured O K-edge spectra of the samples agree well with $\text{InO}_{0.0625}\text{N}_{0.9375}$. The XEOL measurements also confirm the presence of oxygen impurities, which are caused by substituting nitrogen atoms with oxygen atoms, and the impurity phase of In_2O_3 in the samples.

4.1 INTRODUCTION

Group III nitrides are attractive and widely studied semiconductor materials due to their potential applications [128–135]. Among them, InN is the least studied material but it has attracted intense interest due to its distinct physical and optical properties. Because of the relatively small band gap of InN, it has been used for technological applications in opto-electronic devices, particularly in high efficiency solar cells [128–132], and in green and blue light emitting diodes and lasers [133, 134]. Recently, an active debate has arisen about the optical band gap of InN, when a few groups reported that the band gap of InN is between 0.70 eV and 1.0 eV [135–143], which is about half of the initially reported value in the range of 1.89 eV - 2.10 eV [138, 144–152]. It was reported that high-quality InN single crystalline thin films grown by molecular-beam epitaxy [135–139] or metalorganic chemical vapour deposition [141–143] yield the smaller band gap. On the other hand, larger band gaps have been reported for polycrystalline InN films grown by dc discharge [144–148], reactive cathodic sputtering [149] or RF-sputtering [150–152]. Therefore, the synthesis process and impurities play a major role affecting the experimental band gap. In this paper, we have studied InN samples, which were synthesized by the ammonothermal method [153] for the first time. Possible explanations for a smaller band gap of InN include defects, non-stoichiometry and non-uniformity films [142] and Mie-resonance [143]. On the other hand, a strong Moss-Burstein effect due to the residual large carrier concentrations [138, 140, 154], oxygen inclusion [138, 148, 151, 152, 154], and quantum confinement due to spontaneous formation of needle-like

nanocrystals [137] have been proposed as possible reasons for an increased band gap of InN.

The most prominent explanation for a larger band gap is oxygen inclusion [138, 148, 151, 152, 154]. Davydov *et al.* [138] showed that a sample with a band gap in the region of 1.8 - 2.1 eV contained up to 20% of oxygen. Recently, Yoshimoto *et al.* [151] reported that the optical band gap of polycrystalline InN increased from 1.55 eV to 2.27 eV with increasing oxygen contamination from 1% to 6%. More recently, it has been suggested that the larger band gap of InN upon incorporation of oxygen may be due to the formation of indium oxide nitride. Several authors [138, 155–157] have studied indium oxide nitride at different oxygen concentrations and found that for higher oxygen concentrations, the thin film can be considered a solid solution between InN and In₂O₃, resulting in an increased band gap due to the large band gap (3.1 eV) of In₂O₃ [158–161]. Still, there is not any clear experimental and theoretical evidence about the effects of oxygen in InN band gap but oxygen incorporation is commonly accepted and thus it needs further study.

To understand the band gap of InN and its origin, we have used synchrotron-based soft X-ray emission (XES) and absorption spectroscopy (XAS), which are sensitive to the occupied and the unoccupied local partial density of states (pDOS), respectively, X-ray excited optical luminescence (XEOL) spectroscopy as well as density functional theory (DFT) calculations. XEOL spectra can be used for understanding the electronic structure, presence of defects, and luminescence properties of solids [162, 163]. Previous studies have typically used the photo-luminescence (PL) technique to determine the band gap of InN [149, 164, 165]. The use of the XEOL technique is new and it has been used here to estimate the band gap of InN and to identify the oxygen impurities and other impurity phases in InN. XAS and XES are used to probe directly the conduction band and valence band of the material, respectively [158,

166, 167]. The O K-edge XAS and XES measurements and XEOL measurements provide clear evidence for the presence of oxygen impurities and another impurity phase in InN. Meanwhile, to interpret the experimental band gap and spectra, we also have performed DFT calculations. The experimental results agree very well with the calculations. Finally, to understand the structure of InN in the presence of oxygen impurities, we have performed DFT calculations for the hypothetical Wurtzite-type $\text{InO}_{0.5}\text{N}_{0.5}$ and $\text{InO}_{0.0625}\text{N}_{0.9375}$ as well as the known c- In_2O_3 .

4.2 EXPERIMENTAL SECTION

4.2.1 Synthesis

The ammonothermal synthesis process of the InN samples studied in this work is described in detail in Ref. [153]. InN has been synthesized from InCl_3 and KNH_2 in supercritical ammonia at around 280 MPa at two temperatures leading to microcrystals with markedly different morphologies showing differing aspect ratios. In samples synthesized at 663 K furnace temperature mainly plate-shaped crystals with diameters up to 4 μm are present according to SEM, while at 773 K rod like crystals with lengths of up to 4 μm can be found. Figures 4.1(a) and 4.1(b) show typical SEM images of samples from ammonothermal synthesis. We also have used a high-purity (99.999%) c- In_2O_3 sample which was obtained commercially from Sigma-Aldrich.

4.2.2 XAS, XES and XEOL Measurements

XES and XAS spectra at the N K-edge and at the O K-edge were collected at the REIXS [87] beamline and the XEOL spectra were measured at VLS-PGM [88] beamline at the Canadian Light Source in Saskatoon, Saskatchewan, Canada. The absorption spectra were measured in the partial fluorescence yield (PFY) and the total electron yield (TEY) modes. TEY is very surface sensitive and is thus included to explore surface and PFY is used to probe the bulk. The resolving power, $E/\Delta E$, for the monochromator at REIXS is 8000, which corresponds to an energy resolution

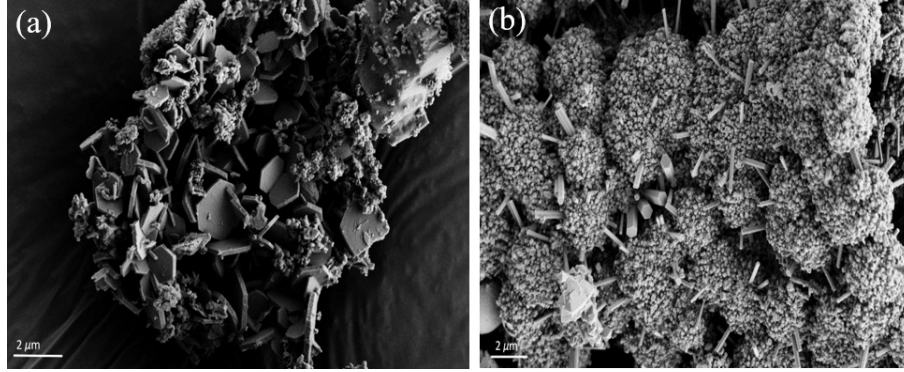


Figure 4.1: (a) SEM image of platelets InN from ammonothermal synthesis at 663 K. (b) SEM image of rods InN from ammonothermal synthesis at 773 K.

value, ΔE , of 0.06 eV at O-K-edge (500 eV) and of 0.05 eV at N K-edge (400 eV) XAS. All spectra were collected at room temperature. The $E/\Delta E$ for the spectrometer at the REIXS is 2000, which is equivalent to an energy resolution of 0.25 eV at 500 eV and 0.20 eV at 400 eV for XES. The XEOL data were collected using the Ocean Optics QE 65000 fast CCD spectrophotometer [168]. For all of the X-ray measurements, the powder samples were pressed into carbon tape, prior to transfer to the ultra-high vacuum chambers. The measured XAS and XES spectra were calibrated using hexagonal boron nitride (h-BN) for the N K-edge and bismuth germanium oxide (BGO) for the O K-edge. The XAS spectrum was calibrated using an initial h-BN (BGO) peak at 402.1 eV (532.7 eV) for N (O) K-edge, while the XES spectra were calibrated using elastic scattering features as this provides a common energy axis with the XAS measurements.

4.3 DFT CALCULATION DETAILS

Density functional theory (DFT) calculations using the available experimentally determined crystal structure of InN [169–172] based on the full-potential augmented plane-wave method with scalar-relativistic corrections were performed using the WIEN2K software package [173]. For the exchange-correlation functional, the Perdew-Burke-Ernzerhof variant of the generalized gradient approximation (PBE-GGA) [174] was

used. Calculations using the modified Becke Johnson (mBJ) exchange potential were conducted to obtain a more accurate estimate of the band gap [123]. The DFT calculations are used to calculate the band gap, the XAS and XES spectra and the pDOS. The spectra were calculated by multiplying the pDOS with the dipole transition matrix and the radial transition matrix [175]. The calculated spectra were broadened using the combination of a Lorentzian function to mimic the core-hole lifetime broadening, and a Gaussian function to mimic the instrumentation-related broadening [176]. Since the PBE-GGA underestimates the band gap of semiconductors, the calculated XAS and XES spectra were rigidly shifted by a constant amount to facilitate comparison with experiment [176]. In the experimental measurements, the XAS and XES spectra depend on the final state, but for the K-edge absorption, the final state has a core-hole in the nitrogen 1s energy level [177, 178], which tends to shift spectral weight to lower energies. To account for this effect, a $2 \times 2 \times 2$ supercell was created and one core electron (1s) was removed from one of the nitrogen atoms in the supercell and one background lattice charge was added to the supercell to preserve charge neutrality.

4.4 RESULTS AND DISCUSSION

4.4.1 N and O K-edge Absorption and Emission spectra

The calculated and measured N K_α XES and 1s XAS spectra are shown in Fig. 4.2. At first, the experimental and calculated N K-edge XAS spectra of InN samples will be discussed, which are shown in Fig. 4.2(b). Black and red spectra shown in this panel correspond to the PFY of the rods and platelets of InN and dotted lines represent the TEY of them. The two absorption spectra for each sample, which are surface and bulk sensitive, respectively, match well, indicating that the surface is not differently contaminated and the same as the bulk. The measured XAS spectra of rods and platelets are identical, which is evidence that the electronic properties

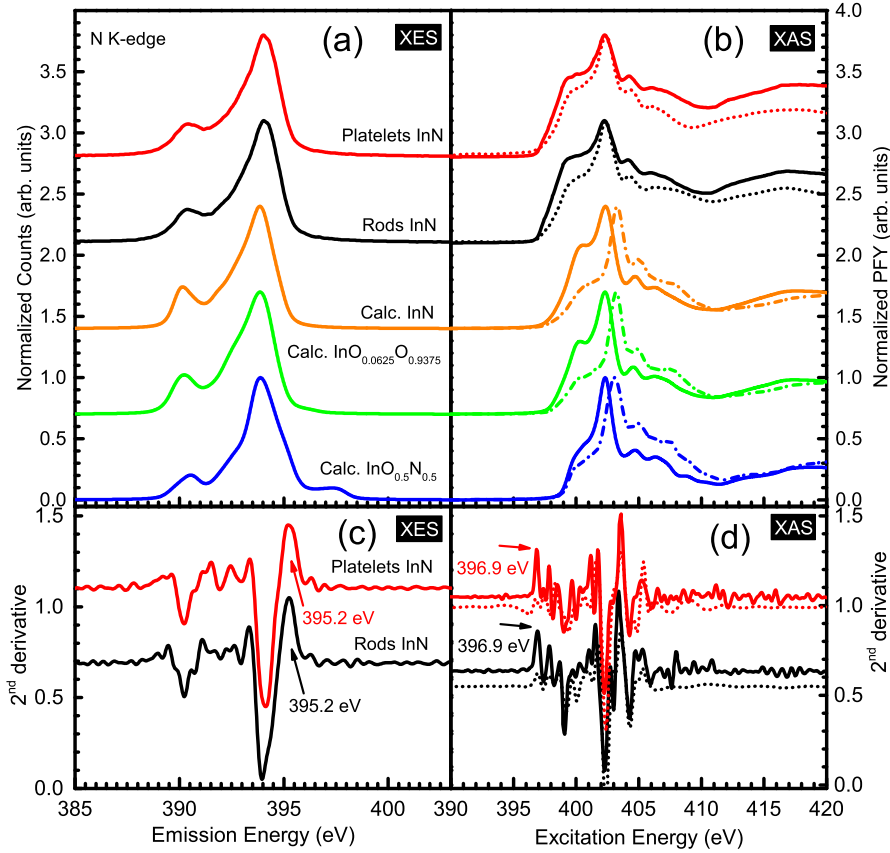


Figure 4.2: Measured and calculated N K-edge XES and XAS spectra. (a): Calculated and measured N K-edge XES spectra. Experimental and calculated (orange) N K-XES spectra of InN are compared with Wurtzite-type $\text{InO}_{0.0625}\text{N}_{0.9375}$ (green) and $\text{InO}_{0.5}\text{N}_{0.5}$ (blue). (b): Measured and calculated N K-edge XAS spectra. Experimental PFY (solid line) and TEY (dotted line) of InN are compared with core hole (solid line) and ground-state calculations (dash - dotted line) of InN, $\text{InO}_{0.0625}\text{N}_{0.9375}$ and $\text{InO}_{0.5}\text{N}_{0.5}$. (c): Second derivatives of the XES spectra of N K-edge of InN, with peaks corresponding to valence band edges indicated by the arrows. (d): Second derivative of PFY (TEY) of XAS spectra of N K-edge of platelets InN in red solid line (dotted line) and rods InN in black solid line (dotted line) with peaks corresponding to conduction band edges indicated by the arrows.

are not dependent on sample morphology, and are uniform throughout the sample. The measured overall spectral features are similar to those reported elsewhere for nanorods [147] and films [139, 147]. The experimental XAS spectra of both InN rods and platelets are compared with the core hole (orange line) and ground state (dash - dotted orange line) calculations and it is found that both measured spectra agree better with the core hole calculation with all major features reproduced at approximately the correct energy position and at the correct peak height and therefore the effect of core hole needs to be taken into account. This agreement supports the structure and space group determined by X-ray diffraction [169–172]. This agreement also provides strong experimental support for the calculated band gap and electronic structure.

As we will discuss later, sufficient oxygen impurities were present to detect O K-edge XES and XAS spectra. To account for this oxygen impurities, we have performed DFT calculations for hypothetical Wurtzite-type $\text{InO}_{0.5}\text{N}_{0.5}$ and $\text{InO}_{0.0625}\text{N}_{0.9375}$ and compared them with measured N K-edge XAS and XES spectra of InN in Fig. 4.2. For the calculations of the hypothetical Wurtzite-type $\text{InO}_{0.5}\text{N}_{0.5}$, half of the nitrogen was substituted by oxygen in the experimental crystal structure of InN, and for hypothetical Wurtzite-type $\text{InO}_{0.0625}\text{N}_{0.9375}$ calculations, a $2 \times 2 \times 2$ supercell of InN was created and one nitrogen atom was substituted by an oxygen atom in the supercell, and the geometry was optimized afterwards for each cases. For force minimization, the crystal structures were allowed to relax for both cases. Y. Hattori *et al.* [154] theoretically found that oxygen is energetically favorable to exist mainly as singly charged isolated defect in InN. The ground state (dash - dotted line) and the core hole calculated N K-edge XAS spectra for $\text{InO}_{0.0625}\text{N}_{0.9375}$ and $\text{InO}_{0.5}\text{N}_{0.5}$ are presented in Fig. 4.2(b). It is clear from Fig. 4.2(b) that there is very little difference between the calculated $\text{InO}_{0.0625}\text{N}_{0.9375}$ (green) and the measurements, while the calculated $\text{InO}_{0.5}\text{N}_{0.5}$ (blue) does not agree with the measurements, indicating that oxygen does not affect the N-sites on a large scale when a small amount of oxygen is present in InN.

The N K_α XES excited at 441.1 eV, well above the N K absorption edge, and calculations of InN are presented in Fig. 4.2(a). The measured XES spectra of both types of InN samples show two features which are consistent with our calculations (orange). The calculated pDOS show that In s and O p hybridization contribute to the peak at 390.3 eV and In p , d and O p contribute to the peak at 394.0 eV. The authors in [139, 147] also reported the same features for bulk InN systems. The calculated XES spectrum of $\text{InO}_{0.0625}\text{N}_{0.9375}$ agrees better with the calculations of pure InN and measurements than $\text{InO}_{0.5}\text{N}_{0.5}$. Since the oxygen impurity concentration is small and the impurities only weakly affect the nearest N atoms, the N K-edge spectra are insufficiently sensitive to distinguish between pure InN and InN with a small amount of oxygen impurities.

We are now turning to the discussion of the measured O K-edge spectra which is presented in Fig. 4.3. To examine the crystal structure of InN in the presence of oxygen impurities, the O K-edge XAS and XES spectra of InN have been measured and compared with experimental and calculated c- In_2O_3 , as well as calculated hypothetical Wurtzite-type $\text{InO}_{0.5}\text{N}_{0.5}$ and $\text{InO}_{0.0625}\text{N}_{0.9375}$, shown in Fig. 4.3. For the calculation of In_2O_3 , the experimental crystal structure of c- In_2O_3 was used as an input [158]. It is shown in Fig. 4.3(b) that the experimental O K-edge XAS spectra of rods and platelets of InN are almost identical and the strong XAS signals confirm that oxygen impurities are present in the InN samples. The calculated and experimental XAS spectra for the c- In_2O_3 reference agree very well. It is also observed that the O K-edge XAS spectra of c- In_2O_3 bear some similarity to those of the InN samples, but there are some additional features and general broadening of features. On the other hand, comparing the XAS experimental and calculated spectra, we see that the spectrum of $\text{InO}_{0.0625}\text{N}_{0.9375}$ agrees better with InN than $\text{InO}_{0.5}\text{N}_{0.5}$. Fig. 4.3(a) describes the O K-edge XES spectra of calculated and measured c- In_2O_3 , measured

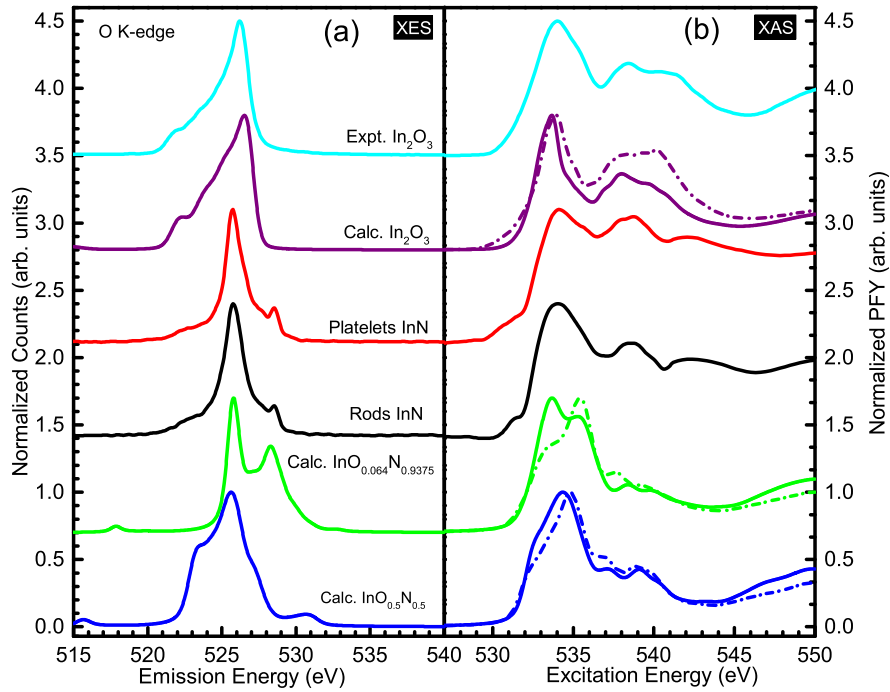


Figure 4.3: Measured and calculated O K-edge XES and XAS spectra. (a): Calculated and measured O K-edge XES spectra. Experimental (cyan) and calculated (purple) XES spectra of c-In₂O₃ are compared with experimental XES spectra of platelets (red) and rods (black) of InN as well as the calculated hypothetical Wurtzite-type InO_{0.0625}N_{0.9375} (green) and InO_{0.5}N_{0.5} (blue). (b): Calculated and measured O K-edge XAS spectra. Measured PFY, core hole and ground state (dash - dotted) calculations of O K-edge XAS spectra of c-In₂O₃ are compared with measured O K-edge XAS of platelets and rods of InN as well as core hole and ground state calculations of hypothetical Wurtzite-type InO_{0.0625}N_{0.9375} and InO_{0.5}N_{0.5}.

InN, calculated $\text{InO}_{0.5}\text{N}_{0.5}$, and $\text{InO}_{0.0625}\text{N}_{0.9375}$. The calculated and measured O K-edge XES spectra of *c*- In_2O_3 agree well. It is found that both experimental spectra of rods and platelets of InN are identical. It is noted that the measured XES spectra of InN show a sharp peak at around 528.5 eV. As for the XAS, the calculated XES spectrum of $\text{InO}_{0.5}\text{N}_{0.5}$ does not match well with these measurements but the calculated $\text{InO}_{0.06}\text{N}_{0.94}$ does. However, the spectrum would agree better in height, width and positions of the peaks if the oxygen concentration is less than 6% but the required supercell of $2 \times 2 \times 3$ instead of the current $2 \times 2 \times 2$ would render such calculations computationally prohibitive. Those impurities are caused by substituting nitrogen atoms with oxygen atoms. Experimental determination of the oxygen content by the hot carrier gas extraction technique for these bulk samples resulted in 4 wt.% [153], meaning a maximum of about 3 % oxygen substituting nitrogen in the InN phase.

4.4.2 Band Gap

The N K_α XES and 1s XAS spectra of InN are used to estimate the band gap of InN samples. The band gap is defined as the energy difference between the top of the valence band and the bottom of the conduction band. To determine the band edges of our InN samples, the second derivatives of the XAS and XES spectra are taken [158, 166, 167]. In this method, the top of the valence band and bottom of the conduction band are taken to be the first peaks above the noise at the upper edge of the XES and at the lower edge of the XAS spectra, as indicated with arrows in Fig. 4.2(c) and Fig. 4.2(d), respectively. This method is less ambiguous than other methods like linear extrapolation yielding a more reproducible band gap. Note that, the XAS second-derivative peak is found at the same energy position (396.9 eV) in both the PFY mode (solid line) and TEY mode (dotted line) for both rods and platelets InN which is presented in Fig. 4.2(d). However, the authors in Ref. [139] found an 0.6 eV larger separation for TEY XAS and claimed that this separation is due to the Fermi

Table 4.1: Measured, calculated and previously reported band gaps for InN. The measured band gap is denoted by $\Delta_{\text{expt.}}$ and the calculated band gap is denoted by Δ_{mBJ} using mBJ functional. The experimental techniques and calculation methods for previously reported band gap determination are also included. All numbers are in eV.

$\Delta_{\text{expt.}}$	Δ_{mBJ}	Other calc. Δ	Other expt. Δ	Determination method
1.7	0.89	0.70 [169]	0.70	Optical absorption
± 0.2		0.80 [170]	[135, 136, 138, 143]	[135, 136, 140–143, 145, 146, 150–152]
		0.85 [171]	0.80	Photoluminescence
		0.89 [154]	[139, 140, 143]	[135–138, 140, 141, 148, 149]
			0.9 [137]	XES and XAS [139, 147]
			1.0 [141, 142]	GGA -mBJ [154] (calc.)
			1.89 [144, 149, 150]	DFT - G_0W_0 [169] (calc.)
			1.90 [142, 147, 148, 151]	DFT - LDA [170, 171] (calc.)
			1.95 [145]	
			2.0-2.1 [143, 146, 152]	

level being pinned high above the conduction band minimum at the surface due to the intrinsic electron accumulation.

As mentioned earlier in the calculations section, XAS probes the conduction band in the presence of core hole instead of in the ground state. Therefore, the band gap can only be determined correctly from XES and XAS onsets once the core hole shift has been accounted for. The core hole shift is calculated by the energy difference between the conduction band onset in the ground and core hole state calculations. For InN, a negligible core hole shift (0 eV) is observed so that the experimentally determined band gap corresponds to the XES and XAS onsets.

The experimentally determined band gap of both rods and platelets of InN samples is found to be 1.7 ± 0.2 eV for both PFY and TEY modes, which is presented in Table 6.1 along with a summary of the band gap values established in the literature. Piper *et al.* [139] have used XAS and XES measurements to estimate the band gap for wurtzite InN (000 $\bar{1}$) thin films and found to be 0.8 eV and 1.4 eV for TEY and TEY modes, respectively, by the linear extrapolation method. The authors in Ref. [147] estimated the band gap for polycrystalline nanorods and films of InN using the combination of XES and XAS measurements and found that it is 1.9 eV using the linear extrapolation method. It should be noted here that we have also examined our measured band gap using the linear extrapolation method. We found that our experimentally determined band gap is unchanged at 1.7 ± 0.2 eV, reflecting that the experimentally determined band gap is insensitive to the specific technique used to determine the onset of spectral weight. The experimental uncertainty originates from the monochromator (0.05 eV at the N K-edge) and spectrometer (0.2 eV at the N K-edge) resolution and the energy calibration. This determination of the band gap is in contrast with the calculated band gap using PBE-GGA which results in a metallic state for Wurtzite-type InN and a band gap of 0.89 eV using the mBJ exchange-correlation potential [123]. This underestimation of the band gap is typical of LDA and GGA exchange - correlation functional and is due to the fundamental limitations of DFT. Specifically, the formal electronic band gap, $\Delta_g = I - A$, where I is the first ionization potential and A is the electron affinity may not match the Kohn - Sham derived band gap due to a derivative discontinuity in the exchange - correlation functional [179]. Our experimentally measured band gap agrees well with determinations made using other experiments [144–152], which are shown in Table 6.1. All our measurements were performed at room temperature. Prior work [180] demonstrates that the band gap of InN varies weakly with temperature. Specifically, the variation of band gap for InN was found to be 0.023 eV between 4.2 K and 300 K. As such, the band gap measured experimentally is representative of the intrinsic electronic band

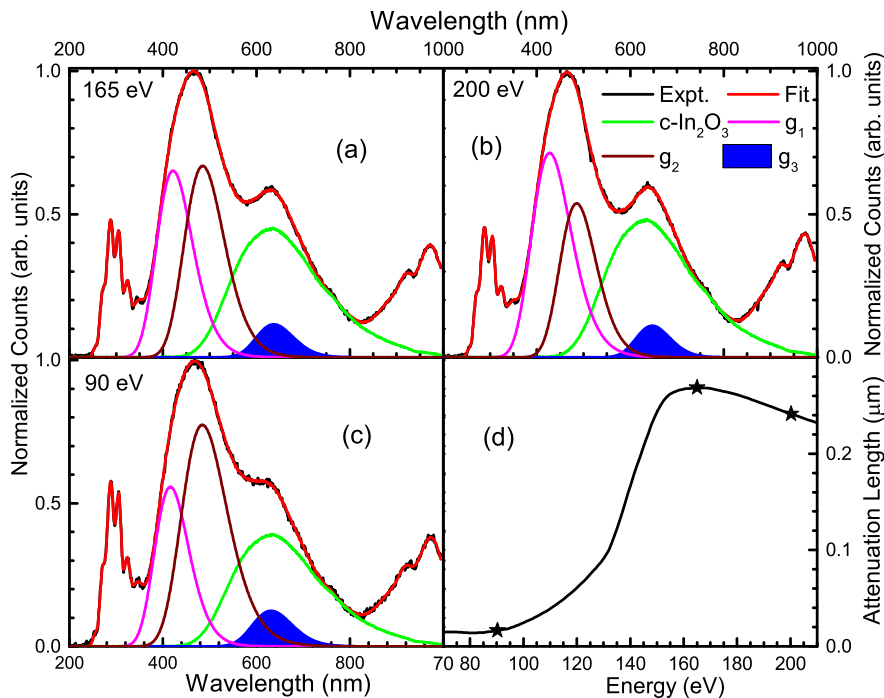


Figure 4.4: XEOL spectra of InN platelets, $c\text{-In}_2\text{O}_3$ and the variation of photon attenuation length with excitation energy. Experimental XEOL spectra of InN at three different excitation energies are presented in (a), (b) and (c). The XEOL spectra exhibit features located at 274 nm, 288 nm, 305 nm, 328 nm, 351 nm, 425 nm, 667 nm, 921 nm and at 973 nm. To fit the two broad peaks located at 425 nm and at 667 nm, three Gaussians and the luminescence spectrum of $c\text{-In}_2\text{O}_3$ (green) are used. The variation of photon attenuation length (logarithmic scale) with excitation energy for InN is presented in (d) with data from Ref. [181]. The three stars labeled in this graph represent the three excitation energies in our measurements.

gap.

4.4.3 X-ray Excited Optical Luminescence (XEOL) Spectra

Recently, researchers have been using X-ray excited optical luminescence (XEOL) spectra to explore electronic structure, presence of defects, and luminescence properties of solids [162, 163]. Here, we have performed XEOL measurements on InN for a variety of excitation energies to probe the depth dependence of luminescence. Figure 4.4 shows XEOL spectra of InN at three excitation energies at 90 eV (Fig. 4.4(a)),

165 eV (Fig. 4.4(b)), and at 200 eV (Fig. 4.4(c)). XEOL spectra of rods (not shown) and platelets (in Fig. 4.4) of InN are identical. Therefore, the XEOL spectra are independent of sample morphology. The lowest excitation energy for InN was at 90 eV, which corresponds to 20 nm photon attenuation length and due to the limitation of excitation energy range of the VLS-PGM beamline [88], the highest excitation was at 200 eV. However, the largest photon attenuation length in this energy range for InN is 270 nm when the excitation energy is 165 eV. The wide variation of excitation energy probes the depth from 20 nm to 270 nm of the sample. For InN, the variation in photon attenuation length with excitation energy is shown in Fig. 4.4(d) [181]. The authors in [182] reported the cathodoluminescence spectra of fluorine-doped c-In₂O₃, which matches well with our spectra, but they were not able to measure the spectra lower than 330 nm and higher than 975 nm due to the instrumental limitations. They observed two broad peaks at 410 nm and 650 nm and claimed that the origin of the former peak corresponds the indirect conduction band to valence band transition of c-In₂O₃ and the 650 nm peak originates from oxygen defects.

Figures 4.4(a) - 4.4(c) reveal the individual Gaussians and the c-In₂O₃ luminescence spectrum (green) that fit the experimental broad luminescence spectral features located at 425 nm and at 667 nm best for all three cases. We also have used more Gaussians in high and low wavelength regions to fit the XEOL spectra which are not presented in Fig. 4.4. Note that, the luminescence feature of c-In₂O₃ at around 667 nm is due to oxygen defects [182–184]. It is shown that the c-In₂O₃ luminescence spectrum is present for all excitation energies and its intensity is almost identical for all excitation energies (for different attenuation lengths), indicating that c-In₂O₃ might be present in the InN samples. According to the Gaussian fitting, a small g₃ Gaussian feature is observed in the same position (at 651 nm) of luminescence spectrum of c-In₂O₃. The g₃ is much narrower (FWHM: 100 nm) than the c-In₂O₃ spectrum (FWHM: 223 nm) and can thus be uniquely distinguished despite occurring

at the same energy. Interestingly, the peak of Gaussian g_3 feature lines up exactly with the N K-edge XES and XAS separation of 1.7 ± 0.2 eV for InN, therefore, it could be a band-to-band transition of InN. The authors in Refs. [149, 164, 165] observed band-to-band transition at 1.8 eV of InN in their PL measurements. The g_1 and g_2 Gaussian features at 422 nm and at 520 nm might be due to the oxygen defects for In_2O_3 . This is because the origin of PL spectra of In_2O_3 in the range from violet to green such as at 506 nm in Ref. [185], at 425 nm, 429 nm, 442 nm, and at 466 nm in Ref. [186], and 442 nm, 468 nm, and at 524 nm in Ref. [187] is due to oxygen impurities. Therefore oxygen impurities and In_2O_3 impurity phase are present in InN. The authors in [138] found the band gap of 1.8 - 2.0 eV for InN and claimed the reason for an increased band gap is to formation of optically transparent solid solution of InN- In_2O_3 at an oxygen concentration of about 20%. Several other authors [155–157] also suggested a solid solution between InN and In_2O_3 and found increased band gap. Note that, the positions of all the Gaussians remain at the same position for different excitation energies. The luminescence features at 274 nm, 288 nm, 305 nm, 328 nm, and 351 nm are due to presence of N_2 gas produced by irradiation-induced decomposition of InN as assigned previously [188, 189]. There are some defects, which are leading to the features at 921 nm and at 970 nm.

4.5 CONCLUSIONS

We have studied the electronic structure and the band gap of ammonothermal InN experimentally and theoretically using soft X-ray synchrotron spectroscopy measurements and DFT calculations, respectively. The measured and calculated band gaps of InN are found to be 1.7 ± 0.2 eV and 0.89 eV, respectively, which are in excellent agreement with prior experiments [144–147, 149–152] and calculations [169–171], respectively. The band gap of InN obtained from the XEOL spectra confirms the measured value from XAS and XES spectra. The origin of the measured band gap

is discussed in terms of the presence of oxygen impurities and impurity phases of InN. The experimental O K-edge XAS and XES spectra of InN and DFT calculations for hypothetical Wurtzite-type $\text{InO}_{0.5}\text{N}_{0.5}$ and $\text{InO}_{0.0625}\text{N}_{0.9375}$ and the known *c*- In_2O_3 suggest that less than 6% oxygen impurities are present in our InN samples. Those impurities originate from substituting nitrogen atoms with oxygen atoms. This oxygen content is an excellent agreement with a previously experimentally determined value [153]. The XEOL spectra also confirm the presence of oxygen impurities and impurity phase of In_2O_3 in InN.

AUTHOR INFORMATION

Corresponding Author

*E-mail: alex.moewes@usask.ca

ORCID

Alexander Moewes: 0000-0002-9218-2280

M. Ruhul Amin: 0000-0002-1289-4713

T. de Boer: 0000-0002-6898-5040

Notes

The authors declare no competing financial interest.

ACKNOWLEDGEMENTS

The experiments for this paper were performed at the Canadian Light Source, which is funded by the Canada Foundation for Innovation, the Natural Science and Engineering Research Council of Canada (NSERC), the National Research Council Canada, the Canadian Institutes of Health Research, the Government of Saskatchewan, Western Economic Diversification Canada, and the University of Saskatchewan. M.R.A. is grateful to the Government of Saskatchewan for financial support of Saskatchewan Innovation and Opportunity Scholarship. We acknowledge support from NSERC and the Canada Research Chair program. The authors also acknowledge Compute Canada. The calculations presented in this paper were performed on the Cedar high-performance computing cluster, which is the part of the WestGrid (www.westgrid.ca)

and Compute Canada Calcul Canada (www.computecanada.ca). We also thank the German Research Foundation (DFG) for financial support within the project “FOR 1600: Chemie und Technologie der Ammonothermal-Synthese von Nitriden”.

Chapter 5

Understanding of Luminescence Properties Using Direct Measurements on Eu^{2+} -doped Wide Band Gap Phosphors

Authors: Muhammad Ruhul Amin^a, Philipp Strobel^b, Amir Qamar^a, Tobias Giftthaler^c, Wolfgang Schnick^c, and Alexander Moewes^a

^aDepartment of Physics and Engineering Physics, University of Saskatchewan, 116 Science Place, Saskatoon, Saskatchewan , S7N 5E2, Canada

^b Lumileds Phosphor Center Aachen Lumileds Germany GmbH Philipsstrasse 8, 52068 Aachen, Germany

^cDepartment of Chemistry, University of Munich (LMU), Butenandtstrasse, 5-13, 81377 Munich, Germany

Reference: Muhammad Ruhul Amin, Philipp Strobel, Amir Qamar, Tobias Giftthaler, Wolfgang Schnick, and Alexander Moewes, *Advanced Optical Materials*, 2020, **8**, 2000504 [65].

Summary and Author Contributions

The authors in Ref. [84] have reported the synthesis process and a few optical prop-

erties of $AELi_2Be_4O_6:Eu^{2+}$ ($AE = Ba, Sr$) phosphor and found an extremely small Stokes-shift and unprecedented ultra-narrow blue emission band with FWHM = 25 at 454-456 nm for both compositions, which is very promising for an application in violet-pumped white RGB phosphor LEDs. The highly promising nature of these materials suggests further exploring electronic and optical properties for commercialization. To gain insight into the transition processes, we use resonant inelastic X-ray scattering (RIXS) and X-ray excited optical luminescence (XEOL) to directly measure the Eu^{2+} 5d-conduction band (CB) separation and the positions of Eu^{2+} levels for these phosphors. These experimental techniques allow direct access to the intragap states that are the source of the luminescence properties of Eu^{2+} -doped phosphors. In addition, to interpret the experimental band gap, density of states (DOS), band structure, and X-ray absorption (XAS) and emission (XES) spectra are calculated using Density functional theory (DFT) calculations. With these measurements and calculations, deep insights are gained into key properties of $AELi_2Be_4O_6:Eu^{2+}$ ($AE = Ba, Sr$) phosphor, such as emission colour, efficiency and thermal quenching behaviour. XES, XAS, and XEOL measurements as well as DFT calculations were performed by M. R. Amin under the supervision of A. Moewes. XAS and non-resonant XES measurements were performed to determine the band gap. Manuscript preparation was performed by M. R. Amin. The energy separation between the conduction band and the 5d Eu^{2+} energy level was measured by performing resonant excitations at the onset of the O K XAS spectrum. The thermal quenching behavior was determined to be similar to other efficient phosphors [37]. This work has been published in *Advanced Optical Materials* [65].

Abstract

Recent developments in solid-state lighting lead to a demand for new phosphors with excellent thermal stability, exhibiting large band gaps for highly efficient emission and excellent thermal stability. We present a detailed characterization of the lumi-

nescent material $AELi_2Be_4O_6:Eu^{2+}$ ($AE = Ba, Sr$) using soft X-ray absorption spectroscopy (XAS), X-ray emission spectroscopy (XES), X-ray excited optical luminescence (XEOL) spectroscopy, and density functional theory (DFT) calculations. The experimental band gap for both $BaLi_2Be_4O_6:Eu^{2+}$ (BLBO:Eu) and $SrLi_2Be_4O_6:Eu^{2+}$ (SLBO:Eu) is found to be 6.5 ± 0.3 eV, which agrees well with our DFT calculations (6.8 eV for BLBO:Eu and 7.4 eV for SLBO:Eu). The DFT calculations and the measurements show that both compounds have an indirect band gap. The crucial Eu^{2+} 5d to conduction band energy separation is determined to be 0.21 ± 0.10 eV and 0.25 ± 0.10 eV for BLBO:Eu and SLBO:Eu, respectively, using resonant inelastic X-ray scattering. These measured values are in good agreement with our thermal quenching measurements (0.20 ± 0.03 eV for BLBO:Eu and 0.26 ± 0.03 eV for SLBO:Eu). Finally, the XEOL measurement confirms the $Eu^{2+} 5d^14f^6 \rightarrow 4f^7$ transition, which is responsible for the ultra-narrow band (Full width at half maximum: 25 nm) blue optical luminescence at 455-457 nm for both compounds. With these measurements and calculations, deep insights are gained into the key properties of those two phosphors.

5.1 Introduction

Solid state lighting, particularly phosphor converted light-emitting diodes (pc-LEDs) have the potential to reduce global energy consumption in the lighting sector by 40% within the next two decades due to the dramatically increased energy efficiency compared to the conventional incandescent [26, 27, 36, 190]. The key advantage of pc-LEDs resides in the combination of the lower energy consumption, high light quality, preservation of colour point stability, and long lifetime. At present, there are several proposed pc-LEDs designs available for various LED application fields like illumination, consumer electronics, and display backlighting [26] with each design having its own advantages and drawbacks [191]. The discovery of the high efficient red emitting $(Ba,Sr)_2Si_5N_8:Eu^{2+}$ and $(Sr,Ca)AlSiN_3:Eu^{2+}$, and narrow band red emitting $Sr[LiAl_3N_4]:Eu^{2+}$ (SLA) and $Sr[Li_2Al_2O_2N_2]:Eu^{2+}$ (SALON) were the significant re-

cent developments in the pc-LEDs field [27, 85, 192–195]. These phosphors are used in highly efficient pc-LEDs processing with very good colour rendition and colour rendering index (CRI) values around 90 [27, 194, 195]. Particularly, pc-LEDs with SALON show an increase of 16% in luminous efficacy when compared to currently available commercial high colour-rendering pc-LEDs, while retaining excellent high colour rendition [85].

The emission colour of a phosphor depends on the type of incorporated activator, the host material and its electronic configuration [37]. A highly condensed network of the host material is a pre-requisite for narrow band-emission of a wide band gap phosphor, required for improving optical performance of pc-LEDs [84]. Mostly, transition metal elements (Mn^{4+}) [196] and rare earth elements (Ce^{3+} , Eu^{2+}) [197] are used as an activator. Among them, the Eu^{2+} luminescence centre is often introduced in these highly condensed host materials to obtain a blue LED due to the $\text{Eu}^{2+} 5d^14f^6 \rightarrow 4f^7$ transition, which is narrow and tunable by the properties of the host material [37, 197]. The energetic separation between $5d^1$ state and $4f^7$ state of the Eu^{2+} ion in the band gap determines the colour emitted by the Eu^{2+} -doped phosphor [37]. The energetic position of the $\text{Eu}^{2+} 5d$ levels in each host material depends on three main factors [37, 53, 54]. The first factor is the nephelauxetic effect, which influences the bonding character of the activator Eu^{2+} ion and its ligands. This factor refers to a decrease in energy separation between the $5d^14f^6$ state and $4f^7$ state with increasing covalent character of the band. The influence of the crystal field on the splitting of the energy of the $5d$ states is the second factor, which depends on the ligand field strength around the activator site and the coordination geometry of the activator. Finally, the third factor is the Stokes-shift, which is the energetic difference between absorption and emission maximum that depends on the vibration rigidity of the host materials [37, 53, 54]. The small Stokes-shift allows shifting the emission of a near ultraviolet primary pump LED in the blue spectral range [84]. Recently, the Schnick group has

reported the synthesis process and a few optical properties of $AELi_2[Be_4O_6]:Eu^{2+}$ ($AE = Ba, Sr$) and found an extremely small Stokes-shift and unprecedented ultra-narrow blue emission band with full width at half maximum (FWHM) = 25 at $\lambda_{em} = 454-456$ nm for both compositions, which would be very promising for an application in violet-pumped white RGB phosphor LEDs [84]. The highly promising nature of these materials suggests further exploring electronic and optical properties for commercialization, particularly the locations of the Eu^{2+} energy levels within the band gaps, which leads to a complete and comprehensive understanding of all involved radiative processes. Moreover, a powerful theoretical approach like Density functional theory (DFT) needs to be performed for studying electronic properties. To gain insight into the transition processes, we utilized resonant inelastic X-ray scattering (RIXS) [27, 37, 73] and X-ray excited optical luminescence (XEOL) [75, 162] to directly measure the Eu^{2+} 5d -conduction band (CB) separation and the positions of Eu^{2+} levels in these phosphors. These experimental techniques allow direct access to the intragap states that are the source of the luminescence properties of Eu^{2+} -doped phosphors. To interpret the experimental band gap, density of states (DOS), band structure, and X-ray absorption (XAS) and emission (XES) spectra, DFT calculations were performed. With these measurements and calculations deep insights are gained into the key properties of $AELi_2[Be_4O_6]:Eu^{2+}$ ($AE = Ba, Sr$) phosphor, such as emission colour, efficiency and thermal quenching behaviour.

5.2 Experimental Sections

5.2.1 Preparation of the Samples

The powder samples of $AELi_2[Be_4O_6]:Eu^{2+}$ ($AE = Sr, Ba$) were synthesized in tantalum ampules through a solid-state reaction technique by heating a stoichiometric mixture of AEO (SrO: Sigma Aldrich, 99.9%; BaO: Sigma Aldrich, 99.99%), Li_2O (Schuchardt, 98%), BeO (Alfa Aesar, 99.95%) and Eu_2O_3 (ABCR, 99.99%) for 2 h

to 1100 °C in Ar gas atmosphere. Detailed synthesis processes including the crystal structure characterization for $AELi_2[Be_4O_6]:Eu^{2+}$ ($AE = Sr, Ba$) are described elsewhere [84]. The experimental crystal structures derived in Ref. [84] using single crystal X-ray diffraction are the only input to our density functional theory (DFT) calculations.

5.2.2 XAS, XES and XEOL Measurements

Two different beamlines, REIXS [87] for XES and XAS measurements and VLS-PGM [88] for the XEOL measurements at the Canadian Light Source in Saskatoon were used. The absorption was measured in the partial fluorescence yield mode (PFY), determined by postprocessing the emission spectra collected by silicon drift detectors. The resolving power, $E/\Delta E$, for the monochromator at REIXS was 8000, which corresponds to an energy resolution, ΔE , of 0.06 eV at the O K-edge (500 eV) XAS. The $E/\Delta E$ for the emission spectrometer at REIXS is 2000, which is equivalent to an energy resolution of 0.25 eV at 500 eV for XES. The XEOL data were collected using an Ocean Optics QE 65000 fast CCD spectrophotometer [168]. For all X-ray measurements, the powder samples were pressed into indium foil, prior to transfer to the ultra-high vacuum chambers. The measured XAS and XES spectra were calibrated using bismuth germanium oxide (BGO). The XAS spectrum was calibrated using an initial BGO peak at 532.7 eV, while the XES spectra were initially calibrated using elastic scattering peaks and then they further were shifted to get final calibration by the same amount as the absorption spectrum was shifted with respect to the BGO peak at 532.7 eV [82].

5.2.3 Thermal Quenching Measurements

Thermal quenching data were collected using an AvaSpec2048 Spectrometer. For excitation, an LED light source (450 nm) was used. Both samples were heated using an IR lamp and the measurements were taken in the temperature range from 323 K

to 548 K with a step size of 25 K. The thermal quenching data were published in Ref. [84].

5.3 Density Functional Theory (DFT) Calculations

The DFT calculations were employed based on the full-potential augmented plane-wave method with scalar-relativistic corrections using the WIEN2k software package [126, 127]. To perform the calculations, experimentally determined crystal structures for $AELi_2Be_4O_6$ ($AE = Ba, Sr$) were used as the input [84]. Note that the incorporated activator Eu^{2+} was not included in the experimental crystal structures for the calculations. For the exchange-correlation functional, the Perdew-Burke-Ernzerhof variant of the generalized gradient approximation (PBE-GGA) [119] was used. Calculations using the modified Becke Johnson (mBJ) exchange potential were conducted to obtain a more accurate estimate of the band gap [123]. The DFT calculations are used to calculate the bandgap, band structure, the XAS and XES spectra, and the partial density of states (pDOS). The spectra were calculated by multiplying the pDOS with the dipole transition matrix and the radial transition matrix [175]. The calculated spectra were broadened using the combination of a Lorentzian function to mimic the core-hole lifetime broadening and a Gaussian function to account for the instrumentation-related broadening [176]. Since the PBE-GGA functionals typically underestimate the band gap of materials, the calculated XAS-XES spectra were precisely shifted by a constant amount to facilitate comparison with experiment [176]. In the experimental measurements, the XAS and XES spectra depend on the final state, but for the O K-edge absorption, the final state has a core-hole in the 1s level [177, 178], which tends to shift spectral weight to lower energies. To account for this effect, a $2 \times 1 \times 1$ supercell was created and one core electron (1s) was removed from one of the oxygen atoms in the supercell and a background lattice charge was added to the supercell to preserve charge neutrality.

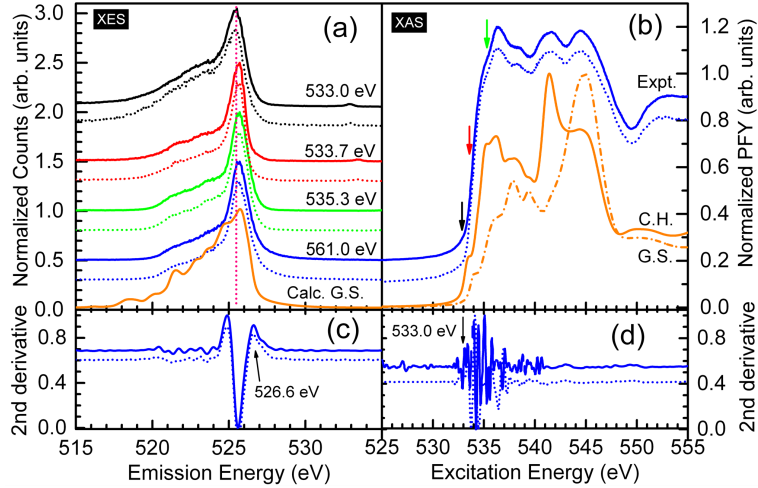


Figure 5.1: Measured and calculated O K-edge XES and XAS spectra of BaLi₂Be₄O₆:Eu²⁺ (solid lines) and undoped BaLi₂Be₄O₆ (dotted lines). (a): NXES spectrum (blue) excited at 561.0 eV and RIXS spectra (black, red and green) collected at various excitation energies for BaLi₂Be₄O₆:Eu²⁺ and BaLi₂Be₄O₆ are compared with ground state (G.S.) calculations (orange). The vertical dotted magenta line indicates that the highest emission energy is observed at the highest excitation energy in the RIXS spectra. (b): Measured PFY, core hole (C.H.) and G.S. calculations of O K-edge XAS spectra of BaLi₂Be₄O₆:Eu²⁺ and BaLi₂Be₄O₆ are compared. The colour-coded arrows indicate where in the conduction band the O 1s electron was excited to obtain the corresponding color-coded emission spectra. Second derivatives of the NXES (c) and XAS (s) spectra, with peaks corresponding to valence band edges and conduction band edges are indicated by the arrow, respectively.

5.4 Results and Discussion

5.4.1 Oxygen K-edge Spectra

Alongside our DFT calculated spectra, soft X-ray emission and absorption spectra for $AELi_2[Be_4O_6]:Eu^{2+}$ ($AE = Sr, Ba$) (1% Eu^{2+}) were collected at the Oxygen K-edge as shown in Fig. 5.1 for $BaLi_2[Be_4O_6]:Eu^{2+}$ (BLBO:Eu) and in Fig. 5.22 for $SrLi_2[Be_4O_6]:Eu^{2+}$ (SLBO:Eu). The absorption measurements were collected in partial fluorescence yield mode and the emission measurements are displayed for different excitation energies. When the excitation energies are near the threshold (here O 1s) of XAS, spectra are referred to as resonant inelastic X-ray scattering (RIXS) spectra. On the other hand, when the excitation energy is well above the threshold of XAS, the spectrum is referred to as non-resonant X-ray emission (NXES) spectrum. The experimental and calculated XAS spectra of $BaLi_2[Be_4O_6]:Eu^{2+}$ will be discussed first and are shown in Fig. 5.1(b). The solid blue line shown in this panel corresponds to the experimental PFY for BLBO:Eu. As a reference sample, we used undoped $BaLi_2Be_4O_6$ (BLBO). The dotted blue line in this panel represents the experimental XAS spectrum of this reference sample. From the comparison, they are identical leaving the O spectra unaffected, which is expected due to the low concentration of Eu^{2+} (1%). There are three distinct features located at 536.3 eV, 541.5 eV, and at 544.4 eV in both of BLBO and BLBO:Eu O K-edge XAS spectra. Our DOS calculations show that the peaks at 536.3 eV and 541.5 eV are mostly due to Ba d-states and Ba f-states, respectively, and the peak at 544.4 eV is due to the admixture of p-states of Li, Be and O. The experimental XAS spectra of both BLBO:Eu and BLBO are compared with the core hole (solid orange line) and ground state (dash-dotted orange line) calculations and it is found that both measured spectra agree well with the core hole calculation, with all major features reproduced at the correct energy position and approximately at the correct peak height. This agreement supports the structure and space group determined by single crystal and power diffraction methods. This

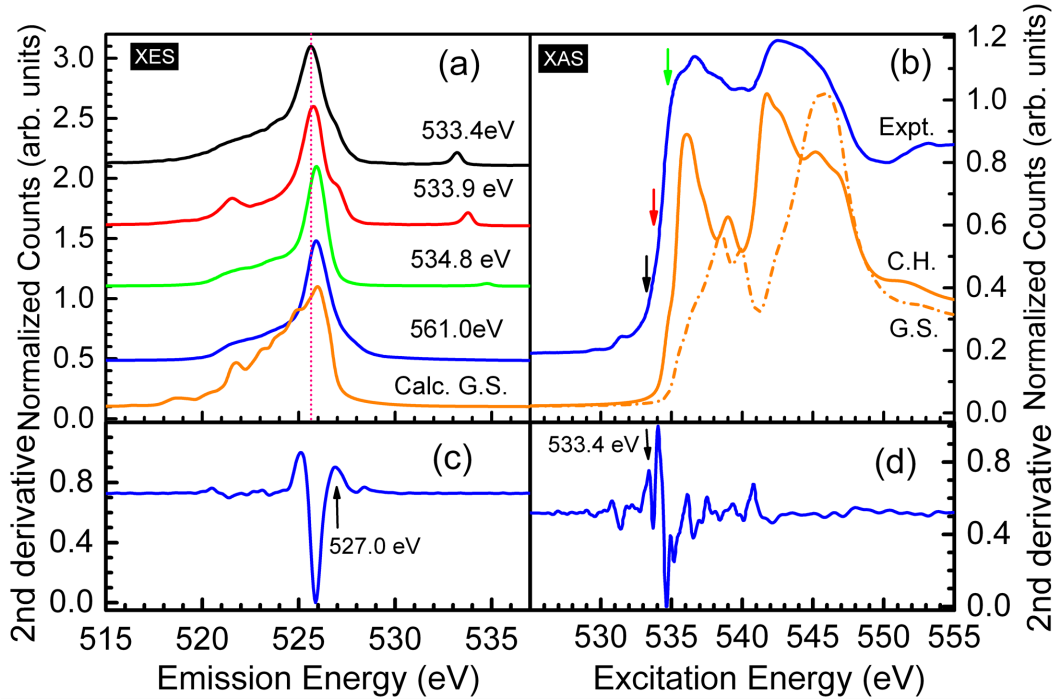


Figure 5.2: XAS and XES spectra of $\text{SrLi}_2\text{Be}_4\text{O}_6:\text{Eu}^{2+}$. The XES (a) and XAS (b) spectra are shown alongside DFT calculations. The calculated ground state (G.S.) and excited state (core hole, C.H.) XAS spectra are shown as solid orange and dash-dotted orange, respectively. The vertical dotted magenta line in (a) is used to guide the eye in finding the highest emission energy among the RIXS spectra. The second derivatives of the experimental NXES spectrum excited at 561.0 eV and the XAS spectrum are shown in panel (c) and (d), respectively.

agreement also provides strong experimental support for our calculated band gap, density of states, and band structure.

Turning to the X-ray emission spectra now, these are compared to our calculations as well and are presented in Fig. 5.1 (a). The XES spectra for BLBO and BLBO:Eu are again almost identical and show two features. The calculated pDOS, which is shown in Fig. 6.3(a), show that O p-states contribute to the peak at 525.6 eV and O p-states, Be s-states, and p-states contribute to the broad peak at 521.5 eV. The measured XES spectra are also in good agreement with our calculations. The measured and the calculated XAS and XES spectra for $\text{SrLi}_2[\text{Be}_4\text{O}_6]:\text{Eu}^{2+}$ are presented in Fig. 5.2.

The comparison shows that there is again an excellent agreement between measurements and calculations. Comparing Fig. 5.1 and Fig. 5.2, it is found that the XES spectra for BLBO:Eu are nearly identical with SLBO:Eu but in the XAS spectrum, an additional peak at 547.5 eV appears for BLBO:Eu. The DOS calculations show that the additional XAS peak located at 547.5 eV for BLBO:Eu appears due to the contribution of the Ba f-states.

5.4.2 Band Gap Determination

After analysing the XAS and XES spectra, we can now use them to estimate the band gap. The band gap is the energy difference between the top of the valence band and the bottom of the conduction band. Since XAS and XES probe the unoccupied density of states (CB) and the occupied density of states (VB), respectively, both spectra are placed on a common energy scale and are used to determine the conduction band and valence band edges, respectively. The top of the valence band and the bottom of the conduction band are determined by taking the second derivatives of the XES and XAS spectra, respectively [37, 82]. In this method, the top of the valence band and bottom of the conduction band are taken to be the first peaks in the second derivative above the noise at the upper edge of the NXES and lower edge of the XAS spectra, respectively, as indicated by vertical arrows in the bottom panels of Fig. 5.1 and Fig. 5.2. This method yields band gap values, which are often more reproducible than the conventional linear extrapolation method. From the band edges of Fig. 5.1 and Fig. 5.2, the initial estimated band gap for both BLBO:Eu and SLBO:Eu is found to be 6.4 ± 0.3 eV. It should be noted here that we have also estimated the band gap of the reference undoped BLBO sample and it is found to be the same value of the Eu²⁺-doped sample, which is presented in the lower panel (dotted line) in Fig. 5.1. We have mentioned earlier in the DFT calculations section that the final quantum state during the XAS measurement has an O 1s core-hole. This core-hole interacts with the excited electron via coulomb interaction effectively shifting in most cases

Table 5.1: Measured and calculated band gaps. The measured band gap is denoted by $\Delta_{\text{expt.}}$ and the calculated band gap is denoted by Δ_{GGA} and Δ_{mBJ} for PBE-GGA and mBJ functional, respectively. The one available literature band gap value is also included. All units are in eV.

Samples	$\Delta_{\text{expt.}}$	Δ_{GGA}	Δ_{mBJ}	literature $\Delta_{\text{expt.}}$
BLBO:Eu	6.5 ± 0.3			
BLBO	6.5 ± 0.3	5.1	6.8	3.8 [84]
SLBO:Eu	6.5 ± 0.3			
SLBO		5.6	7.4	

the conduction band onset to lower energy. To accurately determine the bottom of the conduction band, it is necessary to correct for this energy shift due to the distortion by the core-hole. Therefore, the band gap is determined from XES-XAS onsets once the core hole shift has been accounted for. The core hole shift can be estimated by calculating XAS spectrum for the excited state modelled by a super-cell ($2 \times 1 \times 1$ supercell) where a core electron from an O atom is removed and added as a crystal background charge. The conduction band onset for this excited state is then compared to the calculation for the unperturbed ground state. The core hole shift is found to be 0.1 eV for both materials. Therefore, the final experimental band gap is found to be 6.5 ± 0.3 eV for both BLBO:Eu and SLBO:Eu samples, which is presented in Table 5.1.

The experimental uncertainty in energy originates from the monochromator (0.05 eV at the O K-edge) and spectrometer (0.2 eV at the O-Kedge) resolution as well as the energy calibration. The calculated band gap using PBE-GGA is found to be 5.1 eV for BLBO and 5.6 eV for SLBO. This underestimation is typical for DFT calculations and can be improved upon by using the mBJ exchange-correlation potential [123]. In this case, the calculated band gap is found to be 6.8 eV and 7.4 eV for BLBO and SLBO, respectively, which both are in good agreement with our measurements. However,

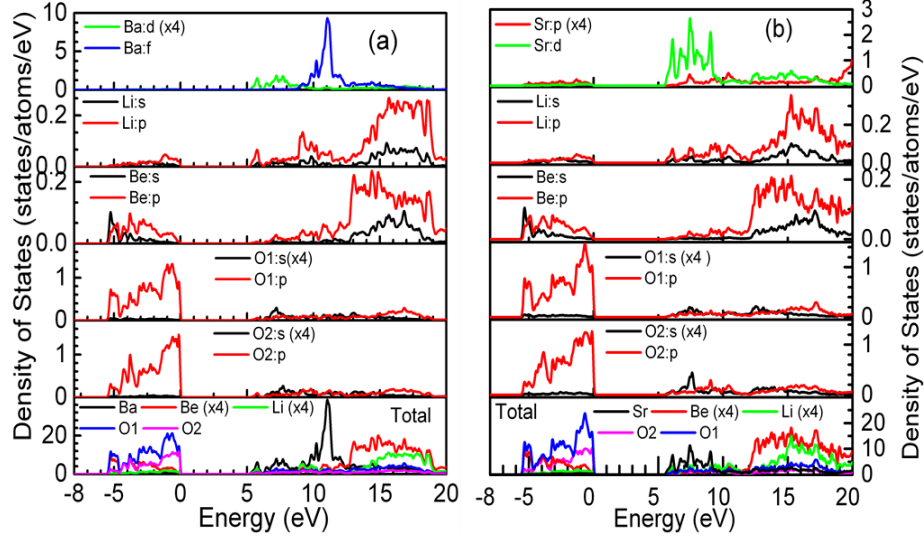


Figure 5.3: Calculated density of states for $AELi_2[Be_4O_6]$ ($AE = Ba, Sr$) based on ground state GGA-PBE calculations. Calculated partial and total DOS of Ba, Be, Li and two inequivalent O atoms for $BaLi_2[Be_4O_6]$ in (a) and Sr, Be, Li and two inequivalent O atoms for $SrLi_2[Be_4O_6]$ in (b) are compared. The energy zero is at the Fermi level.

the calculated band gap for SLBO is about 0.6 eV higher than the calculated value of BLBO and the measured value of SLBO:Eu. The DOS calculations show that the effect of Ba d-states at the lower CB contributes to the band gap of BLBO being about 0.6 eV smaller than that of SLBO. The authors in Ref. [84] estimated the band gap of 3.8 eV for BLBO using diffuse reflectance spectra and analysing corresponding to the Tauc method [198–201]. The method is based on absorption data relative to the wavelength and is ideal for films or single crystals because, either the surface needs to be very smooth providing an ideal reflection measurements or a film deposit on quartz whose band gap is very large allowing for transmission measurements [202]. However, due to the poly-crystalline nature and small quantity of materials, this technique is not usually an ideal method and is often subject to high uncertainty for electronic band gap measurements [202].

5.4.3 Density of States (DOS)

Above, we found excellent agreement between the calculated and experimental XAS and XES spectra. The origin of the XAS and XES features is explained herein by examining the calculated total and partial density of states. In particular why these compounds have similar band gaps despite having different elements (Ba vs Sr). The calculated partial and total DOS for valence band (VB) and conduction band (CB) for BLBO and SLBO, determined by the ground state GGA-PBE functionals calculations, are shown in Fig. 6.3. At first, the DOS for BLBO will be discussed, which is presented in Fig. 6.3(a). The O p-states dominate the valence band (VB), while the Ba f-states dominate the conduction band (CB). There is strong mixing of Be s-states and p-states in the lower VB and little contribution of Li s-states and p-states in the upper VB. The lower CB is due to the Ba d-states and the middle CB is due to the Ba f-states. It is well known for the alkaline earth ion d-states to contribute heavily to the lower CB [42, 43].

On the other hand, overall, the DOS for SLBO in Fig. 6.3(b) are nearly the same as for BLBO. The O p-states dominate the valence band (VB), and the Sr d-states dominate the conduction band (CB). Likewise, the admixture of Be s-states and p-states contribute to the lower VB and Li s-states and p-states contribute slightly in the upper VB. The Ba states show different behaviour than the Sr states, particularly at the lower and middle CB. The contribution of d-states for BLBO in the lower CB affects the band gap of this material. In our DOS calculations, we do not include the Eu^{2+} atoms, however the properties in the presence of Eu^{2+} atoms are of great interest and are discussed in the sections below.

5.4.4 Band Structure and RIXS Spectra

The calculated band structures using GGA-PBE calculations for BLBO and SLBO are shown in Fig. 5.4. The band structures of BLBO and SLBO are nearly identical.

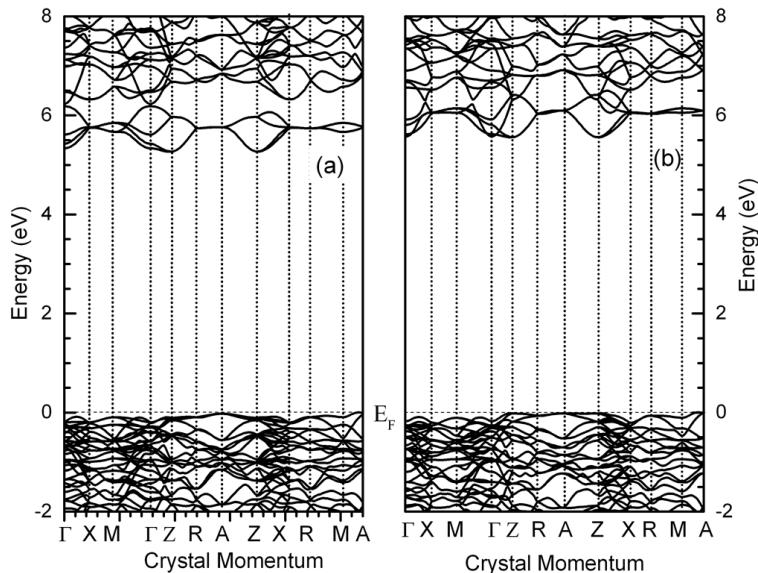


Figure 5.4: Calculated band structure of $\text{BaLi}_2[\text{Be}_4\text{O}_6]$ in (a) and $\text{SrLi}_2\text{Be}_4\text{O}_6$ in (b) based on ground state GGA-PBE calculations. For both samples, the conduction minimum is at the Z point and the VB maximum between the M and A points. The energy scales are set with respect to the Fermi energy, E_F .

It should be noted that the conduction band minimum is located at the Z point, while the valence band maximum is located between the M and A points for both compounds. Therefore, the band gap is indirect, which agrees with the prediction of authors in Ref. [84]. We already have mentioned in the Oxygen K-edge spectra section that during RIXS measurements, the incident energy is selected to be near one of the absorption edges. Therefore, the changes in emission spectra are observed as the excitation energy is varied. This RIXS technique can measure whether a system has a direct or an indirect band gap. As shown in Ref. [78, 203], for direct band gap materials, the RIXS spectrum containing the highest emission energy is obtained by threshold excitation (excitation on the CB onset) while for an indirect band gap material, the highest emission energy is obtained for excitation at some higher excitation energy with respect to the threshold excitation. Figure 5.1(a) and Fig. 5.2(a) show the RIXS spectra excited at threshold excitation (black solid line) and some eV above the threshold excitation (red and green solid line) for BLBO:Eu

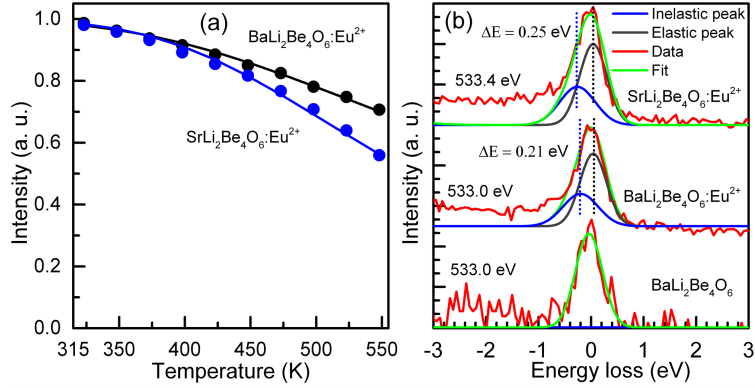


Figure 5.5: (a) Measured luminescence intensity as a function of temperature for BaLi₂Be₄O₆:Eu²⁺ (black) and SrLi₂Be₄O₆:Eu²⁺ (blue), along with the fit (solid line) of Equation 5.1 to the measured data. (b) RIXS spectra (red) for BaLi₂Be₄O₆:Eu²⁺ and BaLi₂Be₄O₆ excited at 533.0 eV (at the CB onset) and for SrLi₂Be₄O₆:Eu²⁺ excited at 533.4 eV (at the CB onset). Two Gaussian black (elastic feature) and blue (loss feature) are used to fit the spectrum (green).

and SLBO:Eu, respectively. The vertical dotted magenta line in Fig. 5.1(a) and Fig. 5.2(a) indicates that the highest emission energy (green solid line) is observed for higher excitation energy with respect to the threshold excitation, which confirms that the band gap is indirect [78, 203]. Again, this agrees with our calculated band structures discussed above.

5.4.5 Position of the Eu²⁺ 5d States in the Band Gap

Eu²⁺-doped phosphors with a single activator site usually show one emission maximum. The Eu²⁺ 5d¹4f⁶ to 4f⁷ transitions are responsible for the optical luminescence. The thermal stability and colour of the luminescence produced by the phosphor depends on the energetic position of Eu²⁺, which is very sensitive to the host matrix and the Eu²⁺ 5d energy depends strongly on the surrounding ligands. Recently, we have developed a method [37], which allows to measure directly the energy position of the Eu²⁺ 5d levels from RIXS at the ligand K-edge. Figure 5.5(b) shows the RIXS spectra excited at the CB onset for both doped compositions. For comparison, we have also measured the RIXS spectrum at the CB onset for the sample without the

Table 5.2: Comparison of the Standard Deviation (σ_1 , for elastic peak; σ_2 , for inelastic peak) and the Eu^{2+} 5d to conduction band energy separations ΔE_{RIXS} from RIXS measurements; ΔE_{TQ} from TQ measurements) from the fits shown in Fig. 5.5. Fitting parameter ($\frac{\Gamma_0}{\Gamma_\nu}$) of Eq. 5.1 is also included in this table.

Samples	σ_1 (eV)	σ_2 (eV)	ΔE_{RIXS} (eV)	ΔE_{TQ} (eV)	$\frac{\Gamma_0}{\Gamma_\nu}$
BLBO	0.254	0	n.a.		
BLBO:Eu	0.253	0.334	0.21 ± 0.1	0.20 ± 0.03	153
SLBO:Eu	0.257	0.339	0.25 ± 0.1	0.26 ± 0.03	195

Eu^{2+} dopant. The spectra are displayed on the energy loss scale, which is obtained by subtracting the excitation energy from the emission energy. This will place the elastically scattered radiation at 0 eV and any energy loss features at lower energies. It is observed that two spectral energy loss features appear for each doped composition, but one spectral feature appears for the undoped composition. The additional feature observed in doped samples just below the elastic scattering peak represents energy losses of the incident X-rays to low-energy excitations. This energy loss is due to the excitation of Eu^{2+} 5d electrons to the conduction band [37]. For BLBO:Eu and SLBO:Eu, the Eu^{2+} 5d to conduction band separations are found to be 0.21 ± 0.10 eV and 0.25 ± 0.10 eV, respectively, which are also presented in Table 5.2.

The fit parameters and uncertainties obtained from fitting are shown as well in Table 5.2. These values are similar to those found for $\text{Sr}[\text{LiAl}_3\text{N}_4]:\text{Eu}^{2+}$ ($\Delta E = 0.2$ eV) [37] and $\text{Sr}[\text{Be}_6\text{ON}_4]:\text{Eu}^{2+}$ ($\Delta E = 0.26$ eV) [73]. We note that the cross section for the 5d to CB inelastic scattering is extremely low and the Eu^{2+} concentration is diluted ($\approx 1\%$) making these measurements are extremely photon hungry and difficult and giving rise to the large error bar in the X-ray measurements.

Thermal stability at a high temperature is an important parameter for pc-LEDs, par-

ticularly in high power pc-LEDs, where the phosphor temperature can increase up to 550 K. With increasing temperature, the 5d electrons can be promoted to the conduction band leading to a decrease in luminescence. This decrease in luminescence with increasing temperature is termed thermal quenching (TQ). We are turning to discuss the TQ behaviour of these compounds. The luminescence intensities for BLBO:Eu and SLBO:Eu as a function of sample temperature are shown in Fig. 5.5(a), along with fitted data. Experimental data are adapted from Ref. [84]. To fit the experimental data, the following Fermi-Dirac-like equation, which can describe the luminescence intensity $I(T)$ at different experimental temperatures with the subsequent thermal depopulation of the Eu^{2+} 5d levels, is used: [37, 64]

$$I(T) = \frac{I_0}{1 + \frac{\Gamma_0}{\Gamma_\nu} e^{-\frac{\Delta E}{k_B T}}} \quad (5.1)$$

where I_0 is the initial luminescence intensity at $T = 0$ K, Γ_ν is the radiative decay transition rate of 5d state of Eu^{2+} , Γ_0 is the attempt rate for TQ process, k_B is the Boltzmann's constant and ΔE is the energy separation of the 5d state from the next-higher-lying level, here assumed to be the CB. In Equation 5.1, the parameters Γ_0/Γ_ν and ΔE are varied to obtain the least squares fit of the data. Γ_0/Γ_ν determines how rapidly the decay occurs with temperature and ΔE determines at what temperature TQ starts to become significant [37, 64]. From the fit of the measurements to Eq. 5.1, the ΔE values for BLBO:Eu and SLBO:Eu are found to be 0.20 ± 0.03 eV and 0.26 ± 0.03 eV, respectively, which are also listed in Table 5.2. The Eu^{2+} 5d to CB band separations measured from the energy loss of the low excitation energy spectra and from the TQ data for both compounds are in strong agreement. The narrow-band blue emitting phosphors of BLBO:Eu and SLBO:Eu show low TQ at high temperature with the relative emission intensity of 71% and 60% at 546 K, respectively.

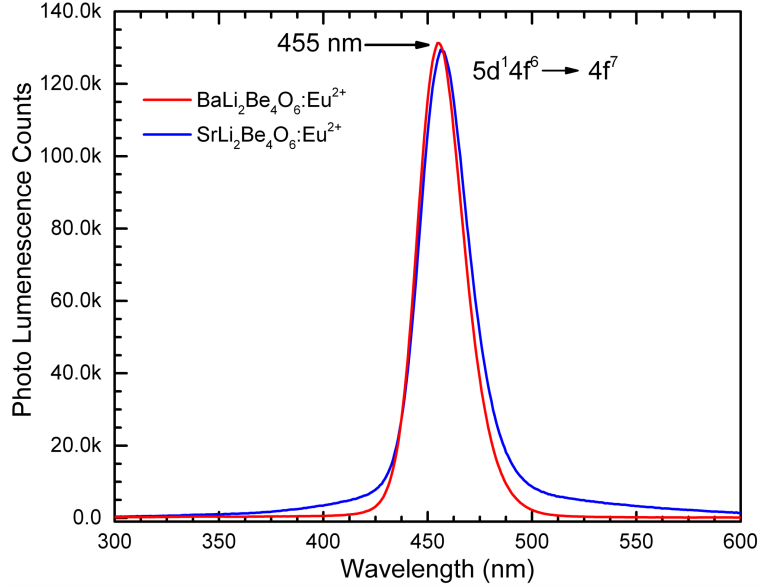


Figure 5.6: XEOL spectra of $\text{BaLi}_2\text{Be}_4\text{O}_6:\text{Eu}^{2+}$ and $\text{SrLi}_2\text{Be}_4\text{O}_6:\text{Eu}^{2+}$ excited at 140 eV. Both Eu^{2+} -doped samples show a strong ultra-narrow band luminescence feature at 455-457 nm, which is due to the $\text{Eu}^{2+} 5d^1 4f^6 \rightarrow 4f^7$ optical transition. Both spectra were accumulated for the same time.

5.4.6 Optical Transition Provided by XEOL

X-ray Excited Optical Luminescence (XEOL) spectroscopy is employed to explore optical transitions, electronic structure, presence of defects, and luminescence properties of solids [37, 75, 162]. Here we have performed XEOL measurements for BLBO:Eu and SLBO:Eu to understand the optical transition and luminescence properties and the luminescence spectra, which are presented in Fig. 5.6. The excitation energy for all samples was 140 eV. It is observed in Fig. 5.6 that there is a strong ultra-narrow band with 25 nm full width at half maximum (FWHM) XEOL feature for BLBO:Eu compound at 455 nm and for SLBO:Eu compound at 457 nm. To the best of our knowledge, this is the narrowest emission band to date from an Eu^{2+} -doped blue phosphor. This strong luminescence feature is due to the transition of $\text{Eu}^{2+} 5d^1 4f^6 \rightarrow 4f^7$ in agreement with the literature [27, 37, 204]. Therefore, the observed emission bands are located in the blue region due to the $5d^1 4f^6 \rightarrow 4f^7$ transitions of Eu^{2+} ions. The results strongly indicate that BLBO:Eu and SLBO:Eu would be very efficient

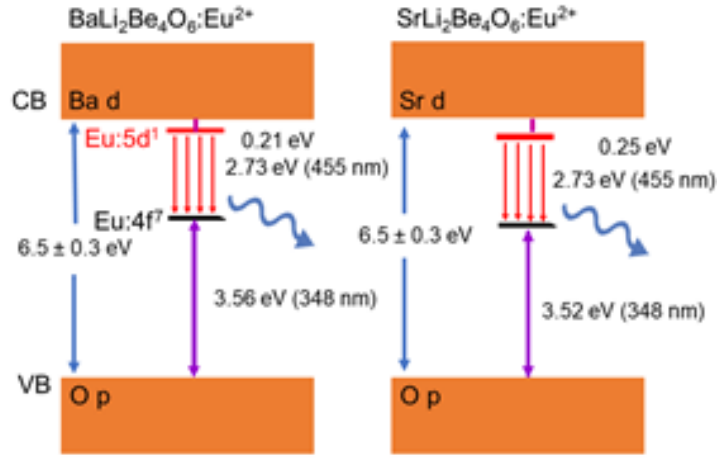


Figure 5.7: Energy level diagram of $\text{BaLi}_2\text{Be}_4\text{O}_6:\text{Eu}^{2+}$ and $\text{SrLi}_2\text{Be}_4\text{O}_6:\text{Eu}^{2+}$. Band gaps are determined from our measurements and calculations. DOS calculations show that the upper edge of the VB is dominated by O p-states for both compounds and the lower edge of the CB is dominated by d-states of Ba and Sr for $\text{BaLi}_2\text{Be}_4\text{O}_6:\text{Eu}^{2+}$ and $\text{SrLi}_2\text{Be}_4\text{O}_6:\text{Eu}^{2+}$, respectively. The Eu^{2+} 5d¹-states are added to the diagram from RIXS measurements and XEOL measurements show the 5d¹4f⁶ → 4f⁷ optical transitions. Both compounds emit blue luminescence at 455 nm.

phosphors, and only traces of activator ions are required to obtain emission upon high energy excitation by synchrotron radiation.

5.5 Conclusions

In this study, we explored several key properties of the novel pc-LED phosphor $\text{AELi}_2[\text{Be}_4\text{O}_6]:\text{Eu}^{2+}$ (AE = Sr, Ba) (1% Eu^{2+}). The band gaps for both BLBO:Eu and SLBO:Eu have been measured to be 6.5 ± 0.3 eV. This large band gap is the prime prerequisite for efficient luminescence of the Eu^{2+} -doped samples. The band gap is found to be indirect for each compound by our GGA-PBE calculations and our RIXS measurements. The DOS for the promising phosphors BLBO and SLBO have been calculated and used to analyse the XAS and XES spectra in a more informing way. The O p-states dominate the valence band (VB) for each composition, while the Ba f-states dominate the conduction band (CB) for BLBO and Sr d-states dominate for SLBO. The Eu^{2+} 5d¹4f⁶ → 4f⁷ transitions are responsible for the optical luminescence of the Eu^{2+} -doped materials. The wavelength and efficiency of the

luminescence of the phosphor depend crucially on the energy position of the Eu^{2+} 5d. For BLBO:Eu and SLBO:Eu compounds, the key parameter for the performance as an LED material, the Eu^{2+} 5d to conduction band energy separations are found to be 0.21 ± 0.10 eV and 0.25 ± 0.10 eV, respectively from RIXS measurements, which both are excellent agreement with our thermal quenching measurements. Finally, we perform XEOL measurements confirming the Eu^{2+} $5d^1 4f^6 \rightarrow 4f^7$ transition, that is responsible for the blue ultra-narrow optical luminescence at 455-457 nm for both compounds. Based on our calculations and measurements, a schematic illustration summarizing all pertinent energy levels and involved all transition processes of these compounds is given in Fig. 5.7. Narrow-band emitting phosphors are crucial for colour tuning of pc-LEDs. Expanded understanding of the electronical properties of these compounds can lead to target-oriented research of new materials. The detailed determination of band gaps and energetic position of activator Eu^{2+} states can be central steps of phosphor design. Our study of these materials serves an important role in the advancement of light emitting diodes and introducing Eu^{2+} -doped diodes to illumination market. In conclusion, $\text{AELi}_2[\text{Be}_4\text{O}_6]:\text{Eu}^{2+}$ ($\text{AE} = \text{Sr}, \text{Ba}$) demonstrates highly promising materials in the ongoing investigations for highly efficient narrow-band phosphors.

Conflicts of interest

The authors declare no competing financial interest.

Acknowledgements

The experiments were performed at the Canadian Light Source, which is funded by the Canada Foundation for Innovation, the Natural Science and Engineering Research Council of Canada (NSERC), the National Research Council Canada, the Canadian Institutes of Health Research, the Government of Saskatchewan, Western Economic Diversification Canada, and the University of Saskatchewan. M.R.A. is grateful to the Government of Saskatchewan for financial support by Saskatchewan Innovation and the Opportunity Scholarship. We acknowledge support from NSERC and the Canada

Research Chair program. The authors also acknowledge Compute Canada. The calculations presented in this paper were performed on the Cedar high-performance computing cluster, which is part of the WestGrid (www.westgrid.ca) and Compute Canada Calcul Canada (www.computecanada.ca).

Chapter 6

Unraveling the Energy Levels of Eu^{2+} -ions in $M\text{Be}_{20}\text{N}_{14}:\text{Eu}^{2+}$ ($M = \text{Sr}, \text{Ba}$) Phosphors

Authors: M. Ruhul Amin¹, Eugenia Elzer², Wolfgang Schnick², and Alexander Moewes¹

¹Department of Physics and Engineering Physics, University of Saskatchewan, 116 Science Place, Saskatoon, Saskatchewan , S7N 5E2, Canada

²Department of Chemistry, University of Munich (LMU), Butenandtstrasse, 5-13, 81377 Munich, Germany

Reference: M. Ruhul Amin, Eugenia Elzer, Wolfgang Schnick, and Alexander Moewes, *Journal of Physical Chemistry C* 2021, **125**, 1182811837 [66]

Summary and Author Contributions

In this manuscript [66], we study two new exotic blue emitting phosphors $M\text{Be}_{20}\text{N}_{14}:\text{Eu}^{2+}$ ($M = \text{Sr}, \text{Ba}$) and determine all participating energy levels of Eu^{2+} ions ($4f^65d^1$ and $4f^7$ states), valence band, conduction band, and band gaps. We identify all radiative processes involved therefore ultimately informing the improvement of next generation pc-LEDs. To gain insight into the radiative processes, we use resonant inelastic X-ray scattering and X-ray excited optical luminescence to directly determine the Eu^{2+}

$4f^65d^1$ to conduction band separation and the positions of Eu^{2+} levels for Eu^{2+} -doped phosphors. These experimental techniques allow direct access to the intragap states that are the source of the luminescence of Eu^{2+} -doped phosphors. In order to interpret the experimental band gap, density of states (DOS), band structure, and X-ray absorption (XAS) and emission (XES) spectra, we performed density functional theory calculations. With these measurements and calculations, deep insights are gained into key properties of $M\text{Be}_{20}\text{N}_{14}:\text{Eu}^{2+}$ ($M = \text{Sr}, \text{Ba}$) phosphor, such as blue emission, efficiency, and thermal quenching behaviour. XES, XAS, and XEOL measurements as well as DFT calculations were performed by M. R. Amin under the supervision of A. Moewes. XAS and non-resonant XES measurements were performed to determine the band gap. Manuscript preparation was performed by M. R. Amin. The energy separation between the conduction band and the $5d$ Eu^{2+} energy level was measured by performing resonant excitations at the onset of the N K XAS spectrum. The thermal quenching behavior was determined to be similar to other efficient phosphors [37]. This work has been published in *Journal of Physical Chemistry C* [66].

Abstract

Band gap, electronic structure, optical properties, and energy levels of the incorporated activator Eu^{2+} ions of the recently synthesized luminescent nitridoberyllates, $M\text{Be}_{20}\text{N}_{14}:\text{Eu}^{2+}$ ($M = \text{Sr}, \text{Ba}$) are studied with a combination of soft X-ray spectroscopy and density functional theory (DFT) calculations. X-ray absorption and X-ray emission spectroscopy at the N K-edge are used to determine the band gap, which is found to be 4.4 ± 0.3 eV for both compounds. The measured value agrees well with the DFT-calculated band gaps of 4.6 eV for $M = \text{Sr}$ and 4.4 eV for $M = \text{Ba}$, employing the modified Becke-Johnson exchange potential. The $4f^65d^1$ energy level of the Eu^{2+} -ions is determined directly from the separation between the bottom of the conduction band and the lowest $4f^65d^1$ states of Eu^{2+} -ions and, is found to be 0.31

± 0.04 eV for $M = \text{Sr}$ and 0.30 ± 0.04 eV for $M = \text{Ba}$ from resonant inelastic X-ray scattering measurements. X-ray excited optical luminescence (XEOL) measurements show luminescence in the blue spectral region at 430 nm for $M = \text{Sr}$ and 427 nm for $M = \text{Ba}$, which are due to the $4f^6 5d^1 \rightarrow 4f^7$ transition. Therefore, XEOL enables the determination of the $4f^7$ energy levels and thus provides a deep understanding of the energy levels and radiative processes involved in $M\text{Be}_{20}\text{N}_{14}:\text{Eu}^{2+}$ ($M = \text{Sr}, \text{Ba}$).

6.1 INTRODUCTION

InGaN-based light emitting diodes (LEDs) are widely used in solid state lighting [26], as they provide higher light quality, better color point stability, and longer bulbs lifetime, while using significantly less energy, compared to incandescent and fluorescent lamps [205]. Several strategies can be used to create white light LEDs (wLEDs) [206]. The simplest way for a phosphor-converted LED is the combination of a blue LED with a broad-band yellow phosphor like $\text{Y}_3\text{Al}_5\text{O}_{12}:\text{Ce}^{3+}$ [34]. Lacking a red component, this LED-design suffers from small color rendering index (CRI) values (< 75) and correlated color temperatures above 4500 K [34]. To overcome these obstacles, a blend of green and red or green, yellow, and red phosphors can be excited with a blue LED. Alternatively, wLEDs with even higher CRI values (> 90) can be realized with a near ultra-violet (nUV)-LED covered with red, green, and blue phosphors [34]. Blue phosphors are more flexible than the blue LED, regarding the tunability of the emission maxima and widths, which is crucial for lumen equivalence and color rendering purposes [207]. In terms of phosphor selection, most of the green, yellow, and red phosphors can be efficiently excited with a nUV-LED [34]. As the emission of the nUV-LED is close to the excitation of the blue phosphor, it is important to find an efficient blue phosphor with high quantum efficiency [208]. In literature, several blue-emitting phosphors have been described but only few of them show efficient luminescence, which is required for applications in combination with nUV-LED, including $\text{Ba}_3\text{MgSi}_2\text{O}_8:\text{Eu}^{2+}$ [207], $(\text{Ca}, \text{Sr}, \text{Ba})_{10}(\text{PO}_4)_6\text{Cl}_2:\text{Eu}^{2+}$ [207],

BaMgAl₁₀O₁₇:Eu²⁺ [207], and *AELi*₂[Be₄O₆]:Eu²⁺ (*AE* = Sr, Ba) [84]. Therefore, the search for efficient blue narrow-band emitting phosphors remains highly important.

It is obvious that selection and development of appropriate phosphors is key in improving the optical properties of the LEDs (e.g. luminous efficacy, CRI). Generally, modern phosphors consist of a suitable host material doped with activator ions, mostly rare-earth (RE) ions like Eu²⁺, Yb²⁺, or Ce³⁺ [34, 206]. The luminescence emerges from the $4f^65d^1 \rightarrow 4f^7$ optical transition in Eu²⁺ doped phosphors is strongly affected by the host lattice, especially the local environment of the activator ion [53]. The energetic position of the 5*d* orbitals depends on the nephelauxetic effect, which is related to anion polarizability, electronegativity of the ions, and dopant-bond distances, and the crystal field splitting (CFS), which is influenced by the nature and the coordination number of the dopant ion, as well as the arrangement and the nature of the ligands [34]. Usually nitrides, in contrast to oxides, feature often a higher nephelauxetic effect and a higher CFS, which reduces the energy of the 5*d* orbitals and often results in red-shifted excitation and emission energies compared to oxides [53]. Even though the search for new luminescent substances in the (oxo)nitride class has been ongoing for some time, this substance class is still good for a surprise [27, 34, 73]. Recently, in the search for new suitable host lattices, the element beryllium was introduced into the anionic networks and, in the process, the Eu²⁺ doped highly condensed nitridoberyllates *MBe*₂₀N₁₄:Eu²⁺ (*M* = Sr, Ba) were studied for the first time [209]. The compounds are promising candidates in the ongoing investigation for efficient phosphors, as they feature thermal and chemical stability, a wide band gap, and a narrow band emission in the blue spectral region. In this contribution, we used X-ray spectroscopy techniques to investigate the novel nitridoberyllates *MBe*₂₀N₁₄:Eu²⁺ (*M* = Sr, Ba). Thereby, we were able to directly determine the energy of the Eu²⁺ states. Resonant inelastic X-ray scattering (RIXS) was used to experimentally determine

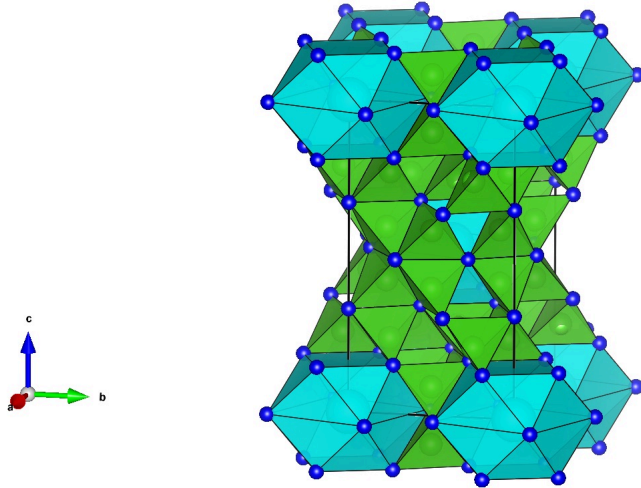


Figure 6.1: Crystal structure of the isotypic compounds $M\text{Be}_{20}\text{N}_{14}$ ($M = \text{Sr}, \text{Ba}$). BeN_4 tetrahedra are presented in green, MN_{12} ($M = \text{Sr}, \text{Ba}$) cuboctahedra in cyan, and N atoms in blue. The figure is adapted from ref. [209].

the energetic positions of the $\text{Eu}^{2+} 4f^6 5d^1$ states with respect to the conduction band (CB) onset and X-ray excited optical luminescence spectroscopy (XEOL) was used to identify the energetic position of the $4f^7$ states of the Eu^{2+} . The combination of these methods lead to a complete and comprehensive understanding of all energy levels and radiative processes involved for $M\text{Be}_{20}\text{N}_{14}:\text{Eu}^{2+}$ ($M = \text{Sr}, \text{Ba}$), which is key in the development of highly efficient phosphors.

6.2 METHODS

6.2.1 Synthesis

The powder samples of $M\text{Be}_{20}\text{N}_{14}:\text{Eu}^{2+}$ ($M = \text{Sr}, \text{Ba}$) were synthesized following the synthesis instruction in the literature [209]. The starting materials $M(\text{NH}_2)_2$ ($M = \text{Sr}, \text{Ba}$), and Be_3N_2 , and small amount of EuF_3 as dopant (resulting in a nominal doping concentration of 2% referred to M) were heated in a radio frequency furnace under N_2 atmosphere at 1400 °C. The crystal structure of $M\text{Be}_{20}\text{N}_{14}$ ($M = \text{Sr}, \text{Ba}$) is displayed in Figure 6.1, which consists of edge- and vertex-sharing BeN_4 tetrahedra forming a highly condensed anionic network. The charge compensation is achieved

by incorporating Sr^{2+} or Ba^{2+} ions. A detailed description of the synthesis and the crystal structure characterization of $M\text{Be}_{20}\text{N}_{14}:\text{Eu}^{2+}$ ($M = \text{Sr}, \text{Ba}$) can be found in ref. [209].

6.2.2 XAS, XES, and XEOL Measurements

Soft X-ray spectroscopy is an excellent tool for probing the electronic properties of materials. Here X-ray absorption spectroscopy (XAS) and X-ray emission spectroscopy (XES) techniques are employed to directly probe the unoccupied and occupied partial density of states, respectively. XEOL measurements are used to characterize the optical transitions. The REIXS beamline [87] was used to collect XAS and XES spectra and the VLS-PGM beamline [88] for recording XEOL spectra at the Canadian Light Source in Saskatoon, Canada. In the REIXS beamline, the X-rays are generated with elliptically polarized undulators (EPUs) made of permanent magnets with 1.6 m long and 75 mm of periodicity, and a spherical grating monochromator is used to select the X-ray energy. The REIXS beamline uses two separate gold-coated sagittal cylindrical mirrors to collect and collimate the X-rays from the EPUs. It uses three different interchangeable grating corresponding to low, medium, and high to cover an energy range of 95 eV–2000 eV. On the low energy grating at 100 eV with 25 μm exit slits, the beamline delivers 10^{12} photons/s of flux. Depending on the desired energy range, four selectable mirrors coatings on the plane mirrors (Ni, Si, C, and Au) are used to suppress the high-order harmonics. REIXS has a large spherical grating spectrometer, using a Rowland circle geometry to measure high-resolution XES spectra. For all X-ray measurements, the powder samples were prepared by affixing them to a metallic sample holder with clean indium foil. All measurements were conducted in the ultrahigh vacuum chambers in the order of 10^{-9} Torr at room temperature thus there is no contribution to the signal from the atmospheric nitrogen. During the measurements, the sample is electrically grounded so that the photoelectrons removed can be replenished. The absorption was measured in the bulk sensitive partial

fluorescence yield (PFY) mode, determined with silicon drift fluorescence detectors. It is known that the size of the nitrogen molecule is about 0.368 nm [210]. If the nitrogen molecules would form 3 layers on the surface of the sample, the thickness of the absorbed layers would be around 1 nm. However, the attenuation length of our samples is about 200 nm at N K-edge [97], making any adsorbant layer practically too dilute to alter the measurements. Nearly all the emitted photons therefore originate from bulk of the sample. 8000 and 2000 are the resolving powers, $E/\Delta E$, for the monochromator and for the emission spectrometer at REIXS, respectively, which corresponds to an energy resolution, ΔE , of 0.05 eV and 0.2 eV at the N K-edge for XAS and XES, respectively. An ocean optics QE 65000 fast CCD spectrophotometer is used to collect the XEOL spectra [168]. For the energy calibration of the XAS and XES spectra at the N K-edge, hexagonal boron nitride (h-BN) is used as a reference compound. The prominent h-BN spectral feature at 402.1 eV was used to calibrate the XAS spectra, while the XES spectra were initially calibrated using elastic scattering peaks, and then further shifted with respect to the h-BN peak at 402.1 eV to obtain the final calibration relative to the absorption spectra [82].

6.2.3 Density Functional Theory Calculations Details

Density functional theory (DFT) is a quantum mechanical modelling method to investigate material properties. The commercially available WIEN2k software package was employed for the DFT calculations [126, 173]. This software code uses Kohn-Sham methodology with spherical wave functions to model core orbitals [126, 173]. The crystal structure for $M\text{Be}_{20}\text{N}_{14}$ ($M = \text{Sr}, \text{Ba}$) from ref. [209] was used as input for the calculations. Note that the incorporated activator Eu^{2+} was not included in the experimental crystal structures for the calculations for several reasons. Firstly, the calculation of $4f$ electrons requires a different multiplet code resulting that the calculation of the Eu^{2+} $5d$ electrons is currently not possible [211]. Secondly, DFT is a ground-state theory, and properly describing the radiative transition of Eu^{2+} requires

a non-ground state approach. Finally, the optimized doping concentration of Eu^{2+} in $M\text{Be}_{20}\text{N}_{14}\cdot\text{Eu}^{2+}$ ($M = \text{Sr}, \text{Ba}$) is 2% because of the balancing between the thermal quenching and the intrinsic luminescence efficiency. In a crystallographic unit cell the $M\text{Be}_{20}\text{N}_{14}$ ($M = \text{Sr}, \text{Ba}$) compounds have 2 Sr/Ba atoms, 40 Be atoms and 28 N atoms. For a single unit cell of $M\text{Be}_{20}\text{N}_{14}$ ($M = \text{Sr}, \text{Ba}$) with one Eu^{2+} ion instead of $\text{Sr}^{2+}/\text{Ba}^{2+}$, the cluster would correspond to a heavily Eu^{2+} -doped $M\text{Be}_{20}\text{N}_{14}$ ($M = \text{Sr}, \text{Ba}$) (with 50% of Eu^{2+}). To perform the calculations for 2% Eu^{2+} concentration in $M\text{Be}_{20}\text{N}_{14}$ ($M = \text{Sr}, \text{Ba}$), it would require a very large supercell, which is computationally not feasible. We used the Perdew-Burke-Ernzerhof variant of the generalized gradient approximation (PBE-GGA) for the exchange-correlation functional [174]. The PBE-GGA functional significantly underestimates the band gap but can calculate soft X-ray spectra well. To obtain a more accurate band gap, the modified Becke-Johnson (mBJ) exchange potential was employed [123]. The calculated XAS and XES spectra were determined from the multiplication of the calculated partial density of states (pDOS), the dipole transition matrix, and the radial transition matrix [175]. Spectra are broadened using a Voigt profile to account for instrumental and lifetime broadening [176]. The experimental N K-edge XAS and XES spectra depend on the final state and the XAS final state has a core-hole (CH) in the N $1s$ [177, 178]. To account for the distortion by the CH, a CH calculation was performed for each nonequivalent N site by including a single CH at the corresponding N-atom inside a $2 \times 1 \times 1$ supercell of the unit cell of $M\text{Be}_{20}\text{N}_{14}$. A background lattice charge was added to the supercell to preserve charge neutrality. The resulting core hole XAS spectrum was obtained by combining all nonequivalent N sites.

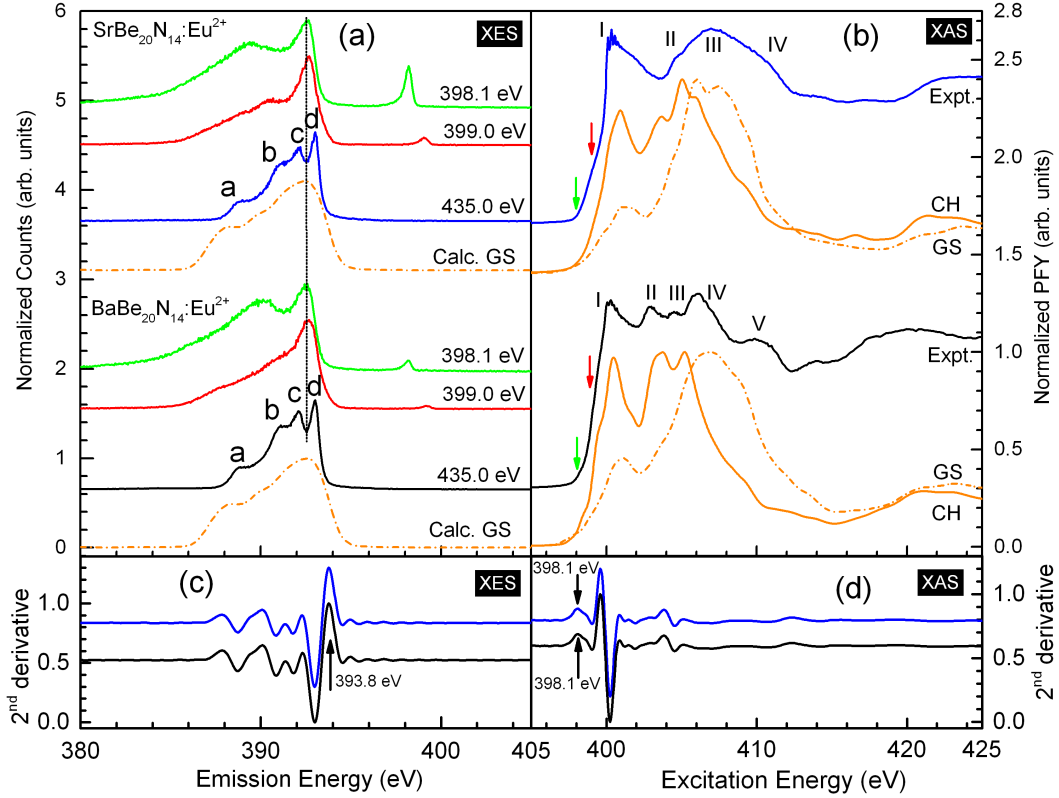


Figure 6.2: (a) NXES spectrum (blue for $M = \text{Sr}$ and black for $M = \text{Ba}$) was excited at 435.0 eV and RIXS spectra were collected at excitation energies of 398.1 eV (green) and 399.0 eV (red), which are compared to the ground state (GS, dotted-dash orange) calculations. The vertical dotted-dash black line indicates the higher emission energy observed at higher excitation energy in the RIXS spectra. (b) Experimental PFY is compared to the CH (solid orange) and the GS (dotted-dash orange) calculations. Two colored downward arrows on the absorption spectra indicate the corresponding excitation energies at which the RIXS spectra were taken. (c) and (d) Second derivative of experimental NXES and XAS spectra with the corresponding valence band and conduction band onsets indicated by black arrows.

6.3 RESULTS AND DISCUSSION

6.3.1 N K-edge Spectra

The experimental XAS and XES spectra and the DFT calculations for $M\text{Be}_{20}\text{N}_{14}:\text{Eu}^{2+}$ ($M = \text{Sr}, \text{Ba}$) are compared in this section. The experimental absorption spectra are shown in Figure 6.2(b). Comparing the experimental XAS spectra for both compounds, it is found that the XAS spectra differ indicating that the alkaline earth metal affects the nitrogen pDOS. There are five main peaks in the measured XAS spectrum for $\text{BaBe}_{20}\text{N}_{14}:\text{Eu}^{2+}$, which are labeled I to V, and four main peaks for $\text{SrBe}_{20}\text{N}_{14}:\text{Eu}^{2+}$. Two colored downward arrows (green and red) in the measured XAS spectra indicate the excitation energies at which the RIXS spectra (Figure 6.2(a)) were collected. The origin of the peaks is assigned using our calculated pDOS (Figure 6.3) of the coordinating atoms. Our calculations show that feature I is the result of Ba d -states, whereas peak II mainly stems from the contribution of Ba f -states, peaks III to IV are due to Ba d - and f -states with small contributions from N p -states, and peak V stems predominantly from the Ba d - and f -states for $\text{BaBe}_{20}\text{N}_{14}:\text{Eu}^{2+}$. For $\text{SrBe}_{20}\text{N}_{14}:\text{Eu}^{2+}$, the Sr d -states contribute to the features I-IV and N p -states contribute to the peaks III and IV and Sr f -states contribute to IV. The experimental XAS spectra of both compounds are compared with CH and GS calculations. Comparing the experimental and calculated XAS spectra, we conclude that the overall agreement with the CH spectrum is excellent. This agreement provides strong justification for the one electron picture employed in the calculations and the absence of electron correlation effects.

Having discussed the features of the XAS spectra of $M\text{Be}_{20}\text{N}_{14}:\text{Eu}^{2+}$ ($M = \text{Sr}, \text{Ba}$), we now turn to the XES spectra in Figure 6.2(a). The XES spectra are displayed for three different excitation energies. The excitation energy at 435.0 eV is well above the N K-edge and the recorded spectrum is typically labelled as nonresonant X-ray

emission spectrum (NXES). The XES spectra of both compounds are nearly identical. All XES spectra have four main peaks labelled ‘a’, ‘b’, ‘c’, and ‘d’. All four features mainly originate from the contribution of the N states of p-symmetry in the valence band (VB) when the VB electrons of *p*-symmetry transition to the N core *s*-orbitals under the emission of soft X-ray photons. For this reason, we chose N K-edge emission spectroscopy to study the valence band. As before, the calculated GS XES spectra for both compounds agree very well with the experiment.

6.3.2 Band Gap Determination

The band gaps of $M\text{Be}_{20}\text{N}_{14}:\text{Eu}^{2+}$ ($M = \text{Sr}, \text{Ba}$) were determined by combining the measured occupied and unoccupied N *p*-states on the common energy scale, as shown in Figure 6.2(a) and Figure 6.2(b), respectively. The band gap is determined from the energy difference between the top of the VB, probed by NXES, and the bottom of the CB, probed by XAS. The top of the VB and the bottom of the CB are determined from the first peaks above the noise in the second derivative at the upper edge of the NXES and lower edge of the XAS spectra, respectively [37, 82]. The VB and the CB onsets are denoted with the vertical black arrows in Figure 6.2(c) and Figure 6.2(d). From the band onsets, the estimated band gap for both compounds is found to be 4.3 ± 0.3 eV. The CH shift was determined to be 0.1 eV by subtracting the CB onset energy calculated including CH from the calculated CB energy location for the ground state. Taking the CH shift into account, the final measured band gap is found to be 4.4 ± 0.3 eV for both compounds, which is displayed in Table 6.1. The experimental uncertainty associated with this band gap originates from the monochromator and spectrometer resolution and the uncertainty in the energy calibration when bringing emission and absorption energies to a common scale [65, 82]. The experimentally determined band gap is compared to the values obtained from DFT calculations. The calculated values are 3.2 eV for $M = \text{Ba}$ and 3.3 eV for $M = \text{Sr}$, using the PBE-GGA functional and 4.4 eV ($M = \text{Ba}$) and 4.6 eV ($M = \text{Sr}$), applying the mBJ

Table 6.1: Measured, calculated, and previously reported band gap values for $M\text{Be}_{20}\text{N}_{14}:\text{Eu}^{2+}$ ($M = \text{Sr}, \text{Ba}$). The measured band gap is denoted by $\Delta_{\text{expt.}}$ and the calculated band gap is denoted by Δ_{GGA} and Δ_{mBJ} for PBE-GGA functional and mBJ functional, respectively. The available literature band gap values are also denoted in the same way. All units are in eV.

System	$\Delta_{\text{expt.}}$	Δ_{GGA}	Δ_{mBJ}	Literature $\Delta_{\text{expt.}}$	Literature Δ_{mBJ}
$\text{BaBe}_{20}\text{N}_{14}:\text{Eu}^{2+}$	4.4 ± 0.3	3.2	4.4	4.2 [209]	-
$\text{SrBe}_{20}\text{N}_{14}:\text{Eu}^{2+}$	4.4 ± 0.3	3.3	4.6	4.1 [209]	4.6 [209]

exchange-correlation potential [123].

The band gap underestimation for PBE-GGA functional arises from the constant exchange-correlation potential that is applied to all electrons orbitals, leading to an underestimation of the electron-electron interaction. The mBJ exchange-correlation potential is an orbital independent exchange-correlation potential, which depends solely on semilocal quantities [123]. For this reason, the mBJ exchange-correlation potential reproduces band gaps more accurately [123]. In the literature the electrical band gap for $M = \text{Sr}$ was calculated using DFT calculations (mBJ functional), while the optical band gap for $M = \text{Sr}$ and Ba was determined from reflectance spectra, using the Tauc method [209]. All measured, calculated, and literature band gap values are included in Table 6.1.

6.3.3 Partial Density of States

The pDOS allow a more detailed analysis of the electronic structure of materials. Particularly, the origin of the XAS and XES features and band gap can be explained by the calculated pDOS. Figure 6.3(a) for $M = \text{Ba}$ and Figure 6.3(b) for $M = \text{Sr}$ show calculated pDOS for the VB and the CB, using the ground state GGA-PBE functional calculations. The calculated pDOS show three non-equivalent N sites (N1, N2, and N3), three non-equivalent Be sites (Be1, Be2, and Be3), and one Ba/Sr site. N p -states contribute mainly to the VB with weak admixture of Be s - and p -states

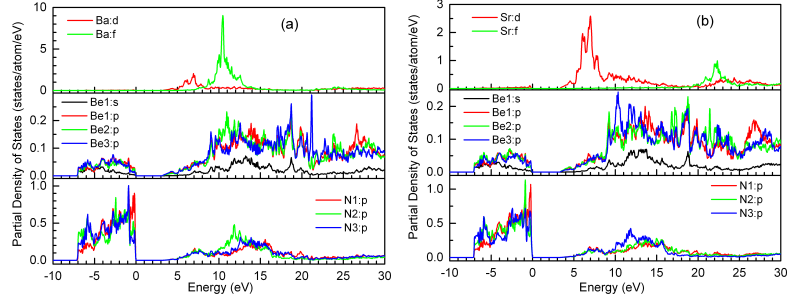


Figure 6.3: The partial density of states for $\text{BaBe}_{20}\text{N}_{14}$ in (a) and for $\text{SrBe}_{20}\text{N}_{14}$ in (b) using GGA-PBE functional. The energy of zero is the Fermi level.

in the lower VB and Ba/Sr d -states in the upper VB. The contribution from the two non-equivalent N1 and N2 p -states are almost identical in the VB but the non-equivalent p -states for N3 are different, particularly in the lower VB. This indicates that not only covalent bonding with the N sites is present, but also some degree of sp -hybridization in Be, as well as pd -hybridization in Ba/Sr. The Ba d -states contribute to the lower CB and Ba f -states contribute to the middle and upper CB for $M = \text{Ba}$. In addition there is a weak mixing of all three non-equivalent Be p -states and N p -states in the middle of the CB for both compounds. The Sr d -states dominate the lower and middle CB, and the Sr f -states contribute to the middle and upper CB for $M = \text{Sr}$. It is common that the alkaline earth ion d -states contribute heavily to the lower CB due to their empty d -states [42, 43].

The contributions of all elements in the VB and the CB suggest a rigid lattice with covalent bonding. Strongly covalent bonded materials are favourable for visible emissions but also should feature a smaller Eu-N distance and consequently higher crystal field splitting, when doped with Eu^{2+} ions [34]. In general, the M -N ($M = \text{Sr}, \text{Ba}$) distances increase with increasing ionic radius, therefore, the expected Sr-N separation would be smaller than the Ba-N separation. A reduction of the bond length will increase the bond-antibond splitting, which in general varies proportionally to the square of the bond length [212]. The increasing covalency of the Sr-N bond drives the hybridization between Sr d -states and N p -states, increasing the energy of the

unoccupied Sr *d*-states [36]. The authors in ref. [209] reported that the bond length of Ba-N is larger by about 0.02% than the bond length of Sr-N. Due to the small increase in covalency of the Sr-N bond, the calculated band gap is found to be 0.2 eV larger.

6.3.4 Band Structure and RIXS Spectra

Figure 6.4 shows the band structures of $M\text{Be}_{20}\text{N}_{14}$ ($M = \text{Sr}, \text{Ba}$) calculated using the mBJ exchange-correlation potential. The band structures of both compounds are almost identical. The upper valence bands are mainly derived from the N *p*-states, while the lower conduction bands are dominated by the *d*-states of Sr/Ba. The VB maximum is located at Γ of the Brillouin zone, while the CB minimum is located at the Z-point. As the two points are not at the same crystal momentum, an indirect band gap of 4.4 eV for $M = \text{Ba}$ and 4.6 eV for $M = \text{Sr}$ is realized. The energy scale is set with respect to the Fermi energy, E_F . The authors in ref. [209] also predict an indirect band gap for these compounds. It is also noted that the lower lying CB has a large curvature and therefore should have relatively high electron mobility [212]. Sr, Ba and Be all have valence electron configurations of s^2 , and N has an s^2p^3 electron configuration. In a crystallographic unit cell both $M\text{Be}_{20}\text{N}_{14}$ ($M = \text{Sr}, \text{Ba}$) compounds contain two formula units [209]. Therefore, the total number of valence electrons in a unit cell is 224 for each compound. Due to the spin degeneracy, the total number of energy bands within VB would be 112 for each material. However, only 42 available bands are found in Figure 6.4 for each compound, which is fewer than expected, due to the energy degeneracy of the bands and some bands appearing well below the Fermi level.

RIXS spectra can also be used to experimentally determine the type of band gap [78, 203]. Previous reports indicate that for direct band gap materials, the RIXS spectrum containing higher emission energy is obtained at lower excitation energy, while for an

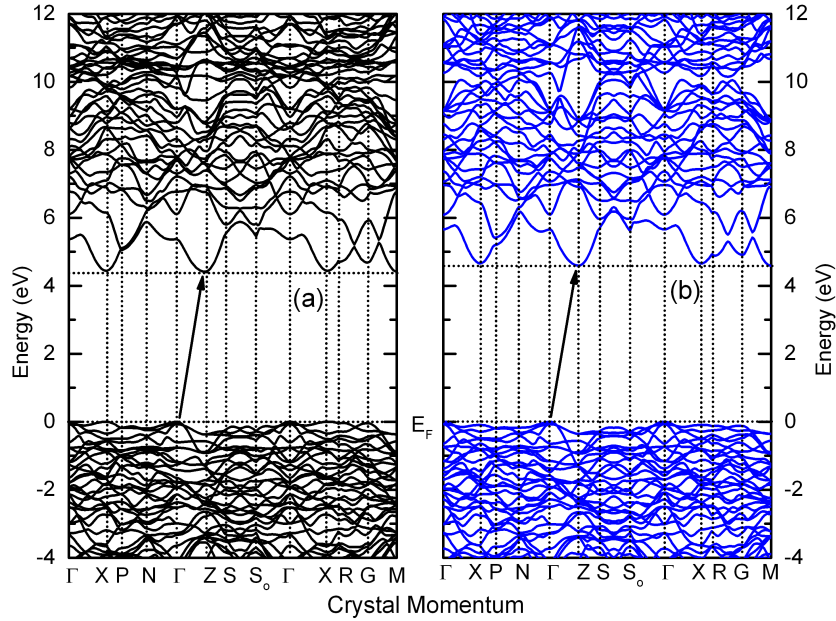


Figure 6.4: Calculated band structure of BaBe₂₀N₁₄ in (a) and SrBe₂₀N₁₄ in (b) based on ground state mBJ functional calculations. For both samples, the conduction minimum and valence band maximum are at the Z point and Γ point, respectively. The energy scales are set with respect to the Fermi energy, E_F .

indirect band gap material, slightly higher emission energy is obtained at higher excitation energy [78, 203]. This is due to the negligible momentum that soft X-ray photons carry. The conservation of momentum requires that transitions into the CB and from the VB due to the same initial exciting photon occur at the same k-vector or momentum in the band diagram. Here RIXS spectra excited at 398.1 eV and 399.0 eV are used to determine the type of the band gap. The vertical dotted-dashed line in the XES spectra of Figure 6.2(a) indicates that the maximum emission energy increases slightly as the excitation energy is increased from 398.1 eV to 399.0 eV, which is indicative of an indirect band gap.

6.3.5 Determination of Eu²⁺ 4f⁶5d¹ Energy Levels

The determination of the Eu²⁺ energy levels of phosphors provide the needed experimental basis for a deeper understanding of all the radiative processes involved, that are critical for tailoring the luminescence properties of phosphors. The nephelaux-

etic effect and CFS influence the position of the $4f^65d^1$ states, as described in the introduction section. Very recently Tolhurst *et al.* [37] connected the position of the $4f^65d^1$ states with respect to the CB onset of the host material by acquisition of RIXS data for several phosphors. Here, we use the RIXS technique to determine the $4f^65d^1$ energy levels of Eu^{2+} for $M\text{Be}_{20}\text{N}_{14}:\text{Eu}^{2+}$ ($M = \text{Sr}, \text{Ba}$) compounds. Figure 6.5(a) shows the RIXS spectra of $M\text{Be}_{20}\text{N}_{14}:\text{Eu}^{2+}$ ($M = \text{Sr}, \text{Ba}$) excited at the CB onset (398.1 eV). The authors in ref. [76] reported that the defect associated energy loss was the strongest for WO_3 from the O K-edge RIXS, when the excitation energy is at the CB band onset. Figure 6.5(a) shows that the relative peak intensity for $\text{SrBe}_{20}\text{N}_{14}:\text{Eu}^{2+}$ compound is higher than $\text{BaBe}_{20}\text{N}_{14}:\text{Eu}^{2+}$. This peak intensity depends on the N- Eu^{2+} orbital overlap and thus the distances between the Eu^{2+} ions and the ligand N atoms. As we mentioned earlier, the Sr-N distance is smaller than the Ba-N, resulting in more N- Eu^{2+} orbitals overlap for $\text{SrBe}_{20}\text{N}_{14}:\text{Eu}^{2+}$ [37]. The spectra are shown in Figure 6.5(a) on an energy loss scale, which is obtained by subtracting the excitation energy of 398.1 eV from the emission energy. As a result the elastically scattered radiation appears at 0 eV and other energy loss features are located at lower energies. Due to the low cross section for the $4f^65d^1$ to CB inelastic scattering and the low Eu^{2+} concentration (2%), the loss feature is weak and only revealed when the elastic peak is fitted with two Gaussians. Figure 6.5(a) shows that two Gaussians are needed to fit the experimental feature for $M\text{Be}_{20}\text{N}_{14}:\text{Eu}^{2+}$ ($M = \text{Sr}, \text{Ba}$) phosphors. The blue Gaussian corresponds to the elastic peak and the additional black Gaussian just below the elastic scattering peak represents energy losses of the incident X-rays to low-energy excitations [77]. This energy loss is due to the excitation of Eu^{2+} $4f^65d^1$ electrons to the CB [37, 65, 73]. As we discussed in the partial density of state section, the CB minimum originates from the Ba/Sr d states. Thus the Eu^{2+} $4f^65d^1$ to CB transition is effectively a Eu^{2+} $4f^65d^1 \rightarrow nd$ ($n = 4$ for Sr and $n = 5$ for Ba) transition. The Eu^{2+} $4f^65d^1$ to the CB separation is determined using $\Delta E_{\text{RIXS}} = E_e - E_i$, where E_e is the elastic scattering peak position and E_i is

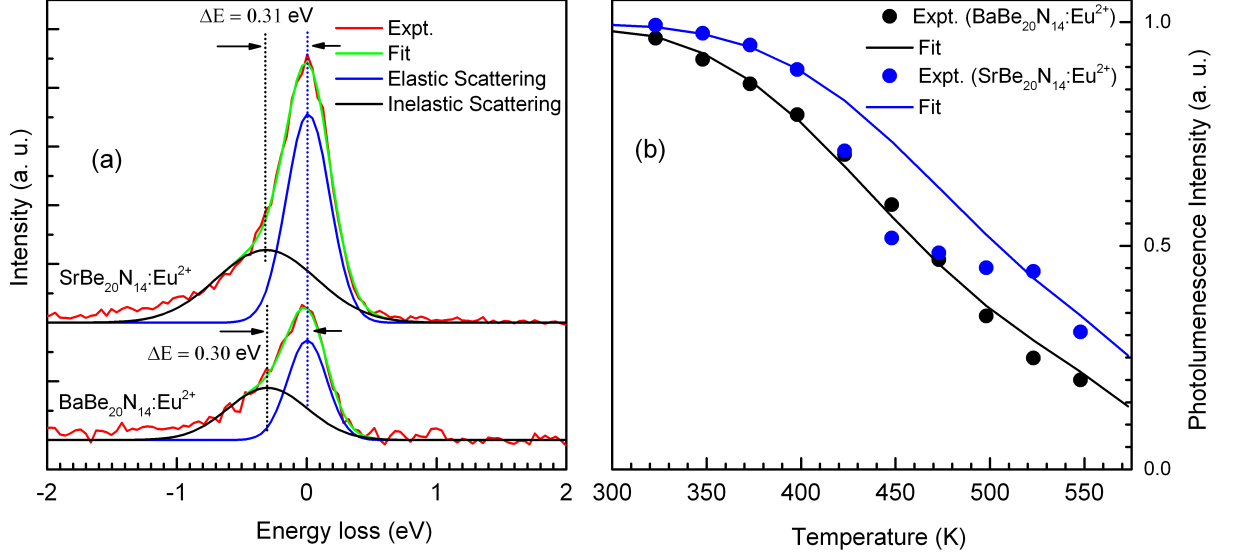


Figure 6.5: (a) RIXS spectra for $M\text{Be}_{20}\text{N}_{14}:\text{Eu}^{2+}$ ($M = \text{Sr}, \text{Ba}$) excited at the CB onset (398.1 eV). Two Gaussians (blue: elastic scattering at 0 eV and black: inelastic scattering at -0.30 eV for $M = \text{Ba}$ and at -0.31 eV for $M = \text{Sr}$) are used to fit the experimental spectrum (red). (b) Measured luminescence of $4f^65d^1 \rightarrow 4f^7$ transition of Eu^{2+} as a function of temperature for $M\text{Be}_{20}\text{N}_{14}:\text{Eu}^{2+}$ ($M = \text{Sr}$ (blue), Ba (black)) along with the fit (solid line) using Equation 6.1 to the measured data. Temperature-dependent data are published in ref. [209].

the inelastic scattering peak position. For $\text{BaBe}_{20}\text{N}_{14}:\text{Eu}^{2+}$ and $\text{SrBe}_{20}\text{N}_{14}:\text{Eu}^{2+}$, the $\text{Eu}^{2+} 5d$ to the CB separation is found to be 0.30 ± 0.04 eV and 0.31 ± 0.04 eV, respectively and both can be found in Table 6.2. The fit parameters and uncertainties obtained from fitting are shown in Table 6.2 as well. These ΔE_{RIXS} values are similar to those found in literature, which can be found in Table 6.3.

Thermally stable luminescence materials are important for high power device applications. The luminescence of a phosphor generally decreases as a phosphor heats up since the increased thermal excitation of $\text{Eu}^{2+} 4f^65d^1$ electrons states to the CB reduces the available $4f^65d^1$ electrons, and hence the $4f^65d^1 \rightarrow 4f^7$ luminescence. The decrease in luminescence with increasing temperature is referred to as thermal quenching. A relatively large energy separation between the lowest $\text{Eu}^{2+} 4f^65d^1$ level and the bottom of the CB leads to better thermal stability of the luminescence. The

Table 6.2: Standard deviation for elastic peak (σ_1) and inelastic peak (σ_2) from the fits shown in Figure 6.5(a), and the Eu^{2+} $5d$ to CB energy separations from RIXS measurements (ΔE_{RIXS}) and from TQ measurements (ΔE_{TQ}). Fitting parameter ($\frac{\Gamma_o}{\Gamma_v}$) of Eq. 6.1 is also included in this table.

Samples	σ_1 (eV)	σ_2 (eV)	ΔE_{RIXS} (eV)	ΔE_{TQ} (eV)	$\frac{\Gamma_o}{\Gamma_v}$
$\text{BaBe}_{20}\text{N}_{14}:\text{Eu}^{2+}$	0.214	0.312	0.30 ± 0.04	0.32 ± 0.03	2600
$\text{SrBe}_{20}\text{N}_{14}:\text{Eu}^{2+}$	0.217	0.327	0.31 ± 0.04	0.35 ± 0.03	3200

luminescence intensity of the $4f^6 5d^1 \rightarrow 4f^7$ transition of Eu^{2+} ions for $\text{SrBe}_{20}\text{N}_{14}:\text{Eu}^{2+}$ and $\text{BaBe}_{20}\text{N}_{14}:\text{Eu}^{2+}$ as a function of temperature is shown in Figure 6.5(b), along with a fitted curve. The experimental temperature-dependent luminescence data are fitted using the following equation to describe thermal quenching of the luminescence intensity $I(T)$ with temperature T [64, 65]:

$$I(T) = \frac{I_o}{1 + \frac{\Gamma_o}{\Gamma_v} e^{-\frac{\Delta E}{k_B T}}}, \quad (6.1)$$

where I_o is the initial luminescence intensity at room temperature (25 °C), Γ_v is the radiative decay rate of the $5d$ state of Eu^{2+} , Γ_o is the attempt rate for TQ process at $T = \infty$, k_B is the Boltzmann's constant, and ΔE is the energy barrier for thermal quenching between the lowest $5d$ level and the bottom of the CB. The pre-exponential factor, $\frac{\Gamma_o}{\Gamma_v}$, and the energy barrier for photoionization, ΔE , are called Arrhenius parameters, which are the variables in Equation 6.1 to fit the data. The Arrhenius equation (Equation 6.1) is commonly used to describe the temperature dependence of processes like chemical reactions or electron transitions. The parameter $\frac{\Gamma_o}{\Gamma_v}$ determines how rapidly the decay occurs with temperature and the parameter ΔE determines at what temperature TQ starts to become significant [37]. From the fit, the calculated energy difference between the lowest $4f^6 5d^1$ excited state of Eu^{2+} ion and the bottom of CB (here, $\Delta E = \Delta E_{TQ}$) for $M = \text{Ba}$ is found to be 0.32 ± 0.03 eV and 0.35 ± 0.03 eV for $M = \text{Sr}$, which are included in Table 6.2. The $M\text{Be}_{20}\text{N}_{14}:\text{Eu}^{2+}$

Table 6.3: The available literature values of the bottom of the CB and the lowest $4f^65d^1$ states of Eu^{2+} -ions from the RIXS measurements (ΔE_{RIXS}) and from TQ measurements (ΔE_{TQ}).

Samples	ΔE_{RIXS} (eV)	ΔE_{TQ} (eV)
$\text{CaAlSiN}_3:\text{Eu}^{2+}$	-	0.56 [67]
$\text{Sr}[\text{LiAl}_3\text{N}_4]:\text{Eu}^{2+}$	0.2 ± 0.1 [37]	0.291 ± 0.009 [37]
$\text{Li}_2\text{Ca}_2[\text{Mg}_2\text{Si}_2\text{N}_6]:\text{Eu}^{2+}$	0.46 ± 0.03 [37]	0.49 ± 0.03 [37]
$\text{Ba}[\text{Li}_2(\text{Al}_2\text{Si}_2)\text{N}_6]:\text{Eu}^{2+}$	0.37 ± 0.03 [37]	0.253 ± 0.008 [37]
$\text{BaLi}_2[\text{Be}_4\text{O}_6]:\text{Eu}^{2+}$	0.21 ± 0.1 [65]	0.20 ± 0.03 [65]
$\text{SrLi}_2[\text{Be}_4\text{O}_6]:\text{Eu}^{2+}$	0.25 ± 0.1 [65]	0.26 ± 0.03 [65]
$\text{Sr}[\text{Be}_6\text{ON}_4]:\text{Eu}^{2+}$	0.26 ± 0.001 [73]	-

($M = \text{Sr}, \text{Ba}$) exhibit relatively large values of ΔE_{TQ} , indicating similar or even greater thermal stability of the nitridoberyllates $M\text{Be}_{20}\text{N}_{14}:\text{Eu}^{2+}$ ($M = \text{Sr}, \text{Ba}$) in comparison to available values from literature (Table 6.3)

6.3.6 Determination of Eu^{2+} $4f^7$ Energy Levels from Luminescence Spectra

The Eu^{2+} $5d$ are basically band-like states and as such are strongly affected by the electronic structure of the host lattice. This is advantageous since it allows the Eu^{2+} luminescence to be tuned to the desired wavelength. The width of the emission band is influenced by different factors such as the symmetry of the activator site, the homogeneity of activator coordination site, the ordering and the rigidity of the host lattice, the degree of condensation, and the distance of activator sites [206]. Eu^{2+} sites, which are surrounded by ligands with different activator-ligand distances lead to an inhomogeneous broadening. The same effect applies for structure disordering, for example if the tetrahedra centers are mixed occupied by two different metals. This effect can be reduced by providing only one (or multiple, but very similar) highly symmetrical co-

ordination site and an ordered network for the activator atom, which would result in narrow-band emission for example $\text{Sr}[\text{LiAl}_3\text{N}_4]:\text{Eu}^{2+}$ [27] or $\text{Sr}[\text{Li}_2\text{Al}_2\text{O}_2\text{N}_2]:\text{Eu}^{2+}$ [85]. Further band broadening can be caused by geometrical relaxation of the network, as the distances between the activator and ligand can change throughout the activation process. Also the coordination site can be slightly larger or smaller than the Eu^{2+} ion, for example, when Eu^{2+} is doped on a site, which is usually occupied by a Sr^{2+} or a Ba^{2+} . Structural relaxation can be expected when such a site will be occupied by an activator ion, which has a different ionic size than the initial ion. A highly condensed and rigid framework can limit such geometrical relaxations [206]. In addition, energy transfer can take place between multiple activators, if the activator sites have a small distance to the next neighbor and the activator concentration is high, leading to further band broadening [206]. In contrast to Eu^{2+} , the luminescence in Eu^{3+} doped phosphors arise from an $f-f$ transition. Sharp line emission is usually observed for these phosphors, since the $4f$ electrons are effectively shielded by the surrounding completely filled $5s$ and $5p$ orbitals. Therefore $f-f$ transitions are very localized and atomic-like giving rise to narrow atomic-like transitions that are relatively independent of any surrounding host matrix [213].

The XEOL is an X-ray photon-in optical photon-out process. This technique probes optical transitions, electronic structure, presence of defects, and overall luminescence properties of phosphors[37, 162, 163]. Here we use XEOL spectra to understand the luminescence processes for $M\text{Be}_{20}\text{N}_{14}:\text{Eu}^{2+}$ ($M = \text{Sr}, \text{Ba}$) and identify the energetic position of the $4f^7$ ground state of Eu^{2+} ion in $M\text{Be}_{20}\text{N}_{14}:\text{Eu}^{2+}$. Figure 6.6 shows the luminescence of the investigated phosphors excited at 100 eV. The $M\text{Be}_{20}\text{N}_{14}:\text{Eu}^{2+}$ ($M = \text{Sr}, \text{Ba}$) shows two emission bands, located at 427 nm (full width at half maximum ($fwhm$) = 22 nm) and at 532 nm for Ba and 430 nm ($fwhm = 22$ nm) and 548 nm for Sr. The remarkably narrow emission band in the blue region of the visible spectrum can be assigned to the $4f^65d^1 \rightarrow 4f^7$ transition of Eu^{2+} and makes $M\text{Be}_{20}\text{N}_{14}:\text{Eu}^{2+}$

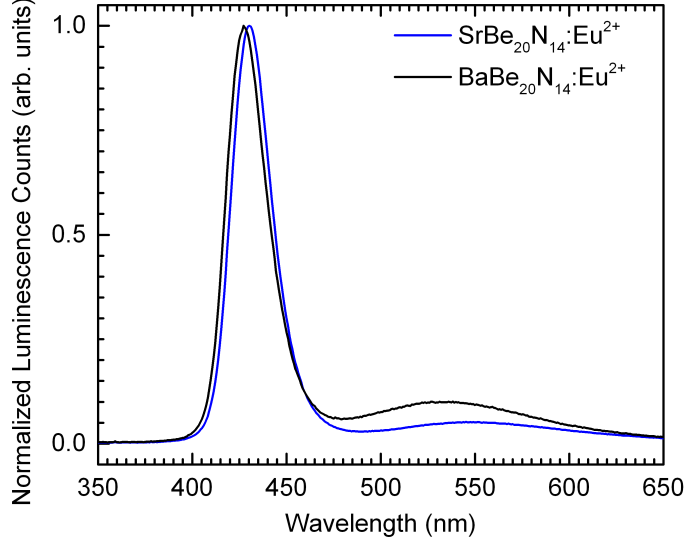


Figure 6.6: X-ray excited optical luminescence spectra of $M\text{Be}_{20}\text{N}_{14}:\text{Eu}^{2+}$ ($M = \text{Ba}$ (black), Sr (blue)) excited at 100 eV. Both compounds exhibit a remarkably narrow emission in the blue spectral region and a broader red-shifted emission band in the green spectral region.

($M = \text{Sr}, \text{Ba}$) a promising narrow-band blue-emitting phosphor. The small *fwhm* is due to the symmetrical coordination of the Sr/Ba-site and the highly condensed network of $M\text{Be}_{20}\text{N}_{14}$. When Eu^{2+} ions are doped into the $M\text{Be}_{20}\text{N}_{14}$ ($M = \text{Sr}, \text{Ba}$), the energy gap between the $4f^65d^1$ level and the $4f^7$ level decreased due to the nephelauxetic effect and the crystal field splitting. Due to the nephelauxetic effect the $4f^65d^1$ energy level of Eu^{2+} shifts toward the $4f^7$ energy level relative to the free Eu^{2+} and the shift is larger for more covalent bonds. This is because of the reduction of the interelectron repulsion, which in turn is ascribed to the sharing of electrons between the Eu^{2+} and the surrounded N^{3-} . The outermost electrons of Eu^{2+} lies in the $5d$ state, their energies are strongly influenced by the coordination environment of the $M\text{Be}_{20}\text{N}_{14}$ ($M = \text{Sr}, \text{Ba}$) leading to the crystal field splitting of the Eu^{2+} d -orbitals. The blue emitting color of these phosphors originates from the weak crystal field splitting and a small nephelauxetic effect, which arises from the large coordination number, the highly condensed host (reducing the covalency between Eu and N) and weak interaction between the N^{3-} and Eu^{2+} ions (large Eu-N distances),

which stems from the high degree of condensation of the BeN_4 tetrahedra as shown in Figure 6.1. The broader red-shifted emission band in the green spectral region is due to the anomalous Eu^{2+} trapped exciton, which is observed when the Eu^{2+} ion is incorporated at sites with large coordination number and large Eu^{2+} -ligand bond lengths [54]. The anomalous Eu^{2+} trapped exciton is described as a state in which the Eu^{2+} ion is ionized to Eu^{3+} and the electron is stabilized in the vicinity by delocalization over the neighboring cations [54, 214, 215]. If the crystal field splitting for the $4f^65d^1$ state is small (e.g., due to a high coordination number) the anomalous Eu^{2+} trapped exciton state can be situated below the $4f^65d^1$ state and anomalous Eu^{2+} trapped exciton emission occurs. The autoionization of the $4f^65d^1$ state leads to the formation of trapped excitons at the Eu^{2+} sites, and the anomalous emission is due to the annihilation of the trapped exciton [54, 216]. It is also observed that the probability of anomalous Eu^{2+} trapped excitons is higher for the $M = \text{Ba}$ compound than the $M = \text{Sr}$, which is expected due to the larger cation sizes of Ba than Sr [54, 212]. The authors in ref. [209] also reported the same luminescence behaviour for $M\text{Be}_{20}\text{N}_{14}:\text{Eu}^{2+}$ using photoluminescence measurements.

6.4 CONCLUSIONS

We study two new exotic phosphors $M\text{Be}_{20}\text{N}_{14}:\text{Eu}^{2+}$ ($M = \text{Sr}, \text{Ba}$) and determine all participating energy levels of Eu^{2+} ions ($4f^65d^1$ and $4f^7$ states), VB, CB, and band gaps. The calculated pDOS for $M\text{Be}_{20}\text{N}_{14}$ ($M = \text{Ba}, \text{Sr}$) show contributions of all elements in the VB and the CB, suggesting a rigid lattice. The doped Eu^{2+} ions are assumed to occupy the Sr/Ba sites due to the same charge and similar ionic radii. For that reason the interaction between the Eu^{2+} ions and its surrounding would be through covalent bonding. The indirect band gap is experimentally determined to be 4.4 ± 0.3 eV for both compounds, which is in good agreement with our calculations, applying the mBJ exchange-correlation potential (4.4 eV for $M = \text{Ba}$ and 4.6 eV for $M = \text{Sr}$). A large band gap is a prerequisite for the $\text{Eu}^{2+} 4f^65d^1 \rightarrow 4f^7$ luminescence

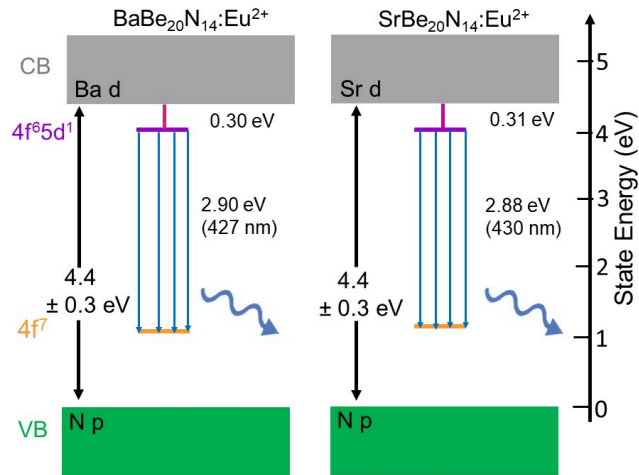


Figure 6.7: Energy levels of $M\text{Be}_{20}\text{N}_{14}:\text{Eu}^{2+}$ ($M = \text{Sr}, \text{Ba}$). The band gap is added from our XAS and NXES measurements. Our DFT calculations show that the CB minimum is dominated by d -states of Ba/Sr and the VB maximum originates from N p -states, which are added accordingly. The energy separation (0.30 eV for $M = \text{Ba}$ and 0.31 eV for $M = \text{Sr}$) between bottom of the CB and lowest level of $4f^6 5d^1$ -states (vertical pink line) is determined from RIXS measurements. The energy level of $4f^7$ is obtained from the $4f^6 5d^1 \rightarrow 4f^7$ transition (origin of blue luminescence) measured by XEOL.

radiation to leave the crystal. The crucial energetic position of the excited $4f^65d^1$ states of Eu^{2+} with respect to the CB onset of the host lattice is determined directly from RIXS measurements. The energy separation between the lowest $4f^65d^1$ states of Eu^{2+} ions and the bottom of the CB is found to be 0.30 ± 0.04 eV and 0.31 ± 0.04 eV for $\text{BaBe}_{20}\text{N}_{14}:\text{Eu}^{2+}$ and $\text{SrBe}_{20}\text{N}_{14}:\text{Eu}^{2+}$, respectively, which agree well with the values obtained from complimentary thermal quenching measurements. These relatively large energy separation values give rise to the excellent thermal stability of luminescence. The XEOL measurements show two luminescence peaks. The first peak is located at 427 nm for $M = \text{Ba}$ (430 nm for $M = \text{Sr}$) and the second peak is at 534 nm for $M = \text{Ba}$ (550 nm for $M = \text{Sr}$). The narrow blue emission band is due to the $\text{Eu}^{2+} 4f^65d^1 \rightarrow 4f^7$ transition, and the broader and less intense red-shifted emission band in the green region is due to the anomalous Eu^{2+} trapped exciton emission. The blue color of these nitrides originate from the highly condensed host lattice (reducing the covalency between Eu and N), long Eu-N distances and a weak CFS. From the calculations and the measurements, a schematic illustration summarizing all pertinent energy levels and all involved transition processes of $M\text{Be}_{20}\text{N}_{14}:\text{Eu}^{2+}$ ($M = \text{Sr}, \text{Ba}$) is presented in Figure 6.7. The energy separation between the lowest $4f^65d^1$ states of Eu^{2+} ions and the bottom of the CB gives the $4f^65d^1$ energy level with respect to Sr/Ba d states of the CB. The $4f^7$ energy level is determined from the $4f^65d^1 \rightarrow 4f^7$ transition of Eu^{2+} ions with respect to the $4f^65d^1$ states. Thus our study shows the applicability and power of RIXS and XEOL techniques for understanding and measuring important properties of phosphors. Recently, the search for efficient narrow-band emitting phosphors has extended research to compounds containing the element beryllium as a network builder. The highly condensed nitridoberyllates $M\text{Be}_{20}\text{N}_{14}:\text{Eu}^{2+}$ ($M = \text{Sr}, \text{Ba}$), recently discovered in this context, not only show high thermal stability but also promising narrow-band blue emission. Our study of these phosphors should broaden and deepen the understanding of the electronic properties of this new compound class and contribute in the ongoing investigation for efficient narrow-band emitting

phosphors.

AUTHOR INFORMATION

Corresponding Author

*E-mail: mua083@mail.usask.ca

ORCID

M. Ruhul Amin: 0000-0002-1289-4713

Alexander Moewes: 0000-0002-9218-2280

Wolfgang Schnick: 0000-0003-4571-8035

Notes

The authors declare no competing financial interest.

Acknowledgements

The experiments were performed at the Canadian Light Source, which is funded by the Canada Foundation for Innovation, the Natural Science and Engineering Research Council of Canada (NSERC), the National Research Council Canada, the Canadian Institutes of Health Research, the Government of Saskatchewan, Western Economic Diversification Canada, and the University of Saskatchewan. M.R.A. is grateful to the Government of Saskatchewan for financial support from the Saskatchewan Innovation and the Opportunity Scholarship. We acknowledge support from NSERC and the Canada Research Chair program. The authors also acknowledge Compute Canada. The calculations presented in this paper were performed on the Cedar high-performance computing cluster, which is part of the WestGrid (www.westgrid.ca) and Compute Canada Calcul Canada (www.computecanada.ca).

Chapter 7

Energy Levels of Eu^{2+} States in the Next-Generation LED-Phosphor $\text{SrLi}_2\text{Al}_2\text{O}_2\text{N}_2:\text{Eu}^{2+}$

Authors: Muhammad Ruhul Amin^a, Philipp Strobel^b, Wolfgang Schnick^c, Peter J. Schmidt^b, and Alexander Moewes^a

^aDepartment of Physics and Engineering Physics, University of Saskatchewan, 116 Science Place, Saskatoon, Saskatchewan , S7N 5E2, Canada

^bLumileds Phosphor Center Aachen Lumileds Germany GmbH Philipsstrasse 8, 52068 Aachen, Germany

^cDepartment of Chemistry, University of Munich (LMU), Butenandtstrasse, 5-13, 81377 Munich, Germany

Reference: Muhammad Ruhul Amin, Philipp Strobel, Wolfgang Schnick, Peter J. Schmidt, and Alexander Moewes, *Journal of Materials Chemistry C*, 2022, **10**, 9740–9747 [83].

Summary and Author Contributions

The authors in this manuscript present a study of the red-emitting phosphor $\text{SrLi}_2\text{Al}_2\text{O}_2\text{N}_2:\text{Eu}^{2+}$ and determine all pertinent energy levels such as the energetic position of Eu^{2+} ions ($4f^65d^1$ state and $4f^7$ state), valence band, conduction band, and

band gap. We utilize RIXS method and XEOL technique to directly determine the $\text{Eu}^{2+} 4f^6 5d^1$ to conduction band energy separation, which is the key parameter for any Eu-doped luminescence material. Here, both the N K- and the O K-edges RIXS measurements are applied and the energy separation between the $\text{Eu}^{2+} 4f^6 5d^1$ and CB is found to be 0.53 ± 0.04 eV and 0.48 ± 0.10 eV, respectively. The $4f^7$ energy level is determined from the $4f^6 5d^1 \rightarrow 4f^7$ transition of Eu^{2+} ions with respect to the $4f^6 5d^1$ states using XEOL techniques. The $4f^6 5d^1 \rightarrow 4f^7$ reveals the red emission band with FWHM of 51 at 610 nm, which is very promising for an application in white RGB phosphor LEDs [84]. Therefore, these experimental techniques allow direct access to the intragap states that are the source of the luminescence in Eu^{2+} -doped phosphors. To interpret the experimental data, we performed full density functional theory calculations. All measurements and calculations were performed by M. R. Amin under the supervision of A. Moewes. Manuscript preparation was performed by M. R. Amin. This manuscript has been published in *Journal of Materials Chemistry C* [83].

Abstract

Understanding electronic structure properties of narrow-band emitting phosphor materials is important for finding and tailoring novel materials for fabrication of phosphor converted (pc)-LEDs. Thereby, illumination quality can be improved while further reduction in worldwide energy consumption is achieved. In pc-LEDs, the energetic position of the $\text{Eu}^{2+} 5d^1$ states with respect to conduction band and valence band of the host lattice determines the electronic structure and the optical properties, such as thermal quenching and quantum efficiency under application conditions. Here, we experimentally determine the energetic position of $\text{Eu}^{2+} 5d^1$ state for the narrow-band red emitting phosphor $\text{SrLi}_2\text{Al}_2\text{O}_2\text{N}_2:\text{Eu}^{2+}$ (SALON) employing resonant inelastic X-ray scattering (RIXS) measurements. The position of the $5d^1$ energy level of the dopant Eu^{2+} is determined directly from RIXS measurements at the N K- and O

K-edges and is found to be 0.53 ± 0.04 eV (N K-edge) and 0.48 ± 0.10 eV (O K-edge) below the conduction band. We further use X-ray excited optical luminescence measurements to provide a deeper understanding of the energy levels and radiative processes involved in SALON, as the method allows to determine the $4f^7$ energy levels thus confirming the narrow-band luminescence in the red spectral region at 610 nm due to the $4f^6 5d^1 \rightarrow 4f^7$ transition.

7.1 Introduction

Phosphor-converted white light emitting diodes (pc-WLEDs) are efficient light sources for applications in lighting, backlight sources for liquid crystal displays and electronic devices. The discovery of the nitridolithoaluminate $\text{Sr}[\text{LiAl}_3\text{N}_4]:\text{Eu}^{2+}$ (SLA) stirred unprecedented interest in the pc-LEDs community [27, 42]. Due to its efficient and narrow emission band in the red spectral region, it quickly became a benchmark phosphor in solid-state lighting. Meanwhile, other luminescent materials have been investigated, some of which show related crystal structures to SLA, but these do not exhibit the same exceptional properties in terms of emission band width and thermal quenching [36, 38–42, 217]. Therefore, in order to design new luminescent materials with outstanding properties and to enhance the luminescence properties of existing phosphors, a deeper understanding of the structure-property relationships is required. This ultimately allows to control the luminescence properties of modern phosphors by varying chemical and structural composition of their host lattices.

We previously developed a new method applying synchrotron radiation on luminescent materials to determine specific materials' properties of interest [37, 65, 66, 73]. Note that the initial luminescence state for Eu^{2+} is of $5d^1$ configuration and therefore an excited state. For this reason, determining the absolute energy levels position of the luminescence state relative to the host conduction band and valence band in phosphors has proven difficult [218, 219]. The intragap $4f^{n-1}5d^1 \rightarrow 4f^n$ luminescence

transition of the activator ions is responsible for the visible emission bands of these Eu^{2+} -doped phosphors. Unlike the highly localized $4f$ electrons, the energetic position of $5d^1$ of the activator ions strongly depends on the host material. It is governed by the nephelauxetic effect and the crystal field splitting (CFS) [34, 37]. The nephelauxetic effect influences the bonding characteristics between the central dopant ion and the anion ligands in the host lattice. This effect leads to a decrease in energy separation between ground state and excited state of the dopant with increasing covalent characteristic of the bond. The influence of the host lattice crystal field on the splitting of the energy of the d-orbitals depends on the nature of dopant ion (here Eu^{2+}), the arrangement, and the nature of the ligands around the dopant ion, as well as the coordination number of the dopant [34, 37]. Therefore, more covalent bonding interaction between dopant Eu^{2+} ion and the ligands, and a strong crystal field splitting of $5d^1$ configuration decreases the energy separation between the ground state ($5d^04f^7$) and the excited state ($5d^14f^6$), resulting in a red shift of the luminescence [34, 37]. For these reasons, highly polarizable anion host lattices, for instance nitrides and sulfides, reveal green-to-red emission shift [34, 37]. Dorenbos showed that thermal quenching of the luminescence materials also depends on the energy separation between the $5d^1$ level and the conduction band minimum of the host material [64]. With increasing temperature, the $5d^1$ electrons can be thermally promoted to the conduction band and these electrons are lost for the luminescence process hence reducing the light output [64]. Therefore, the large energy separation between Eu^{2+} $5d^1$ levels and the conduction band onset results in less luminescence quenching.

In the case of SLA, the Eu^{2+} ion is surrounded by a network of condensed AlN_4 and LiN_4 tetrahedra [27, 42]. Due to the highly polarizable nitridic environment, a large crystal field splitting and a strong nephelauxetic effect are present in this material. As a result, the energy difference between the ground $4f^7$ state and the excited $5d^14f^6$ state is small, leading to the red emission band at 650 nm with full width at

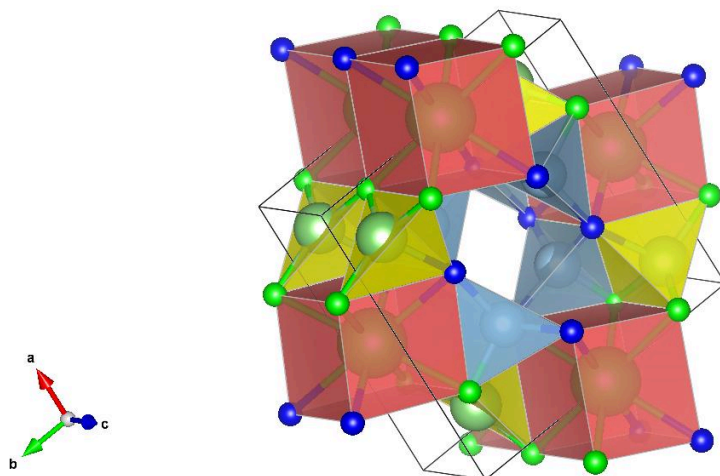


Figure 7.1: Crystal structure of $\text{SrLi}_2\text{Al}_2\text{O}_2\text{N}_2:\text{Eu}^{2+}$. The $[\text{LiO}_3\text{N}]^{8-}$ tetrahedra are presented in green, $[\text{AlON}_3]^{8-}$ tetrahedra in yellow and brown the highly symmetrical cuboid-like polyhedron coordination represents the environment of Sr^{2+} .

half-maximum (FWHM) of 50 nm [27, 42]. However, the wavelength range of the most demanding narrow band emission for a high-performance red phosphor is at shorter wavelength, shifted toward 620 to 630 nm. To achieve a narrow red emission band, the $\text{SrLi}_2\text{Al}_2\text{O}_2\text{N}_2:\text{Eu}^{2+}$ (SALON) compound was synthesized according to the powder sample synthesis published by Hoerder *et al.*, upon optimization to obtain a phase pure powder sample [85]. The latter is based on the crystal structure of SLA, with an adjusted ratio of oxygen (blue spheres) and nitrogen (green spheres) of 1:1, shown in Fig. 7.1. Contrary, only nitrogen atoms are present in the case of SLA [85]. As nitride N^{3-} has a smaller electronegativity, larger formal charge, and higher polarizability than oxide O^{2-} , the metal-N bonds in nitride compounds are usually more covalent than the corresponding metal-O ones. This differing behavior gives rise to larger nephelauxetic effect and stronger CFS acting on rare earth activators (i.e. Eu^{2+}) [85]. This finally results in the lowering of the $5d^1$ energy levels and thus of excitation and emission energies. Since SALON shows some of the nitride structural behavior and some of the oxide structural behavior, SALON exhibits a red

emission band at 610 nm with FWHM of 51 nm because of a smaller nephelauxetic effect and a lower CFS compared to SLA due to the presence of oxygen atoms in the Eu^{2+} coordination [85].

Most of the important properties of luminescence materials such as thermal quenching and quantum efficiency under application conditions depend on the energetic position of Eu^{2+} ions. However, direct measurements of the Eu^{2+} state energies are completely lacking, as only few are accessible through standard optical spectroscopy experiments. As stressed above, this is complicated by the fact that the $\text{Eu}^{2+} 5d^1$ state is an excited state and therefore is not accessible by standard methods. X-ray spectroscopy techniques allow the measurement of these states energies and therefore are a powerful complement to optical studies. Here, we utilize resonant inelastic X-ray scattering (RIXS) [37, 65, 66, 73] and X-ray excited optical luminescence (XEOL) [74, 75] to directly measure the energetic position of Eu^{2+} states particularly the $\text{Eu}^{2+} 5d^1$ state with respect to the conduction band (CB) and $4f^7$ ground state of Eu^{2+} with respect to the $\text{Eu}^{2+} 5d^1$ state for SALON. These experimental techniques allow direct access to the intragap states that are the source of the luminescence of Eu^{2+} -doped phosphors. These measurements lead to a complete and comprehensive understanding of radiative processes and result in a full energy diagram of all energy levels involved in the luminescence of SALON.

7.2 Experimental Techniques and Calculations Method

7.2.1 XAS, XES and XEOL Measurements

Soft X-ray absorption spectroscopy (XAS) and X-ray emission spectroscopy (XES) techniques are employed to probe the unoccupied and occupied partial density of states respectively, and X-ray excited optical luminescence (XEOL) measurements are used to characterize the optical transitions. The REIXS beamline [87] was used

to explore XAS and XES measurements and the VLS-PGM beamline [88] was used to record XEOL measurements, both at the Canadian Light Source. The absorption was measured in the bulk sensitive partial fluorescence yield mode (PFY), using silicon drift X-ray fluorescence detectors. 8000 and 2000 are the resolving powers, $E/\Delta E$, for the monochromator and the emission spectrometer at REIXS, respectively, corresponding to an energy resolution ΔE of 0.05 eV (0.06 eV) and 0.2 eV (0.25 eV) at the N (O) K-edge for XAS and XES, respectively. An ocean optics QE 65000 fast CCD spectrophotometer is used to collect the XEOL data [168]. The measured XAS spectra were calibrated using reference samples (the hexagonal boron nitride peak at 402.1 eV for the N K-edge and the bismuth germanium oxide peak at 532.7 eV for the O K-edge). The XES spectra were calibrated using elastic scattering features [82].

7.2.2 Density Functional Theory Calculations Details

Density functional theory (DFT) is a quantum mechanical modelling method to investigate many material properties. The commercially available WIEN2k software package was employed for the DFT calculations [126, 173]. This software code uses Kohn-Sham methodology with spherical wave functions to model core orbitals [126, 173]. The input for the calculations is the crystal structure (and space group). We used the experimentally determined crystal structures for $\text{SrLi}_2\text{Al}_2\text{O}_2\text{N}_2$ as determined by X-ray diffraction method. We employed the Perdew-Burke-Ernzerhof variant of the generalized gradient approximation (PBE-GGA) for the exchange-correlation functional [174]. The PBE-GGA functional often underestimates the band gap significantly but can compute soft X-ray spectra well. To obtain accurate band gaps, we relied on the PBE-GGA functional in the conjunction of the modified Becke-Johnson (mBJ) exchange potential [123]. The calculated XAS and XES spectra were computed by multiplying the calculated partial density of states (pDOS), the dipole transition matrix and the radial transition matrix [175] and were broadened using the Voigt profile to resemble the experimental spectra accounting for instrumental and lifetime

broadening [176]. The experimental N/O K-edge XAS and XES spectra depend on the final state, and the absorption final state has a core-hole in the N/O 1s level [177, 178]. To account for this core hole effect, a calculation was performed by including a single core hole at the N/O-atom inside a $2 \times 1 \times 1$ supercell of the unit cell of $\text{SrLi}_2\text{Al}_2\text{O}_2\text{N}_2$, where a background charge was added to the supercell lattice to preserve charge neutrality.

7.3 Results and Discussion

7.3.1 N K-edge XAS and XES spectra

We discuss the comparison of experimental and calculated XAS and XES spectra for SALON (0.7 % Eu^{2+}) first. Figure 7.2 shows the N K_α XES and 1s XAS spectra for SALON alongside the DFT-calculated spectra. The experimental absorption spectrum was collected in the bulk sensitive partial fluorescence yield (PFY) mode, shown in Fig. 7.2(b). There are five main peaks in the measured XAS spectrum, which are labeled I to V, and two-colored downward arrows (black and green) in the measured XAS spectrum indicating the excitation energies at which the XES spectra (Fig. 7.2(a)) were collected. The origin of the peaks is assigned using our calculated pDOS of the coordinating atoms, which is shown in Fig. 7.4(a). Our pDOS calculations show that the shoulders are due to excitations to the bands – I is the result of Sr states of d-symmetry (in atomic notation), peaks II to IV are due to Sr *d*-symmetry as well with small contributions from N *p*-states, O *p*-states and peak V stems predominantly from the Sr *f*-states. The experimental XAS spectrum is compared with the core hole (CH, solid magenta) and ground state (GS, solid orange) calculations. Comparing the experimental and calculated XAS spectra, we conclude that the overall agreement with the core hole spectrum is excellent. This agreement provides strong justification for the one electron picture employed in the calculations and the absence of electron correlation effects.

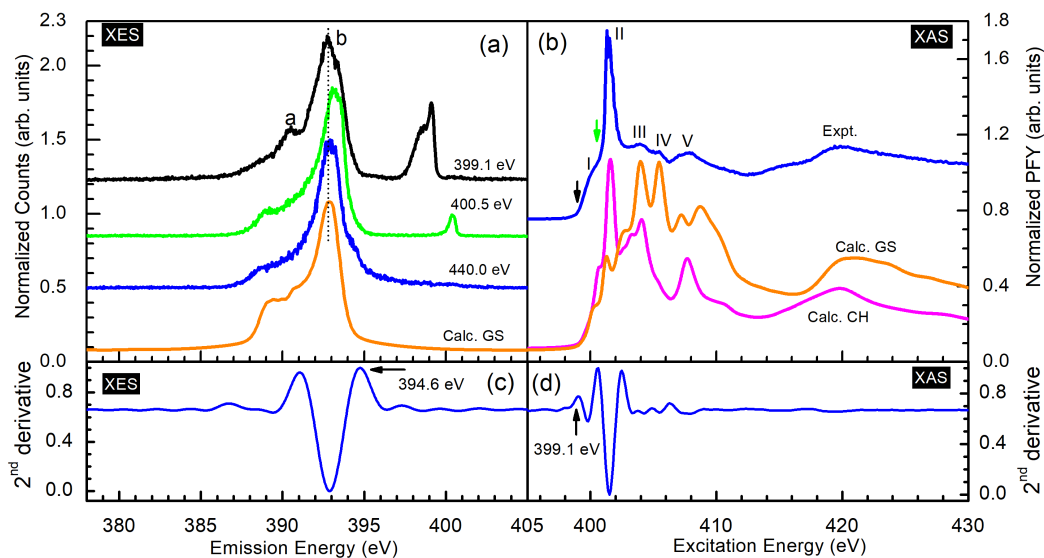


Figure 7.2: (a) Experimental and calculated N K-edge XES spectra of $\text{SrLi}_2\text{Al}_2\text{O}_2\text{N}_2:\text{Eu}^{2+}$ for different excitation energies. NXES spectrum excited at 440.0 eV (blue) and RIXS spectra collected at excitation energies of 399.1 eV (black) and 400.5 eV (green), which are compared to the ground state (GS) calculations. The vertical dotted black line indicates the highest emission energy observed at the highest excitation energy in the RIXS spectra. (b) Experimental PFY is compared to the core hole (CH) and the ground state (GS) calculations. Two colored downward arrows on the absorption spectrum indicate the corresponding excitation energies for the RIXS spectra. (c and d) Second derivative of experimental XES and XAS spectra with the corresponding peaks of valence band and conduction band onsets, respectively indicated by black arrows.

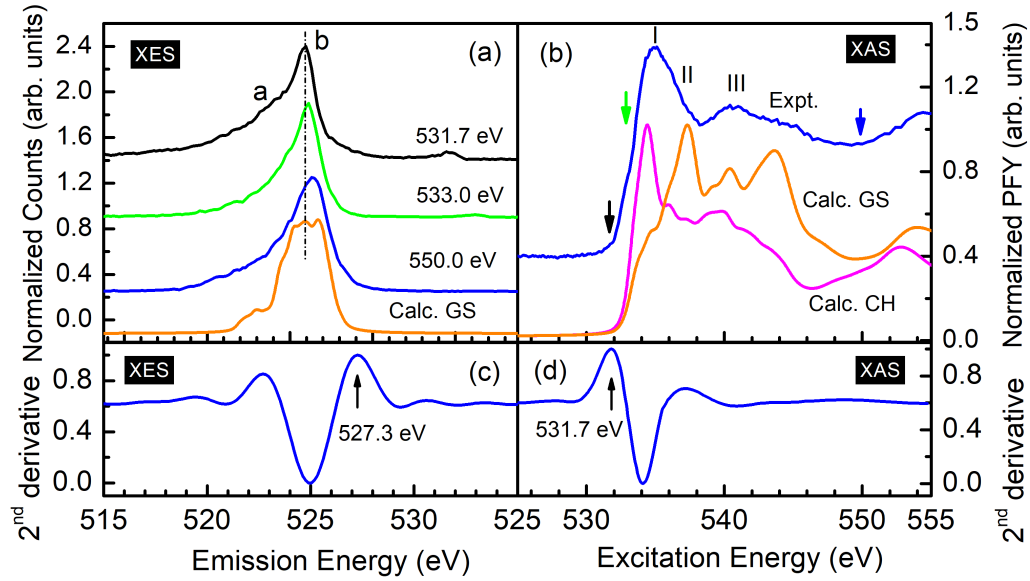


Figure 7.3: O K-edge XAS and XES spectra of $\text{SrLi}_2\text{Al}_2\text{O}_2\text{N}_2:\text{Eu}^{2+}$. The XES (a) and XAS (b) spectra are shown alongside DFT calculations. The calculated ground state (GS) and excited state (CH) XAS spectra are shown as solid gold and solid magenta, respectively. The vertical dotted magenta line in (a) is used to guide the eye in finding the highest emission energy among the RIXS spectra. The second derivatives of the experimental NXES spectrum excited at 550.0 eV and the XAS spectrum are shown in panel (c) and (d), respectively.

Having discussed the features of N K-edge XAS spectra of SALON, we now turn to the N K-edge XES spectra in Fig. 7.2(a). The XES spectra are again displayed for three different excitation energies, which are 399.1 eV, 400.5 eV and 440 eV. All XES spectra have two main peaks labeled as ‘a’ and ‘b’. The feature ‘a’ is due to the contribution of N $2p$ -states, O $2p$ -states and Al s -states and the peak ‘b’ is due to mostly N $2p$ -states, O $2p$ -states with a small admixture of Sr d -states. The calculated ground state XES spectrum (solid orange) agrees very well with the experiment.

7.3.2 O K-edge XAS and XES spectra

We are now turning to the discussion of the measured and calculated O K-edge spectra, which are presented in Fig. 7.3. Figure 7.3(b) shows that there are three distinct features located at I, II, and III in O K-edge XAS spectrum. Our pDOS calculations

show that the peaks at I and II are mostly due to Sr *d*-states, N *p*-states and O *p*-states and the peak located at III is due to the admixture of *p*-states of N and O and *f*-states of Sr. Again, the experimental XAS spectrum agrees well with the core hole calculations. The measured XES spectra with calculations are presented in Fig. 7.3(a). The calculated pDOS show that *p*-states of N and O and *s*-states of Al contribute to the peak at ‘a’ and Sr *d*-states, N and O *p*-states contribute to the broad peak at ‘b’. The measured XES spectra are also in good agreement with our calculations.

7.3.3 Band Gap Determination

The band gap of SALON was determined by combining the measured occupied and unoccupied pDOS on the same energy scale as shown in Fig. 7.2(a) and (b) for N K-edge and Fig. 7.3(a) and (b) for O K-edge, respectively. The band gap is determined from the energy difference between the top of the valence band (VB) probed by NXES and the bottom of the CB probed by XAS. The top of the VB and the bottom of the CB are determined from the first peaks in the second derivative above the noise at the upper edge of the NXES and the lower edge of the XAS spectra, respectively [37, 82]. The VB and the CB onsets are denoted with black arrows in Fig. 7.2(c) and (d) for N K-edge and Fig. 7.3(c) and (d) for O K-edge. From the band onsets, the estimated band gap is found to be 4.5 ± 0.3 eV from N K-edge spectra and 4.4 ± 0.3 eV from O K-edge spectra. The core hole shift was determined to be 0.1 eV for both cases by subtracting the CB energy location calculated without the core hole from the calculated CB energy location including the core hole. Therefore, the measured band gap is found to be 4.6 ± 0.3 eV from N K-edge spectra and 4.5 ± 0.3 eV from O K-edge spectra, which is displayed in Table 7.1. The experimental error associated with this band gap is evaluated by including the error in the experimental accuracy in energy of monochromator and spectrometer and the error in

Table 7.1: Measured, calculated, and previously reported band gap values for $\text{SrLi}_2\text{Al}_2\text{O}_2\text{N}_2:\text{Eu}^{2+}$. The measured band gap is denoted by $\Delta_{\text{expt.}}$ and the calculated band gap is denoted by Δ_{GGA} and Δ_{mBJ} for PBE-GGA and mBJ functional, respectively. The available literature band gap value is also denoted in the same way. All units are in eV.

$\Delta_{\text{expt.}}$	Δ_{GGA}	Δ_{mBJ}	Literature $\Delta_{\text{expt.}}$	Literature Δ_{mBJ}
4.6 ± 0.3 (N K)	3.5	4.9	4.3 [85]	4.9-5.3 [85]
4.5 ± 0.3 (O K)				

the energy calibration. The experimentally determined band gap was compared to the values obtained from DFT calculations. The calculated values are 3.5 eV using the PBE-GGA functional and 4.9 eV applying the modified Becke-Johnson (mBJ) exchange-correlation potential [123]. The band gap underestimation for PBE-GGA functional arises from the constant exchange-correlation potential that is applied to all electron orbitals leading to an underestimation of the electron-electron interaction. The mBJ exchange-correlation potential is an orbital independent exchange-correlation potential, which depends solely on semi-local quantities [123]. For this reason, the mBJ exchange-correlation potential in conjunction with the PBE-GGA functional reproduces the band gap more accurately [123]. In the literature, the band gap was found to be 4.9 eV to 5.3 eV depending on the mBJ parametrisation of DFT calculations, while the optical band gap was determined to be 4.4 eV from reflectance spectra using the Tauc method [85]. The measured, calculated and literature band gap are included in Table 7.1 for comparison. From the comparison, we found that our measured band gap values agree better with calculated values than the literature values.

7.3.4 Partial Density of States

The pDOS allows a more detailed analysis of the electronic structure of materials. Particularly, the origin of the XAS and XES features, and band gap can be explained

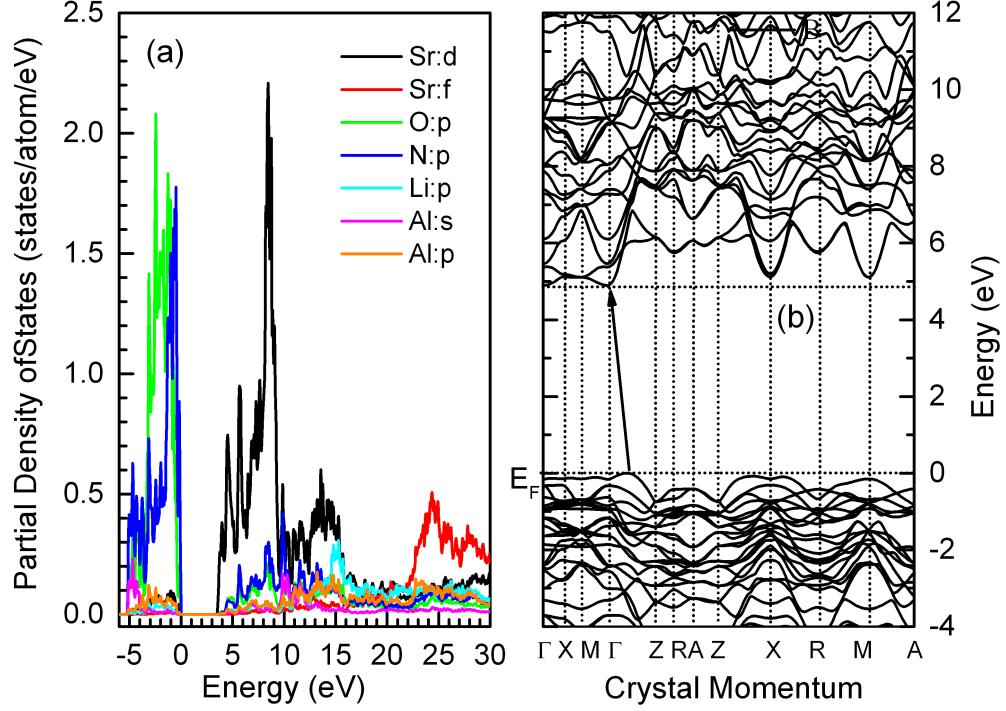


Figure 7.4: (a) The partial density of states for $\text{SrLi}_2\text{Al}_2\text{O}_2\text{N}_2:\text{Eu}^{2+}$ using the GGA-PBE functional. The energy zero is at the Fermi level. (b) Calculated band structure of $\text{SrLi}_2\text{Al}_2\text{O}_2\text{N}_2:\text{Eu}^{2+}$ based on ground state mBJ functional calculations. The energy scale is set with respect to the Fermi energy, E_F .

by the calculated pDOS. Figure 7.4(a) shows the calculated pDOS for the VB and the CB using the ground state GGA-PBE functional calculations. Mostly N and O p -states contribute throughout the VB with weak admixture of Al s -states and Li s -states in the lower VB and Sr d -states in the upper VB and Al p -states in the middle VB. The Sr d -states contribute to the lower CB and Sr d -states, N, O, Al and Li p -states contribute to the middle CB and finally Sr f -states contribute upper CB. Previous reports indicate that the alkaline earth ion d -states contribute heavily to the lower CB [42, 43].

7.3.5 Band Structure and RIXS Spectra

The band structure of SALON was calculated using the mBJ functional and is shown in Fig. 7.4(b). The upper valence bands are mainly derived from the N and O $2p$ -states, while the lower conduction bands are dominated by the d -states of Sr. The VB maximum is located in between Γ - and Z-point of the Brillouin zone while the CB minimum is located at the Γ -point. As the two points are not at the same crystal momentum, an indirect band gap of 4.9 eV is observed. The energy scale is set with respect to the Fermi energy, E_F . The authors in Ref. [85] also predicted an indirect band gap of this material. It is also noted that the lower lying CB has a high curvature and therefore should have a relatively high electron mobility [32]. Sr, Li, Al, O and N have valence electron configuration of s^2 , s^1 , s^2p^1 , s^2p^4 , and s^2p^3 , respectively. The compound has two formula units per crystallographic unit cell [85]. Therefore, the total number of valence electrons in a unit cell is 64. Due to the spin degeneracy, total number of energy bands within VB would be 32. However, only 24 available bands are found in Fig. 7.4(b), which is fewer than expected due to the energy degeneracy of the bands.

RIXS spectra can be used to determine experimentally the type of band gap [78, 203]. Previous reports indicate that for direct band gap materials, the RIXS spectrum containing the highest emission energy is obtained at the lowest excitation energy while for an indirect band gap material, the highest emission energy is obtained for the highest RIXS excitation energy [78, 203]. This is due to the conservation of momentum. Soft X-ray photons carry negligible momentum leading to the fact that the excitation into the CB and the emission decay from the VB at the same k -vector (or momentum) in the band diagram. Here, we have used RIXS spectra for both O and N K-edges to determine the nature of the band gap. Figure 7.2(a) shows the N K-edge RIXS excited at 399.1 eV (black) and 400.5 eV (green) and Fig. 7.3(a) shows

the O K-edge RIXS excited at 531.7 eV (black) and 533.0 eV (green). The vertically dashed black lines in Fig.7.2(a) and Fig. 7.3(a) indicate that the maximum emission energy increases slightly as the excitation energy is increased from lower excitation energy to higher excitation energy, which is an indicator of an indirect band gap.

7.3.6 Energetic Position of the Eu^{2+} $5d^1$ States in the Band Gap

The determination of dopant energy levels in the band gap of phosphors provides the desired experimental basis for a deeper understanding of the structure-property relationships that are critical for tailoring the luminescence properties of phosphors. The influence of the elemental composition on the position of the intragap defect states is responsible for changes in luminescence wavelength. The tunability of these additional energy states - here the $5d^1$ states resulting from doping with Eu^{2+} ions - are a crucial prerequisite for application in illumination grade LEDs. Previously, the energetic position of the $5d^1$ state was determined indirectly by fitting thermal quenching data [37, 42, 64, 67]. Thermal quenching measurements of phosphors provide an overview of the intensity reduction of emission at high temperatures. Thermal quenching data are often unreliable because thermal quenching is strongly influenced by the concentration of the dopant and the presence of defects [68, 69] but the Arrhenius equation (Equation 7.1) does not account of these defects and impurities. We determine the energetic position of the $5d^1$ state with respect to the conduction band of the host material by monitoring the energy losses in resonant inelastic scattering (RIXS) experiments for these phosphors [37, 65, 66, 73].

Figure 7.5(b) shows the RIXS spectra excited at the CB onset from both O and N K-edges measurements. The authors in Ref. [76] reported that the defect associated energy loss was the strongest for WO_3 from the O K-edge RIXS, when the excitation energy is at the band onset. The spectra are shown on an energy loss scale, which is

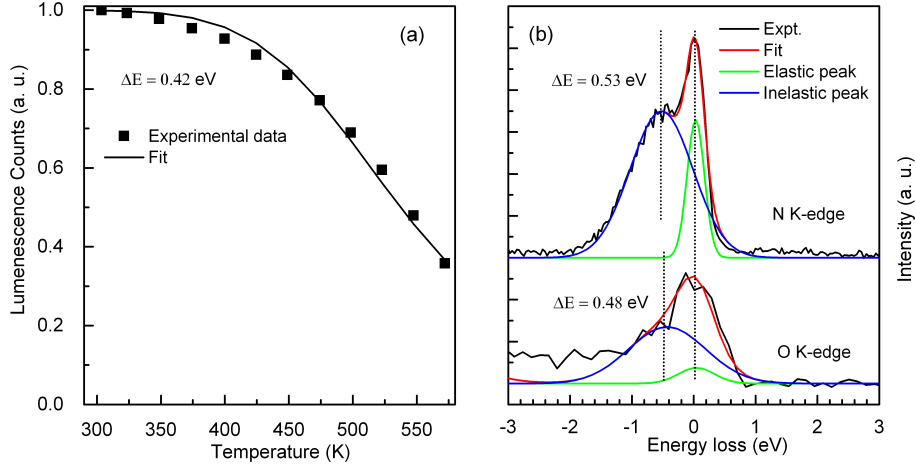


Figure 7.5: (a) Measured intensity of $5d^1 \rightarrow 4f^7$ transition of Eu^{2+} ions as a function of temperature for $\text{SrLi}_2\text{Al}_2\text{O}_2\text{N}_2:\text{Eu}^{2+}$ along with the fit (solid line) of Equation 7.1 to the measured data. (b) Comparison of N K-edge and O K-edge RIXS spectra for $\text{SrLi}_2\text{Al}_2\text{O}_2\text{N}_2:\text{Eu}^{2+}$ excited at the CB onset. Two Gaussian green (elastic feature) and blue (loss feature) are used to fit the spectrum (black).

obtained by subtracting the excitation energy from the emission energy. As a result, the elastically scattered radiation occurs at 0 eV and any other energy loss features locate at lower energies. There are two spectral features for each measurement. The additional feature observed just below the elastic scattering peak represents an energy loss in the incident X-rays due to low-energy excitations [77]. We attribute this energy loss to the promotion of $\text{Eu}^{2+} 5d^1$ electrons to the conduction band [37, 65, 66, 73] and hence are able to determine the energy of the Eu $5d^1$ relative to the lower conduction band edge. The $\text{Eu}^{2+} 5d^1$ to the CB separation is determined using $\Delta E_{\text{RIXS}} = E_e - E_i$, where E_e is the elastic scattering peak position (here its value is 0 eV in the energy loss scale) and E_i is the inelastic scattering peak position. Using this equation, the $\text{Eu}^{2+} 5d^1$ to conduction band separation is found to be 0.53 ± 0.04 eV from N K-edge RIXS and 0.48 ± 0.10 eV from O K-edge RIXS for SALON, which are also presented in Table 7.2. The fit parameters and uncertainties obtained from fitting are shown as well in Table 7.2. These values are comparable to the available

Table 7.2: Standard deviation for elastic peak (σ_1) and inelastic peak (σ_2) from the fits shown in Fig. 7.5(b), and the $\text{Eu}^{2+} 5d^1$ to conduction band energy separations from RIXS measurements (ΔE_{RIXS}) and from TQ measurements (ΔE_{TQ}). Fitting parameter ($\frac{\Gamma_0}{\Gamma_\nu}$) of Eq. 7.1 is also included in this table.

RIXS method	σ_1 (eV)	σ_2 (eV)	ΔE_{RIXS} (eV)	ΔE_{TQ} (eV)	$\frac{\Gamma_0}{\Gamma_\nu}$
N K-edge	0.14	0.51	0.53 ± 0.04	0.42 ± 0.03	8400
O K-edge	0.29	0.62	0.48 ± 0.10		

literature values, which are presented in Table 7.3. We note that the cross section for the $5d^1$ to CB inelastic scattering is extremely low and the Eu^{2+} concentration is diluted (0.7 % Eu^{2+}) making these measurements are extremely photon hungry and difficult and giving rise to the large error bar in the X-ray measurements.

Thermally stable luminescence materials are important for high power devices applications to maintain the temperature of the materials as low as possible. The decrease in luminescence emission with increasing temperature is referred to as thermal quenching, which indicates how stable the luminescent intensity and color coordinates of phosphors are for varying temperature. At room temperature, there is no thermal excitation because the thermal energy is not large enough to overcome the energy barrier from the lowest $5d^1$ level to the conduction band. The luminescence intensities as a function of sample temperature are shown in Fig. 7.5(a) for SALON, along with fitted data. The experimental temperature dependent luminescence intensities are fitted using the following common equation to describe thermal quenching of luminescence intensity $I(T)$ with temperature T [64, 67]:

$$I(T) = \frac{I_o}{1 + \frac{\Gamma_o}{\Gamma_\nu} e^{-\frac{\Delta E}{k_B T}}}, \quad (7.1)$$

where I_o is the initial luminescence intensity at room temperature (25°C), Γ_ν is the radiative decay rate of the $5d^1$ state of Eu^{2+} , Γ_o is the attempt rate for TQ process

Table 7.3: The available literature values of the energy separation between bottom of the CB and the lowest $4f^65d^1$ states of Eu^{2+} -ions from the RIXS measurements (ΔE_{RIXS}) and from TQ measurements (ΔE_{TQ}).

Samples	ΔE_{RIXS} (eV)	ΔE_{TQ} (eV)
$\text{CaAlSiN}_3:\text{Eu}^{2+}$	-	0.56 [67]
$\text{Sr}[\text{LiAl}_3\text{N}_4]:\text{Eu}^{2+}$	0.2 ± 0.1 [37]	0.291 ± 0.009 [37]
$\text{Li}_2\text{Ca}_2[\text{Mg}_2\text{Si}_2\text{N}_6]:\text{Eu}^{2+}$	0.46 ± 0.03 [37]	0.49 ± 0.03 [37]
$\text{Ba}[\text{Li}_2(\text{Al}_2\text{Si}_2)\text{N}_6]:\text{Eu}^{2+}$	0.37 ± 0.03 [37]	0.253 ± 0.008 [37]
$\text{BaLi}_2[\text{Be}_4\text{O}_6]:\text{Eu}^{2+}$	0.21 ± 0.1 [65]	0.20 ± 0.03 [65]
$\text{SrLi}_2[\text{Be}_4\text{O}_6]:\text{Eu}^{2+}$	0.25 ± 0.1 [65]	0.26 ± 0.03 [65]
$\text{Sr}[\text{Be}_6\text{ON}_4]:\text{Eu}^{2+}$	0.26 ± 0.001 [73]	-
$\text{BaBe}_{20}\text{N}_{14}:\text{Eu}^{2+}$	0.30 ± 0.04 [66]	0.32 ± 0.03 [66]
$\text{SrBe}_{20}\text{N}_{14}:\text{Eu}^{2+}$	0.31 ± 0.04 [66]	0.35 ± 0.03 [66]

at $T = \infty$, k_B is the Boltzmann's constant and ΔE is the energy barrier for thermal quenching between the lowest $5d^1$ level and the conduction band. The pre-exponential factors, Γ_0/Γ_ν and ΔE are called Arrhenius parameters. Equation 7.1 is commonly used to describe the temperature dependence of for example chemical reactions or electron transition processes. Arrhenius parameters are the variables in Equation 7.1 to fit the data. The parameter Γ_0/Γ_ν determines how rapidly the decay occurs with temperature and the parameter ΔE determines at what temperature TQ starts to become significant [37, 64, 67]. The calculated energy difference between the lowest $5d^1$ excited state of Eu^{2+} and the bottom of conduction band for SALON is 0.42 eV, which is tabulated in Table 7.2. The SALON shows relatively large value of ΔE_{TQ} , which indicates that it would be more thermally stable in comparison to available literature values in Table 7.3.

We note the following two aspects. First and most importantly the energy separation

of $5d^1$ and conduction band edge determined from the two different methods (RIXS and TQ) agree within the experimental error. Secondly, it is important to realize that impurities or other imperfections can serve as traps for the luminescence electrons and reduce the luminescence. This would affect the thermal quenching curve leading to a quicker decay in luminescence. But the inelastic scattering experiment fundamentally probes the $5d^1$ -CB energy separation and is insensitive to sample imperfections. This is why these values present the upper limits for the energy separation. Thermal $5d$ to CB excitation is not the only quenching mechanism discussed in the literature [220]. The radiationless cross-over relaxation is another possibility [220]. However, since the Stokes shift for SALON is 1100 cm^{-1} , which is rather small [221], the TQ due to $5d$ to CB excitation will be more dominant in the present case.

7.3.7 Energetic Position of the $\text{Eu}^{2+} 4f^7$ States from Luminescence Spectrum

As discussed in the introduction, the nephelauxetic effect is stronger for shorter metal-ligand distances. Eu^{2+} sites, which are surrounded by ligands with different activator-ligand distances lead to an inhomogeneous broadening. The same effect applies for structural disorder, for example if the tetrahedra centers are occupied by two different elements. This effect can be reduced by providing only one (or multiple, but very similar) highly symmetrical coordination sites and an ordered network for the activator atom, which would result in narrow-band emission. Since the outermost electrons of the excited Eu^{2+} reside in the $5d^1$ states, their energies are strongly influenced by the coordination environment of the host lattice leading to the crystal field splitting of the Eu^{2+} d -orbitals. The band broadening can be caused by geometrical relaxation of the network, as the distances between the activator and ligand can change throughout the activation process. Also, the coordination site can be slightly larger or smaller than the Eu^{2+} ion, for example, when Eu^{2+} is doped on a site, which is usually occupied by Sr^{2+} . Structural relaxation can be expected when such a site will

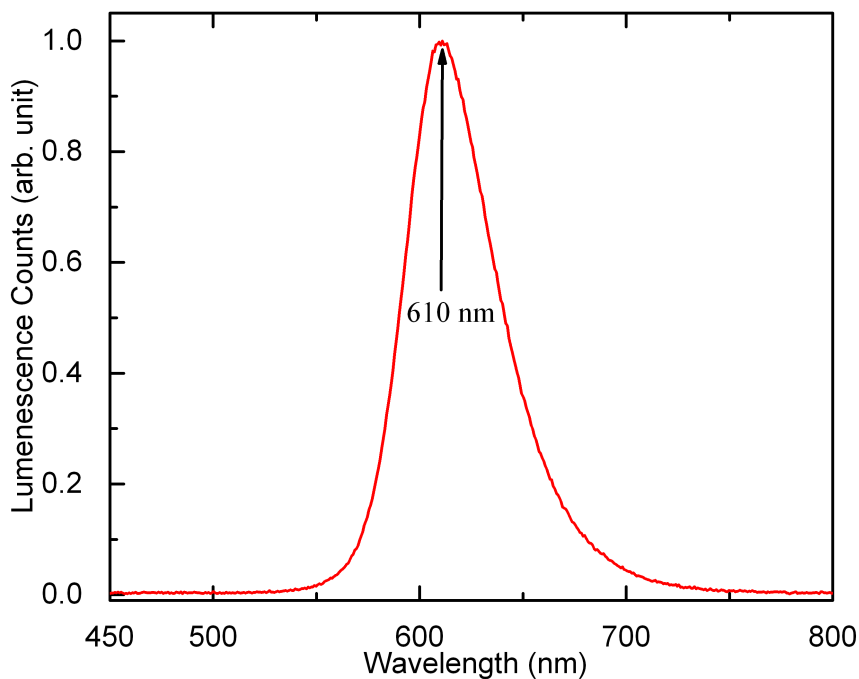


Figure 7.6: X-ray excited optical luminescence spectrum of $\text{SrLi}_2\text{Al}_2\text{O}_2\text{N}_2:\text{Eu}^{2+}$ excited at 160 eV, which exhibits red luminescence at 610 nm with 51 nm full width at half-maximum.

be occupied by an activator ion, which has a different ionic size than the initial ion. A highly condensed and rigid framework can limit such geometrical relaxations [206]. In addition, energy transfer can take place between multiple activators, if the activator sites have a small distance to the next neighbor and the activator concentration is high, leading to further band broadening [206].

X-ray excited optical luminescence spectroscopy (XEOL) is an X-ray photon-in optical photon-out process. This technique can probe optical transitions, electronic structure, presence of defects, and overall luminescence properties of materials [37, 73, 74]. The sample is excited with soft X-rays and the optical luminescence is registered by an optical spectrometer. The advantage is that due to careful selection

of the excitation energy one typically knows the first excitation process. Here we used the XEOL spectrum to understand the optical transition of the SALON compound. Figure 7.6 shows the XEOL spectra for SALON compound excited at 160 eV. The XEOL spectrum exhibits an intense red luminescence located at 610 nm with 51 nm FWHM. The red emission band is caused by the $5d^14f^6 \rightarrow 4f^7$ transitions in the Eu^{2+} ions [27, 37]. The small FWHM is due to the highly condensed network in $\text{SrLi}_2\text{Al}_2\text{O}_2\text{N}_2$ and the single crystallographic site for Eu^{2+} . It should be noted that due to the similar ionic radii (1.26 Å for Sr^{2+} and 1.25 Å for Eu^{2+}), the doped Eu^{2+} ions are assumed to occupy the Sr site [27, 47]. The energy difference between the ground $4f^7$ state and the excited $5d^14f^6$ state of Eu^{2+} ions is smaller for SLA than SALON. For this reason, the red emission band shifts from 650 nm to 610 nm for SALON with respect to SLA.

7.3.8 Energy Levels of Eu^{2+} States in the $\text{SrLi}_2\text{Al}_2\text{O}_2\text{N}_2:\text{Eu}^{2+}$ Phosphor

The band gap of SALON is determined to be 4.6 ± 0.3 eV from N K-edge and 4.5 ± 0.3 eV from O K-edge measurements. This large band gap allows for the $\text{Eu}^{2+} 5d^1 \rightarrow 4f^7$ luminescence transition. We directly determine the energetic separation between the $\text{Eu}^{2+} 5d^1$ state and the bottom of the CB of host lattice using RIXS measurements and it is found to be 0.53 ± 0.04 eV (N K-edge) and 0.48 ± 0.10 eV (O K-edge). Thus, the location of the $\text{Eu}^{2+} 5d^1$ state would be 0.53 ± 0.04 eV (N K-edge) and 0.48 ± 0.10 eV (O K-edge) below the CB onset. Our XEOL measurements provide the transition of $\text{Eu}^{2+} 5d^1 \rightarrow 4f^7$ of SALON and yield a luminescence wavelength of 610 nm (or 2.03 eV) Thus, the $\text{Eu}^{2+} 4f^7$ states reside 2.03 eV below the $\text{Eu}^{2+} 5d^1$ levels. From the soft X-ray measurements, all participating energy levels of Eu^{2+} ions ($4f^65d^1$ and $4f^7$ states), the VB, the CB, and the band gaps of SALON are determined. A schematic illustration summarizing all pertinent energy levels involved in the luminescence of SALON are presented in Fig. 7.7. Fig. 7.7 shows that when

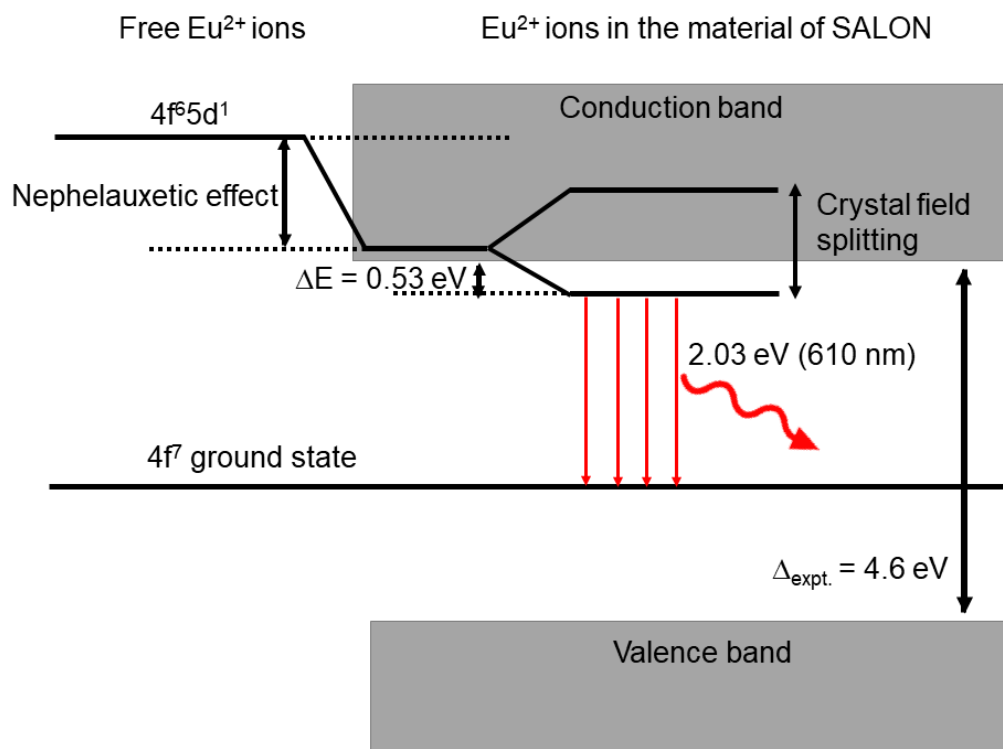


Figure 7.7: Influences of coordination environments of $\text{SrLi}_2\text{Al}_2\text{O}_2\text{N}_2:\text{Eu}^{2+}$ on the $5d^1$ energy levels of Eu^{2+} . Band gap is taken from N K-edge measurements. Energy separation between the conduction band and lowest level of $5d^1$ -states is included from RIXS N K-edge measurements and red emission band energy of 2.03 eV is observed from the XEOL measurements.

a free ion of Eu^{2+} is doped into a compound, the average energy position of the $5d^1$ levels will be lowered relative to that of the free ion. The shift of the $5d^1$ levels depends on the crystal structure of the host materials and allows for tuning of the emission.

7.4 Conclusions

The present study on SALON reports a detailed characterization using X-ray absorption, emission, and X-ray excited optical luminescence spectroscopy together with DFT-calculations. Excellent agreement between the measured and the calculated N and O K-edges spectra supports the validation of one electron picture employed in the calculations for SALON. The experimental band gap is found to be 4.6 ± 0.3 eV from N K-edge and 4.5 ± 0.3 eV from O K-edge. The band gap from N K-edge is in better agreement with our mBJ calculations (4.9 eV) than prior reported measured values. The measured large band gap is necessary to allow for the $\text{Eu}^{2+} 5d^1 4f^6 \rightarrow 4f^7$ luminescence transition. The energy separation between the $\text{Eu}^{2+} 5d^1$ state and the bottom of the CB of host lattice is determined using RIXS measurements and it is found to be 0.53 ± 0.04 eV from N K-edge measurements and 0.48 ± 0.10 eV from O K-edge measurements. Thus, the location of the $\text{Eu}^{2+} 5d^1$ state is 0.53 ± 0.04 eV (N K-edge) and 0.48 ± 0.10 eV (O K-edge) below the CB onset. The XEOL measurements show a sharp luminescence peak at 610 nm with 51 nm FWHM. The narrow red emission band is due to the $\text{Eu}^{2+} 5d^1 4f^6 \rightarrow 4f^7$ transition. Thus, the $\text{Eu}^{2+} 4f^7$ states are 2.03 eV below the $\text{Eu}^{2+} 5d^1$ levels. The nitride ion N^{3-} has a smaller electronegativity, larger formal charge, and higher polarizability than oxide O^{2-} . It is also noted that the metal-nitrogen bonds in nitride compounds are usually more covalent than the corresponding metal-oxygen atoms in oxides, which give smaller nephelauxetic effect and weak crystal field splitting acting on Eu^{2+} ions for SALON than SLA. As a result, the red narrow emission for SALON is observed at 610 nm, which is achieved by introducing oxygen atoms in the crystal structure of SLA. This

finally results in increasing the energy separation between the ground $4f^7$ state and the excited $5d^14f^6$ state of Eu^{2+} compared to SLA. Thus, the red emission band shifts from 650 nm to 610 nm for SALON compared to SLA. The shift of the wavelength is governed by the nephelauxetic effect and crystal field splitting of the material. $5d^1$ levels depends on the crystal structure of the host materials and allows for tuning of the emission. The design of improved materials for pc-LEDs, for example with ultra-narrow band emission, is currently of great importance for tunable LEDs applications as it allows the creation of a variety of overlapping spectra with a pc-LED, when multiple phosphors are used. Applied methods in this report allow direct access to electronic and optical properties, and importantly the energetic position of activator Eu^{2+} states of the SALON phosphor. Our results are valuable for a comprehensive understanding of structure-property relations of SALON and structurally related phosphors and can guide in designing new narrow-band pcLED phosphors.

Conflicts of interest

The authors declare no competing financial interest.

Acknowledgements

The experiments were performed at the Canadian Light Source, which is funded by the Canada Foundation for Innovation, the Natural Science and Engineering Research Council of Canada (NSERC), the National Research Council Canada, the Canadian Institutes of Health Research, the Government of Saskatchewan, Western Economic Diversification Canada, and the University of Saskatchewan. M.R.A. is grateful to the Government of Saskatchewan for financial support from the Saskatchewan Innovation and the Opportunity Scholarship. We acknowledge support from NSERC and the Canada Research Chair program. The authors also acknowledge Compute Canada. The calculations presented in this paper were performed on the Cedar high-performance computing cluster, which is part of the WestGrid (www.westgrid.ca) and

Compute Canada Calcul Canada (www.computecanada.ca).

Chapter 8

Conclusion

In this study, I had two goals: the first goal was to determine the bandgap of the InN powder and its origin, which was grown by ammonothermal synthesis process; the second goal was to use new experimental methods for the determination of the energetic position of the $5d$ state of the Eu^{2+} activator ions with respect to the CB of the host lattice of luminescent materials. To achieve these goals, both soft X-ray spectroscopic techniques at synchrotron facilities and DFT calculations were used. In the synchrotron facilities, XAS, XES, XEOL spectroscopy, and RIXS spectroscopy were performed at the Canadian Light Source, Saskatoon, Saskatchewan, and at the Beamline 8.0.1.1 of Advanced Light Source in Lawrence Berkeley National Laboratory, Berkeley, California, USA. For the DFT calculations, the full-potential APW method with scalar-relativistic corrections using the WIEN2k software package was employed to interpret the experimental band gap, DOS, and band structure. Further, these calculations were used to generate calculated spectra for interpreting the measured spectra.

In the first part of the study, the electronic structure and the bandgap of ammonothermal InN powder were studied [82]. Two types of InN powder samples (platelets and rods) were studied, and it was found that their electronic properties are identical, which is evidence that the electronic properties are not dependent on sample mor-

phology. The measured N K-edge XAS and XES spectra and XEOL spectra were used to estimate the bandgap of InN, and it was found to be 1.7 ± 0.2 eV for both independent measurements, which is close to the initially reported values in the range of 1.89 - 2.10 eV for polycrystalline InN and about twice the value recently obtained for single-crystalline thin films between 0.70 eV and 1.0 eV. The experimental O K-edge XAS and XES spectra of InN, XEOL measurements, and the DFT calculations for hypothetical Wurtzite-type $\text{InO}_{0.5}\text{N}_{0.5}$ and $\text{InO}_{0.0625}\text{N}_{0.9375}$ and the known *c*- In_2O_3 suggested that less than 6% oxygen impurities were present in our InN samples. Those impurities originated from substituting nitrogen atoms with oxygen atoms [82].

The second goal was the main work of this thesis. Here, blue-emitting oxoberyllates $A\text{ELi}_2[\text{Be}_4\text{O}_6]:\text{Eu}^{2+}$ ($AE = \text{Ba}, \text{Sr}$), blue-luminescence nitridoberyllates $M\text{Be}_{20}\text{N}_{14}:\text{Eu}^{2+}$ ($M = \text{Ba}, \text{Sr}$), and red-luminescence $\text{SrLi}_2\text{Al}_2\text{O}_2\text{N}_2:\text{Eu}^{2+}$ phosphors were studied. The band gaps of the material were determined from the energy difference between the top of the VB, probed by NXES, and the bottom of the CB, probed by XAS. The experimentally determined band gaps were compared to the values obtained from DFT calculations and found that our measured band gap values agree better with calculated values than the literature values. The measured, calculated, and literature band gap values of these phosphors are included in Table 8.1. The nature of the band gap (whether it has a direct or an indirect band gap) was determined experimentally using the RIXS technique. In addition, the origin of the XAS and XES features were explained by the calculated pDOS.

Furthermore, new characterization methods with existence techniques such as RIXS and XEOL spectroscopy were used to determine the energetic position of the activator ions with respect to the CB and VB of the host lattice of the studied phosphors. These energetic positions of the activator ions determine the electronic and luminescence properties including multicolor emission, adjustable bandwidth, and thermal quenching under application conditions in pc-LEDs. The crucial energetic position

Table 8.1: Measured, calculated, and previously reported band gap values of the studied phosphors. The measured band gap is denoted by $\Delta_{\text{expt.}}$ and the calculated band gap is denoted by Δ_{GGA} and Δ_{mBJ} for PBE-GGA functional and mBJ functional, respectively. The available literature band gap values are also denoted in the same way. All units are in eV.

System	$\Delta_{\text{expt.}}$	Δ_{GGA}	Δ_{mBJ}	Literature	Literature
				$\Delta_{\text{expt.}}$	Δ_{mBJ}
BaLi ₂ [Be ₄ O ₆]:Eu ²⁺	6.5 ± 0.3 [65]	5.1 [65]	6.8 [65]	3.8 [84]	
SrLi ₂ [Be ₄ O ₆]:Eu ²⁺	6.5 ± 0.3 [65]	5.6 [65]	7.4 [65]		
BaBe ₂₀ N ₁₄ :Eu ²⁺	4.4 ± 0.3 [66]	3.2 [66]	4.4 [66]	4.2 [209]	-
SrBe ₂₀ N ₁₄ :Eu ²⁺	4.4 ± 0.3 [66]	3.3 [66]	4.6 [66]	4.1 [209]	4.6 [209]
SrLi ₂ Al ₂ O ₂ N ₂ :Eu ²⁺	4.6 ± 0.3 (N K) [83]	3.5 [83]	4.9 [83]	4.3 [85]	4.9-5.3 [85]
SrLi ₂ Al ₂ O ₂ N ₂ :Eu ²⁺	4.5 ± 0.3 (O K) [83]				

of the excited $4f^65d^1$ states of Eu²⁺ with respect to the bottom of the CB of the host lattice was determined directly from the energy separation between the bottom of the CB and the lowest $4f^65d^1$ states, ΔE_{RIXS} , for the studied phosphors from the RIXS measurements. In RIXS measurements, energy losses are monitored for these phosphors. This energy loss feature is determined by plotting the graph on the energy-loss scale, which is obtained by subtracting the excitation energy from the emission energy. Thus, the elastically scattered radiation occurs at 0 eV and any other energy loss features are located at lower energies. Then, two spectral features are observed for Eu²⁺-doped samples. The additional feature observed below the elastic scattering peak represents an energy loss in the incident X-rays caused by the low-energy excitations. Owing to the low cross-section for the $4f^65d^1$ to the CB inelastic scattering and low Eu²⁺ concentration, the loss feature is weak and only revealed when the elastic peak is fitted with two Gaussians. The Eu²⁺ $4f^65d^1$ to the CB separation is determined from the Gaussians fit using $\Delta E_{\text{RIXS}} = E_e - E_i$, where E_e represents the elastic scattering peak position and E_i represents the inelastic scat-

Table 8.2: Determined energy separation between the bottom of the conduction band of host material and the lowest $4f^65d^1$ states from the RIXS (ΔE_{RIXS}) and TQ measurements (ΔE_{TQ}).

Studied materials	ΔE_{RIXS} (eV)	ΔE_{TQ} (eV)	Emission color	Wavelength (nm)
BaLi ₂ [Be ₄ O ₆]:Eu ²⁺	0.21 ± 0.1 [65]	0.20 ± 0.03 [65]	blue	455
SrLi ₂ [Be ₄ O ₆]:Eu ²⁺	0.25 ± 0.1 [65]	0.26 ± 0.03 [65]	blue	457
BaBe ₂₀ N ₁₄ :Eu ²⁺	0.30 ± 0.04 [66]	0.32 ± 0.03 [66]	blue	427
SrBe ₂₀ N ₁₄ :Eu ²⁺	0.31 ± 0.04 [66]	0.35 ± 0.03 [66]	blue	430
SrLi ₂ Al ₂ O ₂ N ₂ :Eu ²⁺	0.53 ± 0.04 (N-K) [83]	0.42 ± 0.03 [83]	red	610
SrLi ₂ Al ₂ O ₂ N ₂ :Eu ²⁺	0.48 ± 0.1 (O-K) [83]	-		

tering peak position. Determined ΔE_{RIXS} values from RIXS measurements in this study are presented in Table 8.2. Further, the ΔE_{TQ} values are determined from thermal quenching data (via fitting of thermal quenching curves), which are included in Table 8.2. The comparison between ΔE_{RIXS} and ΔE_{TQ} indicates that they agree well.

Finally, the $4f^7$ energy level is determined from the $4f^65d^1 \rightarrow 4f^7$ luminescence transition of Eu²⁺ ions with respect to the $4f^65d^1$ states using XEOL measurements. The luminescence of interest is caused by the $4f^65d^1 \rightarrow 4f^7$ transition of the activator ions. The spectroscopic features of the $4f^65d^1 \rightarrow 4f^7$ transitions are strongly influenced by the crystal environment. This indicates that the intensity and energy of the transition are strongly affected by the crystal field strength, crystal lattice symmetry, nature of bonds (covalence/ionic), atomic coordination, bond strength, etc. Therefore, RIXS measurements and XEOL techniques allow direct access to the intragap states, which again are the source of the luminescence of Eu²⁺-doped phosphors. Thus, our study shows the applicability and power of the RIXS and XEOL techniques for understanding and measuring important properties of Eu²⁺-doped phosphors. We determine

all participating energy levels of the Eu^{2+} ions ($4f^65d^1$ and $4f^7$ states), the VB, the CB, and bandgaps of phosphors. The detailed determination of the bandgaps and energetic position of the activator Eu^{2+} states can guide central steps of phosphor design. Our study of these materials serves an important role in the advancement of light-emitting diodes and introducing Eu^{2+} -doped diodes to the lighting market.

Bibliography

- [1] S. Aldridge and A. J. Downs, *The Group 13 Metals Aluminium, Gallium, Indium and Thallium: Chemical Patterns and Peculiarities*. John Wiley & Sons, 2011.
- [2] S. Nakamura, T. Mukai, and M. Senoh, “Candela-class high-brightness In-GaN/AlGaN double-heterostructure blue-light-emitting diodes,” *Applied Physics Letters*, vol. 64, no. 13, pp. 1687–1689, 1994.
- [3] M. H. Huang, S. Mao, H. Feick, H. Yan, Y. Wu, H. Kind, E. Weber, R. Russo, and P. Yang, “Room-temperature ultraviolet nanowire nanolasers,” *Science*, vol. 292, no. 5523, pp. 1897–1899, 2001.
- [4] Z. K. Tang, G. K. L. Wong, P. Yu, M. Kawasaki, A. Ohtomo, H. Koinuma, and Y. J. A. P. L. Segawa, “Room-temperature ultraviolet laser emission from self-assembled ZnO microcrystallite thin films,” *Applied Physics Letters*, vol. 72, no. 25, pp. 3270–3272, 1998.
- [5] J. Faist, F. Capasso, D. L. Sivco, C. Sirtori, A. L. Hutchinson, and A. Y. Cho, “Quantum cascade laser,” *Science*, vol. 264, no. 5158, pp. 553–556, 1994.
- [6] P. W. Barone, S. Baik, D. A. Heller, and M. S. Strano, “Near-infrared optical sensors based on single-walled carbon nanotubes,” *Nature Materials*, vol. 4, no. 1, pp. 86–92, 2005.
- [7] G. Blasse, “New luminescent materials,” *Chemistry of Materials*, vol. 1, no. 3, pp. 294–301, 1989.
- [8] E. Auffray, J. Bourotte, T. Beckers, M. Chipaux, V. Commichau, I. Dafinei, P. Depasse, L. Djambazov, U. Dydak, H. El Mamouni, *et al.*, “Test beam results of a cerium fluoride crystal matrix,” *Nuclear Physics B-Proceedings Supplements*, vol. 44, no. 1-3, pp. 57–62, 1995.
- [9] K. Panigrahi and A. Nag, “Challenges and strategies to design phosphors for future white light emitting diodes,” *The Journal of Physical Chemistry C*, vol. 126, pp. 8553–8564, 2022.
- [10] J. W. M. Verwey and G. Blasse, “Luminescence efficiency of ions with broad-band excitation in lithium lanthanum phosphate glass,” *Chemistry of Materials*, vol. 2, no. 4, pp. 458–463, 1990.

- [11] C. R. Ronda, T. Jüstel, and H. Nikol, "Rare earth phosphors: Fundamentals and applications," *Journal of Alloys and Compounds*, vol. 275, pp. 669–676, 1998.
- [12] R. J. Xie and N. Hirosaki, "Silicon-based oxynitride and nitride phosphors for white LEDs—a review," *Science and Technology of Advanced Materials*, vol. 8, no. 7-8, p. 588, 2007.
- [13] S. Tanabe, "Optical transitions of rare earth ions for amplifiers: How the local structure works in glass," *Journal of Non-crystalline Solids*, vol. 259, no. 1-3, pp. 1–9, 1999.
- [14] M. Jayasimhadri, L. R. Moorthy, K. Kojima, K. Yamamoto, N. Wada, and N. Wada, "Optical properties of Dy^{3+} ions in alkali tellurofluorophosphate glasses for laser materials," *Journal of Physics D: Applied Physics*, vol. 39, no. 4, p. 635, 2006.
- [15] K. Tanaka, "Cathode luminescence of samarium, europium, and gadolinium ion doped scintillator CdWO_4 single crystals studied with x-ray photoelectron spectroscopy," *Journal of Applied Physics*, vol. 89, no. 10, pp. 5449–5453, 2001.
- [16] J. Zhang, Z. Hao, X. Zhang, Y. Luo, X. Ren, X. J. Wang, and J. Zhang, "Color tunable phosphorescence in $\text{KY}_3\text{F}_{10}:\text{Tb}^{3+}$ for x-ray or cathode-ray tubes," *Journal of Applied Physics*, vol. 106, no. 3, p. 034915, 2009.
- [17] A. M. Srivastava, "Inter- and intraconfigurational optical transitions of the Pr^{3+} ion for application in lighting and scintillator technologies," *Journal of Luminescence*, vol. 129, no. 12, pp. 1419–1421, 2009.
- [18] S. V. Eliseeva and J. C. G. Bünzli, "Lanthanide luminescence for functional materials and bio-sciences," *Chemical Society Reviews*, vol. 39, no. 1, pp. 189–227, 2010.
- [19] B. S. Richards, "Luminescent layers for enhanced silicon solar cell performance: Down-conversion," *Solar Energy Materials and Solar Cells*, vol. 90, no. 9, pp. 1189–1207, 2006.
- [20] T. Trupke, M. A. Green, and P. Würfel, "Improving solar cell efficiencies by up-conversion of sub-band-gap light," *Journal of Applied Physics*, vol. 92, no. 7, pp. 4117–4122, 2002.
- [21] V. Bachmann, C. Ronda, O. Oeckler, W. Schnick, and A. Meijerink, "Color point tuning for $(\text{Sr}, \text{Ca}, \text{Ba})\text{Si}_2\text{O}_2\text{N}_2:\text{Eu}^{2+}$ for white light LEDs," *Chemistry of Materials*, vol. 21, no. 2, pp. 316–325, 2009.
- [22] H. A. Höpfe, "Recent developments in the field of inorganic phosphors," *Angewandte Chemie International Edition*, vol. 48, no. 20, pp. 3572–3582, 2009.
- [23] M. R. Krames, O. B. Shchekin, R. Mueller-Mach, G. O. Mueller, L. Zhou, G. Harbers, and M. G. Craford, "Status and future of high-power light-emitting diodes for solid-state lighting," *Journal of Display Technology*, vol. 3, no. 2, pp. 160–175, 2007.

- [24] A. Kitai, *Luminescent Materials and Applications*. John Wiley & Sons, 2008, vol. 25.
- [25] M. Lee, D. Mikulik, M. Yang, and S. Park, “The investigation of stress in free-standing GaN crystals grown from Si substrates by HVPE,” *Scientific Reports*, vol. 7, no. 1, pp. 1–6, 2017.
- [26] P. Pust, P. J. Schmidt, and W. Schnick, “A revolution in lighting,” *Nature Materials*, vol. 14, no. 5, pp. 454–458, 2015.
- [27] P. Pust, V. Weiler, C. Hecht, A. Tücks, A. S. Wochnik, A. K. Henß, D. Wiechert, C. Scheu, P. J. Schmidt, and W. Schnick, “Narrow-band red-emitting Sr[LiAl₃N₄]:Eu²⁺ as a next-generation LED-phosphor material,” *Nature Materials*, vol. 13, no. 9, pp. 891–896, 2014.
- [28] D. A. Steigerwald, J. C. Bhat, D. Collins, R. M. Fletcher, M. O. Holcomb, M. J. Ludowise, P. S. Martin, and S. L. Rudaz, “Illumination with solid state lighting technology,” *IEEE Journal of Selected Topics in Quantum Electronics*, vol. 8, no. 2, pp. 310–320, 2002.
- [29] Y. N. Ahn, K. Do Kim, G. Anoop, G. S. Kim, and J. S. Yoo, “Design of highly efficient phosphor-converted white light-emitting diodes with color rendering indices (R_1 - R_{15}) ≥ 95 for artificial lighting,” *Scientific Reports*, vol. 9, no. 1, pp. 1–10, 2019.
- [30] M. Shang, G. Li, D. Geng, D. Yang, X. Kang, Y. Zhang, H. Lian, and J. Lin, “Blue emitting Ca₈La₂(PO₄)₆O₂:Ce³⁺/Eu²⁺ phosphors with high color purity and brightness for white LED: Soft-chemical synthesis, luminescence, and energy transfer properties,” *The Journal of Physical Chemistry C*, vol. 116, no. 18, pp. 10 222–10 231, 2012.
- [31] D. Haranath, H. Chander, P. Sharma, and S. Singh, “Enhanced luminescence of Y₃Al₅O₁₂:Ce³⁺ nanophosphor for white light-emitting diodes,” *Applied Physics Letters*, vol. 89, no. 17, p. 173 118, 2006.
- [32] R. Kasuya, A. Kawano, T. Isobe, H. Kuma, and J. Katano, “Characteristic optical properties of transparent color conversion film prepared from YAG:Ce³⁺ nanoparticles,” *Applied Physics Letters*, vol. 91, no. 11, p. 111 916, 2007.
- [33] G. B. Nair, H. Swart, and S. Dhoble, “A review on the advancements in phosphor-converted light emitting diodes (pc-LEDs): Phosphor synthesis, device fabrication and characterization,” *Progress in Materials Science*, vol. 109, p. 100 622, 2020.
- [34] L. Wang, R. J. Xie, T. Suehiro, T. Takeda, and N. Hirosaki, “Down-conversion nitride materials for solid state lighting: Recent advances and perspectives,” *Chemical Reviews*, vol. 118, no. 4, pp. 1951–2009, 2018.
- [35] K. Y. Jung, H. W. Lee, and H. K. Jung, “Luminescent properties of (Sr,Zn)Al₂O₄:Eu²⁺, B³⁺ particles as a potential green phosphor for UV LEDs,” *Chemistry of Materials*, vol. 18, no. 9, pp. 2249–2255, 2006.

- [36] T. M. Tolhurst, P. Strobel, P. J. Schmidt, W. Schnick, and A. Moewes, “Designing luminescent materials and band gaps: A soft x-ray spectroscopy and density functional theory study of $\text{Li}_2\text{Ca}_2[\text{Mg}_2\text{Si}_2\text{N}_6]:\text{Eu}^{2+}$ and $\text{Ba}[\text{Li}_2(\text{Al}_2\text{Si}_2)\text{N}_6]:\text{Eu}^{2+}$,” *The Journal of Physical Chemistry C*, vol. 121, no. 26, pp. 14 296–14 301, 2017.
- [37] T. M. Tolhurst, P. Strobel, P. J. Schmidt, W. Schnick, and A. Moewes, “Direct measurements of energy levels and correlation with thermal quenching behavior in nitride phosphors,” *Chemistry of Materials*, vol. 29, no. 18, pp. 7976–7983, 2017.
- [38] S. Schmiechen, P. Strobel, C. Hecht, T. Reith, M. Siegert, P. J. Schmidt, P. Huppertz, D. Wiechert, and W. Schnick, “Nitridomagnesosilicate $\text{Ba}[\text{Mg}_3\text{SiN}_4]:\text{Eu}^{2+}$ and structure-property relations of similar narrow-band red nitride phosphors,” *Chemistry of Materials*, vol. 27, no. 5, pp. 1780–1785, 2015.
- [39] S. Schmiechen, H. Schneider, P. Wagatha, C. Hecht, P. J. Schmidt, and W. Schnick, “Toward new phosphors for application in illumination-grade white pc-LEDs: The nitridomagnesosilicates $\text{Ca}[\text{Mg}_3\text{SiN}_4]:\text{Ce}^{3+}$, $\text{Sr}[\text{Mg}_3\text{SiN}_4]:\text{Eu}^{2+}$, and $\text{Eu}[\text{Mg}_3\text{SiN}_4]$,” *Chemistry of Materials*, vol. 26, no. 8, pp. 2712–2719, 2014.
- [40] C. J. Duan, X. J. Wang, W. M. Otten, A. C. A. Delsing, J. T. Zhao, and H. T. Hintzen, “Preparation, electronic structure, and photoluminescence properties of Eu^{2+} - and $\text{Ce}^{3+}/\text{Li}^+$ -activated alkaline earth silicon nitride MSiN_2 ($\text{M} = \text{Sr}, \text{Ba}$),” *Chemistry of Materials*, vol. 20, no. 4, pp. 1597–1605, 2008.
- [41] Y. Q. Li, N. Hirosaki, R. J. Xie, T. Takeka, and M. Mitomo, “Crystal, electronic structures and photoluminescence properties of rare-earth doped LiSi_2N_3 ,” *Journal of Solid State Chemistry*, vol. 182, no. 2, pp. 301–311, 2009.
- [42] T. M. Tolhurst, T. D. Boyko, P. Pust, N. W. Johnson, W. Schnick, and A. Moewes, “Investigations of the electronic structure and bandgap of the next-generation LED-phosphor $\text{Sr}[\text{LiAl}_3\text{N}_4]:\text{Eu}^{2+}$ -experiment and calculations,” *Advanced Optical Materials*, vol. 3, no. 4, pp. 546–550, 2015.
- [43] T. M. Tolhurst, S. Schmiechen, P. Pust, P. J. Schmidt, W. Schnick, and A. Moewes, “Electronic structure, bandgap, and thermal quenching of $\text{Sr}[\text{Mg}_3\text{SiN}_4]:\text{Eu}^{2+}$ in comparison to $\text{Sr}[\text{LiAl}_3\text{N}_4]:\text{Eu}^{2+}$,” *Advanced Optical Materials*, vol. 4, no. 4, pp. 584–591, 2016.
- [44] M. Shang, C. Li, and J. Lin, “How to produce white light in a single-phase host?” *Chemical Society Reviews*, vol. 43, no. 5, pp. 1372–1386, 2014.
- [45] T. V. Balashova, A. P. Pushkarev, A. N. Yablonskiy, B. A. Andreev, I. D. Grishin, R. V. Rummyantsev, G. K. Fukin, and M. N. Bochkarev, “Organic Er-Yb complexes as potential upconversion materials,” *Journal of Luminescence*, vol. 192, pp. 208–211, 2017.
- [46] T. Grzyb and A. Tyimiński, “Up-conversion luminescence of $\text{GdOF}:\text{Yb}^{3+}, \text{Ln}^{3+}$ ($\text{Ln} = \text{Ho}, \text{Tm}, \text{Er}$) nanocrystals,” *Journal of Alloys and Compounds*, vol. 660, pp. 235–243, 2016.

- [47] R. D. Shannon, "Revised effective ionic radii and systematic studies of interatomic distances in halides and chalcogenides," *Acta crystallographica section A: crystal Physics, Diffraction, Theoretical and General Crystallography*, vol. 32, no. 5, pp. 751–767, 1976.
- [48] G. Lee, J. Y. Han, W. B. Im, S. H. Cheong, and D. Y. Jeon, "Novel blue-emitting $\text{Na}_x\text{Ca}_{1-x}\text{Al}_{2-x}\text{Si}_{2+x}\text{O}_8:\text{Eu}^{2+}$ ($x=0.34$) phosphor with high luminescent efficiency for UV-pumped light-emitting diodes," *Inorganic Chemistry*, vol. 51, no. 20, pp. 10 688–10 694, 2012.
- [49] D. Hou, C. Liu, X. Ding, X. Kuang, H. Liang, S. Sun, Y. Huang, and Y. Tao, "A high efficiency blue phosphor $\text{BaCa}_2\text{MgSi}_2\text{O}_8:\text{Eu}^{2+}$ under VUV and UV excitation," *Journal of Materials Chemistry C*, vol. 1, no. 3, pp. 493–499, 2013.
- [50] H. Guo, H. Zhang, J. Li, and F. Li, "Blue-white-green tunable luminescence from $\text{Ba}_2\text{Gd}_2\text{Si}_4\text{O}_{13}:\text{Ce}^{3+}, \text{Tb}^{3+}$ phosphors excited by ultraviolet light," *Optics Express*, vol. 18, no. 26, pp. 27 257–27 262, 2010.
- [51] G. B. Nair, H. C. Swart, and S. J. Dhoble, "Analysis of the electron-vibrational interaction in the $5d$ states of Eu^{2+} ions in LiSrPO_4 host matrix," *Journal of Luminescence*, vol. 214, p. 116 564, 2019.
- [52] Z. Xia and Q. Liu, "Progress in discovery and structural design of color conversion phosphors for LEDs," *Progress in Materials Science*, vol. 84, pp. 59–117, 2016.
- [53] P. Dorenbos, "Energy of the first $4f^7 \rightarrow 4f^65d$ transition of Eu^{2+} in inorganic compounds," *Journal of Luminescence*, vol. 104, no. 4, pp. 239–260, 2003.
- [54] P. Dorenbos, "Anomalous luminescence of Eu^{2+} and Yb^{2+} in inorganic compounds," *Journal of Physics: Condensed Matter*, vol. 15, no. 17, p. 2645, 2003.
- [55] G. Li, Y. Tian, Y. Zhao, and J. Lin, "Recent progress in luminescence tuning of Ce^{3+} and Eu^{2+} -activated phosphors for pc-WLEDs," *Chemical Society Reviews*, vol. 44, no. 23, pp. 8688–8713, 2015.
- [56] B. Wang, Z. Wang, Y. Liu, S. Duan, Z. Huang, and M. Fang, "Valent control and spectral tuning by cation site engineering strategy in Eu-doped $\text{Sr}_{1-x}\text{Ba}_x\text{Al}_2\text{Si}_2\text{O}_8$ phosphor," *Journal of Alloys and Compounds*, vol. 806, pp. 529–536, 2019.
- [57] S. Shionoya, W. M. Yen, and H. Yamamoto, *Phosphor Handbook*. CRC press, 2018.
- [58] S. Zhou and L. Yin, "CdS quantum dots sensitized mesoporous BiVO_4 heterostructures for solar cells with enhanced photo-electrical conversion efficiency," *Journal of Alloys and Compounds*, vol. 691, pp. 1040–1048, 2017.
- [59] S. Ponce, Y. Jia, M. Giantomassi, M. Mikami, and X. Gonze, "Understanding thermal quenching of photoluminescence in oxynitride phosphors from first principles," *The Journal of Physical Chemistry C*, vol. 120, no. 7, pp. 4040–4047, 2016.

- [60] P. Johnson and F. Williams, “Simplified configuration coordinate model for KCl:Tl,” *Physical Review*, vol. 117, no. 4, p. 964, 1960.
- [61] G. Blasse and A. Bril, “Characteristic luminescence,” *Philips Technical Review*, vol. 31, no. 10, p. 303, 1970.
- [62] Y. C. Lin, M. Karlsson, and M. Bettinelli, “Inorganic phosphor materials for lighting,” *Photoluminescent Materials and Electroluminescent Devices*, pp. 309–355, 2017.
- [63] C. W. Struck and W. H. Fonger, *Understanding Luminescence Spectra and Efficiency Using Wp and Related Functions*. Springer Science & Business Media, 2012, vol. 13.
- [64] P. Dorenbos, “Thermal quenching of Eu^{2+} 5d–4f luminescence in inorganic compounds,” *Journal of Physics: Condensed Matter*, vol. 17, no. 50, p. 8103, 2005.
- [65] M. R. Amin, P. Strobel, A. Qamar, T. Giftthaler, W. Schnick, and A. Moewes, “Understanding of luminescence properties using direct measurements on Eu^{2+} -doped wide bandgap phosphors,” *Advanced Optical Materials*, vol. 8, p. 2000504, 2020.
- [66] M. R. Amin, E. Elzer, W. Schnick, and A. Moewes, “Unraveling the energy levels of Eu^{2+} ions in $\text{MBe}_{20}\text{N}_{14}:\text{Eu}^{2+}$ ($M = \text{Sr}, \text{Ba}$) phosphors,” *The Journal of Physical Chemistry C*, vol. 125, no. 22, pp. 11828–11837, 2021.
- [67] Z. Zhang, M. Otmar, A. C. A. Delsing, M. J. H. Stevens, J. Zhao, P. H. L. Notten, P. Dorenbos, and H. T. Hintzen, “Photoluminescence properties of Yb^{2+} in CaAlSiN_3 as a novel red-emitting phosphor for white LEDs,” *Journal of Materials Chemistry*, vol. 22, no. 45, pp. 23871–23876, 2012.
- [68] L. Wang, H. M. Noh, B. K. Moon, S. H. Park, K. H. Kim, J. Shi, and J. H. Jeong, “Dual-mode luminescence with broad near UV and blue excitation band from $\text{Sr}_2\text{CaMoO}_6:\text{Sm}^{3+}$ phosphor for white LEDs,” *The Journal of Physical Chemistry C*, vol. 119, no. 27, pp. 15517–15525, 2015.
- [69] W. Lv, Y. Jia, Q. Zhao, M. Jiao, B. Shao, W. Lü, and H. You, “Crystal structure and luminescence properties of $\text{Ca}_8\text{Mg}_3\text{Al}_2\text{Si}_7\text{O}_{28}:\text{Eu}^{2+}$ for WLEDs,” *Advanced Optical Materials*, vol. 2, no. 2, pp. 183–188, 2014.
- [70] V. B. Zabolotnyy, K. Fürsich, R. J. Green, P. Lutz, K. Treiber, C. H. Min, A. V. Dukhnenko, N. Y. Shitsevalova, V. B. Filipov, B. Y. Kang, *et al.*, “Chemical and valence reconstruction at the surface of SmB_6 revealed by means of resonant soft x-ray reflectometry,” *Physical Review B*, vol. 97, no. 20, p. 205416, 2018.
- [71] M. Sundermann, H. Yavaş, K. Chen, D. J. Kim, Z. Fisk, D. Kasinathan, M. W. Haverkort, P. Thalmeier, A. Severing, and L. H. Tjeng, “4f crystal field ground state of the strongly correlated topological insulator SmB_6 ,” *Physical Review Letters*, vol. 120, no. 1, p. 016402, 2018.

- [72] M. Suta, F. Cimpoesu, and W. Urland, “The angular overlap model of ligand field theory for f elements: An intuitive approach building bridges between theory and experiment,” *Coordination Chemistry Reviews*, vol. 441, p. 213 981, 2021.
- [73] P. Strobel, T. de Boer, V. Weiler, P. J. Schmidt, A. Moewes, and W. Schnick, “Luminescence of an oxonitridoberyllate: A study of narrow-band cyan-emitting $\text{Sr}[\text{Be}_6\text{ON}_4]:\text{Eu}^{2+}$,” *Chem. Mater.*, vol. 30, no. 9, pp. 3122–3130, 2018.
- [74] D. Wang, J. Yang, X. Li, J. Wang, R. Li, M. Cai, T. K. Sham, and X. Sun, “Observation of surface/defect states of SnO_2 nanowires on different substrates from x-ray excited optical luminescence,” *Crystal Growth & Design*, vol. 12, no. 1, pp. 397–402, 2012.
- [75] Z. Wang, C. Li, L. Liu, and T. K. Sham, “Probing defect emissions in bulk, micro-and nano-sized $\alpha\text{-Al}_2\text{O}_3$ via x-ray excited optical luminescence,” *The Journal of Chemical Physics*, vol. 138, no. 8, p. 084 706, 2013.
- [76] M. B. Johansson, P. T. Kristiansen, L. Duda, G. A. Niklasson, and L. Österlund, “Band gap states in nanocrystalline WO_3 thin films studied by soft x-ray spectroscopy and optical spectrophotometry,” *Journal of Physics: Condensed Matter*, vol. 28, no. 47, p. 475 802, 2016.
- [77] L. J. P. Ament, M. Van Veenendaal, T. P. Devereaux, J. P. Hill, and J. Van Den Brink, “Resonant inelastic x-ray scattering studies of elementary excitations,” *Reviews of Modern Physics*, vol. 83, no. 2, pp. 705–767, 2011.
- [78] S. Eisebitt and W. Eberhardt, “Band structure information and resonant inelastic soft x-ray scattering in broad band solids,” *Journal of Electron Spectroscopy and Related Phenomena*, vol. 110, pp. 335–358, 2000.
- [79] T. K. Sham, D. T. Jiang, I. Coulthard, J. W. Lorimer, X. H. Feng, K. H. Tan, S. P. Frigo, R. A. Rosenberg, D. C. Houghton, and B. Bryskiewicz, “Origin of luminescence from porous silicon deduced by synchrotron-light-induced optical luminescence,” *Nature*, vol. 363, no. 6427, pp. 331–334, 1993.
- [80] R. A. Rosenberg, G. K. Shenoy, F. Heigl, S. T. Lee, P. S. G. Kim, X. T. Zhou, and T. K. Sham, “Effects of in situ vacuum annealing on the surface and luminescent properties of ZnS nanowires,” *Applied Physics Letters*, vol. 86, no. 26, p. 263 115, 2005.
- [81] L. Armelao, F. Heigl, S. Brunet, R. Sammynaiken, T. Regier, R. I. Blyth, L. Zuin, R. Sankari, J. Vogt, and T. K. Sham, “The origin and dynamics of soft x-ray-excited optical luminescence of ZnO ,” *ChemPhysChem*, vol. 11, no. 17, pp. 3625–3631, 2010.
- [82] M. R. Amin, T. de Boer, P. Becker, J. Hertrampf, R. Niewa, and A. Moewes, “Bandgap and electronic structure determination of oxygen-containing amonothermal InN : Experiment and theory,” *The Journal of Physical Chemistry C*, vol. 123, pp. 8943–8950, 2019.

- [83] M. R. Amin, P. Strobel, W. Schnick, P. J. Schmidt, and A. Moewes, “Energy levels of Eu^{2+} -states in the next-generation LED-phosphor $\text{SrLi}_2\text{Al}_2\text{O}_2\text{N}_2:\text{Eu}^{2+}$,” *Journal of Materials Chemistry C*, vol. 10, no. 26, pp. 9740–9747, 2022.
- [84] P. Strobel, C. Maak, V. Weiler, P. J. Schmidt, and W. Schnick, “Ultra-narrow-band blue-emitting oxoberyllates $A\text{E}\text{Li}_2[\text{Be}_4\text{O}_6]:\text{Eu}^{2+}$ ($AE = \text{Sr}, \text{Ba}$) paving the way to efficient RGB pc-LEDs,” *Angewandte Chemie International Edition*, vol. 57, no. 28, pp. 8739–8743, 2018.
- [85] G. J. Hoerder, M. Seibald, D. Baumann, T. Schröder, S. Peschke, P. C. Schmid, T. Tyborski, P. Pust, I. Stoll, M. Bergler, *et al.*, “ $\text{Sr}[\text{Li}_2\text{Al}_2\text{O}_2\text{N}_2]:\text{Eu}^{2+}$ -a high performance red phosphor to brighten the future,” *Nature Communications*, vol. 10, no. 1, pp. 1–9, 2019.
- [86] H. Petersen, C. Jung, C. Hellwig, W. B. Peatman, and W. Gudat, “Review of plane grating focusing for soft x-ray monochromators,” *Review of Scientific Instruments*, vol. 66, no. 1, pp. 1–14, 1995.
- [87] M. Boots, D. Muir, and A. Moewes, “Optimizing and characterizing grating efficiency for a soft x-ray emission spectrometer,” *Journal of Synchrotron Radiation*, vol. 20, no. 2, pp. 272–285, 2013.
- [88] Y. F. Hu, L. Zuin, G. Wright, R. Igarashi, M. McKibben, T. Wilson, S. Y. Chen, T. Johnson, D. Maxwell, B. W. Yates, *et al.*, “Commissioning and performance of the variable line spacing plane grating monochromator beamline at the Canadian Light Source,” *Review of Scientific Instruments*, vol. 78, no. 8, p. 083 109, 2007.
- [89] J. J. Jia, T. A. Callcott, J. Yurkas, A. W. Ellis, F. J. Himpsel, M. G. Samant, J. Stöhr, D. L. Ederer, J. A. Carlisle, E. A. Hudson, *et al.*, “First experimental results from IBM/TENN/TULANE/LLNL/LBL undulator beamline at the Advanced Light Source,” *Review of Scientific Instruments*, vol. 66, no. 2, pp. 1394–1397, 1995.
- [90] D. J. Griffiths, *Introduction to Quantum Mechanics*. Pearson International Edition (Pearson Prentice Hall, Upper Saddle River, 2005), 1960.
- [91] P. Willmott, *An Introduction to Synchrotron Radiation: Techniques and Applications*. John Wiley & Sons, 2019.
- [92] D. Attwood, *Soft X-rays and Extreme Ultraviolet Radiation: Principles and Applications*. Cambridge University Press, 2000.
- [93] K. J. Kim, “Characteristics of synchrotron radiation,” in *AIP Conference Proceedings*, American Institute of Physics, vol. 184, 1989, pp. 565–632.
- [94] K. Halbach, “Permanent magnet undulators,” *Le Journal de Physique Colloques*, vol. 44, no. C1, pp. C1–211, 1983.
- [95] G. Brown, K. Halbach, J. Harris, and H. Winick, “Wiggler and undulator magnets-a review,” *Nuclear Instruments and Methods in Physics Research*, vol. 208, no. 1-3, pp. 65–77, 1983.

- [96] H. Winick, G. Brown, K. Halbach, and J. Harris, “Wiggler and undulator magnets,” *Physics Today*, vol. 34, no. 5, pp. 50–63, 1981.
- [97] B. L. Henke, E. M. Gullikson, and J. C. Davis, “X-ray interactions: Photoabsorption, scattering, transmission, and reflection at $E= 50\text{--}30,000$ eV, $Z = 1\text{--}92$,” *Atomic Data and Nuclear Data Tables*, vol. 54, no. 2, pp. 181–342, 1993.
- [98] A. Moewes, “Recent developments in soft x-ray absorption spectroscopy,” *Handbook of Solid State Chemistry*, pp. 361–391, 2017.
- [99] J. Stöhr, *NEXAFS Spectroscopy*. Springer Science & Business Media, 1992, vol. 25.
- [100] B. K. Teo and P. A. Lee, “Ab initio calculations of amplitude and phase functions for extended x-ray absorption fine structure spectroscopy,” *Journal of the American Chemical Society*, vol. 101, no. 11, pp. 2815–2832, 1979.
- [101] B. K. Teo, P. A. Lee, A. L. Simons, P. Eisenberger, and B. M. Kincaid, “EXAFS: Approximation, parameterization, and chemical transferability of amplitude functions,” *Journal of the American Chemical Society*, vol. 99, no. 11, pp. 3854–3856, 1977.
- [102] A. Kotani and S. Shin, “Resonant inelastic x-ray scattering spectra for electrons in solids,” *Reviews of Modern Physics*, vol. 73, no. 1, p. 203, 2001.
- [103] F. De Groot and A. Kotani, *Core Level Spectroscopy of Solids*. CRC press, 2008.
- [104] T. K. Sham and R. A. Rosenberg, “Time-resolved synchrotron radiation excited optical luminescence: Light-emission properties of silicon-based nanostructures,” *ChemPhysChem*, vol. 8, no. 18, pp. 2557–2567, 2007.
- [105] R. Reininger, K. Tan, and I. Coulthard, “An insertion device beamline for 5–250 eV at the Canadian Light Source,” *Review of Scientific Instruments*, vol. 73, no. 3, pp. 1489–1491, 2002.
- [106] R. Prasad, *Electronic Structure of Materials*. CRC press, 2013.
- [107] S. Cottenier, “Density functional theory and the family of (L)APW-methods: A step-by-step introduction,” *Instituut voor Kern-en Stralingsfysica, KU Leuven, Belgium*, vol. 4, no. 0, p. 41, 2002.
- [108] M. Born, “Quantenmechanik der stoßvorgänge,” *Zeitschrift für Physik*, vol. 38, no. 11, pp. 803–827, 1926.
- [109] W. Koch and M. C. Holthausen, *A chemist’s guide to density functional theory*, wiley, 2001.
- [110] N. Zettili, *Quantum mechanics: Concepts and applications*, 2003.
- [111] K. Capelle, “A bird’s-eye view of density-functional theory,” *Brazilian Journal of Physics*, vol. 36, pp. 1318–1343, 2006.
- [112] E. Schrödinger, “An undulatory theory of the mechanics of atoms and molecules,” *Physical Review*, vol. 28, no. 6, p. 1049, 1926.

- [113] P. Hohenberg and W. J. P. R. Kohn, “Density functional theory (DFT),” *Physics Review B*, vol. 136, p. 864, 1964.
- [114] W. Kohn, *Electronic Structure of Matter: Wave Functions and Density Functionals*. Norstedts Tryckeri, 1999.
- [115] W. Koch and M. C. Holthausen, *A Chemist’s Guide to Density Functional Theory*. John Wiley & Sons, 2015.
- [116] M. Born and R. Oppenheimer, “Zur quantentheorie der molekeln,” *Annalen der physik*, vol. 389, no. 20, pp. 457–484, 1927.
- [117] W. Kohn, A. D. Becke, and R. G. Parr, “Density functional theory of electronic structure,” *The Journal of Physical Chemistry*, vol. 100, no. 31, pp. 12 974–12 980, 1996.
- [118] W. Kohn and L. J. Sham, “Self-consistent equations including exchange and correlation effects,” *Physical Review*, vol. 140, no. 4A, A1133, 1965.
- [119] J. P. Perdew, K. Burke, and M. Ernzerhof, “Generalized gradient approximation made simple,” *Physical Review Letters*, vol. 77, no. 18, p. 3865, 1996.
- [120] J. P. Perdew and Y. Wang, “Pair-distribution function and its coupling-constant average for the spin-polarized electron gas,” *Physical Review B*, vol. 46, no. 20, p. 12 947, 1992.
- [121] A. D. Becke, “Density-functional exchange-energy approximation with correct asymptotic behavior,” *Physical Review A*, vol. 38, no. 6, p. 3098, 1988.
- [122] P. P. Rushton, “Towards a non-local density functional description of exchange and correlation,” Ph.D. dissertation, Durham University, 2002.
- [123] F. Tran and P. Blaha, “Accurate band gaps of semiconductors and insulators with a semilocal exchange-correlation potential,” *Physical Review Letters*, vol. 102, no. 22, p. 226 401, 2009.
- [124] A. D. Becke and E. R. Johnson, “A simple effective potential for exchange,” *The Journal of chemical physics*, vol. 124, no. 22, p. 221 101, 2006.
- [125] F. Tran and P. Blaha, “Importance of the kinetic energy density for band gap calculations in solids with density functional theory,” *The Journal of Physical Chemistry A*, vol. 121, no. 17, pp. 3318–3325, 2017.
- [126] K. Schwarz and P. Blaha, “Solid state calculations using WIEN2k,” *Computational Materials Science*, vol. 28, no. 2, pp. 259–273, 2003.
- [127] K. Schwarz, P. Blaha, and G. K. Madsen, “Electronic structure calculations of solids using the WIEN2k package for material sciences,” *Computer Physics Communications*, vol. 147, no. 1-2, pp. 71–76, 2002.
- [128] Y. Feng, P. Aliberti, B. P. Veetil, R. Patterson, S. Shrestha, M. A. Green, and G. Conibeer, “Non-ideal energy selective contacts and their effect on the performance of a hot carrier solar cell with an indium nitride absorber,” *Applied Physics Letters*, vol. 100, no. 5, p. 053 502, 2012.

- [129] S. C. Jain, M. Willander, J. Narayan, and R. V. Overstraeten, "III-nitrides: Growth, characterization, and properties," *Journal of Applied Physics*, vol. 87, no. 3, pp. 965–1006, 2000.
- [130] Y. Sayad, "Photovoltaic potential of III-nitride based tandem solar cells," *Journal of Science: Advanced Materials and Devices*, vol. 1, no. 3, pp. 379–381, 2016.
- [131] T. Yamaguchi, C. Morioka, K. Mizuo, M. Hori, T. Araki, Y. Nanishi, and A. Suzuki, "Growth of InN and InGaN on Si substrate for solar cell applications," in *Compound Semiconductors: Post-Conference Proceedings, 2003 International Symposium on*, IEEE, 2003, pp. 214–219.
- [132] A. Yamamoto, M. Tsujino, M. Ohkubo, and A. Hashimoto, "Metalorganic chemical vapor deposition growth of InN for InN/Si tandem solar cell," *Solar Energy Materials and Solar Cells*, vol. 35, pp. 53–60, 1994.
- [133] W. J. Lai, S. S. Li, C. C. Lin, C. C. Kuo, C. W. Chen, K. H. Chen, and L. C. Chen, "Near infrared photodetector based on polymer and indium nitride nanorod organic/inorganic hybrids," *Scripta Materialia*, vol. 63, no. 6, pp. 653–656, 2010.
- [134] E. Dimakis, A. Y. Nikiforov, C. Thomidis, L. Zhou, D. J. Smith, J. Abell, C. K. Kao, and T. D. Moustakas, "Growth and properties of near-UV light emitting diodes based on InN/GaN quantum wells," *Physica Status Solidi A*, vol. 205, no. 5, pp. 1070–1073, 2008.
- [135] J. Wu, W. Walukiewicz, K. M. Yu, J. W. Ager III, E. E. Haller, H. Lu, W. J. Schaff, Y. Saito, and Y. Nanishi, "Unusual properties of the fundamental band gap of InN," *Applied Physics Letters*, vol. 80, no. 21, pp. 3967–3969, 2002.
- [136] J. Wu, W. Walukiewicz, K. Yu, J. W. Ager III, E. E. Haller, H. Lu, and W. J. Schaff, "Small band gap bowing in $\text{In}_{1-x}\text{Ga}_x\text{N}$ alloys," *Applied Physics Letters*, vol. 80, no. 25, pp. 4741–4743, 2002.
- [137] V. Y. Davydov, A. A. Klochikhin, R. P. Seisyan, V. V. Emtsev, S. V. Ivanov, F. Bechstedt, J. Furthmüller, H. Harima, A. V. Mudryi, and J. Aderhold, "Absorption and emission of hexagonal InN. evidence of narrow fundamental band gap," *Physica Status Solidi B*, vol. 229, no. 3, R1–R3, 2002.
- [138] V. Y. Davydov, A. A. Klochikhin, V. V. Emtsev, D. A. Kurdyukov, S. V. Ivanov, V. A. Vekshin, F. Bechstedt, J. Furthmüller, J. Aderhold, and J. Graul, "Band gap of hexagonal InN and InGaN alloys," *Physica Status Solidi B*, vol. 234, no. 3, pp. 787–795, 2002.
- [139] L. F. J. Piper, L. Colakerol, T. Learmonth, P.-A. Glans, K. E. Smith, F. Fuchs, J. Furthmüller, F. Bechstedt, T.-C. Chen, and T. D. Moustakas, "Electronic structure of InN studied using soft x-ray emission, soft x-ray absorption, and quasiparticle band structure calculations," *Physical Review B*, vol. 76, no. 24, p. 245 204, 2007.

- [140] W. Walukiewicz, S. X. Li, J. Wu, K. M. Yu, J. W. Ager III, E. E. Haller, H. Lu, and W. J. Schaff, "Optical properties and electronic structure of InN and In-rich group III-nitride alloys," *Journal of Crystal Growth*, vol. 269, no. 1, pp. 119–127, 2004.
- [141] M. Hori, K. Kano, T. Yamaguchi, Y. Saito, T. Araki, Y. Nanishi, N. Teraguchi, and A. Suzuki, "Optical properties of $\text{In}_x\text{Ga}_{1-x}\text{N}$ with entire alloy composition on InN buffer layer grown by RF-MBE," *Physica Status Solidi B*, vol. 234, no. 3, pp. 750–754, 2002.
- [142] K. Scott, A. Butcher, M. Wintrebert Fouquet, P. P.-T. Chen, K. E. Prince, H. Timmers, S. K. Shrestha, T. V. Shubina, S. V. Ivanov, and R. Wuhrer, "Non-stoichiometry and non-homogeneity in InN," *Physica Status Solidi C*, vol. 2, no. 7, pp. 2263–2266, 2005.
- [143] T. V. Shubina, S. V. Ivanov, V. N. Jmerik, D. D. Solnyshkov, V. A. Vekshin, P. S. Kop'ev, A. Vasson, J. Leymarie, A. Kavokin, and H. Amano, "Mie resonances, infrared emission, and the band gap of InN," *Physical Review Letters*, vol. 92, no. 11, p. 117407, 2004.
- [144] K. L. Westra, R. P. W. Lawson, and M. J. Brett, "The effects of oxygen contamination on the properties of reactively sputtered indium nitride films," *Journal of Vacuum Science & Technology A: Vacuum, Surfaces, and Films*, vol. 6, no. 3, pp. 1730–1732, 1988.
- [145] K. Osamura, K. Nakajima, Y. Murakami, P. H. Shingu, and A. Ohtsuki, "Fundamental absorption edge in GaN, InN and their alloys," *Solid State Communications*, vol. 11, no. 5, pp. 617–621, 1972.
- [146] K. Osamura, S. Naka, and Y. Murakami, "Preparation and optical properties of $\text{Ga}_{1-x}\text{In}_x\text{N}$ thin films," *Journal of Applied Physics*, vol. 46, no. 8, pp. 3432–3437, 1975.
- [147] C. W. Pao, P. D. Babu, H. M. Tsai, J. W. Chiou, S. C. Ray, S. C. Yang, F. Z. Chien, W. F. Pong, M. H. Tsai, and C. W. Hsu, "Electronic structures of group-III-nitride nanorods studied by x-ray absorption, x-ray emission, and raman spectroscopy," *Applied Physics Letters*, vol. 88, no. 22, p. 223113, 2006.
- [148] Z. H. Lan, W. M. Wang, C. L. Sun, S. C. Shi, C. W. Hsu, T. T. Chen, K. H. Chen, C. C. Chen, Y. F. Chen, and L. C. Chen, "Growth mechanism, structure and IR photoluminescence studies of indium nitride nanorods," *Journal of Crystal Growth*, vol. 269, no. 1, pp. 87–94, 2004.
- [149] Q. X. Guo, T. Tanaka, M. Nishio, H. Ogawa, X. D. Pu, and W. Z. Shen, "Observation of visible luminescence from indium nitride at room temperature," *Applied Physics Letters*, vol. 86, no. 23, p. 231913, 2005.
- [150] T. L. Tansley and C. P. Foley, "Optical band gap of indium nitride," *Journal of Applied Physics*, vol. 59, no. 9, pp. 3241–3244, 1986.

- [151] M. Yoshimoto, H. Yamamoto, W. Huang, H. Harima, J. Saraie, A. Chayahara, and Y. Horino, “Widening of optical bandgap of polycrystalline InN with a few percent incorporation of oxygen,” *Applied Physics Letters*, vol. 83, no. 17, pp. 3480–3482, 2003.
- [152] Motlan, E. M. Goldys, and T. L. Tansley, “Optical and electrical properties of InN grown by radio-frequency reactive sputtering,” *Journal of Crystal Growth*, vol. 241, no. 1-2, pp. 165–170, 2002.
- [153] J. Hertrampf, P. Becker, M. Widenmeyer, A. Weidenkaff, E. Schlücker, and R. Niewa, “Ammonothermal crystal growth of indium nitride,” *Crystal Growth & Design*, vol. 18, no. 4, pp. 2365–2369, 2018.
- [154] Y. Hattori, J. F. D. Chubaci, M. Matsuoka, J. A. Freitas Jr, and A. F. da Silva, “Investigation of oxygen defects in wurtzite InN by using density functional theory,” *Journal of Crystal Growth*, vol. 456, pp. 168–173, 2016.
- [155] K. Amnuyswat, C. Saributr, P. Thanomngam, A. Sungthong, S. Porntheeraphat, S. Sopitpan, and J. Nukeaw, “XAFS analysis of indium oxynitride thin films grown on silicon substrates,” *X-Ray Spectrometry*, vol. 42, no. 2, pp. 87–92, 2013.
- [156] J. T-Thienprasert, J. Nukeaw, A. Sungthong, S. Porntheeraphat, S. Singkarat, D. Onkaw, S. Rujirawat, and S. Limpijumnong, “Local structure of indium oxynitride from x-ray absorption spectroscopy,” *Applied Physics Letters*, vol. 93, no. 5, p. 051 903, 2008.
- [157] Y. Yi, S. Cho, Y. Roh, M. Noh, C.-N. Whang, K. Jeong, and H.-J. Shin, “The instability of nitrogen bonds in oxygen incorporated InN_{1-x}O_x films,” *Japanese Journal of Applied Physics*, vol. 44, no. 1R, pp. 17–20, 2005.
- [158] T. De Boer, M. F. Bekheet, A. Gurlo, R. Riedel, and A. Moewes, “Band gap and electronic structure of cubic, rhombohedral, and orthorhombic In₂O₃ polymorphs: Experiment and theory,” *Physical Review B*, vol. 93, no. 15, p. 155 205, 2016.
- [159] F. Fuchs and F. Bechstedt, “Indium-oxide polymorphs from first principles: Quasiparticle electronic states,” *Physical Review B*, vol. 77, no. 15, p. 155 107, 2008.
- [160] V. Scherer, C. Janowitz, A. Krapf, H. Dwelk, D. Braun, and R. Manzke, “Transport and angular resolved photoemission measurements of the electronic properties of In₂O₃ bulk single crystals,” *Applied Physics Letters*, vol. 100, no. 21, p. 212 108, 2012.
- [161] P. D. C. King, T. D. Veal, F. Fuchs, C. Y. Wang, D. J. Payne, A. Bourlange, H. Zhang, G. R. Bell, V. Cimalla, and O. Ambacher, “Band gap, electronic structure, and surface electron accumulation of cubic and rhombohedral In₂O₃,” *Physical Review B*, vol. 79, no. 20, p. 205 211, 2009.

- [162] D. Wang, J. Yang, X. Li, J. Wang, R. Li, M. Cai, T. K. Sham, and X. Sun, "Observation of surface/defect states of SnO₂ nanowires on different substrates from x-ray excited optical luminescence," *Crystal Growth & Design*, vol. 12, no. 1, pp. 397–402, 2011.
- [163] Z. Wang, C. Li, L. Liu, and T. K. Sham, "Probing defect emissions in bulk, micro- and nano-sized α -Al₂O₃ via x-ray excited optical luminescence," *The Journal of Chemical Physics*, vol. 138, no. 8, p. 084706, 2013.
- [164] M. Amirhoseiny, Z. Hassan, and S. S. Ng, "Photoluminescence spectra of nitrogen-rich InN thin films grown on Si (110) and photoelectrochemical etched Si (110)," *Vacuum*, vol. 101, pp. 217–220, 2014.
- [165] W. D. Yang, K. W. Cheah, P. N. Wang, and F. M. Li, "Synthesis of oxygen-free nanosized InN by pulse discharge," *MRS Online Proceedings Library Archive*, vol. 693, 2001.
- [166] T. M. Tolhurst, P. Strobel, P. J. Schmidt, W. Schnick, and A. Moewes, "Direct measurements of energy levels and correlation with thermal quenching behavior in nitride phosphors," *Chemistry of Materials*, vol. 29, no. 18, pp. 7976–7983, 2017.
- [167] A. Qamar, K. LeBlanc, O. Semeniuk, A. Reznik, J. Lin, Y. Pan, and A. Moewes, "X-ray spectroscopic study of amorphous and polycrystalline PbO films, α -PbO, and β -PbO for direct conversion imaging," *Scientific Reports*, vol. 7, no. 1, p. 13159, 2017.
- [168] M. J. Ward, J. G. Smith, T. Z. Regier, and T. K. Sham, "2D XAFS-XEOL spectroscopy—some recent developments," *Journal of Physics: Conference Series*, vol. 425, no. 13, p. 132009, 2013.
- [169] P. Rinke, M. Scheffler, A. Qteish, M. Winkelkemper, D. Bimberg, and J. Neugebauer, "Band gap and band parameters of InN and GaN from quasiparticle energy calculations based on exact-exchange density-functional theory," *Applied Physics Letters*, vol. 89, no. 16, p. 161919, 2006.
- [170] P. Carrier and S. H. Wei, "Theoretical study of the band-gap anomaly of InN," *Journal of Applied Physics*, vol. 97, no. 3, p. 033707, 2005.
- [171] S. H. Wei, X. Nie, I. G. Batyrev, and S. B. Zhang, "Breakdown of the band-gap-common-cation rule: The origin of the small band gap of InN," *Physical Review B*, vol. 67, no. 16, p. 165209, 2003.
- [172] W. Paszkowicz, R. Černý, and S. Krukowski, "Rietveld refinement for indium nitride in the 105–295 K range," *Powder Diffraction*, vol. 18, no. 2, pp. 114–121, 2003.
- [173] K. Schwarz, P. Blaha, and G. K. H. Madsen, "Electronic structure calculations of solids using the WIEN2k package for material sciences," *Computer Physics Communications*, vol. 147, no. 1-2, pp. 71–76, 2002.
- [174] J. P. Perdew, K. Burke, and M. Ernzerhof, "Generalized gradient approximation made simple," *Physical Review Letters*, vol. 77, no. 18, p. 3865, 1996.

- [175] K. Schwarz, A. Neckel, and J. Nordgren, "On the x-ray emission spectra from FeAl," *Journal of Physics F: Metal Physics*, vol. 9, no. 12, pp. 2509–2521, 1979.
- [176] J. A. McLeod, R. J. Green, E. Z. Kurmaev, N. Kumada, A. A. Belik, and A. Moewes, "Band-gap engineering in TiO₂-based ternary oxides," *Physical Review B*, vol. 85, no. 19, p. 195201, 2012.
- [177] G. D. Mahan, "Final-state potential in x-ray spectra," *Physical Review B*, vol. 21, no. 4, p. 1421, 1980.
- [178] U. von Barth and G. Grossmann, "Dynamical effects in x-ray spectra and the final-state rule," *Physical Review B*, vol. 25, no. 8, pp. 5150–5179, 1982.
- [179] J. P. Perdew, R. G. Parr, M. Levy, and J. L. Balduz Jr, "Density-functional theory for fractional particle number: Derivative discontinuities of the energy," *Physical Review Letters*, vol. 49, no. 23, pp. 1691–1694, 1982.
- [180] Q. Guo and A. Yoshida, "Temperature dependence of band gap change in InN and AlN," *Japanese Journal of Applied Physics*, vol. 33, no. 5R, pp. 2453–2456, 1994.
- [181] B. L. Henke, E. M. Gullikson, and J. C. Davis, "X-ray interactions: Photoabsorption, scattering, transmission and reflection E= 50-30,000 eV, Z= 1-92," *Atomic Data and Nuclear Data Tables*, vol. 54, no. 2, pp. 181–342, 1993.
- [182] A. El Hichou, M. Addou, M. Mansori, and J. Ebothé, "Structural, optical and luminescent characteristics of sprayed fluorine-doped In₂O₃ thin films for solar cells," *Solar Energy Materials and Solar Cells*, vol. 93, no. 5, pp. 609–612, 2009.
- [183] M. S. Lee, W. C. Choi, E. K. Kim, C. K. Kim, and S. K. Min, "Characterization of the oxidized indium thin films with thermal oxidation," *Thin Solid Films*, vol. 279, no. 1-2, pp. 1–3, 1996.
- [184] S. T. Jean and Y. C. Her, "Growth mechanism and photoluminescence properties of In₂O₃ nanotowers," *Crystal Growth & Design*, vol. 10, no. 5, pp. 2104–2110, 2010.
- [185] Z. P. Wei, D. L. Guo, B. Liu, R. Chen, L. M. Wong, W. F. Yang, S. J. Wang, H. D. Sun, and T. Wu, "Ultraviolet light emission and excitonic fine structures in ultrathin single-crystalline indium oxide nanowires," *Applied Physics Letters*, vol. 96, no. 3, p. 031902, 2010.
- [186] M. J. Zheng, L. D. Zhang, G. H. Li, X. Y. Zhang, and X. F. Wang, "Ordered indium-oxide nanowire arrays and their photoluminescence properties," *Applied Physics Letters*, vol. 79, no. 6, pp. 839–841, 2001.
- [187] C. Wang, D. Chen, and X. Jiao, "Flower-like In₂O₃ nanostructures derived from novel precursor: Synthesis, characterization, and formation mechanism," *The Journal of Physical Chemistry C*, vol. 113, no. 18, pp. 7714–7718, 2009.

- [188] C. Braun, S. L. Börger, T. D. Boyko, G. Mieke, H. Ehrenberg, P. Höhn, A. Moewes, and W. Schnick, “Ca₃N₂ and Mg₃N₂: Unpredicted high-pressure behavior of binary nitrides,” *Journal of the American Chemical Society*, vol. 133, no. 12, pp. 4307–4315, 2011.
- [189] P. Glans, P. Skytt, K. Gunnelin, J. H. Guo, and J. Nordgren, “Selectively excited x-ray emission spectra of N₂,” *Journal of Electron Spectroscopy and Related Phenomena*, vol. 82, p. 193, 1996.
- [190] S. Ye, F. Xiao, Y. X. Pan, Y. Y. Ma, and Q. Y. Zhang, “Phosphors in phosphor-converted white light-emitting diodes: Recent advances in materials, techniques and properties,” *Materials Science and Engineering: R: Reports*, vol. 71, no. 1, pp. 1–34, 2010.
- [191] C. C. Lin and R. S. Liu, “Advances in phosphors for light-emitting diodes,” *The Journal of Physical Chemistry Letters*, vol. 2, no. 11, pp. 1268–1277, 2011.
- [192] H. Huppertz and W. Schnick, “Eu₂Si₅N₈ and EuYbSi₄N₇. the first nitridosilicates with a divalent rare earth metal,” *Acta Crystallographica Section C: Crystal Structure Communications*, vol. 53, no. 12, pp. 1751–1753, 1997.
- [193] R. J. Xie, N. Hirosaki, T. Suehiro, F. F. Xu, and M. Mitomo, “A simple, efficient synthetic route to Sr₂Si₅N₈:Eu²⁺-based red phosphors for white light-emitting diodes,” *Chemistry of Materials*, vol. 18, no. 23, pp. 5578–5583, 2006.
- [194] H. A. Höpfe, H. Lutz, P. Morys, W. Schnick, and A. Seilmeier, “Luminescence in Eu²⁺-doped Ba₂Si₅N₈: Fluorescence, thermoluminescence, and upconversion,” *Journal of Physics and Chemistry of Solids*, vol. 61, no. 12, pp. 2001–2006, 2000.
- [195] H. Watanabe and N. Kijima, “Crystal structure and luminescence properties of Sr_xCa_{1-x}AlSiN₃:Eu²⁺ mixed nitride phosphors,” *Journal of Alloys and Compounds*, vol. 475, no. 1-2, pp. 434–439, 2009.
- [196] J. Liang, B. Devakumar, L. Sun, Q. Sun, S. Wang, and X. Huang, “Novel Mn⁴⁺ doped Ca₂GdSbO₆ red-emitting phosphor: A potential color converter for light-emitting diodes,” *Journal of the American Ceramic Society*, vol. 102, no. 8, pp. 4730–4736, 2019.
- [197] N. C. George, K. A. Denault, and R. Seshadri, “Phosphors for solid-state white lighting,” *Annual Review of Materials Research*, vol. 43, pp. 481–501, 2013.
- [198] J. Tauc, R. Grigorovici, and A. Vancu, “Optical properties and electronic structure of amorphous germanium,” *Physica Status Solidi B*, vol. 15, no. 2, pp. 627–637, 1966.
- [199] S. Kalyanaraman, P. M. Shajinshinu, and S. Vijayalakshmi, “Refractive index, band gap energy, dielectric constant and polarizability calculations of ferroelectric ethylenediaminium tetrachlorozincate crystal,” *Journal of Physics and Chemistry of Solids*, vol. 86, pp. 108–113, 2015.

- [200] M. Sathya and K. Pushpanathan, "Synthesis and optical properties of Pb doped ZnO nanoparticles," *Applied Surface Science*, vol. 449, pp. 346–357, 2018.
- [201] A. Modwi, M. A. Ghanem, A. M. Al-Mayouf, and A. Houas, "Lowering energy band gap and enhancing photocatalytic properties of Cu/ZnO composite decorated by transition metals," *Journal of Molecular Structure*, vol. 1173, pp. 1–6, 2018.
- [202] J. Pawlak, S. K. J. Al Ani, *et al.*, "Inverse logarithmic derivative method for determining the energy gap and the type of electron transitions as an alternative to the tauc method," *Optical Materials*, vol. 88, pp. 667–673, 2019.
- [203] R. J. Green, T. Z. Regier, B. Leedahl, J. A. McLeod, X. H. Xu, G. S. Chang, E. Z. Kurmaev, and A. Moewes, "Adjacent Fe-vacancy interactions as the origin of room temperature ferromagnetism in $(\text{In}_{1-x}\text{Fe}_x)_2\text{O}_3$," *Physical Review Letters*, vol. 115, no. 16, p. 167 401, 2015.
- [204] P. Strobel, S. Schmiechen, M. Siegert, A. Tucks, P. J. Schmidt, and W. Schnick, "Narrow-band green emitting nitridolithoalumosilicate $\text{Ba}[\text{Li}_2(\text{Al}_2\text{Si}_2)\text{N}_6]:\text{Eu}^{2+}$ with framework topology whj for LED/LCD-backlighting applications," *Chemistry of Materials*, vol. 27, no. 17, pp. 6109–6115, 2015.
- [205] M. Pattison, M. Hansen, N. Bardsley, C. Elliott, K. Lee, L. Pattison, and J. Tsao, "2019 lighting R & D opportunities. *doe bto lighting r & d program*; US department of energy," Jan. 2020.
- [206] J. L. Leano Jr, M. H. Fang, and R. S. Liu, "Critical review-narrow-band emission of nitride phosphors for light-emitting diodes: Perspectives and opportunities," *ECS J. Solid State Sci. Technol.*, vol. 7, no. 1, R3111–R3133, 2017.
- [207] J. McKittrick, M. E. Hannah, A. Piquette, J. K. Han, J. I. Choi, M. Anc, M. Galvez, H. Lugauer, J. B. Talbot, and K. C. Mishra, "Phosphor selection considerations for near-UV LED solid state lighting," *ECS Journal of Solid State Science and Technology*, vol. 2, no. 2, R3119–R3131, 2012.
- [208] A. Piquette, W. Bergbauer, B. Galler, and K. C. Mishra, "On choosing phosphors for near-UV and blue LEDs for white light," *ECS Journal of Solid State Science and Technology*, vol. 5, no. 1, R3146–R3159, 2015.
- [209] E. Elzer, R. Niklaus, P. J. Strobel, V. Weiler, P. J. Schmidt, and W. Schnick, " $\text{MBe}_{20}\text{N}_{14}:\text{Eu}^{2+}$ (M= Sr, Ba): Highly condensed nitridoberyllates with exceptional highly energetic Eu^{2+} luminescence," *Chemistry of Materials*, vol. 31, no. 9, pp. 3174–3182, 2019.
- [210] A. F. Ismail, K. C. Khulbe, and T. Matsuura, *Gas Separation Membranes*. Springer, Switzerland, 2015.

- [211] H. Ramanantoanina, M. Sahnoun, A. Barbiero, M. Ferbinteanu, and F. Cimpoesu, “Development and applications of the LFDFT: The non-empirical account of ligand field and the simulation of the f - d transitions by density functional theory,” *Physical Chemistry Chemical Physics*, vol. 17, no. 28, pp. 18 547–18 557, 2015.
- [212] W. A. Harrison, *Electronic Structure and the Properties of Solids: the Physics of the Chemical Bond*. Dover Publication INC, New York, 2012.
- [213] G. Blasse and B. C. Grabmaier, *A General Introduction to Luminescent Materials*. Springer-Verlag Berlin, Heidelberg, 1994.
- [214] P. F. Smet, J. E. Van Haecke, F. Loncke, H. Vrielinck, F. Callens, and D. Poelman, “Anomalous photoluminescence in BaS: Eu,” *Physical Review B*, vol. 74, no. 3, p. 035 207, 2006.
- [215] D. Dutczak, C. Ronda, T. Justel, and A. Meijerink, “Anomalous trapped exciton and d-f emission in $\text{Sr}_4\text{Al}_{14}\text{O}_{25}$: Eu^{2+} ,” *The Journal of Physical Chemistry A*, vol. 118, no. 9, pp. 1617–1621, 2014.
- [216] B. Moine, C. Pedrini, and B. Courtois, “Photoionization and luminescences in $\text{BaF}_2\text{:Eu}^{2+}$,” *Journal of Luminescence*, vol. 50, no. 1, pp. 31–38, 1991.
- [217] M. Dadsetani, S. Namjoo, and H. Nejati, “Optical study of filled tetrahedral compounds Li_3AlN_2 and Li_3GaN_2 ,” *Journal of Electronic Materials*, vol. 39, no. 8, pp. 1186–1193, 2010.
- [218] U. Happek, S. A. Basun, J. Choi, J. K. Krebs, and M. Raukas, “Electron transfer processes in rare earth doped insulators,” *Journal of Alloys and Compounds*, vol. 303, pp. 198–206, 2000.
- [219] C. W. Thiel, Y. Sun, and R. L. Cone, “Progress in relating rare-earth ion $4f$ and $5d$ energy levels to host bands in optical materials for hole burning, quantum information and phosphors,” *Journal of Modern Optics*, vol. 49, no. 14-15, pp. 2399–2412, 2002.
- [220] M. Amachraa, Z. Wang, C. Chen, S. Hariyani, H. Tang, J. Brgoch, and S. P. Ong, “Predicting thermal quenching in inorganic phosphors,” *Chemistry of Materials*, vol. 32, no. 14, pp. 6256–6265, 2020.
- [221] R. Shafei, D. Maganas, P. J. Strobel, P. J. Schmidt, W. Schnick, and F. Neese, “Electronic and optical properties of Eu^{2+} -activated narrow-band phosphors for phosphor-converted light-emitting diode applications: Insights from a theoretical spectroscopy perspective,” *Journal of the American Chemical Society*, vol. 144, no. 18, pp. 8038–8053, 2022.

Appendix A: Copyright Information

A.1 Copyright Agreements for Reproduced Articles

A.1.1 Journal of Physical Chemistry C

- In Chapter 4, the manuscript “Bandgap and Electronic Structure Determination of Oxygen - Containing Ammonothermal InN: Experiment and Theory” has been published by the American Chemical Society. The following statement is included to permit reproduction in this thesis: Reprinted with permission from Bandgap and Electronic Structure Determination of Oxygen - Containing Ammonothermal InN: Experiment and Theory, *The Journal of Physical Chemistry C* **2019**, 123, 89438950 [82]. Copyright (2019) by American Chemical Society.
- In Chapter 6, the manuscript “Unraveling the Energy Levels of Eu^{2+} -ions in $\text{MBe}_{20}\text{N}_{14}:\text{Eu}^{2+}$ ($M = \text{Sr}, \text{Ba}$) Phosphors” has been published by the American Chemical Society. The following statement is included to permit reproduction in this thesis: Reprinted with permission from Unraveling the Energy Levels of Eu^{2+} -ions in $\text{MBe}_{20}\text{N}_{14}:\text{Eu}^{2+}$ ($M = \text{Sr}, \text{Ba}$) Phosphors, *The Journal of Physical Chemistry C* **2021**, 125, 1182811837 [66]. Copyright (2021) by American Chemical Society.

A.1.2 Journal of Material Chemistry C

The article in Chapter 7 (reference [83]) was originally published in *Journal of Material Chemistry C*. It is published by the Royal Society of Chemistry. It is reproduced from Ref. [83] with permission from The Royal Society of Chemistry.

A.1.3 Advanced Optical Materials

The article reproduced in chapter 5 [reference [65]] was originally published in *Advanced Optical Materials* by Wiley-VCH. As an author, I can include this article in my thesis. Here, the article is reproduced by permission of Wiley-VCH:

As a Wiley author, you retain certain reuse rights when you sign your Copyright Transfer Agreement (CTA). Refer back to this agreement if you are seeking permission to:

- Republish an extract of your own published work.
- Include your article in your thesis.
- Use copies for your internal teaching purposes.

Quoted from: <https://www.wiley.com/en-ca/permissions/Author-of-Work>

A.2 Permissions to Reproduce Figures

- Fig. 1.1 is taken from Ref. [23] with permission provided by Journal of Display Technology. The license number is 1231594.
- Fig. 1.2 is taken from Ref. [26] with permission provided by Nature Materials and Copyright Clearance Center. The license number is 5325790252053.
- Fig. 1.3 is adapted from Ref. [34]. Reprinted figure with permission from L. Wang *et al.*, Chemical Reviews, 118, 1951–2009 (2018). Copyright (2018) by American Chemical Society.
- Fig. 1.4 is adapted from Ref. [34]. Reprinted figure with permission from L. Wang *et al.*, Chemical Reviews, 118, 1951–2009 (2018). Copyright (2018) by American Chemical Society.
- Fig. 1.5 is adapted from Ref. [59]. Reprinted figure with permission from S. Ponce *et al.*, Journal of Physical Chemistry C, 120, 4040–4047 (2016). Copyright (2016) by American Chemical Society.
- Fig. 2.1 is reprinted from Ref. [91] with permission provided by Wiley Books and Copyright Clearance Center. The license number is 5325751163409.
- Fig. 2.6 is reprinted from Ref. [91] with permission provided by Wiley Books and Copyright Clearance Center. The license number is 5325751163409.